The Dissertation Committee for Yazhi Zhu Certifies that this is the approved version of the following dissertation:

Studies on Strain Localization, Ductile Fracture and Damage in Structural Metals

Committee:

Michael D. Engelhardt, Supervisor

Todd A. Helwig

Eric B. Williamson

Patricia M. Clayton

Eric M. Taleff

Studies on Strain Localization, Ductile Fracture and Damage in Structural Metals

by

Yazhi Zhu

Dissertation

Presented to the Faculty of the Graduate School of

The University of Texas at Austin

in Partial Fulfillment

of the Requirements

for the Degree of

Doctor of Philosophy

The University of Texas at Austin

August 2017

Dedication

To my beloved family members

Acknowledgements

I would like to express my gratitude and appreciation, but cannot find any simple words, to my supervisor Dr. Michael Engelhardt for his support, encouragement, and guidance to the current research work. His kindness, wisdom, and diligence motivated me to live, study and work in the way it should be during the past four years when I was in Austin. All his admirable personalities, graciousness, full of responsibility, will discipline myself to be the person like him for the rest of my life.

I would also like to acknowledge my committee members: Dr. Todd Helwig, Dr. Eric Williamson, Dr. Patricia Clayton, Dr. Eric Taleff for their helpful discussion and guidance for the dissertation, without which this dissertation would have been impossible.

I also acknowledge the National Science Foundation for partial support of this work under Award No. 1344592.

I would also like to thank professor Shao-ping Meng, professor Zhen Zhou at my previous university, Southeast University. Without their care, support, and assistance, I would have never been here to write this dissertation in Austin. I am also grateful to Mr. Canjun Li and Mr. Chao Wu for their assistance of testing at Southeast University. I acknowledge my best friend Mr. Hao Hong for his continuous help during the past ten years. I am grateful to my fellow students and best friends from my hometown for their friendship given to me and their support.

Finally, I would like to express my gratitude to my parents, my wife and my son Mr. Zicheng Zhu, the cutest boy I have ever seen, for their strong and consistent love, moral support that get me persisted in the dream I am fighting for.

Studies on Strain Localization, Ductile Fracture and Damage in Structural Metals

Yazhi Zhu, Ph.D.

The University of Texas at Austin, 2017

Supervisor: Michael D. Engelhardt

One of the most important limit states in structural metals is ductile fracture, and the prediction of ductile fracture is of great importance in many engineering applications. The overall objective of the research reported in this dissertation is to advance the understanding and modeling of ductile fracture in metals. This research addresses three main issues: micromechanical modeling of ductile fracture, the development of a micromechanics-based ductile fracture model and its numerical implementation, and a numerical investigation of geometry and damage induced strain localization based on a nonlocal formulation.

It has long been recognized that stress triaxiality is a key parameter affecting initiation of ductile fracture. More recently, shear stress has been identified as another important parameter, in addition to stress triaxiality, that influences the process of ductile fracture. In this research, a micromechanics-based model is proposed for predicting initiation of ductile fracture that couples both stress triaxiality and shear stress. The new model is based on a combination of the existing Rice-Tracey and modified maximum shear stress models. The new model is applied to construct the fracture locus of different types of metal alloys and is used to predict fracture initiation by numerical tools. The predicted

results are in good agreement with experimental data reported in literature that covers a wide range of triaxialities and shear stress.

Another portion of this research, within the framework of micromechanics, investigated the effect of combined normal and shear stress components on micro-void evolution and material behavior. This work involved finite element modeling of a cubic unit cell associated with a spherical void. The results show that the void growth process and macroscopic stress-strain response is highly dependent on the shear stress component. At different ranges of triaxialities, and with different void growth and coalescence mechanisms, shear stress has an important effect on the ductile fracture process.

Numerical modeling of strain localization in ductile metals based on standard continuum mechanics exhibits non-convergent mesh sensitivity. This issue is addressed in the final portion of this research. A one-dimensional model based on the nonlocal theory is proposed to analyze geometry-induced strain localization, i.e., necking in structural metals. A nonlocal continuum damage model using the same enhanced continuum law is developed to deal with the damage induced strain localization in metals. Both models provide encouraging performance in eliminating the non-convergent mesh sensitivity problem. Such improved strain localization modeling techniques show potential to be useful for further exploration of ductile fracture phenomena.

Table of Contents

List of Tables

List of Figures

CHAPTER 1

Introduction

1.1 IMPORTANCE OF DUCTILE FRACTURE

Fracture is an important failure mode in many components and structures, including steel structures, concrete structures, ships, cars, and many others. The focus of this dissertation is fracture of steel and other ductile metals. Some examples of fractures in structural steel components are shown in Fig. 1.1. In a common sense, fracture is understood as the separation of an intact object or material. This physical phenomenon, in most situations, is undesirable since it can lead to collapse of structures. The investigation of fracture serves to reveal the limitations of the strength of materials, to identify the ultimate state of structural components, and to predict, and if possible, to prevent any potential dangers imposed to the systems.

The study of fracture has a long history. Considerable development in the fracture studies can be traced back to World War II when fracture mechanics was treated as a critical subject. At that period, however, the existing fracture approaches were only applicable to materials where fracture occurs nominally in the elastic range of behavior. These early approaches in linear elastic fracture mechanics (LEFM) were then extended to account for material nonlinearity, e.g. nonlinear elastic and plastic behaviors, which gave rise to elastic-plastic fracture mechanics (EPFM) since 1960s. Two most common parameters in EPFM are the crack-tip-opening displacement (CTOD) and the *J*-contour integral, each of which is used to quantify the fracture toughness in elastic-plastic materials, and is used as a fracture criterion.

(a) Fracture in web of a stiffened steel beam (Okazaki, 2004)

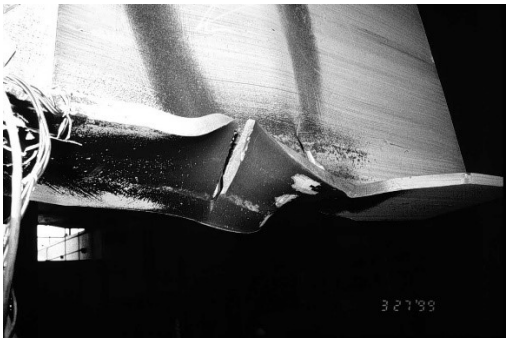

(b) Fracture in flange of a steel beam (Engelhardt et al., 2000)

(c) Fracture of a steel member in an earthquake (Clifton et al., 2011)

Fig. 1.1 Examples of fractures in structural steel components

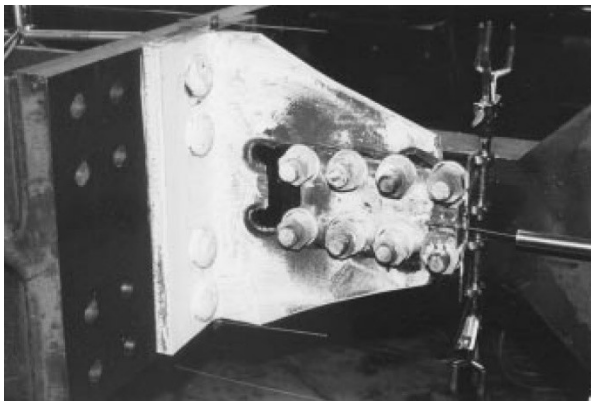

(d) Block shear fracture in bolted connection (Swanson and Leon, 2000)

Fig. 1.1, cont.

Fracture mechanisms are of great complexity and variety, and are strongly dependent on the materials themselves, the geometry of the component, and the state of stress and strain. For materials experiencing fracture in the elastic range, LEFM is usually used to describe the fracture process. Such phenomena are generally understood as brittle fracture.

In contrast to brittle fracture, the study described in this dissertation focuses on structural metals that undergo extensive plastic deformation before fracture, a process referred to as ductile fracture. When examining ductile fracture in a large-scale structure with limited yielding or in a small-scale component, conventional fracture mechanics in terms of EPFM provides a tool to describe the fracture process without providing the microscopic details of fracture. However, fracture mechanics parameters such as CTOD are less applicable when used to predict fracture following the development of extensive plastic deformation. The critical value of parameter such as CTOD from a test specimen, which is considered as a material constant in EPFM, is no longer adequate to indicate the behavior of a structure made from the same material. Several alternatives to the single

parameter fracture mechanics measures have been developed for the case of ductile fracture, motivated by a more fundamental understanding of the microscopic mechanisms of fracture.

1.2 RESEARCH OBJECTIVE

With the help of increasingly advanced computing technologies, it is possible to facilitate exploration of ductile fracture in metals at the micromechanical level, both for studying the physical mechanisms of fracture and for predicting fracture phenomena. Micromechanics-based models are therefore developed based on microscopic observations and are applied to capture fracture events in ductile solids using the finite element method. Challenges remain due to an incomplete understanding of the physical mechanisms of ductile fracture and their influence on the indicators to quantify the fracture process. Further challenges exist in the numeral implementation of ductile fracture models in finite element analysis.

Ductile fracture has generally been attributed to a mechanism involving void nucleation, growth and coalescence, and this mechanism provides the basis of many current models for ductile fracture. Nonetheless, the roles of stress and strain parameters in this mechanism are not fully understood. The objective of this dissertation is to develop a phenomenological model to predict the initiation of ductile fracture in metals that builds on current knowledge of fracture mechanisms, with the goal of improving predictive accuracy while avoiding excessive computational cost. The proposed model is expected to be suitable for numerical implementation and have model parameters that are relatively easy to calibrate. Another objective of this dissertation makes effort is to provide deeper insight into the fracture mechanisms by studying void evolution using micromechanical

modeling based on a finite element platform. The benefit of this approach provides a straightforward examination on the roles of stress states on void evolution. The stress states under investigation are not only the common variables in terms of stress triaxiality and Lode parameter, but also include the shear stress ratio. Ductile fracture mechanisms are strongly related the evolution of void shape and dimensions. Studying the behavior of the numerical micromechanical model leads to observations about fracture mechanisms under more complex loading conditions. Of particular interest in this dissertation is the effect of shear stress on void growth and coalescence over a wide range of triaxiality.

The character of strain localization in structural metals is significant and cannot be neglected if one is to study the ultimate behavior of materials, since the strain localization phenomenon is always the precursor of ductile fracture events. This kind of instability in structural metals can be induced by geometric nonlinearity, internal damage accumulation and thermal factors. This dissertation will examine geometry and damage induced strain localization. When reproducing the strain localization phenomenon in numerical simulations, enhanced constitutive relations are needed to overcome numerical difficulties raised by the standard continuum law. This dissertation aims to introduce the nonlocal formulation to the current local material behavior, to develop plasticity models appropriate for simulation of strain localization. The models are intended to accurately capture strain localization, for example, necking in a standard tensile test, while overcoming numerical difficulties of conventional FE approaches, to give a more reasonable indicator of ductile damage and fracture initiation.

1.3 OUTLINE OF DISSERTATION

Chapter 2 summarizes previous work in fracture prediction. A brief review of classical methods for prediction of brittle fracture is provided. This is followed by more detailed and extensive review of previous work on ductile fracture in metals. Some popular models for ductile fracture and damage are discussed in the context of physical observations and predictive performance. Mechanisms of the ductile fracture process are described. The current state of research in micromechanical modeling as well as analytical solutions for microvoid evolution are presented. The strain localization phenomenon in structural metals is discussed, along with the mechanisms of strain localization and numerical issues that arise in the simulation of strain localization.

Chapter 3 proposes a new micromechanics-based ductile fracture model. The ductile fracture micro-mechanisms are briefly reviewed, where the role of shear stress in the fracture process is highlighted. Two popular existing models including the void growth model and the maximum shear stress model are reviewed and provide the basis of the new model. The proposed model couples two important variables; triaxiality and a shear stress related factor. Some details of the proposed model, such as the model parametric behaviors, the stress state dependency, the bounds of fracture locus predicted by the model and its correlation to the physical observations are discussed. A validation analysis is performed by predicting ductile facture in three different metals. The characteristics of fracture in those materials is investigated.

Chapter 4 presents the application of the proposed criterion in chapter 3 to predict ductile fracture using the finite element method. Two representative series of ductile fracture tests covering different loading cases, which also refer to two different metal materials, are adopted. The stress and strain evolution in each specimen is monitored and

characterized. The methodology of fracture initiation determination is discussed. By evaluating the predictive performance of both the proposed model and the void growth model, the important role of the shear stress factor is emphasized.

Chapter 5 presents micromechanical modeling of void growth and coalescence to provide a better understanding of the shear stress effect on the ductile fracture process. The approach used in this chapter is to develop a finite element model of the representative volume element with a void embedded. Besides the normal stress components, shear stress is also applied to the numerical model. The global mechanical behavior of the unit cell under various triaxialities, Lode parameter and shear stress ratios is studied. The dimension, shape and location of the void during the loading history is investigated to characterize the mechanisms of void growth and coalescence under combined normal and shear stress.

Chapter 6 proposes a one-dimensional model to deal with the post-necking analysis for the uniaxial tension bar in structural metals. The model is constructed within the nonlocal framework and concentrates on the mesh dependency issue in structural metals, which rises when modeling such necking type of geometric induced strain localization by the standard continuum law. The source of mesh dependency based on the local constitutive law is first studied by analytical approaches. Subsequently, analytical solutions using a nonlocal approach for the length of the necking region is presented. A FE one-dimensional model is then used to show the mesh sensitivity of the global mechanical response, the length of necking region and the plastic strain profile.

Chapter 7 presents a continuum damage model for finite strain elastoplasticity. The model considers the shear stress effect on the fracture process, handles the damage induced strain localization in structural metals, and is also established within the nonlocal

framework. The model describes the continuous stress degradation process during the loading history before and after fracture initiation. To improve the accuracy of the results, the arbitrary Lagrangian-Eulerian method is employed to improve the mesh quality during simulation. Two numerical examples, i.e., uniaxial tension tests on a rectangular plate and a notched round bar, are given to demonstrate the performance of this nonlocal and ALE coupled continuum damage model.

Chapter 8 presents the summary and conclusions. The work done in this study as well as the major conclusions and limitations are summarized. Recommendations for future research on the prediction of ductile fracture in metals are discussed.

CHAPTER 2

Background on Current State of Research in Ductile Fracture of Structural Metals

2.1 CONVENTIONAL FRACTURE MECHANICS

Fracture mechanics is a relatively recently established subject. An early significant development in this field was the energy balance criterion proposed by Griffith (1921). Griffith's concept led to many subsequent developments in fracture mechanics. Orowan (1949) modified the Griffith theory by incorporating local plastic flow. Mott (1948) applied the Griffith concept to solve the problem of a rapidly propagating crack. Irwin (1956) proposed the energy release rate concept based on the Griffith theory to facilitate engineering applications. Irwin (1957) suggested the stress at the crack-tip can be related to the crack length by a single parameter known as the stress-intensity factor. The need for engineering applications in 1960s motivated researchers to focus on fracture with plasticity.

When predicting fracture in a highly ductile material, where plasticity drives failure, linear elastic fracture mechanics (LEFM) has limitations. To address some of these limitations, Wells (1961) proposed a crack-tip-opening displacement (CTOD) related criterion as a measure of facture toughness for inelastic materials. Rice (1968) developed another concept to quantify the fracture toughness of nonlinear materials. The concept, known as the *J*-integral, involves the energy release rate evaluated by an integral along an arbitrary path around the crack tip. The CTOD and the *J*-integral are two important parameters in elastic-plastic fracture mechanics (EPFM) and are two main criteria to

characterize crack-tip conditions in nonlinear materials. Despite some limitations in their applicability, these two approaches are still useful for a wide range of materials.

2.1.1 Linear Elastic Fracture Mechanics

Stress concentrations

It was believed at the beginning of the twentieth century that the fracture occurred when the stresses at the atomic level were sufficient to break the bonds among atoms and when there existed flaws that the local stresses were magnified to be many times higher than the globally applied stresses. Inglis (1913) quantitatively studied the stress concentration effect of flaws by analyzing elliptical holes in flat plates (see Fig. 2.1) and gave the expression of the stress around the hole:

$$\sigma_a = \kappa\sigma = \sigma\left(1 + 2\sqrt{\frac{c}{\rho}}\right) \tag{2.1}$$

In this equation, c is the long dimension of the hole and ρ is the radius of the curvature at the tip a. The factor κ in Eq. (2.1) is defined as the stress concentration factor, where κ=3 for a circular hole.

When this approach is applied to calculate the stress concentration at an infinitely sharp crack, where ρ=0, the predicted stress tends to infinity, implying that a material with a sharp crack would break under an infinitesimal load. Also, as can be seen from Eq. (2.1), the stress concentration factor depends only on the geometric shape, not the absolute dimension of the crack. In fact, a long crack propagates more easily than short crack. These shortcomings in Inglis's approach to predict fracture subsequently led Griffith to explore fracture based on the energy principles rather than the stress field.

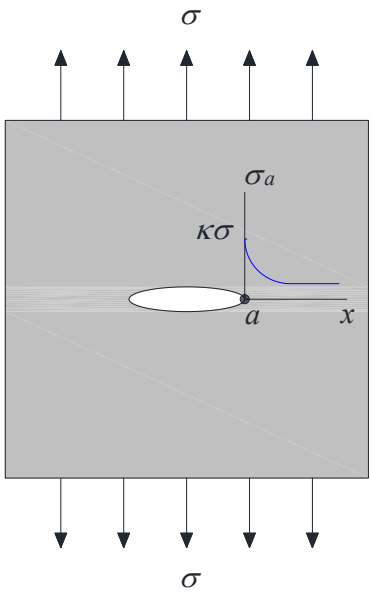

Fig. 2.1 Stress concentration around an elliptical hole in a flat plate.

Griffith's energy balance

Griffith's analysis (Griffith, 1921) was based on the first law of thermodynamics, which points out the principle of net energy decrease when a system transfers from a nonequilibrium state to equilibrium. Accordingly, the amount of strain energy reduction due to the extension of a crack must be equal to or greater than the amount of the surface energy increment required by the new crack, which reads

$$\frac{dW_s}{dc} \geq \frac{dW_\gamma}{dc} \tag{2.2}$$

where W_s is the strain energy, W_γ is the surface energy and dc is the increment of crack length. Considering a plate with a $2c$ long sharp crack that is subjected to a uniform stress σ, Griffith followed Inglis's stress field derivation and obtained the strain energy released in a unit width

$$W_s = \frac{\pi \sigma_a^2 c^2}{E} \tag{2.3}$$

where E is the modulus of elasticity. The total surface energy required to create two new surfaces when the crack forms is given as

$$W_\gamma = 4\gamma c \tag{2.4}$$

where γ is the surface energy of the material. Substituting Eq. (2.3) and (2.4) into Eq. (2.2), and using the concept of minimum potential energy, the critical condition for a stable equilibrium reads:

$$\sigma_a \sqrt{c} = \sqrt{\frac{2E\gamma}{\pi}} \tag{2.5}$$

The above expression gives the relation between the fracture stress on the crack tip and the crack length for the plane stress case. The apparent difference of Griffith's energy criterion from the local stress approach is that the fracture stress depends on the absolute size of crack and is insensitive to the radius of the curvature at the tip. For a crack with a given length and an extremely small ρ, Griffith's criterion reduces the fracture strength by hundreds or thousands of times of which predicted by the local stress approach.

Stress intensity factor

While the energy balance approach gives insights into stress at the crack tip, an extension is to quantitatively determine the stress state in the vicinity of a sharp crack. In general, the modes of a crack are classified into three types, i.e., mode I (in-plane opening), mode II (in-plane shear) and mode III (out-of-plane shear). The main interest in this section is the first one. Defining a local coordinate with the origin at the crack tip (see Fig. 2.2), the in-plane stress components are given as

$$\sigma_{xx} = \frac{K_I}{\sqrt{2\pi r}}\cos\frac{\theta}{2}\left(1-\sin\frac{\theta}{2}\sin\frac{3\theta}{2}\right)+\cdots$$
$$\sigma_{yy} = \frac{K_I}{\sqrt{2\pi r}}\cos\frac{\theta}{2}\left(1+\sin\frac{\theta}{2}\sin\frac{3\theta}{2}\right)+\cdots \quad (2.6)$$
$$\tau_{xy} = \frac{K_I}{\sqrt{2\pi r}}\cos\frac{\theta}{2}\cos\frac{3\theta}{2}\sin\frac{\theta}{2}\cdots$$

where K_I is the stress intensity factor for mode I crack. The term $K_I/\sqrt{2\pi r}$ reflects the magnitude of stress at the distance r ahead of the crack tip while the θ related terms in Eq. (2.6) describe the distribution. For a distance r close to zero, the higher order terms in Eq. (2.6) denoted by dots will be negligible. The stress field shows its singular nature due to the $\sqrt{2\pi r}$ term in the denominator since the stress would tend to infinity when approaching the crack tip and is $r^{-1/2}$ dependent. Considering the factors that influence the stress distribution, the stress intensity factor is defined as

$$K_I = \sigma Y\sqrt{\pi c} \quad (2.7)$$

where σ is the remote applied stress, c is the half length of the opening crack and Y is a geometry related factor. For a given geometric configuration, where Y is constant, K_I only depends on the external stress and the crack length.

The stress at the sharp crack tip predicted by LEFM such as the stress concentration method approaches infinity. In the real situation, earlier failure would interrupt the stress before it reaches infinity. One reason is the radius of crack tip is always finite. Besides, plastic behavior in metals would also reduce the stress at the crack tip. The accuracy of LEFM in determining the stress field is strongly dependent on the degree of plasticity near the crack. Some modifications can be accomplished within LEFM for small or moderate yielding, while for extensive yielding, other alternatives to elastic fracture stress analysis are necessary.

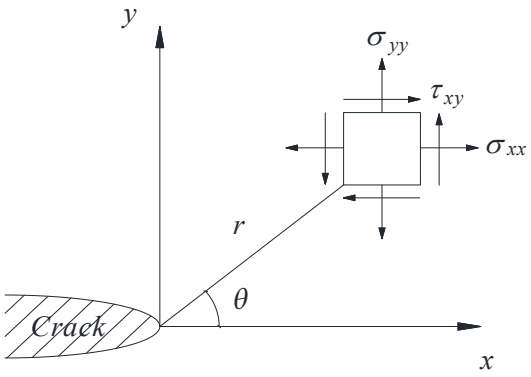

Fig. 2.2 Local coordinate ahead of a crack tip.

2.1.2 Elastic-Plastic Fracture Mechanics

Crack-tip opening displacement

Wells (1961) noticed the faces of a sharp crack moved apart and were blunted by the plastic deformation in many structural steels (see Fig. 2.3). He attempted to quantify the degree of crack blunting as a measure of fracture toughness and gave an alternative to LEFM when it was no longer valid for the small-scale yielding case. Through analytical derivations, Wells obtained an explicit expression of CTOD for the plane stress case with small scale yielding

$$\delta = \frac{K_I^2}{\sigma_{YS} E} \tag{2.8}$$

where E is the modulus of elasticity and σ_{YS} is the yield stress.

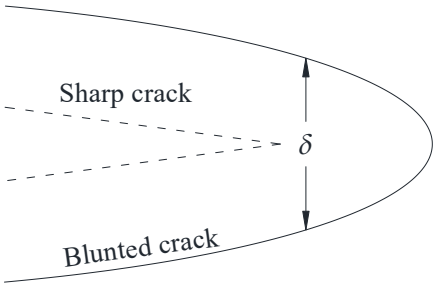

Fig. 2.3 Crack-tip-opening displacement (CTOD).

J-integral

Another approach to characterize fracture in nonlinear materials is the *J*-integral, which was basically given by Rice (1968). Rice idealized the plastic material as a nonlinear elastic material, and noticed that the nonlinear energy release rate *J* could be obtained by an integration along an arbitrary path around the tip

$$J = \int_{\Gamma} \left(w dy - T_i \frac{\partial u_i}{\partial x} ds \right) \tag{2.9}$$

where w is the strain energy density, T_i is the component of the traction vector, u_i is the component of displacement vector, Γ is the path of integration and ds is the incremental length along the integral path (shown in Fig. 2.4).

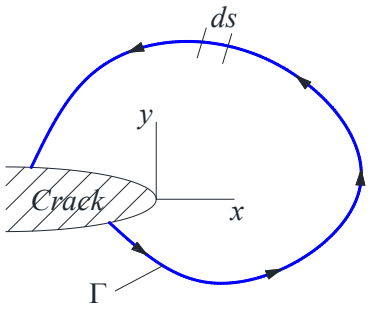

Fig. 2.4 Arbitrary contour around a crack tip.

The *J*-integral is a useful fracture mechanics measurement for elastic-plastic materials if there has been no elastic unloading condition and the nonlinear elastic approximation gives a reasonable representation of the real material. The strong credibility of *J*-integral as a fracture mechanics parameter can be also distinguished by its strong correlation to the stress intensity factor, the CTOD and the energy release rate. In some cases, the *J*-integral also works as a stress intensity parameter.

Compared to the zone dominated by the stress intensity factor *K*, the *J*-integral controls a larger region and therefore has a greater applicability than LEFM. However, limitations arise when the *J*-integral is applied to the case with large-scale yielding, where the size of the finite strain zone is comparable to the size of the specimen. There is no longer a region that can be embedded by *J* and as a consequence, the single parameter is invalid to characterize the facture toughness. This same problem also exists in the crack growth issue where the length the crack growth is considerable or the crack growth is significantly influenced by the stress and strain history while the crack-tip fields are calculated only upon the current states. Besides, when the crack grows, the elastic unloading around the crack tip is inevitable for the elastic-plastic material, and this violates the assumption of *J*-integral.

The discussion above indicates that the LEFM and EPFM are useful to characterize the stress and strain field near the crack tip for some limited cases. However, both approaches are insufficient to characterize fracture under the condition of large-scale yielding. A reason for this drawback is the strict assumptions made in conventional fracture mechanics that restricts the applicability to materials that exhibit brittle or quasi-brittle behavior. Also, conventional fracture mechanics can only deal with the fracture in materials with a pre-existing crack. However, fracture in structural metals sometimes

occurs without any apparent pre-existing flaws. Further, although these classical approaches give analytical solutions to the fracture problems, they provide little insight into the underlying fracture mechanisms at a microscopic scale. However, by taking advantage of computational approaches, it is possible to investigate more fundamental features of fractures, to better characterize the stress and strain states at the crack tip, and to establish the micromechanics-based models. Through these, one can expect the improvement of fracture prediction and the broader application of fracture mechanics, especially for the structural metals with high ductility and strong plasticity.

2.2 MICROMECHANICS-BASED INVESTIGATION OF DUCTILE FRACTURE

2.2.1 Overview of brittle and ductile fracture

Brittle fracture

Brittle fracture in structural metals can be characterized by a crack with rapid propagation and by its growth along a specific crystallographic plane (see Fig. 2.5(a)), also known as cleavage fracture (Anderson and Anderson, 2005). In brittle fracture, apparent plastic deformation is not required to propagate the fracture. Brittle fracture takes place as the result of local tensile stress that is sufficient break bonds within or at the boundary of grains. There is another mode of brittle fracture in metals referred to as intergranular fracture (see Fig. 2.5(b)). This kind of fracture can be activated by ductile crack growth, which is associated with large-scale plasticity. As can be readily understood, the grain boundary is the preferred path for crack propagation at some special situations such as intergranular corrosion or grain boundary cavitation at high temperatures.

Almost all the factors the influence the yield strength of metals, including

temperature, stress triaxiality, radiation damage, strain rate and strain aging, will simultaneously influence susceptibility to cleavage fracture (Anderson and Anderson, 2005; Campbell, 2012). As is well known, for example, lower temperatures, higher stress triaxialities or higher strain rates are associated with increasing the yield stress of a metal and the increase tendency toward cleavage. These factors also influence cleavage fracture initiation and propagation. A macroscopic crack does not provide sufficient stress concentration to break molecular bonds, since molecular bond strength is sometimes 50 times greater than the level of the stress that can be achieved at the crack tip. One way to initiate cleavage fracture is the presence of a preexisting microcrack ahead of the macroscopic crack, at which the local stress concentration can lead to stresses exceeding the bond strength. Microcrack formation is related to microstructural features such as inclusions and second-phase particles.

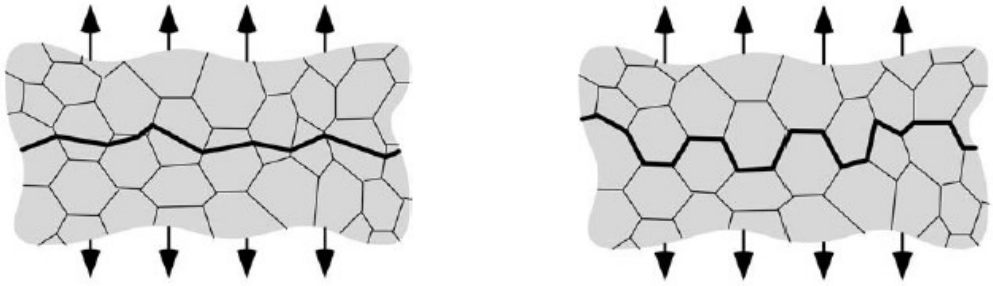

(a) (b)

Fig. 2.5 Micro-mechanisms of fracture in metals: (a) cleavage; (b) intergranular fracture. (Anderson and Anderson, 2005).

Cleavage fracture initiation does not necessarily result in subsequent crack propagation or the total failure of a structure, since there is the possibility of the crack propagation arresting. While initiation relies on the local stress concentration at a

microcrack, propagation depends on the microstructure of the grains and the global force. For example, if the microcrack propagates to the interface of the particle-matrix, the crack may not continuously propagate. This is because the deformation in the matrix changes the sharp tip of microcrack to be blunted so that it would no longer give sufficient stress to rupture cohesion of the material. The normal stress on the cleavage plane plays an important role in crack propagation. A large amount of evidence shows the normal stress would guide the crack development and reorient the crack propagation to the plane with maximum normal stress (Campbell, 2012). However, the cleavage crack due to dislocation motion in crystalline materials would also require shear stress on the slip planes.

Ductile fracture

In contrast to brittle fracture, ductile fracture takes place after the material undergoes considerable inelastic deformation and energy absorption, both of which are the manifestation of high ductility. Perhaps the most representative example to illustrate the ductile fracture process is attributed to the uniaxial tensile specimen. As can be seen from Fig. 2.6, ductile fracture can be decomposed into five common stages. The beginning mechanisms leading to the ductile fracture event do not necessarily involve a preexisting macrocrack or microcrack in the material. Necking induced stress and strain concentration is first observed (Fig. 2.6(a)). Such concentration at the macroscopic level activates the nucleation of microvoids, as shown in Fig. 2.6(b). The formation of microvoids occur at inclusions or second-phase particles and is commonly accomplished by four ways: (1) interface de-cohesion, (2) cracking within a pre-cracked particle, (3) cracking of an intact particle and (4) cracking in a matrix. Continuous straining subsequently causes the void's growth to a critical size. This growth depends not only on the plastic strain, but also on the

stress constraints, e.g., hydrostatic stress and shear stress. Similar as the microvoid nucleation, the growth of voids is often associated with plastic instabilities such as microscopic necking and shear banding. Further growth leads to the interaction of neighboring voids so that material breaks between voids. This is referred to as microvoid coalescence, and is shown in Fig. 2.6(c). The initial crack, due to microvoid coalescence, is oriented at a plane approximately 90° to the tensile stress for this uniaxial tensile case. Through microscopic observations, the surface of initial crack is characterized by tiny cups or dimples, which are essentially half-voids. The strain concentration at the tip of the initial crack at the center and the reduced area of the cross section is sufficient to provide local strain or stress to nucleate small microvoids near the edge of the necked region. The spread speed of microvoid growth and coalescence toward the surface of the necked zone is quite fast. However, the spread orientation is different from the growing path of the initial crack, and is oriented 45° to the uniaxial loading direction (see Fig. 2.6(d)). It is also interesting that the inclined surface is relatively smooth, distinctive from the fibrous appearance of the central region. The total fracture surface is therefore characterized as the cup-and-cone shape in Fig. 2.6(e).

As described above, the main stages of ductile fracture include microvoid nucleation, growth, and coalescence. However, the mechanism of each stage is not always similar to that in the uniaxial tensile specimen. The diversity of mechanisms of microvoid evolution reflects the complexity of ductile fracture process. This is particularly apparent in the stages of microvoid growth and coalescence. As in the previous example, void size enlargement controls the process of void linkage, coalescence, and incipient crack growth. Void linkage for this mechanism occurs at the plane with maximum normal stress, and is resulting from necking between voids. The other mechanism for void coalescence is void

ligaments taking place upon slip band deformation. Either the development of localized shear bands or the necking between voids can result in such slip deformation on a plane with high shear stress. Distinguishing these two mechanisms from both microscopic and macroscopic observations is not an easy task, since the factors influencing the micro-mechanisms and the relation between microscopic mechanisms and macroscopic crack growth are not well established. Nevertheless, the stress and strain fields, the plastic behavior, the voids size and spacing and the microstructures are under extensive current investigation and are believed to have great effects on these two mechanisms. Micromechanical modeling is thus used for micromechanics-based studies. The objectives are to capture the behavior of microstructures under various mechanical fields, to quantify the effects of factors on the void evolution, to develop correlations with micromechanical observations, and to provide guidance and effective tools for ductile fracture prediction.

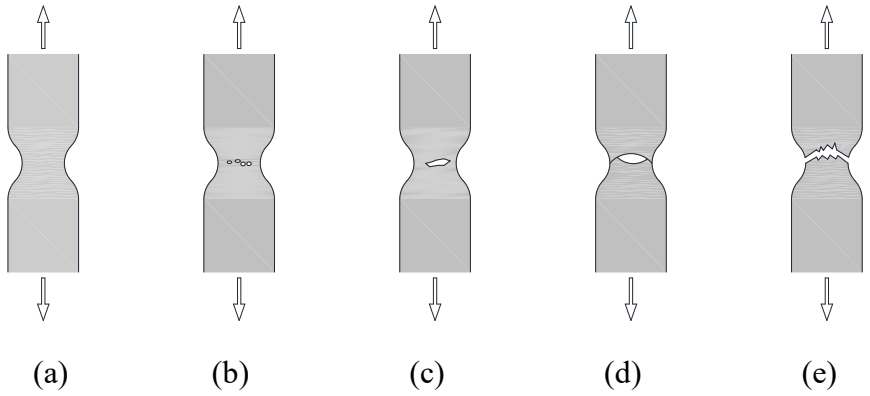

Fig. 2.6 Ductile fracture stages in a uniaxial tensile specimen: (a) necking; (b) formation of microvoids; (c) coalescence of microvoids; (d) crack propagation; (e) fracture.

2.2.2 Void nucleation

2.2.2.1 Micromechanical mechanisms

Goods and Brown (1979) categorized void nucleation into homogenous and heterogeneous types, and emphasized the latter was the most common case in engineering materials which involve second-phase particles and grain interfaces. Void formation in this case mainly occurs due to particle decohesion or to particle cracking (see Fig. 2.7). Pineau et al. (2016) analyzed the factors that influence the pattern of void formation, such as the material matrix hardness, matrix strength, particle elongation, stress triaxiality and load orientation. Particle decohesion is dominated in soft matrixes while particle cracking is preferred in hard matrixes. Increasing matrix strength and particle elongation lead to a propensity from particle cracking to interface de-bonding while stress triaxiality has the opposite effect to the mechanism of void nucleation. Weck (2007) reviewed other parameters including particle size aspect ratio, particle volume and temperature. In particular, it was suggested that increasing temperature can directly decrease matrix strength and thus weaken the bonding strength among particles.

In terms of the void nucleation under a shear dominated state of stress, Achouri et al. (2013) conducted a series of shear type ductile fracture tests on high strength low alloy (HSLA) steel and investigated the microscopic aspects of void evolution under shearing. As can be seen in Fig. 2.8, two main different mechanisms discussed above were both observed from different regions of the specimen. The region with intensive shearing (see Fig. 2.8(a)) involves both particle cracking and debonding between matrix and inclusions. A combination of two mechanisms occur at that region. The microvoid at the region with weak shearing is characterized by particle debonding, with no particle cracking. This

implies that even with low hydrostatic stress, microvoid formation can be also accomplished by the shear effect. But the quantitative comparison of the strain at which void nucleation occurs between these two mechanisms is still required.

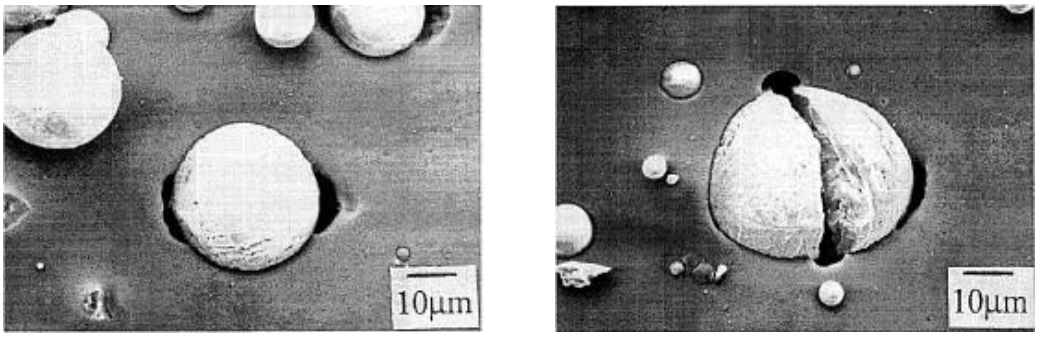

(a) (b)

Fig. 2.7 Microvoid nucleation in an aluminum 6061 matrix reinforced with Al_2O_3 particles: (a) debonding; (b) particle cracking. (Kanetake et al., 1995).

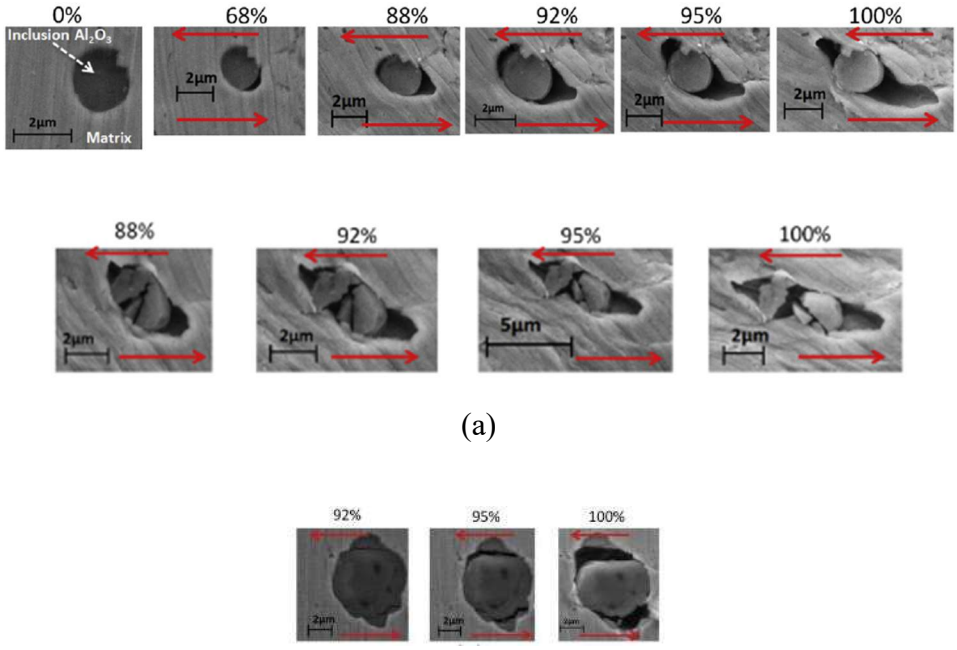

(a)

(b)

Fig. 2.8 The evolution of the void nucleation of HSLA steel in the shear zone: (a) at the region with intensive shearing; (b) at the region with weak shearing. The percentage denotes the relative displacement and the red arrows represents the shear loading direction. (Achouri et al., 2013).

2.2.2.2 Micromechanical modeling

The criterion of either stress, strain, or energy has been adopted to capture the void nucleation event and to explain the phenomenon in an analytical level. The idea of the energy approach is from Griffith's energy criterion, and is necessary to satisfy the requirement of creating new surfaces. However, this traditional fracture mechanics approach is only valid for the elastic range or with slight plasticity. Argon et al. (1975) proposed a stress based criterion to quantify the condition for particle decohesion

$$\sigma_{eq} + \sigma_m = \sigma_c \tag{2.10}$$

where σ_{eq} is the equivalent stress, σ_m is the hydrostatic stress and σ_c is the critical stress for void nucleation. A deficiency of this approach is that it gives a uniform condition for particles with different sizes, while the size effect has a significant contribution to the strain and stress at void nucleation. Using the single parameter measurement of ductile fracture, i.e., the void volume fraction *f*, the void nucleation condition developed by Gurson (1975) and Chu and Needleman (1980) in a rate form reads

$$\dot{f}_{nuc} = A\dot{\bar{\varepsilon}} + B(\dot{\sigma}_{eq} + C\dot{\sigma}_m) \tag{2.11}$$

where A, B and C are three parameters, and the former two are functions of $\bar{\varepsilon}$ and $\sigma_{eq}+C\sigma_m$, respectively. Note that the above expression takes both the strain and stress contribution into account. This criterion overcomes the shortcomings of both strain-controlled and stress-dependent approaches. In terms of the strain-based criterion, it simply implies the amount of void nucleation increases with the accumulated plastic strain regardless of stress triaxiality, which does not follow the facts from either experimental observations (Beremin, 1981) or analytical solutions (Needleman, 1987; Shabrov and Needleman, 2002).

The void nucleation criterion in Eq. (2.11) does not distinguish between the two mechanisms of void formation. In other words, it treats both particle debonding and cracking in the same manner. For cases such as particle cracking, the voids initiates with penny-like shapes, which is not considered by Eq. (2.11). It is necessary to incorporate such factor to make a more systematic explanation of void nucleation. Lee and Mear (1999) and Wilner (1988) distinguished particle debonding and cracking in void nucleation based on the framework of micromechanics. The fundamentals of the criterion above are some

empirical experiments and micromechanical analyses, which, to some extent, restrict the scope of investigation to high and moderate triaxialities. Increasing interest in ductile fracture at low triaxialities are motivating micromechanical studies to evaluate void nucleation at that range of triaxialities. Particularly, the abovementioned shear dominated void nucleation mechanisms are still not well-established. Some cell modeling studies concentrating on triaxialities below 2/3 have been completed (Fleck et al., 1989; Kuna and Sun, 1996; Siruguet and Leblond, 2004), but are still far away from developing a void nucleation criterion.

Factors such as particle size and distribution are merit exploration if a more fundamental void nucleation criterion is expected. Shabrov and Needleman (2002) performed micromechanical studies involving a void cluster with various sized voids and a variety of void distributions. The results indicate a void nucleation strain is more sensitive to particle size and distribution at lower triaxialities than at high triaxialities. Far more micromechanical investigations are needed to enhance the current understanding and characterization of void nucleation and to better evaluate the subsequent void growth and coalescence.

2.2.3 Void growth

2.2.3.1 Micromechanical mechanisms

Early experimental investigations on void growth are attributed to work by Puttick (1959), Floreen and Hayden (1970) and Cox and Low (1974). These investigations used metallographic techniques to examine the void surface at a two-dimensional plane for information on void growth. The main findings of these studies are that void growth has a strong relationship with the plastic strain and the stress triaxiality. Marini et al. (1985)

extended these works to three-dimensional exploration of void growth and the results show agreement with the void enlargement law proposed by Rice and Tracy (1969). The studies by Becker et al. (1988) guide the parameter establishment of the Gurson model (Gurson, 1977). More recently, Pardoen and Delannay (1998), Chae and Koss (2004) and Benzerga et al. (2004) conducted experiments to explore void evolution at small porosity levels. By using X-ray tomography, Weck et al. (2008) studied void growth in a uniaxial tension plate made from high-purity copper, and for which a void was initially embedded. As can be seen from Fig. 2.9, the rate of the void elongation in the vertical direction is quite larger than in the horizontal direction. The void enlargement vertically is due to the tensile loading applied to the specimen, and the horizontal growth is induced by macroscopic necking phenomenon. It was also observed that the final void coalescence occurred first horizontally, suggesting the important roles of necking and microscopic plastic localization during the void evolution process.

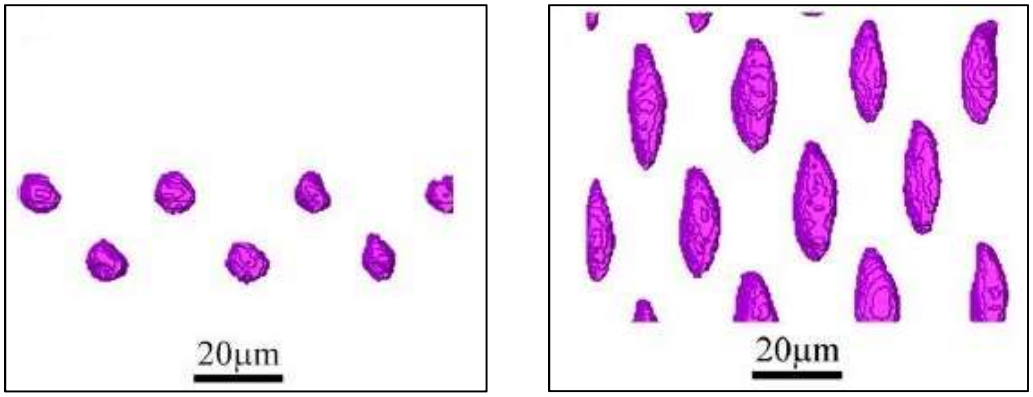

(a) (b)

Fig. 2.9 Void growth in a copper uniaxial tension specimen: (a) at strain=0; (b) at strain=0.5. (Weck et al., 2008).

Besides the void volumetric evolution, the void shape effect on the void growth stage is also notable. Cox and Low (1974) conducted axisymmetric tension tests and suggested that the void mainly deformed in the direction of tensile stress at the beginning of straining and grew both longitudinally and laterally under intensive strain. The observations of void shape change by Cox and Low (1974) are for the void at high triaxialities, while this void shape evolution is even more apparent at low triaxialities. Relatively insensitive to the volumetric enlargement, the void growth in this regime is almost characterized by void distortion, which is commonly the combination of void elongation and void rotation, and can be the source of final material failure. The extent of void distortion is generally based on the level of shear stress and the level of void-particle interaction. The shear stress or remote shear loading flattens the void or induces shear band localization. If the void rotates and is finally flattened into closure before shear localization occurs, the localization would also be preceded by such drastic void distortion. No matter which aspect induces the shear localization, another factor can contribute to failure under intensive shearing. The other factor is the void-particle interaction, where the interactive force is known as void locking. This void locking appears not only at high triaxialities but also at low triaxialities, e.g., under shear loading. In void distortion dominated void growth, void locking plays a role in preventing complete closure of a void. The consequence of void locking for such cases is plastic flow localization that is the precursor of failure (Tvergaard, 2012). However, it is unclear if such void locking generally facilitates void growth or not. This phenomenon requires further investigation (Pineau et al., 2016).

The size effect is another important factor that may influence the process of microvoid evolution, particularly for structural metals with multiple populations of second-phase particles. In some situations, while the large particles significantly affect void

growth, the small ones may remain intact even though all the particles with different sizes are under the same stress and strain fields. Thus, the assumption that void growth is independent of void size may not be true at some scales. Another critical aspect that the size effect may contribute to is the void-dislocation interaction. Such interaction is observed to be apparent at submicron scales (Ashby, 1966; Ahn et al., 2006). This would not only affect the plastic behavior regarding strain hardening and strength, but also the evolution of microstructures and void growth process.

2.2.3.2 Micromechanical modeling

Rice and Tracey model

The Rice and Tracey model is one of the most popular criteria for void growth and ductile fracture prediction. This model, developed by McClintock (1968) and Rice and Tracey (1969), accounts for an isolated spherical void in an infinite solid. The solid, subjected to remote strain rate and stress fields, was considered to be either perfectly plastic or linear strain hardening. With the ordered strain rates $\dot{\varepsilon}_1 \geq \dot{\varepsilon}_2 \geq \dot{\varepsilon}_3$, the analytical solution for the void growth rate in each direction is given as

$$\dot{R}_i = \left[\left(1+G\right)\dot{\varepsilon}_i + \sqrt{\frac{2}{3}\dot{\varepsilon}_j\dot{\varepsilon}_j}D \right] R_0 \tag{2.12}$$

where G and D are two constants related to stress state and strain hardening, and R_0 is the initial radius of the spherical void. The first term of Eq. (2.12) considers the length change rate at the corresponding direction and the second term represents the contribution of void volume change rate to the radius change. Following the incompressibility condition that $\dot{\varepsilon}_1 + \dot{\varepsilon}_2 + \dot{\varepsilon}_3 = 0$, the radius change rates at all three directions are derived as

$$\begin{cases} R_1 = \left(A + \dfrac{B(3+\nu)}{2\sqrt{\nu^2+3}} \right) R_0 \\ R_2 = \left(A - \dfrac{B\nu}{\sqrt{\nu^2+3}} \right) R_0 \\ R_3 = \left(A + \dfrac{B(\nu-3)}{2\sqrt{\nu^2+3}} \right) R_0 \end{cases} \tag{2.13}$$

where

$$\nu = -\frac{3\dot{\varepsilon}_2}{\dot{\varepsilon}_1 - \dot{\varepsilon}_3}, \quad A = \exp\left(\frac{2\sqrt{\nu^2+3}}{3+\nu} D\varepsilon_1 \right), \quad B = \frac{1+G}{D}(A-1) \tag{2.14}$$

Considering various stress states, Rice and Tracey (1969) gave the solutions for Eq. (2.13)

$$\frac{\dot{\bar{R}}}{R_0} = \alpha \exp\left(\frac{3}{2}\frac{\sigma_m}{\bar{\sigma}} \right) \dot{\varepsilon}_{eq} \tag{2.15}$$

where $\dot{\bar{R}} = \left(\dot{R}_1 + \dot{R}_2 + \dot{R}_3 \right) \Big/ 3$ is the average radius change rate and $\dot{\varepsilon}_{eq}$ is the equivalent plastic strain rate. The coefficient α is essentially a function of the parameter ν. For the axisymmetric tension case, ν is constant at 1, so that Rice and Tracey (1969) obtained the value of α=0.283. Besides, the ν sensitivity of the coefficient α is quite small in the original model, so it is widely accepted that α is independent of ν.

Numerous subsequent studies have supported the Rice and Tracey model. Le Roy (1978) conducted experiments in low-, medium-, and high-carbon spheroidized steels and analytically calculated the strain at damage initiation based upon the Rice and Tracey model. The comparisons indicate a strong correlation between test results and analytical predictions. The experiments conducted by Marini et al. (1985) in a composite material made from a steel matrix and alumina inclusions also show agreement between the experimental results and the analytical solutions by the Rice and Tracey model. However,

deviations of the analytical solutions from tests also existed. Marini et al. (1985) concluded this discrepancy was due to the fact that the Rice and Tracey model does not consider void interaction effects.

The Rice and Tracey model only considers an isolated void. However, interactions among neighboring voids will affect void growth when void spacing is small enough. Additionally, final failure results from void coalescence, which involves multiple voids. Consequently, void interaction ultimately plays an important role. Another shortcoming of the Rice and Tracey model is that it neglects the void shape effect. The original void shape is difficult to maintain, particularly at low triaxialities. When the shape change mechanism dominates the void growth process rather than the volumetric enlargement mechanism, the fundamental assumptions of the Rice and Tracey model are violated. This becomes a critical issue for the Rice and Tracey model that requires a modification or an alternative.

Gurson model

Different from the Rice and Tracey model that gives an explicit expression of void size evolution, the Gurson model describes void growth using a single parameter f defining as the void volume fraction. The Gurson model (Gurson, 1975, 1977) was derived based on a hollow sphere with a single central void by assuming an approximate homogenization problem and by limit-analysis. The material was assumed to behave as a continuum and obey J_2 flow theory with isotropic strain hardening. The void volume fraction directly enters the plastic flow potential so that it influences the global material behavior. The rate of porosity is given as

$$\frac{\dot{f}}{f\left(1-f\right)}=\frac{3}{2}q\frac{\bar{\sigma}}{\sigma_{eq}}\sinh\left(\frac{3}{2}\frac{\sigma_m}{\bar{\sigma}}\right)\dot{\varepsilon}_{eq} \tag{2.16}$$

where $\bar{\sigma}$ is the matrix flow strength, σ_{eq} is the macroscopic effective stress, σ_m is the macroscopic hydrostatic stress and q is a constant. The porosity change rate exponentially increases with the stress triaxiality, which is similar to the Rice and Tracey model. Comparison between Eq. (2.15) and (2.16) shows the porosity function in the Gurson model provides greater consideration to the effect of yield strength and effective stress. Indeed, the porosity plays a role as a damage variable that influences the current yield strength. The Gurson model in terms of the yield function is given as

$$\Phi = \frac{\sigma_{eq}^2}{\bar{\sigma}^2} + 2qf\cosh\left(\frac{3}{2}\frac{\sigma_m}{\bar{\sigma}}\right) - \left(1+q^2f^2\right) = 0 \tag{2.17}$$

When f=0, the equation reduces to the Von Mises potential function. In the original Gurson model (Gurson, 1977), the parameter q=1, which was further modified by Tvergaard (1982) to be q=1.5. This parameter is sometimes treated as a function of porosity f once the effects of void shape and strain hardening are neglected (Pineau et al., 2016). The physical meaning of q is unclear, although it is believed that the void interaction is of one important factor affecting the value of q.

Tvergaard (1982) modified the original Gurson model on the non-spherical shape of the cell to achieve better agreement with the results from micromechanical studies

$$\Phi = \frac{\sigma_{eq}^2}{\bar{\sigma}^2} + 2q_1f\cosh\left(\frac{3}{2}q_2\frac{\sigma_m}{\bar{\sigma}}\right) - \left(1+q_3f^2\right) = 0 \tag{2.18}$$

The typical magnitudes of q_i (i=1, 2, 3) are q_1=1.5, q_2=1 and $q_3 = q_1^2$. However, extensive micromechanical studies have shown the values of q_i are quite inconsistent for different loading conditions (Gao et al., 1998; Koplik and Needleman, 1988). Benzerga and Leblond (2010) suggested the introduction of q_2 and q_3 is more likely to improve the accuracy of original Gurson model than to reflect the physical facts of void growth.

Other investigators have proposed modifications of the Gurson model to account for the strain hardening effect (kinematic hardening). This includes work by Mear and Hutchinson (1985), Tvergaard (1986, 1987) and Leblond et al. (1995). However, implementations of these modifications are limited by their unclear fundamentals and numerical difficulties. Another modification regarding the porosity is attributed to Chu and Needleman (1980), which incorporated the nucleation related porosity to the total porosity evolution

$$\dot{f} = \dot{f}_{nuc} + \dot{f}_{g} \tag{2.19}$$

The second term $\dot{f}_g$ is synonymous to the one in Eq. (2.16), representing the growth of preexisting voids. The first term is the one used to describe the rate of new voids formation, the expression of which is already given by Eq. (2.11). The coefficients of strain and stress related terms in Eq. (2.11) are functions of the strain variables. For instance, the coefficient of strain variable is given as

$$A\left(\bar{\varepsilon}\right) = \frac{f_N}{s_N\sqrt{2\pi}} \exp\left[-\frac{1}{2}\left(\frac{\bar{\varepsilon} - \varepsilon_N}{s_N}\right)^2\right] \tag{2.20}$$

It is clearly seen that the coefficient follows a normal distribution by giving a mean value ε_N, a standard deviation s_N and a volume fraction of void-nucleating particles f_N.

More recently, Nahshon and Hutchinson (2008) proposed modification of the Gurson model for cases of low triaxiality conditions. This modification, based on experimental evidence and micromechanical observations, is more likely a phenomenological than physical interpretation. By introducing an extra term to the porosity rate in Eq. (2.19), the modified rate of porosity by Nahshon and Hutchinson (2008) is given as

$$\dot{\bar{f}} = \dot{f} + k_{\omega} f \omega(\sigma) \frac{s_{ij} D_{ij}^{p}}{\bar{\sigma}} \tag{2.21}$$

where k_ω is a parameter serving to quantify the magnitude of the rate of porosity in pure shear states, s_{ij} is the stress deviator tensor and D_{ij}^{p} is the plastic strain rate tensor. The parameter $\omega(\sigma)$ is a function of stress state defined as

$$\omega(\sigma) = 1 - \left(\frac{27 J_3}{2\sigma_{eq}^3} \right)^2 \tag{2.22}$$

where J_3 is the third stress invariant. The reason the Nahshon and Hutchinson modification loses its physical interpretation for the porosity growth rate at low triaxialities is due to the fact the actual porosity under such stress states ceases to increase or even decreases while the porosity variable in Eq. (2.21) continues to grow. Indeed, the role of the porosity variable in this modified Gurson model is quite similar as that of the damage variable in continuum damage mechanics. However, it is undeniable that the modification to the Gurson model makes it possible to address ductile fracture and damage at low triaxialities with encouraging accuracy and an easy-to-implement approach. One potential alternative to this kind of modification for describing the void growth at low triaxialities is to address the voids volumetric and shape change in an explicit form and account for the corresponding effects on the material behavior.

Shape effect coupled models

The Gurson-like models are derived based on spherical voids. However, void shape evolution becomes significant when one is addressing the problems regarding low triaxiality cases, shear-dominated loadings cases with void coalescence being the critical stage. In order to consider the initial void shape effect on void growth, Gologanu et al.

(1993, 1994, 1997) extends the Gurson model by changing its basic ingredients that the representative volume element (RVE) becomes a spheroidal volume confocal with the void, and the spherical void is replaced by a prolate and oblate one. Upon the simple case of axisymmetric loading condition such that $\sigma_{xx}=\sigma_{yy}\neq\sigma_{zz}$ and without any shear components, the yield condition for the Gologanu-Leblond-Devaux (GLD) model is given as

$$\Phi=\frac{C}{\bar{\sigma}^2}\left(\sigma_{zz}-\sigma_{xx}+\eta\sigma_h\right)^2+2\left(1+g\right)\left(1+f\right)\cosh\left(\frac{\kappa\sigma_h}{\bar{\sigma}}\right)-\left(1+g\right)^2-\left(f+g\right)^2=0 \qquad (2.23)$$

where C, η, g and κ are four model parameters. Herein, σ_h is the effective hydrostatic stress obtained by the weight average of normal stresses

$$\sigma_h=\alpha_{xx}\sigma_{xx}+\alpha_{yy}\sigma_{yy}+\alpha_{zz}\sigma_{zz} \qquad (2.24)$$

The weight factors require $\alpha_{xx}+\alpha_{yy}+\alpha_{zz}=1$ and $0\le\alpha_{xx},\alpha_{yy},\alpha_{zz}\le 1$. Different from the hydrostatic stress in the Gurson model, the effective hydrostatic stress herein is to account for the fact that the non-spherical voids are not equally sensitive to three axial stresses. With the axis of rotational symmetry of the micromechanical model Oz, the weight factors are dependent on the ratio (w) of the axis of the void in Oz and Ox (or Oy), and the porosity. Also, the model parameters rely on these two variables (w, f).

The critical aspect of the GLD model different from the Gurson model is with respect to $S=\ln w$. It is also necessary to account for the evolution of this parameter. The expression for $\dot{S}$ was derived by Gologanu et al. (1997) based on both analytical and numerical solutions. Another notable aspect of void growth disregarded by the GLD model is the angle between the axis of rotational symmetry of the voids and that of the material since Gologanu et al. (1997) simply assumed both axes coincide with each other throughout

the void growth process. The effect of relative rotation between two axes has further been analyzed by Scheyvaerts et al. (2011).

The void in the GLD model is essentially a special ellipsoidal void for which the two main axes in the plane perpendicular to *Oz* is equivalent. To obtain a more general solution to GLD model, the extension developed by Madou and Leblond (2012a, b, 2013) and Madou et al. (2013) considered that the ellipsoidal void had three distinct axes. The yield potential derived by Madou and Leblond (2012a, b) has a quite similar form as the GLD model, which reads

$$\Phi = \frac{\sigma_q^2}{\bar{\sigma}^2} + 2\left(1+g\right)\left(1+f\right)\cosh\left(\frac{\kappa\sigma_h}{\bar{\sigma}}\right) - \left(1+g\right)^2 - \left(f+g\right)^2 = 0 \tag{2.25}$$

where σ_q is a quadratic form of the stress components. The equivalent stress σ_q reduces to the von Mises stress when the void is spherical. The ML model has two internal parameters, i.e., w_1 and w_2, for characterizing the void shape effect. Instead by giving the explicit expression of these two parameters, Madou and Leblond (2012a, b) provided the magnitudes of the variables using a computational way, for which updates the values at each time step.

2.2.4 Void coalescence

2.2.4.1 Micromechanical mechanisms

As the last stage of ductile fracture, void coalescence is no doubt of great importance since it is the indicator of the material ductility. However, fewer investigations have considered this stage of ductile fracture compared to the previous two. The main reason is that the occurrence of coalescence is such a short time period that it is hard to capture by experimentally. Though not well understood, the physics of void coalescence

has been documented by a few observations. There are generally three types of modes that are most frequently obtained including (1) internal necking, (2) internal shearing and (3) "necklace" coalescence.

As can be seen in Fig. 2.11(a), the first mode is internal necking of the ligament between voids until the material necks down to a point of failure between voids. The necking occurs perpendicular to the tensile loading direction. This mode of coalescence is very common, particularly in uniaxial tensile tests (Benzerga et al., 2004; Le Roy, 1978; Park and Thompson, 1988). The internal shearing mode in Fig. 2.11(b), involves the development of a shear localization band among main voids. The shear band facilitates void nucleation on a second population of inclusions as well as quickens the coalescence among those small voids, and then causes the coalescence between remote large voids. This kind of failure is also known as void sheeting (see Fig, 2.11(c)), and was observed to take place at an orientation 45° from the loading direction (Weck and Wilkinson, 2008). The third mode is "necklace" coalescence (Fig. 2.11(d)). It is observed to occur as a link up in elongated clusters of the voids. Different from previous modes, the coalescence in this mode takes place within a localization region parallel to the main loading direction and is believed to be gentle to the ductility of materials (Benzerga and Leblond, 2010).

It is not an easy task to distinguish or predict the occurrence of each mode of void coalescence, since the mechanism of each is one not yet well established. At least, it is believed that void coalescence is closely tied to strain localization at both the macroscopic and microscopic levels. Factors such as microstructural evolution, loading conditions, plastic behavior of materials and even thermal effects would independently or conjunctly affect the void coalescence mode. For instance, the microstructures can influence the process of localization in two aspects. First, microscopic inhomogeneities can activate

plastic strain localization such as shear banding and internal necking. Secondly, the evolution of microstructures would ultimately impact the constitutive behavior that depends on the process of localization as well as void growth. As discussed in section 2.2.1, two modes of void coalescence, i.e., internal necking and shearing, are concurrent in the uniaxial tension specimen. One can envision that the stress state is not the only factor in a single case that can determine the coalescence mode. Others may include the interaction of macroscopic and macroscopic localization, and the interaction of microvoids and particles.

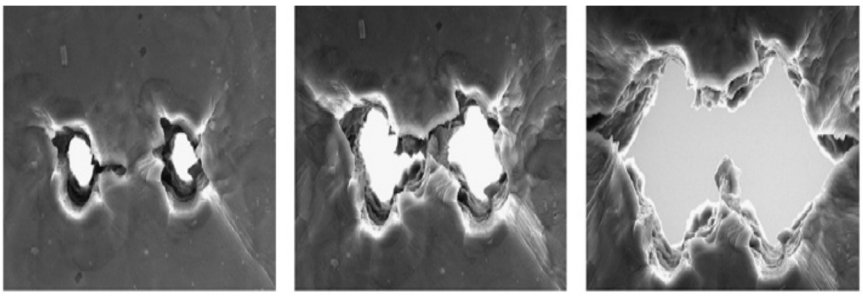

(a)

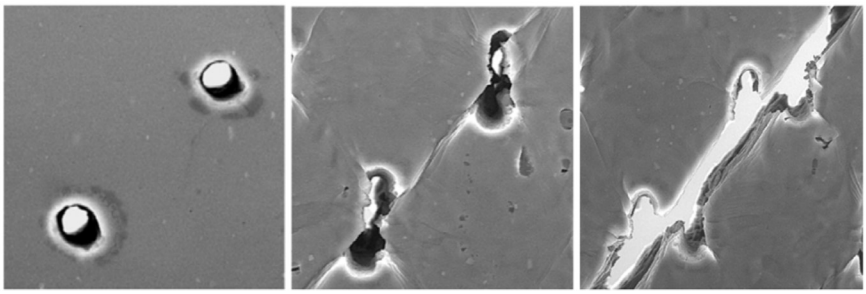

(b)

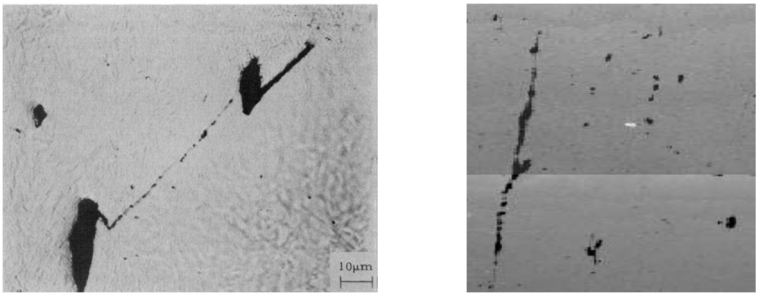

(c) (d)

Fig. 2.10 Different void coalescence modes: (a) internal necking (Weck and Wilkinson, 2008); (b) internal shearing (Weck and Wilkinson, 2008); (c) void sheeting (Cox and Low, 1974); (d) "necklace" coalescence (Benzerga et al., 2005). Loading is longitudinal for all three cases.

2.2.4.2 Micromechanical modeling

Modified Gurson model

Early attempts to model void coalescence included work by Tvergaard and Needleman (1984) and Needleman and Tvergaard (1984). These investigators modified the original Gurson model to account for the effect of coalescence on the yield function. This version, known as the GTN model, has become a complete phenomenological model to describe the constitutive law for all stages of the ductile fracture process. The modification involves the substitution of the porosity in Eq. (2.18) by its effective counterpart f^*, which reads

$$f^* = \begin{cases} f & f < f_c \\ f_c + \dfrac{1/q_1 - f_c}{f_f - f_c}\left(f - f_c\right) & f \geq f_c \end{cases} \tag{2.26}$$

where f_c and f_f are two parameters, and $1/q_1=f_u$ is the ultimate effective porosity when $f=f_f$, at which point the material completely loses loading carrying capacity. The expression above indicates that when the porosity is smaller than f_c, the effective porosity remains the same as that in original model. Once f is greater than f_c, the effective porosity accounting for the acceleration of void growth enters the model. The f_c term therefore denotes the porosity at the onset of void growth acceleration. The f_c is not necessarily referred to the porosity at the onset of void coalescence. The underlying physical meanings for these two parameters are not well understood. Therefore, the implementation of this phenomenological model requires calibrating the model parameters using empirical approaches, either by experiments or by micromechanical modeling. Attempts to determine these porosity related parameters can be found in Benzerga et al. (1999) and Benzerga

(2002).

Thomason's model

An early attempt to model the onset of internal necking was by Thomason (1968), which focused on attaining the limit stress on the intervoid ligament in a two-dimensional model. Thomason (1985) then extended the early work to study the three-dimensional square-prismatic cell model. It was assumed the plastic flow was restricted to the intervoid ligaments and the material above and below the ligament region was rigid. He then proposed an empirical expression to achieve the best fit to the numerical results from Thomason (1985) and Kudo (1960). Later, Pardoen and Hutchinson (2000) extended the cylindrical voids in Thomason's original model to spheroidal voids by introducing the void aspect ratio w in terms of the ratio of height and diameter of the void. Provided that the internal necking takes place in the X_1-X_2 plane and incorporating the notation of Benzerga et al. (1999), Thomason's condition is given as

$$\Phi = \frac{\sigma_{33}}{\bar{\sigma}} - \left(1-\chi^2\right)\left[0.1\left(\frac{\chi^{-1}-1}{w}\right)^2 + 1.2\sqrt{\chi^{-1}}\right] = 0 \tag{2.27}$$

where σ_{33} is the normal stress at the major axis X_3, and χ is the ratio of lateral void width to lateral cell radius. A difficulty with this criterion is that for $w \to 0$ representing a flat void, Eq. (2.27) exhibits a singularity. Benzerga (2002) made efforts to deal with this difficulty. The implementation of the coalescence criterion need to be associated with the void growth model incorporating void shape effects.

Benzerga and Leblond model

Upon Thomason's analysis, Benzerga and Leblond (2014) considered the

cylindrical cell model with a coaxial cylindrical void and obtained an analytical solution for the coalescence condition

$$\Phi = \sigma_{33} - \sigma^{vol} - \sigma^{surf} = 0$$

$$\sigma^{vol} = \frac{\bar{\sigma}}{\sqrt{3}}\left[2 - \sqrt{1+3\chi^4} + \ln\left(\frac{1+\sqrt{1+3\chi^4}}{3\chi^2}\right)\right], \quad \sigma^{surf} = \frac{\bar{\sigma}}{3\sqrt{3}}\frac{\chi^3 - 3\chi + 2}{\chi w} \tag{2.28}$$

Several observations can be obtained from the explicit expression above. First, as χ=1, both the σ^{vol} and σ^{surf} terms vanish. This is true since the radius of the voids approaches the radius of the cell. Second, when w is infinity, i.e., the void is infinitely elongated, the σ^{surf} reduces to 0 and the main axial stress σ_{33} is independent of the aspect ratio of the void. Besides, when $w \to 0$, the singularity of the expression still exists.

Tekoglu model

Another critical issue in the analysis of void coalescence is to account for the shear stress effect as well as the internal shearing mechanism. However, very few models consider this issue. Some attempts to emphasize the role of shear stress on the ductile fracture process can be found from Tvergaard (2008, 2009, 2012) and Nielsen et al. (2012). Xue (2008) modified the GTN model by introducing the Lode parameter as a measurement of the shear stress effect. However, the development of this modified model is based on the hypothesis that the mechanism of void coalescence is an internal necking-like mode.

Based on Thomason's model, Tekoglu et al. (2012) have considered a more general loading condition by introducing a combination of normal and transverse deformation fields applied to the cell model. A quadratic form of coalescence criterion has been obtained

$$\Phi = \frac{\sigma_{33}^2}{\left(\sigma^A\right)^2} + 4\frac{\sigma_{31}^2 + \sigma_{32}^2}{\tau^2} - 1 = 0 \tag{2.29}$$

where σ^A either has the expression in Eq. (2.30) or equals to Benzerga's heuristic limit load (Benzerga, 2002)

$$\sigma^A = \bar{\sigma}\left(1-\chi^2\right)\left[0.1\left(\frac{\chi^{-1}-1}{w}\right)^2 + 1.2\sqrt{\chi^{-1}}\right] \tag{2.30}$$

τ is a function of the ligament parameter χ and the yield strength:

$$\tau(\chi) = \frac{2\bar{\sigma}}{\sqrt{3}}\left(1-\chi^2\right) \tag{2.31}$$

2.3 DUCTILE FRACTURE AND DAMAGE MODELS

Micromechanics-based analysis, modeling and experimental studies offers a strong basis for ductile fracture investigations. Such efforts can qualitatively relate ductile fracture phenomena and macroscopic field variables. Such variables can be the components of strain and stress fields as well as their change rates, the material plastic behavior and sometimes the temperature. For instance, the role of the normal stress in void enlargement in a specific cell model can be clarified either by analytical solutions or by computational results. However, neither the qualitative correlation of those variables to the micro-mechanisms is completed nor has the gap between microscopic and macroscopic phenomenon has been bridged. For the former, many factors restrict the realization of micro-mechanism quantification. As discussed above, the shear stress component is quite a considerable variable in affecting both void growth and coalescence. In addition, the shearing localization mechanism gives rise to difficulties in micromechanical studies. Currently, it is difficult to explain the source of such mechanisms, to mathematically

describe the shearing localization, and to predict its occurrence at the microscopic level. Also, the variables present in the explicit expression are sometimes only suitable on a case-by-case basis. The proposed micromechanical models significantly rely on the basic cell model's shape and size. The multiple void shapes and cell model configurations and the interactions among them, microstructures and plastic behavior evolutions can be other important factors that are rarely incorporated into ductile fracture modeling.

Most of the micromechanical void growth and coalescence criteria have been developed based on the cell model contained a single void. Even though some of the micromechanical modeling provides insight of the neighboring voids interaction, the current proposed micromechanics-based models rarely consider the different populations of voids. The multi-voids effect is particularly apparent in the void coalescence stage. It is questionable whether the single-void model can be physically representative of the situation at fracture loci. Another critical issue is with respect to the length scale effect. From macroscopic to microscopic level, the length effect is believed to increase. Unfortunately, the present analytical expressions for void nucleation, growth and coalescence are developed disregarding the size effect. Drawbacks of the micromechanical modeling restrict their implementation to the macroscopic ductile fracture determination.

Except for a few micromechanical models that can be directly used for ductile fracture prediction, e.g., the GTN model and the GLD model, most of the void growth coalescence related derivations are inappropriate for engineering failure analysis. For instance, the explicit form of the void coalescence expression in Eq. (2.28) is a function of cell and void geometric parameters. The macroscopic modeling of fracture prediction has no access to the microvoid geometric variables. Those micromechanics related model parameters are also hard to measure by current experimental technologies. In addition,

computational expense is another aspect that needs to be considered for the use of fracture models in the engineering application. Most of void growth and coalescence criteria described in section 2.2 are associated with a considerable number of parameters and are numerically inefficient.

The greatest contribution of micromechanical studies is that they provide the fundamentals for understanding ductile fracture and suggest directions for developing phenomenological models for fracture analysis. For example, the void growth model described in section 2.2.3.2 has gained significant attention. Other models, such as the continuum damage models, are also constructed within the framework of micro-mechanisms of ductile fracture. In the following section, some popular ductile fracture models, including the conventional and micromechanics-based phenomenological models as well as the continuum damage models will be reviewed and compared.

2.3.1 Ductile fracture models

Wilkins model

Wilkins et al. (1980) considered the effects of mean stress, the deviatoric stress ratio and the length scale on ductile fracture. The model assumes the fracture takes place when the damage variable D exceeds the critical value D_c over a critical length scale R_c, where the expression of D_c is given as

$$D_c = \int_0^{\bar{\varepsilon}_f} \frac{1}{\left(1 - a\sigma_m\right)^{\lambda}} \left(2 - A\right)^{\mu} d\varepsilon_p \tag{2.32}$$

where,

$$A = \max\left\{\frac{s_2}{s_1}, \frac{s_2}{s_3}\right\} \tag{2.33}$$

and $s_1 \geq s_2 \geq s_3$ are three deviatoric principal stress components, and a, λ, μ are three model constants. Bai and Wierzbicki (2015) introduced the Lode parameter and converted the parameter A into a function of the Lode parameter. Three model constants as well as D_c and R_c can be determined by experimental calibration. The basic expression of the Wilkins model in Eq. (2.32) is related to the absolute mean stress, the Lode parameter and the accumulated plastic strain. The Wilkins's model implies that the ductility of a material relies not only on the strain and stress state but also on the absolute strength of the material itself.

McClintock model

McClintock (1968) theoretically analyzed the growth of cylindrical voids with elliptical cross section. Assuming the material were only subjected to transverse tensile stress, a closed-form expression of a damage-like variable D is expressed as

$$\frac{dD}{d\varepsilon_p} = \frac{1}{\ln F_{zb}}\left[\frac{\sqrt{3}}{2(1-n)}\sinh\left(\frac{\sqrt{3}(1-n)}{2}\frac{\sigma_a+\sigma_b}{\bar{\sigma}}\right)+\frac{3}{4}\frac{\sigma_a-\sigma_b}{\bar{\sigma}}\right] \tag{2.34}$$

where F_{zb} is a relative void growth factor in terms of the initial and current geometries of the void and the cell, σ_a and σ_b are two principal stresses, and n is the hardening exponent. Fracture is postulated to occur when D=D_c and $F_{zb} = F_{zb}^f$. The only parameter in McClintock model that needs to be calibrated is the critical damage variable D_c. It can be observed that the plastic strain to fracture is related to the void geometric evolution in addition to the stress and strain states. Strain hardening effect is also incorporated by this model.

Rice and Tracey model

The void growth model proposed by Rice and Tracey (1969) has been already reviewed in section 2.2.3.2. As void growth proceeds to a critical state, it offers a good estimation of void coalescence and fracture initiation. By integrating Eq. (2.15) and considering a more general material hardening property, the damage-like variable can be obtained as

$$D = \ln \frac{R}{R_0} = \int_0^{\varepsilon_p} \alpha \exp\left(\beta \frac{\sigma_m}{\bar{\sigma}} \right) d\varepsilon_p \tag{2.35}$$

where α and β are two model parameters. Failure takes place once the criterion reaches the critical value D_c.

Johnson-Cook model

The Johnson-Cook model (Johnson and cook, 1985) is one of the most widely used models both for the constitutive law but also the associated fracture model. The model considers three factors that affect the ductility and hardening property of materials, i.e., triaxiality, strain rate and temperature. The Johnson-Cook constitutive equation is essentially an empirical function, which represents a product of three factors

$$\bar{\sigma} = \left[A + B\left(\varepsilon_p \right)^n \right] \left[1 + C \ln\left(\frac{\dot{\varepsilon}_p}{\dot{\varepsilon}_0} \right) \right] \left[1 - \left(\frac{T - T_0}{T_{melt} - T_0} \right)^q \right] \tag{2.36}$$

where A, B, C, n, q are five material constants, among which, n is the strain hardening exponent, q is the temperature related exponent, $\dot{\varepsilon}_p$ is the plastic strain rate, T_0 and T_{melt} are the room temperature and the material melting temperature, respectively. Regardless of the effects of temperature and strain rate, the Johnson-Cook model reduces to an

exponential strain hardening function. Similarly, the Johnson-Cook model's fracture criterion can be expressed as

$$\varepsilon_f = D_1 + D_2 \exp\left(D_3 \frac{\sigma_m}{\bar{\sigma}} \right) \tag{2.37}$$

where D_1, D_2 and D_3 are three parameters for the fracture model. D_1 and D_2 are positive, and D_3 is negative. When compared to the Rice-Tracey model, the Johnson-Cook model has an extra constant term D_1, which means that as the triaxiality tends to infinity the plastic strain to fracture becomes equal to D_1 instead of 0. The Johnson-Cook model was developed based on a void growth model. It is empirical in accounting for the effects of temperature and strain rate and all the material constants need to be calibrated using suitable experimental procedures.

Cockcroft-Latham model

Cockcroft and Latham (1968) proposed a phenomenological model for ductile fracture prediction. The model considers that fracture is related to the maximum principal stress and the accumulated plastic strain, which reads

$$D = \int_0^{\varepsilon_p} \langle \sigma_1 \rangle d\varepsilon_p \tag{2.38}$$

where,

$$\langle \sigma_1 \rangle = \begin{cases} 0 & \sigma_1 < 0 \\ \sigma_1 & \sigma_1 \geq 0 \end{cases} \tag{2.39}$$

and σ_1 is the maximum principal tensile stress. When the criterion predicts that the damage-like variable $D=D_c$, then ductile facture occurs and the corresponding plastic strain is the strain at fracture $\varepsilon_f=\varepsilon_p$. Later, Oh et al. (1979) modified the Cockcroft and Latham model

by including the stress ratio in the fracture criterion, which is given as

$$D = \int_0^{\varepsilon_p} \frac{\langle \sigma_1 \rangle}{\bar{\sigma}} d\varepsilon_p \tag{2.40}$$

Oh et al. (1979) also noticed that the modified version of the Cockcroft and Latham model can be equivalent to the McClintock model if the hyperbolic sine function is expanded to a linear function. Bai and Wierzbicki (2015) also performed some conversions of this criterion and their modified function implies the Cockcroft and Latham model is a function of both triaxiality and Lode parameter.

Maximum shear stress model

The maximum shear stress model is one of the oldest failure criteria. This model predicts that fracture takes place when the maximum shear stress reaches a critical value, which is written as

$$\tau_{\max} = \tau^f \tag{2.41}$$

where τ^f is the only material constant for this criterion. This model is essentially Lode parameter dependent disregarding the triaxiality sensitivity of ductile fracture. Though crude, the maximum shear stress model offers the basis of many studies in developing ductile fracture models in terms of Bai and Wierzbicki (2010), Wen and Mahmoud (2015) and the model proposal in chapter 3.

Hooputra model

Hooputra et al. (2004) classified failure in ductile solids into three modes including instability, ductile fracture due to void growth, and shear fracture. Only the latter two are considered in this section. In terms of the second mode, the strain to fracture is given as a

function of triaxiality

$$\varepsilon_f = d_0 \exp(-c\eta) + d_1 \exp(c\eta) \tag{2.42}$$

where $\eta = \sigma_m / \bar{\sigma}$ is the triaxiality, d_0, d_1 and c are three model parameters. For the shear dominated fracture, the criterion is assumed to be the function of a shear fracture parameter

$$\varepsilon_f = d_2 \exp(-f\theta_s) + d_3 \exp(f\theta_s) \tag{2.43}$$

where d_1, d_2 and f are three model parameters. The shear fracture parameter is defined as a function of triaxiality and shear stress factor

$$\theta_s = \frac{1 - k_s \eta}{\phi} \tag{2.44}$$

where $\phi = \tau_{\max} / \bar{\sigma}$ is the ratio of the maximum shear stress and the equivalent stress, and k_s is another model constant to be calibrated. The difficulty for the implementation of this model is that neither does it explicitly distinguish between the two modes of ductile fracture nor does it give the applicable range for these two branches of the fracture model.

Gurson-like models

The framework of the Gurson model has been described earlier. The original version and its extensions of the Gurson model can be directly applied to ductile fracture prediction (Mear and Hutchinson, 1985; Leblond et al., 1995; Nahshon and Hutchinson, 2008; Cazacu et al., 2014). The most prominent characteristic of the Gurson like models are the porosity related constitutive law. The void growth evolution influences the process of ductile fracture. It also influences the yield strength wherein the growth of porosity is associated with the degradation of yield surface size. In this case, the porosity can be considered as a damage variable. Sometimes, ductile fracture models are classified as uncoupled and

coupled types, depending on whether the yield functions are linked with the damage accumulation. Even though the porosity evolution in the Gurson-like models are divided into several stages, i.e., void nucleation, growth and coalescence, it is not explicitly distinct in the application of the Gurson model, which is implemented as an integrated model. To some extent, the Gurson-like models can be also treated as a continuum damage model even though its basis is different from typical continuum damage models.

There are some inherent shortcomings of the Gurson-like models. The single parameter measurement of damage by the porosity in the model is likely inadequate since damage accumulation is more complex than the void volumetric growth mechanism. For instance, the microcracks that lead to increasing damage and loss of material loading carry capacity can occur with little volumetric change, which cannot be captured by the porosity variable alone. The second drawback of Gurson-like models, which is also the concurrent defect of many other micromechanics-based models, is its incapability in describing the shear localization induced fracture. Though some modifications have been done to improve the situation, the essence of this mechanism is difficult to incorporate into the framework of current micromechanics-based models, which rely on the void volumetric growth and internal necking mechanism. Thirdly, the material parameters of the Gurson-like microscopic approach is difficult to calibrate. The uncertainties of void size, shape, distribution, and heterogeneity of microstructure make it impossible to measure the parameters by pure experimental approaches. Alternatively, combining experimental calibration and inverse numerical analysis can be used to estimate the model parameters.

2.3.2 Continuum damage mechanics

Engineering practice requires a rational predictive tool with reasonable accuracy.

Since the objective of failure analysis is to capture failure behavior of engineering materials, to assess safety factors and to determine the suitability of a certain material for a specific engineering application in a direct and reasonably simple way, the fracture prediction approaches directly based physical failure phenomena are often too complex. The ductile fracture models described above represent significant progress towards practical implementation. Based on microscopic studies, these local fracture approaches can predict the macroscopic fracture initiation, propagation and even the strength degradation using local stress and strain information. Continuum damage mechanics provides another approach for describing the effects of microcracks or microvoids on the mechanical behavior of materials that provides a bridge from microstructural evolution to macroscopic material mechanical response. This is accomplished by the concept, termed damage, that represents the progress of degradation of a material due to the growth of microscopic defects, such as microvoids and microcracks that lead to ductile fracture. This gives rises to the critical issue involving appropriately characterizing the damage variables to reflect the physical nature of mechanical behaviors as well as fracture mechanisms acting on multiple scales from micro- to meso- to macro-scale.

In continuum damage mechanics, contrary to the facts that the microvoids and microcracks are discontinuous, the corresponding damage measurement is considered to be continuous in a medium at a larger scale (Lemaitre and Desmorat, 2005). In this case, the damage variable is the basic concept that represents average material deterioration on a macro-mechanics scale. This, incorporated with the concept of effective stress, was first introduced by Kachanov (1958) in studying the creep fracture of a metallic material. The approach of continuum damage mechanics (CDM) was thus developed. The early consideration of the damage variable in CDM was just treating the critical value of damage

as a threshold. When exceeded, the material was assumed to have no further loading carrying capacity (Rabotnov, 1969; Lemaitre and Chaboche, 1994). Since this early work, research on damage mechanics was heavily focused on creep and creep-cyclic failure (Chaboche, 1987; Lin et al., 1999). Later, Lemaitre (1972), Chaboche (1981) and Krajčinović and Fonseka (1981) contributed to the development of continuum damage mechanics by advancing the damage factor from a state variable to a field variable using the principles of continuum mechanics. Lemaitre and Chaboche (1978) developed the damage representation based on the principles of thermodynamics and continuum mechanics. This became a new branch of CDM and provided the basis of many other subsequent CDM approaches (Kachanov, 2013; Lemaitre, 1985; Krajcinovic, 1985; Voyiadjis and Kattan, 1990; Wu et al., 2006).

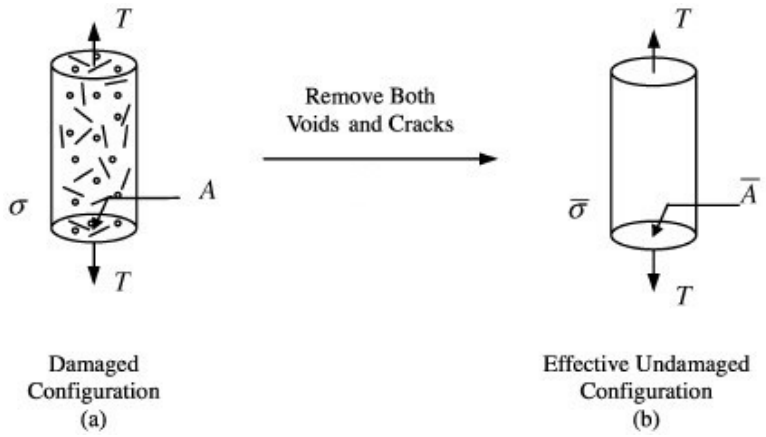

Fig. 2.11 Damaged and effective undamaged representations (Kattan and Voyiadjis, 2012).

There are different ways in continuum damage mechanics to measure or define the damage variable, such as by the lifetime of a structure, by the microstructure of the material,

or by mechanical parameters. Early consideration of damage involving the surface density of micro-defects was considered by several investigators (Chaboche, 1981; Dyson and McLean, 1977; Levaillant and Pineau, 1982). Considering a damaged body with a cylindrical shape (see Fig. 2.11(a)) and a fictitious counterpart by removing all the damage that the body has undergone (see Fig. 2.11(b)), the interpretation of the damage can be considered through comparison between these two configurations. The damage variable D can be expressed in terms of the net cross-sectional area reduction

$$D = \frac{A - \bar{A}}{A} \tag{2.45}$$

where A is the cross-sectional area of the bar and $\bar{A}$ is the effective cross-sectional area. Moreover, the damage variable works with the concept of effective stress, which states that a damaged solid subjected to the applied stress σ exhibits the same strain response as the corresponding undamaged one subjected to the effective stress $\tilde{\sigma}$. It is worth noting that the effective stress concept has the underlying hypothesis of elastic strain equivalence gives $\varepsilon = \tilde{\varepsilon}$. The effective stress can be therefore obtained as

$$\tilde{\sigma} = \sigma \frac{A}{\bar{A}} = \frac{\sigma}{1 - D} \tag{2.46}$$

The other definition of the damage variable is in terms of the elastic modulus reduction. Using the concept of effective stress and assumption of equivalent strain, gives rise to the relations

$$\sigma = E\varepsilon; \qquad \tilde{\sigma} = \tilde{E}\tilde{\varepsilon} = \tilde{E}\varepsilon \tag{2.47}$$

Hence,

$$\tilde{\sigma} = \frac{E}{\tilde{E}}\sigma = \frac{\sigma}{1-D} \Rightarrow D = 1 - \frac{\tilde{E}}{E} \tag{2.48}$$

where $\tilde{E}$ is the effective elastic modulus in the damaged solid. However, either the surface density related or the elastic modulus related scalar damage variable described herein are for the simple isotropic case. These definitions and their underlying hypotheses cannot be directly applied to cases such as anisotropic damage, where some necessary modifications are needed. The above discussion provides the basic idea of damage variable measurement, and more importantly, the consideration in describing the damage in continuum damage mechanics. What's more, the damage can be established based on energy principles and thermodynamics to overcome the difficulties arising from the usage of abovementioned damage variable definitions. For example, micro-defects as well as area reductions are hard to observe and measure.

Lemaitre model

Lemaitre (1985) proposed a continuum damage model based on the works of Kachanov (1958) and Rabotnov (1969). This model was derived within the framework of thermodynamics using energy principles and then became the milestone of continuum damage mechanics development. In this section, the simple version of Lemaitre model including isotropic strain hardening is presented. The yield function is given as

$$\Phi = \frac{\sigma_{eq}}{1-D} - \bar{\sigma} = 0 \tag{2.49}$$

The damage variable evolution law is defined as

$$\dot{D} = \frac{\dot{\varepsilon}_p}{1-D}\left(-\frac{Y}{r}\right)^s \tag{2.50}$$

where s and r are material constants, $\dot{\varepsilon}_p$ is the increment of internal variable associated with isotropic hardening, and Y denotes the strain energy release rate, given as

$$Y = -\frac{\sigma_{eq}^2}{2E(1-D)^2}\left[\frac{2}{3}(1+\upsilon)+3(1-2\upsilon)\left(\frac{\sigma_m}{\sigma_{eq}}\right)^2\right] \tag{2.51}$$

where υ is poisson's ratio. Note that the strain energy release rate is essentially a function of σ_m/σ_{eq} representing stress triaxiality. In fact, even though the Lemaitre model is developed based on the principles of continuum damage, it also takes into account some microscopic aspects of ductile fracture. The derivation partly follows the Rice and Tracey model that correlates triaxiality to microvoid growth in evaluating damage evolution (Lemaitre, 2012).

Rousselier model

Rousselier (1987) proposed another important damage model to describe the constitutive behavior and the failure of the ductile solids. The model is developed based on the framework of Lemaitre and Chaboche (1978). Slightly different from the Lemaitre model, the Rousselier model considers the basics of both the Gurson model and the Rice and Tracey model in considering the porosity variable in the model development. The continuum yield function of the Rousselier model is given as

$$\Phi = \frac{\sigma_{eq}}{\rho} + \sigma_1 f\tilde{D}\exp\left(\frac{\sigma_m}{\rho\tilde{\sigma}_1}\right) - \bar{\sigma} = 0 \tag{2.52}$$

where ρ is the relative density in terms of the ratio of the density of the damaged material and that of the undamaged material, f is the porosity, $\tilde{D}$ is the material constant and $\tilde{\sigma}_1$ is the material parameter related to the Von Mises effective stress.

2.3.3 Comparison of ductile fracture and damage models

This section compares a number of existing ductile fracture and damage models, which were either described previously or will be discussed in later parts of this dissertation. The models for comparison and their respective kernel functions are listed in Table 2.1.

The models provided in Table 2.1 can be classified from several perspectives. From the theoretical basis point of view, these models are categorized into ductile fracture (DF) and continuum damage mechanics models (CDM), as described earlier in this chapter. The greatest difference between two categories are whether the damage (porosity) evolution influences the yield strength of the material or not. For all the ductile fracture models except the GTN, the model is in terms of the damage variable itself. In fact, the damage variable in those models ((1) -(8)) are not the real damage of the material, but the indicator of fracture initiation so that the variable does not involve in the material behavior. In this case, the models ((1) -(8)) are referred to as uncoupled models, where the CDM family of models are known as coupled models. Sometimes, the GTN model is referred to as a CDM model, since the critical parameter, porosity in this model is essentially the damage that affects the yield function. The basis of the Rousselier model is the combination of Gurson and Lemaitre models so that it can viewed as either DF or CDM model.

Although developed within different frameworks, these models still have a common characteristic. Through the kernel functions, one can find that the internal variable associated with plasticity is proportional to the damage or damage-like variable for a given stress state. This, in contrast to conventional fracture mechanics where the plastic strain history has no influence on the failure behavior, reflects the advancement of the fracture approaches based on micromechanical investigations. However, the stress state variables

involved in the kernel functions are quite different from each other. Currently, there are two parameters to evaluate the stress state for ductile fracture studies, i.e., the triaxiality accounting for the effect of hydrostatic stress and the Lode parameter considering the deviatoric stress. In general, models (3), (4), (9), (10) and (11) are only dependent on the former variable. Bai and Wierzbicki (2015) did some simple conversion for models (1), (2) and (5) and suggested that these models are all functions of both stress state variables even though they use different forms of expression. The motivation of developing the relatively new models (6), (7) and (8), each of which is the function of Lode parameter and triaxiality, is to take into account the shear effect and make the ductile fracture applicable for a wider range of stress states than the triaxiality dependent models. Triaxiality controls void growth at relatively high levels of triaxiality and these triaxiality dependent models are only suitable for ductile fracture controlled by the void volumetric growth mechanism. The mechanism of void shearing is not well established up to now so that all the extensions of ductile damage and fracture models to couple the shearing effect with the triaxiality effect are based on empirical observations.

The performance of each model in fracture prediction has been evaluated and compared by Bai and Wierzbicki (2015), Li et al. (2011) and Xue (2007), and their accuracy varies on a case-by-case basis. Comparison among the ductile fracture models indicates none has overwhelming superiority over the others. This is understandable in that all the models are developed based on a few assumptions to simplify the problem, while neglecting some factors affecting the ductile fracture process. At present, it appears that there is not an available model that can incorporate all the characteristics of ductile fracture. Generally, the uncoupled family of models have the advantage of being easy-to-implement with little computational expense. Although the damage coupled models are still

phenomenological, they provide more physical interpretation to the ductile fracture process so that they may offer more reasonable predictions. From the predictive accuracy point of view, the damage and shear effect coupled models are favored.

Table 2.1 Various ductile fracture and damage models.

No.	Model	Kernel function	Type
1	Wilkins	$dD = \left(2 - \max\left\{s_2/s_1, s_2/s_3\right\}\right)^{\mu} \Big/ \left(1 - a\sigma_m\right)^{\lambda} d\varepsilon_p$	DF/uncoupled
2	McClintock	$dD = d\varepsilon_p \left[\sqrt{3}/2\left(1-n\right)\sinh\left(\sqrt{3}\left(1-n\right)\left(\sigma_a+\sigma_b\right)/2\bar{\sigma}\right) + 3\left(\sigma_a-\sigma_b\right)/4\bar{\sigma}\right] \Big/ \ln F_{zb}$	DF/uncoupled
3	Rice-Tracey	$dD = \alpha \exp\left(\beta\,\sigma_m/\bar{\sigma}\right) d\varepsilon_p$	DF/uncoupled
4	Johnson-Cook	$dD = \left[D_1 + D_2 \exp\left(D_3\,\sigma_m/\bar{\sigma}\right)\right] d\varepsilon_p$	DF/uncoupled
5	Cockcroft-Latham	$dD = \left\langle \sigma_1 \right\rangle / \bar{\sigma}\, d\varepsilon_p$	DF/uncoupled
6	Hooputra	$dD = \left[D_4 \exp\left(-D_5\theta_s\right) + D_6 \exp\left(D_5\theta_s\right)\right] d\varepsilon_p$	DF/uncoupled
7	Xue-Wierzibicki	$dD = \left[b_1 \exp\left(-b_2\eta\right) - \left[b_1 \exp\left(-b_2\eta\right) - b_3 \exp\left(-b_4\eta\right)\right]\left(1-\xi^m\right)^{\frac{1}{m}}\right] d\varepsilon_p$	DF/uncoupled
8	Modified Mohr-Coulomb	$dD = \left\{A/b_5\left[\sqrt{\left(1+b_6^2\right)/3}\cos\left(\pi\bar{\theta}/6\right) + b_6\left(\eta + \sin\left(\pi\bar{\theta}/6\right)/3\right)\right]\right\}^{-\frac{1}{n}} d\varepsilon_p$	DF/uncoupled
9	Gurson-Tvergaard-Needleman	$\Phi = \dfrac{\sigma_{eq}^2}{\bar{\sigma}^2} + 2q_1 f \cosh\left(\dfrac{3}{2} q_2 \dfrac{\sigma_m}{\bar{\sigma}}\right) - \left(1 + q_3 f^2\right) = 0$	DF/CDM/coupled
10	Lemaitre	$\Phi = \sigma_{eq}/\left(1-D\right) - \bar{\sigma} = 0, \quad dD = d\varepsilon_p/\left(1-D\right)\left(-Y/r\right)^s$	CDM/coupled
11	Rousselier	$\Phi = \dfrac{\sigma_{eq}}{\rho} + \sigma_1 f\tilde{D}\exp\left(\dfrac{\sigma_m}{\rho\tilde{\sigma}_1}\right) - \bar{\sigma} = 0$	DF/CDM/coupled

2.4 PLASTIC STRAIN LOCALIZATION IN METALS

Strain localization involves the deformation or strain distribution mode changing from a homogenous one to an intensively localized pattern (Borja, 2000). It takes place in a wide range of materials, from sand and rocks to concrete and structural metals (Desrues and Viggiani, 2004; Desrues et al., 2007; Pijaudier-Cabot and Bažant, 1987; Okazawa, 2010), over broad size scales, from macroscopic to microscopic level and under various loading conditions (Bandstra et al., 2004; Tvergaard and Niordson, 2004; Audoly and Hutchinson, 2016), from tensile to shear. Factors that give rise to strain localization can be material strain-softening behavior (Bažant and Jirásek, 2002), geometric constraints (Kolwankar et al., 2017), thermal effect (Wcisło and Pamin, 2017), or a combination of these (Benallal and Bigoni, 2004). Compared to the localization phenomena in softening materials such as soils and sand that it is the direct consequence of the material softening property, localization in structural metals is more complex (Antolovich and Armstrong, 2014). In some limited cases, such as when the material behavior of metals is described by a damage accumulation coupled plasticity or the porous metal plasticity model, such as GTN (Enakoutsa et al., 2007; Samal et al., 2009; Xue, 2010), the situations are quite similar to that in geomaterials or concrete. More generally, the plastic strain localization in structural metals with strain hardening is possibly driven by geometric nonlinearity or thermal diffusion (Tvergaard, 1993; Lemonds and Needleman, 1986).

Strain localization plays a key role in the ductile fracture process. Its significance can be seen from both macroscopic and microscopic points of view. From the macroscale point of view, the large strain localized region will become the underlying fracture initiation zone since the material outside the localization region experiences unloading

while the strain inside the localized zone intensifies quickly. As discussed in section 2.2.1, both fracture initiation and crack propagation in a tensile specimen take place in the necked region. The high local strain can arise from either macroscopic or microscopic localization such as internal necking and shearing described in section 2.2.4.1, which will precipitate void nucleation, growth and coalescence. Although the interaction of the strain localization at different scales is not easy to distinguish, their importance in ductile fracture is clear. The following section will focus on the mechanics of strain localization occurring at different scales and under different loading conditions. Also, the approaches that are used for mathematically characterizing and modeling strain localization will be reviewed.

2.4.1 Strain localization in tensile loading

The most recognized strain localization phenomenon in structural metals is with respect to ordinary tensile testing, from which one can observe that the strain localized into a small region shaped as a neck. The necking type of localization is representative since it reflects the competition of hardening and the applied stress under the simplest loading condition, namely uniaxial tension. The early analytical solution to the onset of macroscopic necking pertains to the Considère's criterion (Considère, 1885) that provides the condition $dP=0$ at the peak of the experimental loading-displacement curve, wherein P represents the uniaxial tensile load. The interpretation of this condition can be simplified by that fact that the applied force from the increasing state to the decreasing state follows the reduction of cross-sectional area in the necking region. The slight change in cross section outside the necking zone is associated with unloading, referring to the reduction of not only the applied load but also the stress. The situation of unloading inside the necking region is to some extent different since the applied stress still increases due to strain

hardening, so that all subsequent deformation concentrates on this very localized region.

The derivation of Considère's criterion is based on the rate independent constitutive relation. Without considering the time effect, the onset of strain localization represents a bifurcation between stable and unstable equilibrium, and can therefore be viewed as an instability condition. Later, Hart (1967) included strain rate in the problem formulation to explicitly analyze the instability condition. Start by assuming a common constitutive equation

$$\sigma = K\varepsilon^{n}\dot{\varepsilon}^{m} \tag{2.53}$$

where σ, ε and $\dot{\varepsilon}$ are true stress, true strain and strain rate, respectively, K is a material constant, and n and m are strain and strain rate related exponents, respectively. Defining the parameter q as

$$q = \frac{1}{\varepsilon}\left(\frac{\partial \ln \sigma}{\partial \ln \varepsilon}\right)_{\dot{\varepsilon}} \tag{2.54}$$

Hart (1967) obtained a simple relation through some analytical calculations to characterize the instability occurrence as

$$q + m = 1 \tag{2.55}$$

The equation will reduce to the Considère's criterion once m=0. This condition implies that the onset of strain localization does not necessarily coincide with the bifurcation point when incorporating the loading rate effect. Some other criteria based on various definitions of instability can be found from Duncombe (1972), Hutchinson and Neale (1977), Lin et al. (1981) and Ha (1995).

Based on the mechanical description of instability, those criteria provide simple

while useful approaches to approximate the onset of strain localization. Better understanding of the underlying physics and more accurate quantification of the instability condition requires study of strain localization at the microscopic level. For instance, the strain and strain rate related exponents that are considered as material constants are, in fact, material history dependent parameters. From a general point of view, the prerequisite for occurrence of strain localization is the need for inhomogeneities of the microstructures. Among others, dislocation pile-ups provides one of the most important potential sources of inhomogeneity. Within the framework of the Hall-Petch relationship (Hall, 1951; Petch, 1953), Antolovich and Armstrong (2014) reviewed the influence of microstructures on the onset of plastic instability. Their study suggested that it is the process at the level of dislocations and grains, which are influenced by the Hall-Petch parameters, that consequently impact the strain concentration at a microstructural level. On the other hand, the thermal effect is another key factor that directly influences the strain rate and indirectly affects the process of strain localization. Consider a simple relationship between the shear strain rate, the dislocation density, and the dislocation velocity:

$$\dot{\nu} = b\rho\upsilon \tag{2.56}$$

where $\dot{\nu}$ is the shear strain rate, b is the Burgers vector, ρ is the dislocation density and υ is the dislocation velocity. The dislocation velocity is dependent on the thermal component of the applied stress τ_{th}, which reads

$$\upsilon = \upsilon_0 \left(\frac{\tau_{th}}{\tau_{th0}} \right)^t \tag{2.57}$$

where υ_0 is the reference velocity for applied stress equals to τ_{th0} that is the reference stress, and t is the stress related exponent.

2.4.2 Shear banding

Shear banding is another form of strain localization. Shear localization is an even more representative instability than necking. If necking did not take place beforehand, shear localization would be observed in ordinary tensile testing. Sometimes, they are concurrent in the uniaxial tensile testing specimen. A special case of shear localization is referred to as the adiabatic shear band (ABS) involving dynamic loading. High temperature develops within the band due to the extreme high strain rate without any heat transfer. However, this discussion of shear banding will be restricted to the quasi-static case with low strain rates, so that this extreme strain localization (ASB) will not discussed further herein.

Material subjected to dominant compression can be a typical candidate for shear localization formation within thin planar zones. However, neither uniaxial compression nor pure shear can be simply understood as the only loading condition where shear localization is favored. From the macroscopic point of view, strain localization takes place when the deformation is preferred to proceed within a deformed zone than to initiate elsewhere. The interpretation of the onset of shear localization is less straightforward than that of necking initiation. Without losing generality, strain localization involves the bifurcation of a deformation into a discontinuity in terms of strain or acceleration, namely a weak discontinuity. There exist numerous criteria to identify the presence of discontinuous solutions involving either the loss of positive definiteness, strong ellipticity or the appearance of a singularity for the governing equation (Rice, 1977; Hill and Hutchinson, 1975; Rice and Rudnicki, 1980). To simplify the discussion, attention in the following review will still be focused on the shear localization under uniaxial tensile conditions. Noting the straining, material properties and geometry all affect strain localization, the

discussion of shear localization will begin with a standard constitutive relation that couples the strain and strain rate

$$\tau = \tau_0 \gamma_i^n \dot{\gamma}_i^m \tag{2.58}$$

where τ is the resolved shear stress, τ_0 is a strength related constant, and γ and $\dot{\gamma}$ are resolved shear strain and shear strain rate, respectively, with respect to the slip direction. For common polycrystalline metals, assuming equivalent slip systems that are activated under a given resolved shear stress, the relations between Cauchy stress and shear measurements of stress and strain can be written as

$$\begin{aligned} \sigma &= M\tau \\ \Sigma_i \gamma_i &= M\varepsilon \end{aligned} \tag{2.59}$$

Hence,

$$\sigma = M^{(1+n+m)} \left(\Sigma \tau_0\right) \varepsilon^n \dot{\varepsilon}^m \tag{2.60}$$

where M is the Taylor factor (Kocks, 1958; Dillamore et al., 1979). The instability criterion is established upon the loading carrying capacity $P=A\sigma$, so that the underlying condition can be given as $(d\ln F)/(d\ln\varepsilon)\leq 0$

$$\left(1+n+m\right)\frac{d\ln M}{d\varepsilon} + \frac{d\ln \tau_0}{d\varepsilon} + \frac{n}{\varepsilon} - m\frac{d\ln\dot{\varepsilon}}{d\varepsilon} \leq -\frac{d\ln A}{d\varepsilon} \tag{2.61}$$

The right-hand side of Eq. (2.61) representing the geometric constraints holds positive for the tension case and equals zero for simple or pure shear, and this section is not intended to investigate such factor for localization initiation. Instead, the material structurally geometric softening will be under consideration. The active slip plane would rotate towards the more favorable orientation at which the resolved shear stress becomes greater. In this

case, the Taylor factor M decreases with an increasing ε. However, the M factor has been minimized during most processing operations for manufacture so that a constant orientation is always observed in polycrystalline materials (Jonas and Luton, 1978; Poirier, 1980). Hence, this kind of material softening can be neglected for the common usage of structural metals at ambient temperature. The second term of the left-hand side (LHS) of Eq. (2.61) denotes the material structural factor that has potential to induce softening. This aspect is generally considered as constant unless dynamic recrystallization or second-phase rearrangement takes place. The strain softening factor plays very similar role as that in the necking problem. For a positive exponent n, the strain mechanism can directly result in shear localization. It is necessary to work with other terms in the LHS of Eq. (2.61) to meet the condition for the onset of localization. This is also the case for the effect of strain rate on the localization.

2.4.3 Regularization approaches

Several approaches and models have been proposed to theoretically analyze strain localization not only in ductile metals, but also in geomaterials and concrete (Needleman and Tvergaard, 1977; Rice and Rudnicki, 1980; Bardet, 1990; Ottosen and Runesson, 1991; Alshibli and Akbas, 2007). With the development of computational technology, analysis on strain localization can be accomplished by finite element modeling. This section will review some of the most popular methods and theories that have incorporated FE simulations to capture the macroscopic phenomenon in a reasonable and accurate sense. Since the strain localization involves a jump or discontinuity of the displacement field, classical finite element technologies or material constitutive laws result in difficulties with

mesh dependency. In this case, the implementation of FE modeling requires enhancement to conventional FE approaches.

Adaptive meshing technologies provided early improvement to mesh dependency of strain localization simulations (Ortiz and Quigley, 1991; Ghosh and Raju, 1996; Belytschko and Tabbara, 1993; Zienkiewicz and Huang, 1990). This enhanced numerical technology, though avoiding excessive mesh distortion and mesh locking, disregarded the actual material behavior so that did not give physical sense to the localization results. Ortiz et al. (1987) introduced additional shape functions to the element interpolation to provide a fixed localization width and to reproduce the localization mode. Simo et al. (1993) employed the discontinuous strain field to the continuous displacement within the framework of continuum mechanics to deal with the strong discontinuity for bifurcation analysis. Borja (2000) described the strong discontinuity using the standard Galerkin approximation on material points instead of element nodes. All these modifications, however, encounter problems when determining the physical material response inside the localization band and do not eliminate the mesh sensitivity. More effective alternatives to the finite element modifications are attributed to the improvement of classical continuum mechanics by introducing a characteristic length scale that regularizes the governing equation to keep its well-posed and to allow continuation of the analysis after bifurcation. The following section will review four popular kinds of theories that incorporate this approach. The common characteristic of these theories is to give a length parameter to the standard constitutive relation serving as the localization limiter. The basic idea of these approaches is to consider the mechanical response at a certain point as the consequence of material interaction among not the neighboring points but all the points at a given spatial domain via the length scale.

Cosserat (micro-polar) continuum theory

The fundamental of Cosserat continuum theory has more than 100 years' history. This approach was first introduced by the Cosserat brothers (Cosserat and Cosserat, 1909), and involves the addition of three rotational degrees of freedom to the three translational degrees of freedom in the general continuum models. The additional deformation and stress measurements in the Cosserat theory are microrotation, micro-curvature as well as couple stress. The immediate extension of the Cosserat theory is the micropolar theory, the early work of which was done by Mindlin (1964) and Eringen (1968). Compared to classical continuum mechanics, the micropolar theory is more general since it takes the effects of the length scale, the internal microstructures, and the stress gradient into account, all of which have been verified by experiments at small scales. Another branch of the Cosserat theory family is the couple stress theory. This approach treats the microrotation as the true kinematical rotation, i.e., neglecting the microrotation in the formulation of kinematics. The couple stress theory is the direct enhancement of classical continuum mechanics by adding macro-rotational degrees of freedom to the continuum media. The couple stress theory offers advantages for analysis of strain localization.

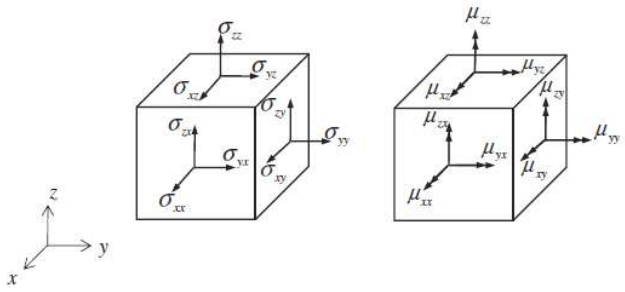

Fig. 2.12 General stress and couple-stress components in the couple stress theory (Khoei et al., 2010).

To examine this approach, its components of the strain tensors will be first presented. Defining the displacement field $\boldsymbol{u} = (u_x, u_y, u_z)$ and the rotation field $\boldsymbol{\omega} = (\omega_x, \omega_y, \omega_z)$, the strain $\boldsymbol{\varepsilon}$ and curvature tensors $\boldsymbol{\chi}$ can be given as

$$\begin{aligned} \varepsilon_{ij} &= \varepsilon_{ij} + \omega_{ij} - \omega_{ij}^{c} \\ \chi_{ij} &= \omega_{i,j} \end{aligned} \tag{2.62}$$

where,

$$\varepsilon_{ij} = \frac{1}{2}\left(\frac{\partial u_j}{\partial x_i} + \frac{\partial u_i}{\partial x_j}\right), \qquad \omega_{ij} = \frac{1}{2}\left(\frac{\partial u_j}{\partial x_i} - \frac{\partial u_i}{\partial x_j}\right), \qquad \boldsymbol{\omega}^{c} = \begin{bmatrix} 0 & \omega_z & \omega_y \\ -\omega_z & 0 & \omega_x \\ -\omega_y & -\omega_x & 0 \end{bmatrix} \tag{2.63}$$

Regarding the stress measurement, as shown in Fig. 2.12, it is decomposed into the general stress $\boldsymbol{\sigma}$ and couple stress vectors $\boldsymbol{\mu}$. For an elastic continuum medium, the constitutive relation can be given as

$$\begin{bmatrix} \boldsymbol{\sigma} & \boldsymbol{\mu} \end{bmatrix}^{\mathrm{T}} = \boldsymbol{D}_e^{c} \begin{bmatrix} \boldsymbol{\varepsilon} & \boldsymbol{\chi} \end{bmatrix}^{\mathrm{T}} \tag{2.64}$$

The formulation of the linear elastic operator neglects the interaction between stress and couple stress, and is given as

$$\boldsymbol{D}_e^{c} = \begin{bmatrix} \boldsymbol{D}_{e,uu} & \boldsymbol{0} \\ \boldsymbol{0} & \boldsymbol{D}_{e,\omega\omega} \end{bmatrix} \tag{2.65}$$

The fourth order isotropic tensors $\boldsymbol{D}_{e,uu}$ are the same as that in classical theory, while $\boldsymbol{D}_{e,\omega\omega}$ is a function of shear modulus and two characteristic length parameters related to torsion and bending.

de Borst (1991) derived the elasto-plastic constitutive law based on the von Mises criterion for the Cosserat continuum medium. He also gave the algorithm for the numerical

implementation of this couple stress model. Khoei (2010) developed the three-dimensional version of a similar model. Examples of strain localization modeling using the couple stress method include Nübel and Huang (2004), Khoei and Bakhshiani (2005) and Khoei et al (2005). However, these implementations are primarily for granular materials. To the author's knowledge, little work has been done to model localization in ductile solids with strain hardening plasticity. For geometry induced localization in structural metals, e.g., necking, the couple stress theory has great potential to capture this phenomenon with reasonable accuracy. Compared to other approaches that implement a simple enhancement to the material constitutive law, the couple stress approach incorporates the geometric effect into the formulation of the continuum mechanics. Future work is expected to focus on the application of couple stress theory to the strain localization in metals.

Strain gradient theory

Using the framework of couple stress theory, Fleck and Hutchinson (1993) developed a phenomenological strain gradient theory, which provides a simple generalization of J_2 isotropic hardening plasticity. The strain gradient is incorporated to the effective strain so that

$$\varepsilon_{CS} = \sqrt{\varepsilon_e^2 + l_{CS}^2 \chi_e^2} \tag{2.66}$$

where,

$$\varepsilon_e = \sqrt{\frac{2}{3}\varepsilon_{ij}\varepsilon_{ij}}, \qquad \chi_e = \sqrt{\frac{2}{3}\chi_{ij}\chi_{ij}} \tag{2.67}$$

and ε_e and χ_e are the von Mises invariant of strain and second invariant of the curvature, respectively, and l_{CS} is the material length scale. This theory, however, only considers the

gradients of rotation. More generally, another version of strain gradient theory proposed by Fleck and Hutchinson (1997) couples both the rotation and stretch gradients into the formulation of the overall effective strain, which gives

$$\varepsilon^2 = \frac{2}{3}\varepsilon'_{ij}\varepsilon'_{ij} + c_1\eta'_{iik}\eta'_{jjk} + c_2\eta'_{ijk}\eta'_{ijk} + c_3\eta'_{ijk}\eta'_{kji} \tag{2.68}$$

where $\boldsymbol{\eta}$ is the second gradient of displacement such that $\eta_{ijk}=u_{k,ij}$, and $\boldsymbol{\eta'}$ is the deviatoric part of $\boldsymbol{\eta}$. The values of three factors c_n are related to the length scale.

Based on the micro-mechanism of plastic deformation, Nix and Gao (1998) developed a mechanics-based strain gradient theory using the Taylor relation (Taylor, 1938)

$$\tau = \alpha\mu b\sqrt{\rho_T} = \alpha\mu b\sqrt{\rho_S + \rho_G} \tag{2.69}$$

where α is a material constant, b is the Burgers vector, μ is the shear modulus, ρ_T is the total dislocation density, ρ_S and ρ_G are the density of statistically stored dislocations (SSD) and the density of geometrically necessary dislocations (GND), respectively. The Cauchy stress can be related to the shear stress by Eq. (2.59). The strain gradient is only dependent on the GND, and has the relation

$$\eta = \rho_G b \tag{2.70}$$

Assuming an exponential form of strain hardening $\sigma = \sigma_{ref}\varepsilon^N$,the Cauchy stress can be obtained as

$$\sigma = \sigma_{ref}\sqrt{\varepsilon^{2N} + l\eta} \tag{2.71}$$

where,

$$l = M^2 \alpha^2 \left(\frac{\mu}{\sigma_{ref}} \right)^2 b \tag{2.72}$$

The parameter l is the intrinsic material length for the mechanics-based strain gradient theory (MSG). In the constitutive law of this plastic theory, the higher order of stress and strain gradients are presented. This generates the higher order terms in the governing equation and requires additionally boundary conditions to solve initially boundary value problem upon the MSG. It gives rises to the difficulties and limitations of the MSG implementation and further motivates the development of conventional theory of mechanism-based strain gradient plasticity (CMSG) (Huang et al., 2004). To illustrate the characteristic of CMSG, the equivalent plastic strain rate is introduced

$$\dot{\varepsilon}_p = \dot{\varepsilon} \left[\frac{\sigma_{eq}}{\sigma_{ref} \sqrt{\varepsilon^{2N} + l\eta}} \right]^m \tag{2.73}$$

The determination of the equivalent plastic strain rate essentially follows the formulation of visco-plasticity, which uses the effective stress instead of its rate. This theory is established on the same Taylor dislocation model as MSG, but does not involve the higher-order stress, thus additional boundary conditions are not needed.

The primary purpose of the strain gradient family of theories is to physically describe the size effect of microstructures at small scales. Due to its advanced characteristics (strain gradient and intrinsic length), it has also been applied to strain localization modeling by several researchers, including Jirásek and Rolshoven (2009), Matsushima et al. (2002), Shi et al. (2000), de Borst et al. (1999), Voyiadjis and Abu Al-Rub (2006). The strain localization in these simulations are induced either by material strain softening or by damage accumulation. The regularization effect of the strain gradient

theory can only be achieved based on the material constitutive law. No evidence has been found that the strain gradient theory can incorporate the geometry nonlinearity in strain localization modeling.

Nonlocal theory

All the theories including the Cosserat continuum, strain gradient and peridynamic theories can be considered as nonlocal theories. However, the nonlocal theory reviewed in this section refers to the one developed by Edelen et al. (1971), Eringen and Kim (1974) and Bažant and Lin (1988), for which the local material internal variables are replaced by their nonlocal counterparts calculated by integration over the surrounding spatial domains. The basic function of this theory is expressed as

$$\bar{g}(x) = \int_V \alpha(x, y)\, g(y)\, dy \tag{2.74}$$

where $g(x)$ is a certain local variable at material point x, α is the characteristic length related averaging function for the nonlocal treatment, which can be, for instance, the gauss error function or the bell-shaped function, $\bar{g}(x)$ is the nonlocal variable, and V is the spatial domain. The above equation represents the integral-type of nonlocal model, while there are two other kinds of nonlocal approaches involving the explicit and implicit gradient type of nonlocal models, details of which can be found in Engelen et al. (2003). Unlike the strain gradient theory or the couple stress theory, the nonlocality in this theory can be formulated based on various quantities, such as the plastic strain, the internal plastic variable, the damage variable, or the stress tensors. The fundamental concept of the nonlocal theory is to consider that the mechanical behavior at a given material point is dependent not only on its contacting neighboring points, but also on the surrounding points within the domain.

By using a certain averaging function and expanding Eq. (2.74) into a Taylor series, the nonlocal equation can be converted to the basis of strain gradient theory, indicating a strong relationship between two theories. In fact, these two theories associated with the couple stress theory have very similar physical interpretations that take account the contribution of the material points within the whole domain, which is the primary difference from the classical theory of continuum mechanics. In addition to the advantages that the previous two theories present, the nonlocal theory exhibits a more flexible formulation, since the field it can process is not limited to the strain gradient but includes damage and thermal variables. More detailed review of the nonlocal theory can be found in chapter 6&7 of this dissertation.

Peridynamic theory

Peridynamics (PD) is a recently proposed and developed theory, the basic idea of which was first introduced by Silling (2000). It is also a nonlocal extension of classical continuum mechanics. The significant difference of this new theory from the previous nonlocal theories as well as the classical theory of continuum mechanics is that the peridynamic theory is established based on integral equations instead of partial differential equations. Hence, the peridynamic theory is valid not only for the cases of displacement discontinuities (strain localization) but also for spatial discontinuities, e.g., cracking and separation of interfaces. The basic equation of motion that was proposed in the original peridynamic theory reads

$$\rho(x)\ddot{u}(x,t)=\int_H f\left(u(x',t)-u(x,t),x'-x,x\right)dV_{x'}+b(x,t) \tag{2.75}$$

where ρ is the mass density, u is the displacement vector field, b is the body force density, f is the bonds force density for all bonds ξ=x'-x, H is the family of x within δ and δ is the

horizon of the material point x (see Fig. 2.13). Compared to the classical governing equation, the above function has its integral of nonlocal forces in the right-hand side replacing the divergence of stress. The bonding interaction between two material points (x, x') does not require they separate with zero distance. The function f, also known as the pairwise force function, models all the constitutive relations of materials, i.e., describes the relationship between the internal force and the deformation. Similar to other nonlocal theories, peridynamics involves a length scale that is introduced by the peridynamic horizon.

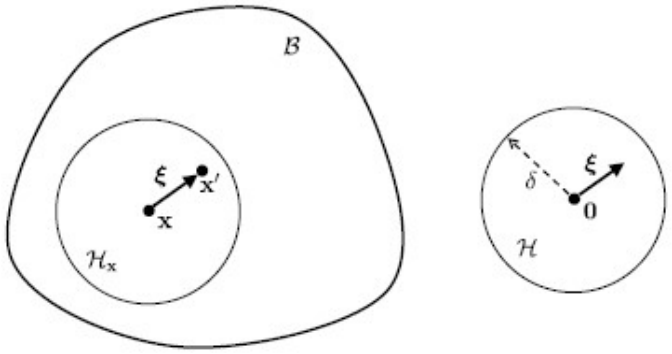

Fig. 2.13 Illustration of interaction between material points (Silling and Lehoucq, 2010).

Although this is a new theory and improvement is needed, the peridynamic theory has great potential to address the problems for which the classical theory of continuum mechanics has exhibited difficulties. It has achieved encouraging progress and great success in applications including discontinuous failure predictions, multiscale modeling and multiphysics modeling. Ha and Bobaru (2010) and Askari et al. (2008) analyzed the dynamic crack branching in brittle materials, and offered a reasonable interpretation of the

underlying physics of crack branching based on the results of PD. This work indicates peridynamics may be an effective formulation for modeling the entire process of dynamic crack propagation. Silling and Askari (2014) and Zhang et al. (2016) predicted fatigue crack growth based on the PD approach and obtained results of fatigue lives that agree with experiments for different crack growth conditions. Rahman and Foster (2014) and Rahman and Haque (2012) established the uniform framework using PD approach, working towards multiscale modeling for complex materials. Since the PD approach is not well suited to the finite element framework, part of its numerical implementation must be done using the particle element method. Its applications to strain localization, especially for ductile solids, has not yet been extensively investigated. In the future, however, the PD approach may be attractive in strain localization as a localization limiter and even ductile fracture modeling.

2.5 SUMMARY

This chapter reviewed background and current research in ductile fracture from different aspects, from the methodologies to the mechanisms. First, some basic concepts as well as the advantages and limitations of traditional fracture mechanics approaches in predicting ductile fracture were discussed. It was noted that for fracture involving extensive plasticity, conventional fracture mechanics is not able to describe the underlying physics of the fracture phenomena.

The micromechanical fundamentals of ductile fracture involving microvoid nucleation, growth and coalescence was then discussed. The mechanisms associated with the mathematical models for each void evolution stage were provided. Several popular micromechanics-based ductile fracture models were then discussed and compared. When accounting for the balance of predictive accuracy and computational expense, no model

stands out as superior, which implies efforts are still required to advance ductile fracture predictive technologies.

As an important field strongly related to ductile fracture, strain localization was briefly reviewed including its mechanisms and mathematical descriptions. To better capture observed physical phenomena by finite element modeling, four popular enhancements to the classical theory of continuum mechanics were introduced. They have different formulations while quite similar physical interpretations and exhibit great potential to advance strain localization modeling in ductile metals.

CHAPTER 3

Prediction of Ductile Fracture for Metal Alloys Using a New Micromechanics-based Criterion

3.1 INTRODUCTION

Prediction of ductile fracture in crack-free bodies has been of great interest and extensively studied during recent decades. Starting with the micro-mechanisms of ductile fracture, which consists of microvoid nucleation, growth, and coalescence, McClintock (1968) and Rice and Tracey (1969) developed several micromechanics-based fracture models. They suggested that void growth is dominated by two main factors, which are equivalent plastic strain and stress triaxiality. However, the interaction among voids during the growth process was neglected in their studies. The interaction as well as the microvoids shape change effect were further studied by Le Roy et al. (1981). Moreover, Hancock and Mackenzie (1976), Mackenzie et al. (1977), Hancock and Brown (1983), Marini et al. (1985), Panontin and Sheppard (1995), Bandstra et al. (2004) and Benzerga et al. (2004) conducted experiments to verify the mechanism of microvoid growth and coalescence. Johnson and Cook (1985) extended these findings to develop an empirical model, which also takes into account of temperature and strain rate effects. In the abovementioned studies, the internal damage evolution and accumulation before fracture initiation is not considered, and the fracture is considered to occur when the state variable accumulates to a critical value and the actual damage evolution is evaluated in subsequent steps (Kiran and Khandelwal, 2014a). In contrast, another series of models couple plasticity with damage variables at the material point level to describe the continuous stress degradation phenomena before fracture initiation. Gurson (1977) proposed an approximate porous

plasticity constitutive model by introducing a damage related void volume fraction variable. Tvergaard and Needleman (1984) further modified Gurson's model to consider the rapid loss of load-carrying capacity of the material at the onset of microvoid coalescence. The integrated Gurson-Tvergaard-Needleman (GTN) model has gained considerable attention in ductile fracture prediction applications (Tvergaard and Needleman, 1984; Zhang et al., 2000). Lemaitre (1985), Chaboche (1988, 2008), Brunig et al. (2008) and Xue (2007b) proposed similar coupled models based on Continuum Damage Mechanics (CDM) theory. However, when compared to the uncoupled models, the coupled models are always associated with a considerable number of model parameters that require calibration. For instance, the GTN model has nine parameters and each significantly influences convergence speed and prediction accuracy (Mahnken, 1999; Bai and Wierzbicki, 2008). As the parameter calibration procedure is difficult, the implementation of coupled constitutive models is computationally expensive (Kiran and Khandelwal, 2014a). On the other hand, the existing uncoupled constitutive models often have acceptable accuracy in engineering applications and are convenient in large-scale structural simulations. For example, two popular uncoupled models, i.e., the void growth model (Rousselier, 1987) and the stress modified critical strain model, (MacKenzie et al., 1977) have gained success in many practical ductile fracture predictions (Chi et al., 2006; Kanvinde and Deierlein, 2004, 2006, 2007; Kiran and Khandelwal, 2013).

Based on more recent work, stress triaxiality dependent fracture criteria appear to have some limitations in predicting fracture initiation at low stress triaxialities and under various loading conditions other than axisymmetric tension (Bao, 2003; Bao and Wierzbicki, 2004b; Wierzbicki et al., 2005; Bai, 2008; Barsoum, 2006; Smith et al., 2014). Bao and Wierzbicki (2004a) conducted experiments on ductile fracture at a wide range of

triaxialities, and the results pointed to the effect of shear stress on ductile fracture at low positive and negative triaxialities (Bai and Wierzbicki, 2008; Nahshon and Hutchinson, 2008; Zhang et al., 2001; Kim et al., 2004; Gao and Kim, 2006; Xue, 2007a). Two different mechanisms of microvoid coalescence, including internal necking of ligaments between voids resulting from volumetric void growth and shear-linkup in the ligaments between voids caused by void elongation, have been observed in microscopic studies (Pardoen and Brechet, 2004; Barsoum and Faleskog, 2007b; Besson, 2010; Li et al., 2011). While the necking mechanism controlled by the triaxiality is dominant at high triaxialities, the shearing mechanism is important at low triaxialities and is sensitive to shear stress. Xue (2007a) introduced another parameter, Lode angle, to describe the shear stress effect on ductile fracture mechanisms. Bai and Wierzbicki (2010) modified the Mohr-Coulomb fracture criterion to a function of triaxiality and Lode parameter (MMC) to explore ductile fracture over a wide range of triaxiality. Xue (2008) and Malcher et al. (2014) incorporated Lode parameter to the Gurson-Tvergaard-Needleman (GTN) model to consider the microvoid elongation and void shearing damage effect. Lou et al. (2012) focused on the combined effect of internal necking and shear linking on the microvoid coalescence and proposed a new ductile fracture criterion. For many engineering applications, the aim of ductile fracture modeling is to predict the ductility of metal alloy components and structures with reasonable accuracy and with low computational cost. In this case, the applicability of various fracture models needs to be verified considering both efficiency and accuracy. The objective of this chapter is to develop an engineering tool for ductile fracture prediction that is both efficient and that provides reasonable for many engineering applications. Additional requirements for this new tool is that it should be easy-to-calibrate and be well-correlated with the physical micro-mechanisms of ductile fracture.

In this chapter, micro-mechanisms of void nucleation, growth and coalescence as well as the roles of stress triaxiality and shear stress will be first described. A new fracture criterion is then developed based on two existing fracture criteria, which are the Rice-Tracey model (R-T) and modified Maximum Shear Stress model (MSS). Parametric studies are carried out to investigate the effects of model parameters on the fracture locus construction. The proposed model is then applied to predict fracture loci of Al 2024-T351, steel A572 and steel 1045 to validate the performance of the proposed model on the prediction of metal alloy ductile fracture over a wide range of triaxiality and to demonstrate the shear stress effect on the fracture locus. Finally, comparison between the newly proposed model and several existing models including R-T model, MSS model, MMC model, X-W model and Smith model is conducted.

3.2 CHARACTERIZATION OF THE STRESS STATE

The three invariants of the stress tensor are given respectively:

$$I_1 = \sigma_1 + \sigma_2 + \sigma_3 = 3\sigma_m \tag{3.1}$$

$$J_2 = \frac{1}{6}\left[(\sigma_1 - \sigma_2)^2 + (\sigma_1 - \sigma_3)^2 + (\sigma_2 - \sigma_3)^2 \right] \tag{3.2}$$

$$J_3 = (\sigma_1 - \sigma_m)(\sigma_2 - \sigma_m)(\sigma_3 - \sigma_m) \tag{3.3}$$

where σ_1, σ_2, σ_3 and σ_m denote three principal stresses and the hydrostatic stress, respectively. It is assumed that three principal stresses have the order as $\sigma_1 \geq \sigma_2 \geq \sigma_3$. Herein, J_2 plastic flow is employed, and the Von Mises stress $\bar{\sigma}$ is defined as a function of the second invariant:

$$\bar{\sigma} = \sqrt{3J_2} \tag{3.4}$$

The terminologies of the stress triaxiality η, the maximum shear stress ratio ϕ and the nominal third stress invariant ξ are defined as:

$$\eta = \frac{\sigma_m}{\bar{\sigma}} \tag{3.5}$$

$$\phi = \frac{\tau_{\max}}{\bar{\sigma}} = \frac{\sigma_1 - \sigma_3}{\bar{\sigma}} \tag{3.6}$$

$$\xi = \frac{27 J_3}{2\bar{\sigma}^3} \tag{3.7}$$

Furthermore, the Lode angle θ is related to the nominal third stress invariant, which is given as (Fung and Tong, 2001; Wierzbicki and Xue, 2005):

$$\cos(3\theta) = \xi \tag{3.8}$$

Note that the Lode angle is between 0 and π/3 and the normalized Lode angle is expressed as:

$$\bar{\theta} = 1 - \frac{6\theta}{\pi} = 1 - \frac{2}{\pi}\arccos(\xi) \tag{3.9}$$

Bai and Wierzbicki (2010) constructed a stress deviatoric plane to describe the geometrical relationship among three principal stresses (σ_1, σ_2, σ_3) and derived the expression of each principal stress in terms of $\bar{\sigma}$, η and θ, as follows:

$$\sigma_1 = \left[\eta + \frac{2}{3}\cos(\theta)\right]\bar{\sigma} \tag{3.10}$$

$$\sigma_2 = \left[\eta + \frac{2}{3}\cos\left(\frac{2\pi}{3} - \theta\right)\right]\bar{\sigma} \tag{3.11}$$

$$\sigma_3 = \left[\eta + \frac{2}{3}\cos\left(\frac{4\pi}{3} - \theta\right)\right]\bar{\sigma} \tag{3.12}$$

Combining Eq. (3.10) -(3.12) and Eq. (3.6), the maximum shear stress ratio can be correlated to the Lode angle as:

$$\phi = \frac{\sigma_1 - \sigma_3}{2\bar{\sigma}} = \frac{1}{\sqrt{3}} \cos\left(\frac{\pi}{6}\bar{\theta}\right) \tag{3.13}$$

As the normalized Lode angle varies from -1 to 1, the ϕ factor varies between 0.5 to $1/\sqrt{3}$. The relationship between these two parameters implies the ϕ factor has a similar role as the Lode angle in quantifying the nominal third stress invariant. Herein, the ϕ factor together with the triaxiality η are adopted in the following development.

A 2D space of η and ϕ representing a variety of loading cases is plotted in Fig. 3.1 (Bai and Wierzbicki, 2008). As can be seen, the lower and upper limits of the ϕ factor represent the axisymmetric loading and the plastic plane strain cases, respectively. The typical axisymmetric cases represent notched and smooth round bars. Moreover, a flat grooved plate with tension and pure shear loading conditions can achieve the plastic plane strain case. Three half sine-cycles plotted in Fig. 3.1 denote the plane stress condition and each half-cycle corresponds to the stress state of σ_1=0, σ_2=0 and σ_3=0, respectively. Wierzbicki and Xue (2005) and Bai and Wierzbicki (2008) also give the expression of a particular plane stress case where σ_3=0 as:

$$\cos\left[\frac{\pi}{2}\left(1-\bar{\theta}\right)\right] = -\frac{27}{2}\eta\left(\eta^2 - \frac{1}{3}\right) \tag{3.14}$$

Numerous ductile fracture experiments have been conducted with on the axisymmetric tension tests on smooth and notched round bars, which result in stress states with triaxiality greater than 0.33 and at a single ϕ factor equal to 0.5 (McClintock, 1968; Kanvinde, 2004; Chi et al., 2006; Jia and Kuwamura, 2013). Clearly, only limited cases of η and ϕ are covered by smooth and notched round bar tests. In many situations of

engineering practice, such as in bolted connections and welded connections, and shear panel zones, pure shear and combined shear and tension are common loading conditions. In other words, the triaxiality alone is insufficient to characterize all the loading cases shown in Fig. 3.1. Therefore, it is necessary to introduce an additional variable such as the ϕ factor to extend ductile fracture prediction to a wider range of loading conditions.

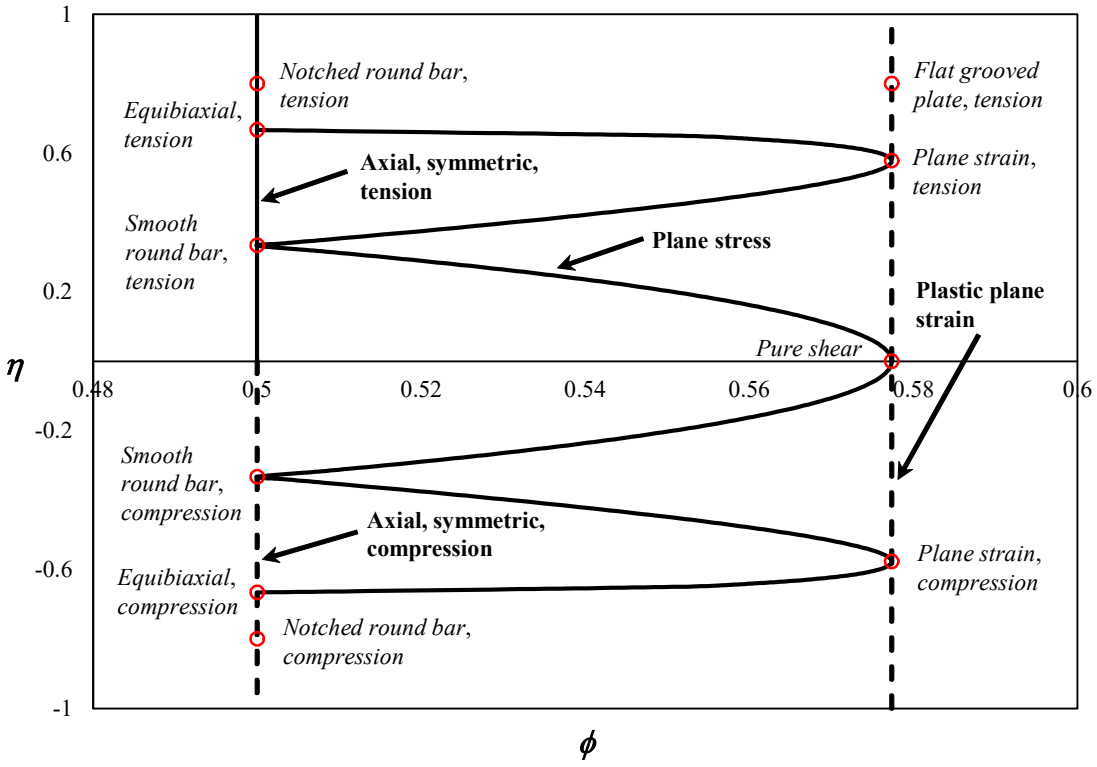

Fig. 3.1 Representations of Loading Cases in the plane of η and ϕ.

3.3 MICRO-MECHANISMS AND EXISTING MODELS FOR DUCTILE FRACTURE

3.3.1 Micro-mechanisms of ductile fracture

The mechanism of ductile fracture is comprised of three stages: micro-void

nucleation, growth, and coalescence. Detailed descriptions of each stage as well as the roles of stress and strain states in the process of ductile fracture will be provided in the following sections. The mechanism for ductile fracture and the existing fracture models provide the basis of the proposed new model.

Microvoid nucleation

As discussed in chapter 2, voids form around second-phase particles or the inclusions at the interfaces between the particles and the matrices. For a given material, void nucleation is considered to occur at either a critical stress or a critical strain. Argon et al. (1975) observed that voids nucleate when there is sufficient stress, approximately equals to the sum of the mean stress and the Von Mises stress, to break the interfacial bonds. Subsequently, Beremin (1981) modified this model by considering the influence of the yield stress. However, there is a problem with these models in that dilation of voids under negative mean stress conditions would be suppressed and there would be no subsequent void growth. This is in conflict with experimental observations by Bao and Wierzbicki (2004a) and Li et al. (2010). On the other hand, Gurson (1977) and Garrison and Moody (1987) suggested that the nucleation of voids occurs when the plastic strain reaches a critical value, and the rate of void nucleation depends on the equivalent plastic strain. Tvergaard and Needleman (1984) found there does not exist a unique plastic strain at which voids nucleate. Alternatively, they introduced a standard nucleation strain derivation into the strain-based model to quantify the void nucleation strain at a statistical level.

Microvoid growth

In early studies on ductile fracture, microvoid dilation was the primary mode of void growth being investigated (McClintock, 1968; Rice and Tracey, 1969; Gurson, 1977;

Tvergaard, 1982; Tvergaard and Needleman, 1984). Dilation of voids driven by the stress triaxiality represents the volumetric growth of voids (Kiran and Khandelwal 2014a). Among various microvoid dilation models, the one by Rice and Tracey (1969) was developed based on a mechanical model involving a singly spherical void in an unbounded solid of a perfectly plastic material. The problem was mathematically expressed as:

$$\frac{d\ln f}{d\varepsilon_p} = 0.85\exp\left(1.5\eta\right) \tag{3.15}$$

where f and ε_p are the porosity and equivalent plastic strain, respectively. The function describes the positive influence of the stress triaxiality on the void growth rate as well as on the damage evolution. Thereafter, the model was adopted and extended by Hancock and Mackenzie (1976), Johnson and Cook (1985) and Kanvinde and Deierlein (2004). It was found that this series of triaxiality-dependent models had good performance on prediction of ductile fracture at high triaxialities.

However, many factors, such as the initial shape of voids, the shape evolution, and the interaction among voids, which would influence the process of void growth, are neglected by the Rice and Tracey model. Meanwhile, another mode of void growth in terms of the shape change and rotation of microvoid with little volumetric change is found to be prominent at low triaxialities and is known as microvoid elongation (Xue and Wierzbicki, 2007; Barsoum and Faleskog, 2007a, 2007b; Bai and Wierzbicki, 2010; Malcher et al., 2014; Kiran and Khandelwal, 2014a, 2015). These two modes compete and are determined by the triaxiality range under which the void grows. At high triaxialities, microvoid dilation dominates over microvoid elongation. In contrast, the elongation of microvoids driven by the deviatoric stress components is the primary mode of void growth at low triaxialities. Transition between the two modes during void evolution depends not only on the triaxiality

but also on the deviatoric stresses.

Microvoid coalescence

Following void growth, microvoid coalescence is the final stage before ductile fracture initiation. Corresponding to void growth, there also exists two modes for the void coalescence, i.e. void ligament necking and shearing, that have been extensively investigated by Rice and Tracey (1969), Brown and Embury (1973), Le Roy et al. (1981), Weck and Wilkinson (2008) and Weck et al. (2008). Similar as the void growth modes, the internal necking and shearing linking are also determined by triaxiality and shear stress. While the necked ligaments between break perpendicular to the loading direction, the shear-linking up of voids follows the intrinsic slip-based deformation and occurs in the localized shear direction. Meanwhile, different macroscopic fracture phenomena attributed to these two types of mechanisms are reported by Weck and Wilkinson (2008) and Li et al. (2011). As η increasing from negative to positive, fracture including shear, mixed shear-dimple and cup-cone types are successively observed in the tests.

Through micro-mechanical studies, the interactive roles of the stress triaxiality and the shear stress in the mechanisms of microvoid growth and coalescence in a wide range of triaxiality have been identified. The stress triaxiality and shear stress sensitive mechanisms motivate the fracture criteria to be more than triaxiality dependent. Based on the aforementioned micro-mechanisms and physical observations, a macroscopic ductile fracture criterion that incorporates both two stress variables (η, ϕ) will be proposed herein.

3.3.2 Existing local fracture models

Rice-Tracey (R-T) model

Some early contributions to local ductile fracture criteria development are attributed to the works by McClintock (1968) and Rice and Tracey (1969). Based on analytical solutions of void growth, they derived an exponential form of ductile fracture criterion that can be expressed as

$$\bar{\varepsilon}_f = b_1 \exp\left(-b_2 \eta\right) \tag{3.16}$$

where b_1 and b_2 are two positive material parameters that need to be calibrated, and $\bar{\varepsilon}_f$ is the equivalent plastic strain at fracture initiation. The original criterion gave b_2 as a constant of 1.5, which was found to be suitable for many engineering materials. This equation, known as the R-T model, is also referred to the void growth model (VGM) due to its physical basis that fracture occurs when each void grows to a critical size, at which point the current plastic strain represents the fracture strain. The initial intention of their derivations was for fracture at high triaxialities, i.e., $\eta > 2$. The following applications of this simple exponential relationship between the triaxiality and the fracture strain have been subsequently validated for fracture at triaxialities between 1 and 2 (Johnson and Cook, 1985; Smith et al., 2017). As the triaxiality decreases to lower and even negative levels, the experimental evidence does not support the exponential relationship for fracture strain reflected by R-T model. From the void growth point of view, the volumetric growth at that range of triaxiality significantly eases and even ceases, and the void failure mechanism becomes less relevant to the basis of R-T model.

Smith model

To address the deficiency of R-T model in predicting fracture at low triaxialities while maintaining its accuracy of fracture prediction at high triaxiality, Smith et. al (2017) proposed a unified criterion for both positive and negative triaxiality levels. This model employs a hyperbolic sine function of the stress triaxiality in an exponential form

$$\frac{dD}{d\varepsilon_p} = B^{+}\exp\left(A^{+}\eta\right) - B^{-}\exp\left(-A^{-}\eta\right) \tag{3.17}$$

where A^{+}, A^{-}, B^{+} and B^{-} are four model parameters and D is the damage indicator that has similar role as the void volume fraction in R-T model. By introducing the second exponential term in the right-hand of Eq. (3.17), the damage rate is reduced as the triaxiality decreases. The implied damage rate decreases to zero as triaxiality tends to zero and becomes negative for triaxiality less than zero. Smith et. al (2017) also noticed that a cutoff triaxiality for the implementation of the proposed model was needed to ensure the damage rate accumulates in the positive range.

Rather than describing the physical facture mechanism at low triaxialities, the Smith model appears to be a mixed mathematics and mechanics-based fracture criterion. Intended to reduce the strain to fracture at low triaxialities attained by the R-T model, this model incorporates more model parameters, which provides more flexibility and more accuracy in predicting fracture at a wider range of triaxialities. However, the targeted applicability of this model is to ductile fracture under axisymmetric conditions, for which the ϕ factor is constant as 0.5. The use of this model to predict fracture under various conditions, e.g. with different ϕ factors is still unclear. Additional validation of this model applied under a wider range of conditions is needed.

Modified Mohr-Coulomb model (MMC)

The Mohr-Coulomb criterion is a function of both normal stress and shear stress. Bai and Wierzbicki (2010) modified the original expression to one in terms of the triaxiality and lode angle parameter, and therefore extended the initial applicability to ductile fracture in crack-free solids. The full function of MMC model reads

$$\bar{\varepsilon}_f = \left\{ \frac{A}{b_4}\left[1 - b_\eta\left(\eta - \eta_0\right)\right] \times \left[b_\theta^s + \frac{\sqrt{3}}{2-\sqrt{3}}\left(b_\theta^{ax} - b_\theta^s\right)\left(\sec\left(\frac{\pi\bar{\theta}}{6}\right) - 1\right)\right] \right. \\ \left. \times \left[\sqrt{\frac{1+b_3^2}{3}}\cos\left(\frac{\pi\bar{\theta}}{6}\right) + b_3\left(\eta + \frac{1}{3}\sin\left(\frac{\pi\bar{\theta}}{6}\right)\right)\right]\right\}^{-\frac{1}{n}} \tag{3.18}$$

where A, n, b_3, b_4, b_η, η_0, b_θ^{ax} and b_θ^s are eight model parameters, among which A and n are material plasticity related constants, and b_3 and b_4 are loading condition dependent parameters, and b_η, η_0, b_θ^{ax} and b_θ^s describe the triaxiality dependency and Lode angle dependency of material ductility.

Xue-Wierzibicki (X-W) model

Based on the experimental observations by Bao and Wierzbicki (2004a) that the fracture strain is not necessarily a monotonic function of triaxiality, the Xue-Wierzbicki model was then proposed by introducing the effect of the third deviatoric stress invariant J_3 (Wierzbicki et al., 2005). The X-W model keeps the exponential form of the triaxiality dependent function and gives rise to more sensitivity to shear stress, and is expressed as

$$\bar{\varepsilon}_f = b_4\exp\left(-b_5\eta\right) - \left[b_4\exp\left(-b_5\eta\right) - b_6\exp\left(-b_7\eta\right)\right]\left(1-\xi^m\right)^{\frac{1}{m}} \tag{3.19}$$

where b_4, b_5, b_6, b_7 and m are five model parameters for the X-W criterion, and m is an even integer. There exist two bounds of this criterion, which are the lower bound for the

plane strain condition and the upper bound for the axisymmetric condition. The nominal third stress invariant related term in Eq. (3.19) refers to a symmetric non-quadratic elliptic function.

3.4 DEVELOPMENT OF A NEW DUCTILE FRACTURE CRITERION

3.4.1 Proposed ductile fracture criteria

As discussed above, both the triaxiality and the third stress invariant play important roles in ductile fracture. The triaxiality dependent criteria are found to perform well at high triaxialities, whereas shear stress related models perform well prediction of shear-type fractures, which prevail at low triaxialities. In this chapter, these two types of models will be combined for the construction of a new criterion in terms of triaxiality and shear stress. The new model is intended to predict ductile fracture over a wide range of triaxiality. The Rice and Tracey model (R-T) and the Maximum shear stress model (MSS) provide the basis of the new fracture model.

The weighted product method was used for the models developed by Johnson and Cook (1985), Nahshon and Hutchinson (2008), Xue and Wierzbicki (2008), Lou et al. (2012) and Wen and Mahmoud (2015). This method is also used to combine two separate functions so that the basic form of the new model can be expresses as:

$$\bar{\varepsilon}_f = D_f\left(\eta,\phi\right) = g\left(\eta,\phi\right) f\left(\eta,\phi\right) \tag{3.20}$$

where $g(\eta, \phi)$ and $f(\eta, \phi)$ represent R-T and MSS related functions, respectively. Regarding the function $g(\eta, \phi)$, the R-T function is adopted as follows:

$$g\left(\eta,\phi\right) = c_1 \exp\left(c_2\eta\right) \tag{3.21}$$

where c_1 and c_2 are two parameters of the function $g(\eta, \phi)$.

The MSS model only involves shear stress. This model has predicted results for plane stress cases that agree well with experimental data (Wierzbicki et al., 2005; Bai and Wierzbicki, 2015; Li et al., 2011). The reason this criterion has encouraging performance is that there exists an inherent correlation between triaxiality and the shear stress parameter for the plane stress cases, as shown in Fig. 3.1. Even though it is a function of shear stress, the MMS model is essentially related to both variables of triaxiality and shear stress. However, difficulties are found when it is applied to cases other than the plane stress condition. Assuming the power hardening material law, i.e., $\sigma=K\varepsilon^n$, the MSS model reads:

$$\bar{\varepsilon}_f = \left(K\phi\right)^{-\frac{1}{n}} = A\left(\phi\right)^{-\frac{1}{n}} \tag{3.22}$$

where K and n are two strain hardening constants, and $A = K^{-\frac{1}{n}}$. Since the process of ductile fracture involves the interplay of stress triaxiality and shear stress, the interaction between these two parameters need to be strengthened in the new fracture criterion. Besides, it is suggested that the stress states not only affect the process of ductile fracture but also material behavior (Bai and Wierzbicki, 2008; Gao et al., 2009; Li et al., 2011). Therefore, modification is required before the MSS model can be introduced to be the remaining part of $D_f(\eta, \phi)$. Herein, it is assumed that the hardening exponent n is a triaxiality related parameter, while the relation between the two variables are simplified so that the expression of $f(\eta, \phi)$ is written as:

$$f\left(\eta,\phi\right) = c_3\phi^{-\frac{1}{n(\eta)}} \rightarrow f\left(\eta,\phi\right) = c_3\phi^{-\frac{1}{c_4\eta+c_5}} \tag{3.23}$$

where c_3, c_4 and c_5 are three parameters of the function $f(\eta, \phi)$. Combining functions $g(\eta, \phi)$ and $f(\eta, \phi)$ and re-organizing the product $\bar{\varepsilon}_f = D_f\left(\eta,\phi\right)$, the new fracture criterion is

written as:

$$\bar{\varepsilon}_f = D_f(\eta,\phi) = \alpha \exp(\beta\eta)\phi^{\frac{\gamma}{\eta+k}} \tag{3.24}$$

This proposed model has four parameters α, β, γ and k that need to be calibrated.

3.4.2 Damage evolution rule

In some special cases, the stress state parameters (η, ϕ) are constant during the whole strain history. Such cases achieved by Bao and Wierzbicki (2004a) are the equi-biaxial punch test and the pure shear test. More generally, the parameters (η, ϕ) continuously vary and are described as functions of the equivalent plastic strain ε_p. However, a reasonable assumption can be made that the stress state parameters are constant in a small increment of plastic strain and that the damage accumulation per incremental step is described as:

$$dw_D = \frac{d\bar{\varepsilon}_f}{D_f(\eta,\phi)} \tag{3.25}$$

where w_D is the damage index and is integrated over the loading history to be the damage accumulation written as:

$$w_D = \int_0^{\bar{\varepsilon}_f} dw_D = \int_0^{\bar{\varepsilon}_f} \frac{d\varepsilon_p}{D_f(\eta,\phi)} \le 1 \tag{3.26}$$

Once w_D=1, the material element is considered to reach its ductility limit, and the upper limit of the integral is defined as the fracture equivalent plastic strain $\bar{\varepsilon}_f = \varepsilon_p$. For cases where the stress state parameters are constant, Eq. (3.26) will reduce to Eq. (3.24). Obviously, the variations of the stress state parameters give rise to difficulties in constructing the fracture locus map. Alternatively, the first mean value theorem for

integrals is employed to simplify the calibration process. This represents an approach to construct the fracture locus map by the average value of stress state parameters during the strain history. The strain-weighted average of parameters (η, ϕ) are calculated by:

$$\eta_{avg} = \frac{1}{\bar{\varepsilon}_f}\int_0^{\bar{\varepsilon}_f} \eta\left(\varepsilon_p\right)d\varepsilon_p$$
$$\phi_{avg} = \frac{1}{\bar{\varepsilon}_f}\int_0^{\bar{\varepsilon}_f} \phi\left(\varepsilon_p\right)d\varepsilon_p \tag{3.27}$$

The accuracy of the average method can be examined by comparing the fracture plastic strain $\bar{\varepsilon}_f$ obtained by the strain-weighted average approach with the damage accumulation rule. Good predictive results achieved in applications by Bao and Wierzbicki (2004a), Bai and Wierzbicki (2010), Smith et al. (2014) and Wen and Mahmoud (2015) demonstrate the reliability of this estimation approach.

3.4.3 Stress triaxiality and ϕ factor dependency

Given a group of model parameters, (α=0.03, β=0.2, γ=-20, k=5), the effects of triaxiality η and shear stress factor ϕ on the fracture locus are investigated to have a better understanding on how the triaxiality and the ϕ factor affect the fracture locus in the new criterion. The curves representing the fracture locus under various stress states are shown in Fig. 3.2. Obviously, when the ϕ factor remains constant, increasing the triaxiality decreases the fracture strain in Fig. 3.2(a). This feature follows that of the R-T model, but the difference is the fracture strain in this model is no longer a simply exponentially increasing with the triaxiality. Further, a greater ϕ factor leads to a lower fracture strain with a given triaxiality (see Fig. 3.2(b)). On the other hand, the contribution of the ϕ factor to the fracture locus varies with the triaxiality. As shown in Fig. 3.2(b), the facture strain changes with ϕ factor more significantly at low triaxialities than at high triaxialities. It is

almost constant as the ϕ factor varies when the triaxiality equals to 1. These two stress state parameters compete, as increasing the value of either parameter suppresses the effect of the other. However, there is no clear transition or distinct domain for either variable that can be obtained in the current example, and it is observed that the fracture strain and the effects of two stress states gradually vary with triaxiality.

The partial derivatives of the fracture locus with respect to both triaxiality η and the ϕ factor are computed to further investigate the interaction of these two variables on the fracture locus. The partial differential equations can be written as:

$$\frac{\partial \bar{\varepsilon}_f}{\partial \eta} = \bar{\varepsilon}_f(\eta, \phi)\left[\frac{\gamma \ln \phi}{(\eta + k)^2} + \beta\right] \tag{3.28}$$

$$\frac{\partial \bar{\varepsilon}_f}{\partial \phi} = \bar{\varepsilon}_f(\eta, \phi)\frac{\gamma}{(\eta + k)\phi} \tag{3.29}$$

Using the same set of parameters as in the previous example, the partial derivatives with respect to both variables are plotted in Fig. 3.3. Note that a small absolute value of the partial derivative indicates only minor sensitivity of the fracture locus to the corresponding variable. As observed in Fig. 3.3(a), the absolute value of the partial derivative with respect to triaxiality increases with a decreasing ϕ factor under a given η. This indicates that the fracture locus is more sensitive to the triaxiality while the ϕ factor is in a lower range. In addition, the absolute value of the partial derivative with respect to the ϕ factor becomes smaller as triaxiality becomes greater (see Fig. 3.3(b)). This implies the fracture strain is less sensitive to the ϕ factor at high triaxialities than at low triaxialities. Even though the effects of two stress state parameters on the fracture locus correlate with the micro-mechanisms of ductile fracture, they cannot be easily determined quantitatively. This is because knowledge of how stress triaxiality and ϕ factor work together during the micro-

void growth and coalescence process remains limited. In addition, other factors such as the macroscopic loading history, the loading rate, the microstructure as well as its interaction with the mechanical field also influence the effects of triaxiality and ϕ factor on ductile fracture. The proposed model is not intended or able to cover all the factors that would affect the ductile fracture process. Instead, it provides a phenomenological tool to describe the fracture locus in terms of triaxiality and ϕ factor. The model follows previous observations regarding the stress triaxiality and the ϕ factor dependency of ductile fracture, extends fracture prediction to wider range of stress states, and does not significantly increase computational expense.

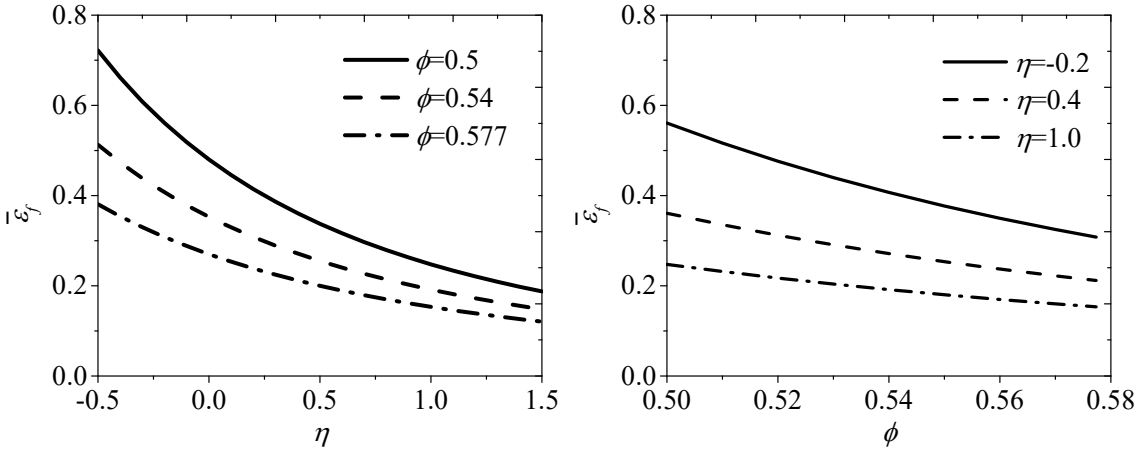

Fig. 3.2 Dependency of stress state variables: (a) dependency of triaxiality η; (b) dependency of ϕ factor.

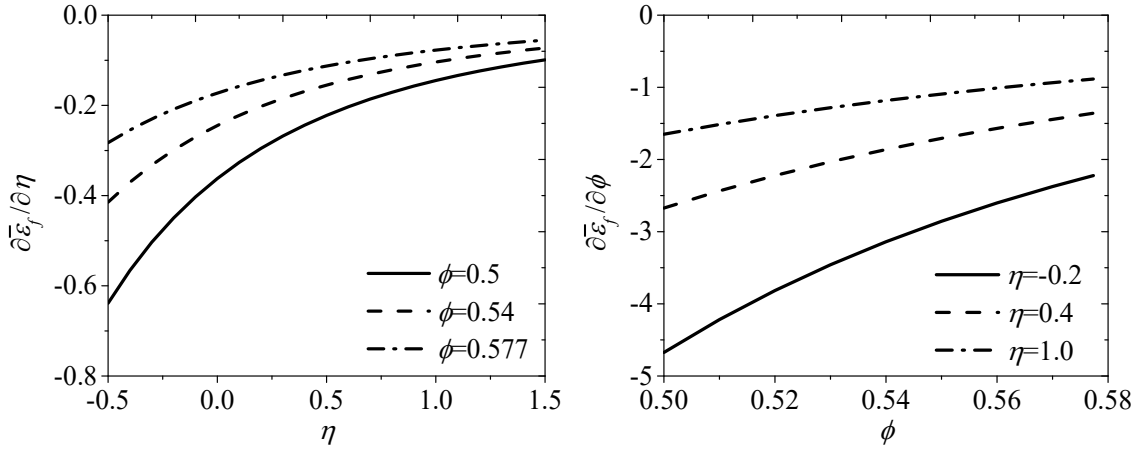

(a) (b)

Fig. 3.3 Partial derivatives of the fracture locus: (a) derivative with respect to triaxiality η; (b) derivative with respect to ϕ factor.

3.4.4 Parametric study

This section will evaluate the effect of each of the four parameters on the behavior of the new model and on the fracture locus by performing parametric studies. Each parameter is examined by alternating its value while keeping the other parameters constant as the values given in the previous example (α=0.03, β=0.2, γ=-20, k=5).

In Fig. 3.4, the fracture locus is plotted using various values of the parameter α. The parameter α serves as the amplification factor of the fracture criterion. Without influencing the shape of the fracture locus, the value of α only scales up and down the material ductility. In addition, the parameter α needs to be positive to guarantee a positive value of the equivalent plastic strain at fracture. Similarly, three different values of parameter β are applied and a series of fracture loci are plotted in Fig. 3.5. A prominent feature is the shape of each fracture locus is quite different from each other. The reason is that the parameter β partly influences the dependency of the fracture locus on the stress triaxiality. With fixed

values of the other parameters, the decreasing absolute value of β monotonically reduces the triaxiality dependency of the fracture locus. When β equals to 0, the new criterion will reduce to the modified MSS criterion. The parameter γ influences both the triaxiality and the ϕ factor sensitivities of the fracture locus, as shown in Fig. 3.6. The larger the absolute value of γ, the greater dependency on both the triaxiality and the ϕ factor on the fracture locus. The denominator $\eta+k$ holds a positive value to ensure a nonzero term as the triaxiality decreases from positive to negative. Accordingly, an increasing ϕ factor will reduce the fracture strain for a given triaxiality. In this case, the parameter γ will have a non-positive value to guarantee that the new criterion is a monotonically decreasing function of the ϕ factor. When γ=0, which is its maximum value, the new fracture criterion simplifies to the R-T model, which eliminates the effect of the ϕ factor on the fracture locus.

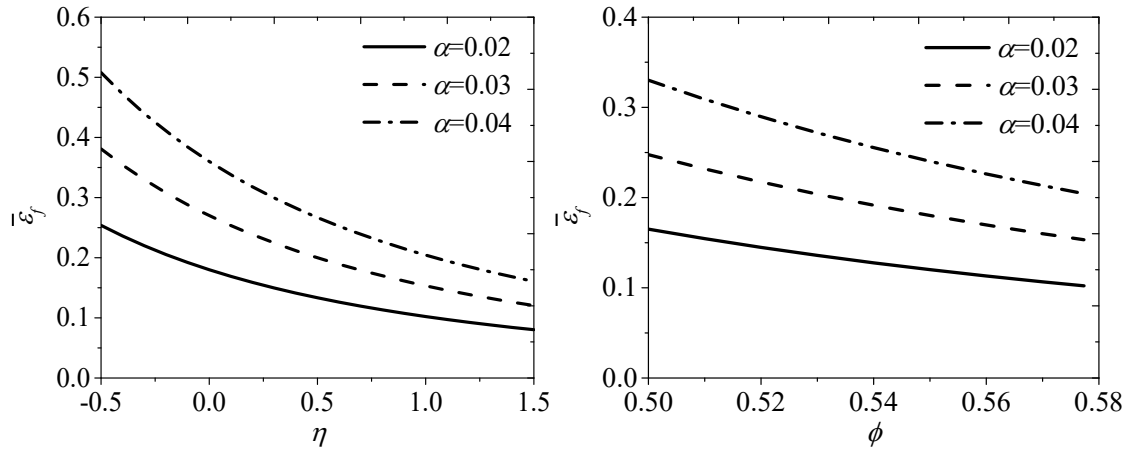

(a) (b)

Fig. 3.4 Effect of parameter α on the fracture locus: (a) ϕ=0.577; (b) η=1.0.

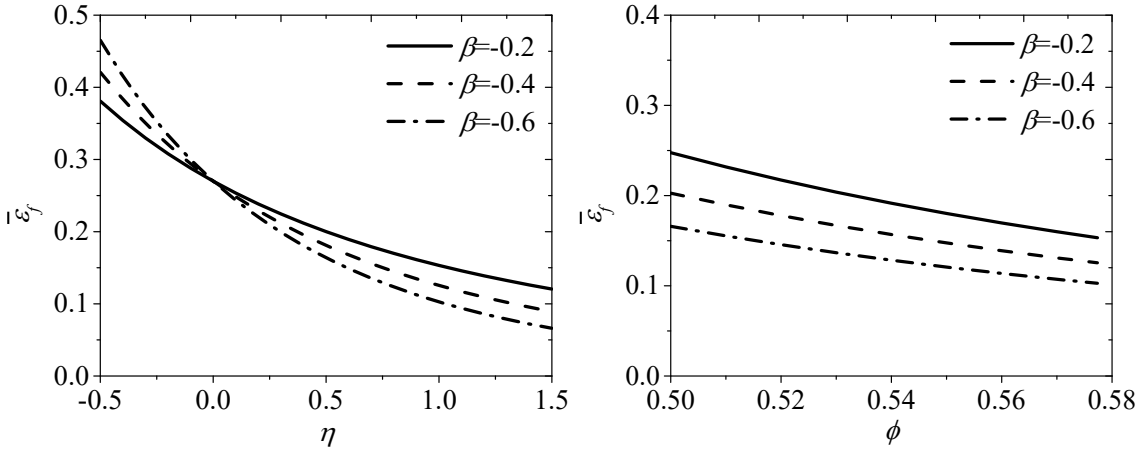

(a) (b)

Fig. 3.5 Effect of parameter β on the fracture locus: (a) ϕ=0.577; (b) η=1.0.

The parameter k plays a similar role as parameter γ since it also influences the triaxiality and the ϕ factor sensitivities of the fracture locus. As discussed above, a positive value of $(\eta+k)$ requires the parameter k to be greater than $-\eta$ as triaxiality varies from the cut-off value to positive. As shown in Fig. 3.7, increasing the value of k reduces both the stress triaxiality and the ϕ factor dependency. When the value of k becomes large when compared to the triaxiality and the absolute value of γ, the exponent $\gamma/(\eta+k)$ is closed to 0. Thereafter, the shear stress related function $f(\eta, \phi)$ in Eq. (3.24) tends to be constant at 1, so that the new fracture criterion simplifies to the R-T model.

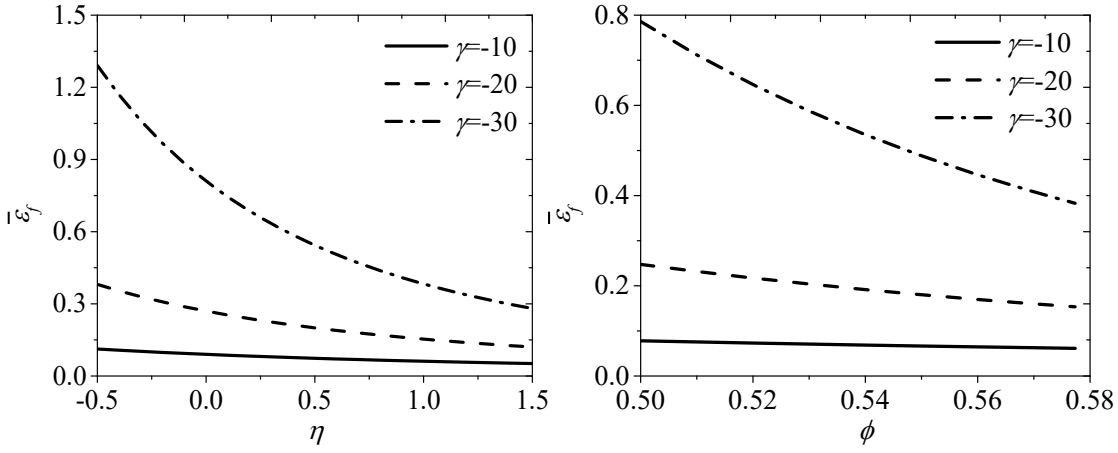

Fig. 3.6 Effect of parameter γ on the fracture locus: (a) ϕ=0.577; (b) η=1.0.

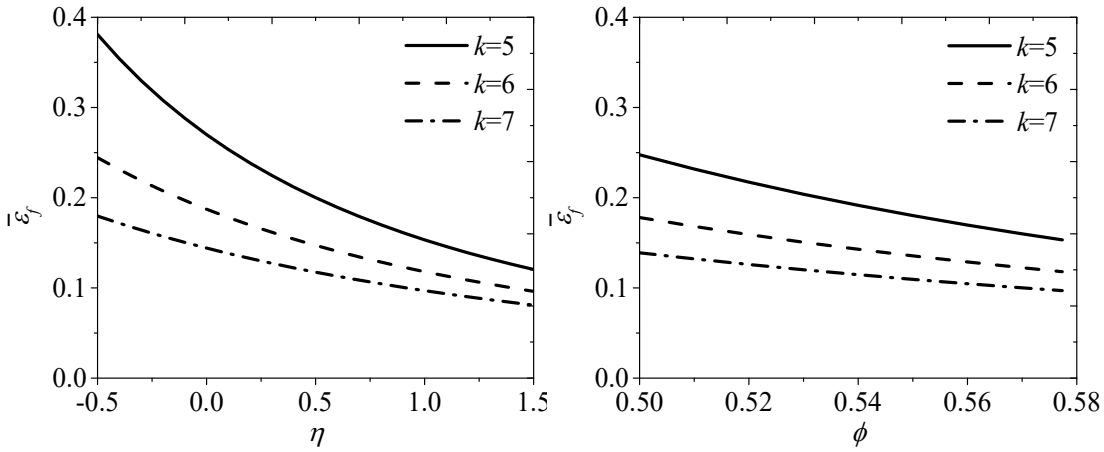

Fig. 3.7 Effect of parameter k on the fracture locus: (a) ϕ=0.577; (b) η=1.0.

3.4.5 Bounds of fracture locus and triaxiality cut-off

As discussed above, the partial derivative with respect to the ϕ factor maintains a non-positive value, which implies the fracture locus is a monotonically decreasing function

of the ϕ factor. Therefore, the fracture locus corresponding to ϕ=0.5 and ϕ=1/√3 represent the upper and lower limits, respectively, both of which are plotted in Fig. 3.8. With increasing triaxiality, the two bounds approach one another and trend to overlap at infinity. This plots also demonstrates that the influence of shear stress can be neglected at high triaxialities. The fracture locus for plane stress cases consisting of two half sine-cycles are plotted between two bounds. These special cases lie in a limited range of triaxiality from -0.33 to 0.66.

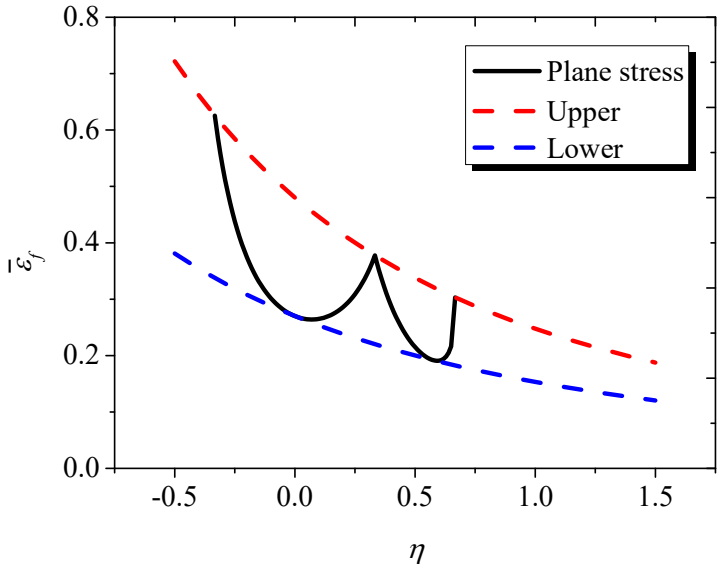

Fig. 3.8 Bounds on ϕ and plane stress cases of the new fracture locus.

In addition, Bao and Wierzbicki (2005) assumed a cut-off triaxiality value of -0.33, below which ductile fracture is not expected. This hypothesis was later challenged by experimental results showing that fracture takes place at a triaxiality of -0.495 (Khan and Liu, 2012). On the other hand, Bai and Wierzbicki (2008), Lou and Huh (2013), Lou et al. (2014) and Wen and Mahmoud (2015) proposed several triaxiality and lode angle related

functions to describe the triaxiality cut-off as a variable rather than a constant. In this paper, the cut-off value of triaxiality is simplified at -0.33 since this current study does not evaluate fracture at a triaxiality lower than -0.33. With this bound on triaxiality, the model parameter k must be greater than 0.33 to guarantee a non-zero value of $\eta+k$.

3.4.6 Correlation to micromechanical and to strain hardening behavior

The validity of the new fracture criterion is strongly dependent on its correlation to physical observations including micromechanical aspects and macroscopic material behavior in terms of strain hardening. This is due to the fact that the model is fundamentally developed based on micromechanics-based observations and the consideration of stress states sensitive to strain hardening. Micromechanical evidence is mostly obtained though computational microvoid modeling since it is not possible to measure plastic strain at fracture or at the onset of void coalescence directly by experimental approaches.

Micromechanical behavior

Numerous micromechanical studies have been performed to understand the effect of stress states on fracture mechanisms. Among those, numerical modeling of microvoid evolution is popular, as it is straightforward and computationally inexpensive. Kiran and Khandelwal (2014b) developed a microscopic finite element model with respect to a unit cube with a spherical void embedded to study the effect of triaxiality and Lode parameter on microvoid growth and final void failure for ASTM A992 steel. For comparative purpose, a representative set of results in terms of macroscopic strain at void failure (void coalescence) is adopted in the current study. The results are for the micro-cube under the constant Lode parameter $\bar{\theta} = -1$, i.e., ϕ=0.5, and for various triaxialities from η=0 to 3. As shown in Fig. 3.9(a), there exist two different branches in the relationship between

triaxiality and strain at void failure. For $\eta < 0.62$, the plastic strain at void failure increases with triaxiality. For the high triaxiality range ($\eta > 0.62$), the plastic strain at void failure decreases rapidly with increasing triaxiality. While showing a similar trend at high triaxialities, the computational modeling results are completely contrary to the predictions by the R-T model at low triaxialities.

The curve in Fig. 3.9(a) for the proposed model is given using the model parameters α=2.82, β=-0.85, γ=-1.45 and k=0.5. With the ϕ factor being constant, the criterion reduces to a triaxiality-dependent function. Regardless of the influence of the ϕ factor, the proposed model is not a simple monotonic function of triaxiality. According to Kiran and Khandelwal (2014b), there exists a triaxiality limit at which two different void growth mechanisms intersect, as shown by the highlighted dashed line in Fig. 3.9(a) for the present case. The new model also reflects this critical triaxiality, as evidenced from its parabolic shape. Despite some differences between the two approaches, the predicted plastic strain at void failure for the new model has a similar variation as the micromechanical result. The deviation, however, cannot be simply understood as an inherent deficiency of the proposed model, since the macroscopic strain at void failure is not equivalent to the strain at fracture, even though they are strongly linked. The parabolic feature illustrates that the proposed model has great potential to quantify the influence of void growth mechanisms on the fracture locus not only at high triaxiality but also at low triaxiality.

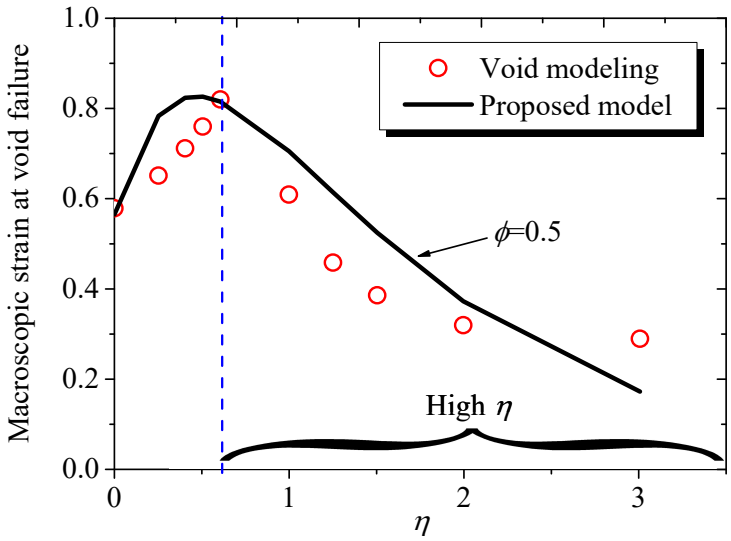

(a)

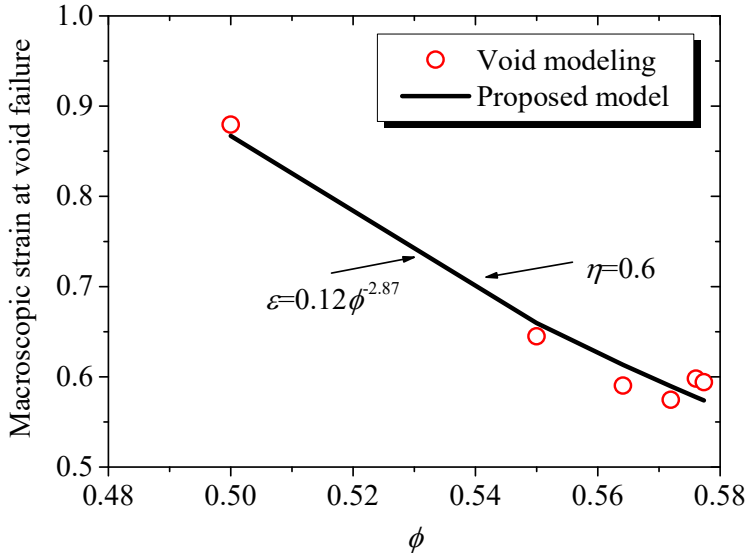

(b)

Fig. 3.9 Comparison of void failure strain predicted by the proposed model with computational results: (a) triaxiality dependency; (b) ϕ factor dependency.

Bomarito and Warner (2015) developed another series of three-dimensional finite element periodic cell models to investigate the effect of stress states on the ductile fracture of Al 5083-H116. Multiple normal and shear stresses were applied to the cubic cell to achieve different combinations of triaxiality and Lode parameter. The computational results for the cases with a given triaxiality η=0.6 are introduced to demonstrate the ϕ factor dependency of the void failure strain. As is shown in Fig. 3.9(b), the failure strains predicted by the proposed model with a group of parameters (α=0.3, β=-1.5, γ=-3.16 and k=0.5) agree well with the results from micromechanical modeling. With a constant triaxiality, the computational failure strain monotonically decreases with an increasing ϕ factor. This is due to the fact that a larger ϕ factor corresponds to a greater effect of shear stress on the void growth and failure. As previously discussed, the shear stress controls the void elongation instead of dilation. At a low triaxiality such as η=0.6, the void failure mechanism is attributed to the shear-linkup followed by shear localization, which was also reported by Bomarito and Warner (2015). Due to its ϕ factor dependence, the proposed model shows the same void failure strain variation as microvoid modeling.

Strain hardening behavior

The power term of the ϕ factor in Eq. (3.24), i.e., $\gamma/(\eta+k)$, has two physical meanings including the interactive effects of triaxiality and ϕ factor on the fracture locus as well as the triaxiality dependency of strain hardening. The effect of the stress state on the work hardening of structural metals has attracted much attention over the last a few years. This includes work by Jacques et al. (2007), Renard et al. (2012) and Liu et al. (2017), which conducted tests on the mechanical response of twinning-induced plasticity steels (TWIP) and transformation-induced plasticity steels (TRIP). The experimental

results of Fe-20Mn-1.2C TWIP steel by Liu et al. (2017) are adopted in the current study to demonstrate the triaxiality dependency of the strain hardening property. As shown in Fig. 3.10, the strain hardening exponent increases with the applied triaxiality. The relationship between these two parameters is also highlighted in Fig. 3.10. The experimental evidence supports the necessity of treating the strain hardening as a triaxiality dependent material property, which would of course influence the ultimate ductility of structural metals. However, the plastic behavior of TWIP steels does not necessarily represent the behavior of other types of structural metals. The consideration of such stress state dependency of strain hardening given by the proposed model is to maintain generality of its application. As noted above, the other function of the term $\gamma/(\eta+k)$ is to describe the interaction of triaxiality and ϕ factor on the ductility of metal alloys. The combination of these two factors is quantified by the model parameters γ and k, and currently it is hard to distinguish between the two.

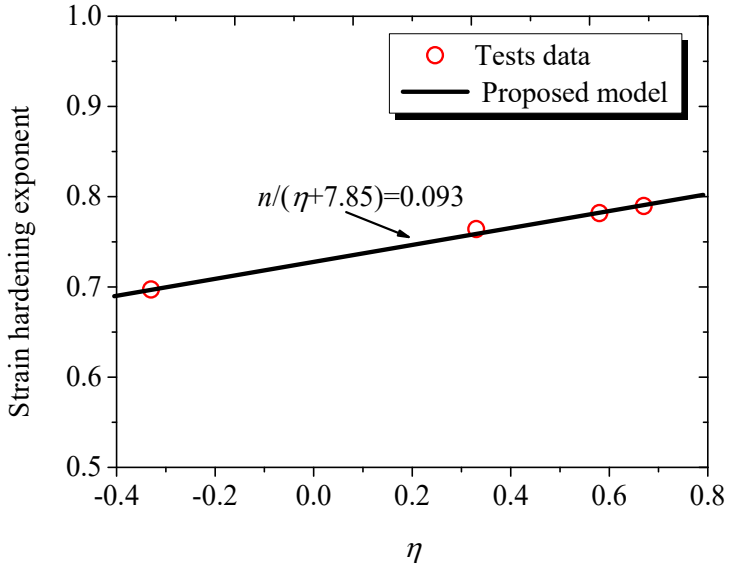

Fig. 3.10 Effect of triaxiality on the strain hardening behavior.

3.5 NEW FRACTURE MODEL VALIDATION

3.5.1 Experiments on 2024-T351 aluminum alloy

Among experimental studies on ductile fracture, one conducted by Bao (2003) is widely used to investigate the fracture locus of metal alloys over a wide range of stress triaxialities (Lou et al., 2012; Wierzbicki et al., 2005a; Bai and Wierzbicki, 2010; Wen and Mahmoud, 2015; Khan and Liu, 2012). The tests, using a variety of specimen types, including smooth round bars, notched round bars, flat grooved plates, and cylindrical compression specimens, achieved ductile fracture of 2024-T351 aluminum alloy at triaxialities ranging from -0.28 to 0.93 and at ϕ factors from 0.5 to 0.577. The equivalent plastic strain to fracture for each specimen as well as its corresponding average stress triaxiality and shear stress factor are listed in Table 3.1. The stress state parameters (η, ϕ) and the fracture strain were developed by numerical analysis of the experiments and taken as an average using Eq. (3.22). It is observed that even the specimens with similar triaxialities may have quite different ductility, such as No. 12, plate with a circular hole and No. 13, dog-bone specimen. This trend emphasizes the importance of the ϕ factor effect on the fracture locus.

In terms of parameter calibration process, the parameters in the new fracture criterion are identified by employing a MATLAB code using a nonlinear surface fitting program. The least squares method is used in the program as the optimization strategy to obtain the best fit to the experimental data in Table 3.1. Moreover, the average error function in Eq. (3.30) is used to evaluate the predictive accuracy of the fracture criteria.

$$Error\left(\bar{\varepsilon}_f^{predicted}\right)_{avg} = \frac{1}{N}\sum\nolimits_N \left|\frac{\bar{\varepsilon}_f^{predicted} - \bar{\varepsilon}_f}{\bar{\varepsilon}_f}\right| \tag{3.30}$$

The new fracture criterion with the parameters α=0.021, β=-0.41, γ=-43.11 and k=9.74 is found to be the best fit to the experimental results. The predicted fracture locus as well as the experimental data are then plotted in the 2D space of triaxiality and fracture strain, shown in Fig. 3.11(a). Comparing with the experimental data, the predicted fracture locus matches well except for several specimens, notably Nos. 1, 9 and 13, where the relative errors are greater than 25%. Three distinct curves are plotted in Fig. 3.11(a). The upper and lower bounds represent the predicted fracture locus corresponding to the axisymmetric and the plane strain case, respectively. Besides, two half sine-cycles referring to the plane stress cases cover most of the data points. Herein, one half sine-cycle describing the cases with triaxiality lower than -0.33 are omitted since tests conducted by Bao (2003) and numerical analyses only focus on the fracture at triaxialities greater than -0.33.

Other ductile fracture models will also be used to predict the fracture locus of the tests. These are the R-T model, MMC model, MSS model, X-W model, and Smith model. As discussed above, the R-T model is a triaxiality-dependent approach, which is widely used in predicting fracture at high triaxialities. It is also found from the tests that the cases at high triaxialities are usually also with low ϕ factors, the effect of which can be neglected. Meanwhile, the cases with low triaxialities always have high ϕ factors. Therefore, the fact that R-T model offers good prediction for the fracture at high triaxialities results from either the high triaxiality itself or the low ϕ factor, or both. In terms of the other triaxiality dependent model, the Smith criterion is expected to improve the performance of the R-T model through extending its application range. On the other hand, while it provides quite good predicted accuracy for the plane stress conditions, the original MSS model shows insufficiency to predict the fracture at other cases where there is no inherent relation

between the triaxiality and the ϕ factor. This is because, in most cases, the stress triaxiality is an essential variable to quantify the fracture loci, especially at the high triaxiality region. Moreover, the MMC approach proposed by Bai and Wierzbicki (2010) is believed to have good accuracy in capturing the shear fracture of metal in a wide range of stress state parameters (Bai and Wierzbicki, 2015; Wen and Mahmoud, 2015). The X-W model, together with the proposed model and the MMC model, can be put into the same category and can be distinguished from the R-T type of triaxiality dependent model due to their second stress state parameter coupled feature.

Table 3.1 Experimental and predictive data points for 2024-T351 aluminum. (After Bai and Wierzbicki, 2010).

Test number	Specimen	η_{avg}	ϕ_{avg}	$\overline{\varepsilon}_f$	$\overline{\varepsilon}_f^{predicted}$
1	Smooth round bar, tension	0.40	0.5001	0.47	0.32
2	Round large notched bar, tension	0.63	0.5001	0.28	0.28
3	Round small notched bar, tension	0.93	0.5002	0.17	0.23
4	Flat-grooved, tension	0.60	0.5769	0.21	0.17
5	Cylinder (d_0/h_0=0.5), compression	-0.28	0.5248	0.45	0.44
6	Cylinder (d_0/h_0=0.8), compression	-0.23	0.5411	0.38	0.37
7	Cylinder (d_0/h_0=1.0), compression	-0.23	0.5412	0.36	0.37
8	Cylinder (d_0/h_0=1.5), compression	-0.22	0.5440	0.34	0.36
9	Round notched, compression	-0.25	0.5375	0.62	0.39
10	Pure shear plate	0.01	0.5773	0.21	0.24
11	Shear and tension plate	0.12	0.5683	0.26	0.24
12	Plate with a circular hole, tension	0.34	0.5051	0.31	0.33
13	Dog-bone specimen, tension	0.36	0.5119	0.48	0.31
14	Pipe, tension	0.36	0.5104	0.33	0.31
15	Solid square bar, tension	0.37	0.5001	0.36	0.33

As shown in Fig. 3.11(b), the fracture locus predicted by all six models are plotted together with the test data points. The monotonic dash curve representing the predicted results by the R-T model obviously has quite large discrepancy with the experimental data.

This triaxiality-dependent approach provides good accuracy in predicting fracture locus for the cases of the Nos. 1, 2, 3 and 15 tests, which are at high triaxialities and under a constant ϕ factor of 0.5. For the other cases with low triaxialities, the predicted results do not match so well with the experimental data, for which the relative errors are greater than 25%. In terms of the Smith model, it improves the predicted accuracy of R-T model in that it achieves predicted fracture strains with the relative errors smaller than 20% for most tests except for Nos. 1, 4, 9, 10, 11, and 13. The two series of half sine-curves denote the fracture locus predicted by the MMC and MSS models. These two types of curves coincide with each other and show encouraging predictive performance for the plane stress cases. The X-W model has excellent prediction accuracy when compared to the other predictive results. However, two tests including No.9 and No.13 have predictive strains by the X-W model that deviate from the experimental data for greater than 35%.

The comparison of predicted fracture loci by different fracture models is listed in Table 3.3. The relative errors are calculated using Eq. (3.30). This indicates that the R-T model and the Smith model have predictive errors greater than 20%, and the MSS model has the largest error among those six. For the category of models that have triaxiality and second stress state parameter coupled functions, the predictive errors are all smaller than 15%. Obviously, both the triaxiality and the second stress state parameter in terms of Lode parameter or ϕ factor play significant roles in characterizing the ductile fracture in Al 2024-T351. Besides, it is hard to distinguish the performances of the MMC, the X-W and the proposed model since they have comparable predictive errors. Considering the computational expense, the proposed model has the least parameters that must be calibrated.

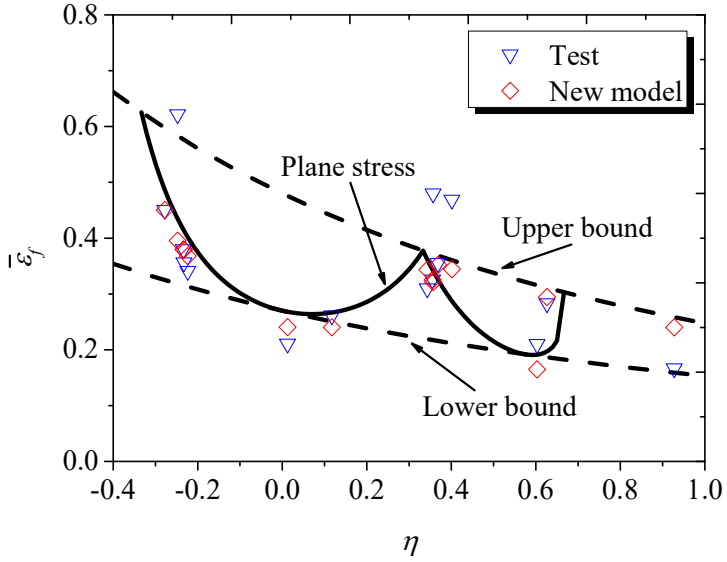

(a)

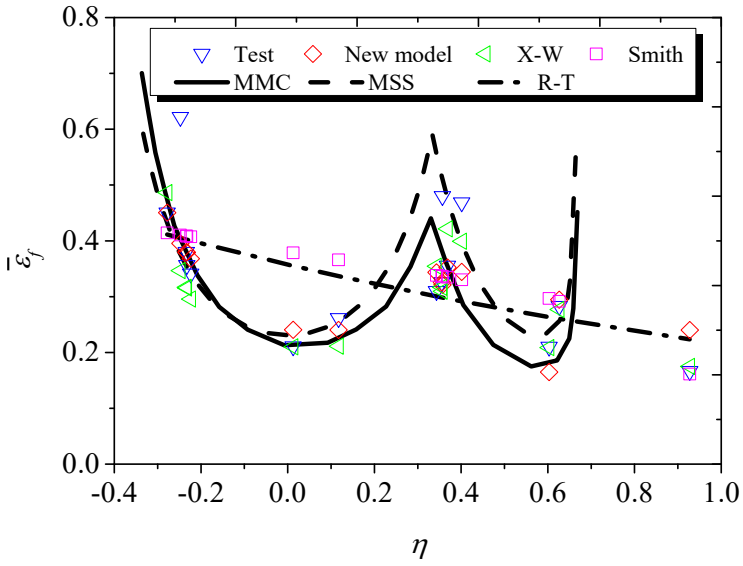

(b)

Fig. 3.11 The predicted fracture locus for Al 2124-T351 by various models: (a) prediction by the new fracture criterion; (b) comparison with various fracture models.

3.5.2 Experiments on structural steels

Smith et al. (2014) carried out a series of tests on structural steel ASTM A572 to study ductile fracture under a wide range of stress states. Four types of specimens were used during the tests, including round notched bar (CNT), grooved plate (GP), rectangular notched bar (RNB) and inclined notched plate (INP). The CNT, GP and RNB types of specimens achieve fracture at high levels of triaxiality, while the INP type of specimens exhibits ductile fracture in the intermediate and low ranges of triaxiality. The CNT and GP specimens are axisymmetric cases (ϕ=0.5) and plane strain cases (ϕ=1/√3), respectively. The RNB and INP types of specimens have ductile fracture with ϕ factors that vary from 0.5 to 1/√3. The measured strain at fracture as well as the strain at fracture predicted by the proposed model, along with the corresponding stress state parameters are listed in Table 3.2.

The calibration process resulted in α=2.45, and β=-1.44. The parameter γ was very close to 0, which implies the ϕ factor related term is eliminated and the proposed model is reduced to the R-T model. The experimental and predicted fracture loci are plotted in Fig. 3.12(a). The fracture locus predicted by the new criterion agrees well with the experimental results for most specimens. The upper bound (for ϕ = 0.577) and lower bound (for ϕ = 0.5) of the predicted fracture locus are also highlighted in Fig. 3.12(a). However, these two bounds obviously coincide with each other. The fracture locus with arbitrary ϕ factors between the lower and upper limits would always fall into the overlapped bounds. In fact, the ϕ factor has no contribution to the fracture locus of structural steel A572.

The comparison of the fracture loci predicted by various models is plotted in Fig. 3.12(b). It is expected that the data points predicted by the new criterion lie on the curve constructed by R-T model, and they have the same accuracy in A572 steel fracture locus

prediction. Both the fracture loci predicted by the MMC model and by the X-W model also agrees well with test data. Obviously, the MSS approach is incapable of capturing the fracture locus for most specimens.

Table 3.2 Experimental and predictive data points for ASTM A572 steel. (After Smith et al., 2014).

Test number	Specimen	η_{avg}	ϕ_{avg}	$\overline{\varepsilon}_f$	$\overline{\varepsilon}_f^{predicted}$
1	CNT-1	1.57	0.5	0.21	0.26
2	CNT-2	1.57	0.5	0.20	0.26
3	GP-1	1.08	0.577	0.71	0.52
4	GP-2	1.28	0.577	0.53	0.39
5	GP-3	0.92	0.577	0.73	0.65
6	RNB-1	1.14	0.5	0.39	0.47
7	RNB-2	1.15	0.545	0.43	0.47
8	RNB-3	1.12	0.548	0.37	0.49
9	RNB-4	1.15	0.562	0.48	0.47
10	RNB-5	1.09	0.569	0.42	0.51
11	RNB-6	1.09	0.574	0.51	0.51
12	RNB-7	1.05	0.577	0.67	0.54
13	INP-1	0.54	0.545	0.93	1.13
14	INP-2	0.48	0.563	1.30	1.23
15	INP-3	0.45	0.565	1.14	1.28
16	INP-4	0.34	0.575	1.68	1.50
17	INP-5	0.14	0.577	1.86	2.01
18	INP-6	0.13	0.577	2.15	2.03

The relative predictive accuracy for all six models are listed in Table 3.3. The new approach and R-T model have smaller relative errors compared to the other four models. Since the R-T model has the fewest parameters to be calibrated among all six criteria, it is of the greatest computational effectiveness in predicting fracture for steel A572.

Bai and Wierzbicki (2008) and Bai et al. (2009) conducted a series of tests to investigate ductile fracture in AISI 1045 steel. The specimens, including notched and smooth bars, grooved plates, tubular specimens, and butterfly specimens, cover a wide

range of stress state parameters (η, ϕ). The predicted fracture locus together with the test data are provided in Fig. 3.13(a). The parameter calibration process for 1045 steel results in α=0.094, and β=-1.76. Both γ and k are found to be thousands of times of the triaxiality with γ/k=3.5. This implies the ϕ factor related term in the new criterion is reduced to MSS-type function without the influence of triaxiality. With the ϕ factor being constant, the new criterion serves as the R-T model. As shown in Fig. 3.13(a), the predicted and experimental results are in good agreement. Contrary to steel A572, the fracture locus for steel 1045 have two separated bounds. It implies that the influence of ϕ factor on the fracture locus of steel 1045 is more significant than steel A572.

Table 3.3 Comparison of relative error of fracture locus predictions for Al 2124-T351, steel A572 and 1045.

Material	New criterion	R-T	Smith	MSS	MMC	X-W
Al 2124-T351	14.24%	23.18%[a]	21.91%	24.87%[a]	17.22%[a]	13.8%[a]
A572 Steel	15.89%	15.89%	19.8%	54.45%	19.93%	16.74%
1045 Steel	10.02%	16.02%	14.58%	87.2%	10.27%	12.68%

([a]The R-T model and MMC model parameters are calibrated by Wen and Mahmoud (2015), and the parameters for the MMC and the X-W model are provided by Bai and Wierzbicki (2015).)

As before, all the same models were applied to predict the fracture locus of 1045 steel, and the results are plotted in Fig. 3.13(b). The MMC and the X-W models provide acceptable predictions, and the predicted fracture loci highly coincide with that predicted by the new criterion. Even though the R-T and the Smith model have less predictive accuracy than the proposed model, the X-W and the MMC models, these two models do not deviate too much in predicting the fracture at 1045 steel. Furthermore, the MSS model has quite considerable predictive errors for most cases except two plane stress ones. The overall relative errors for each model is also provided in Table 3.3.

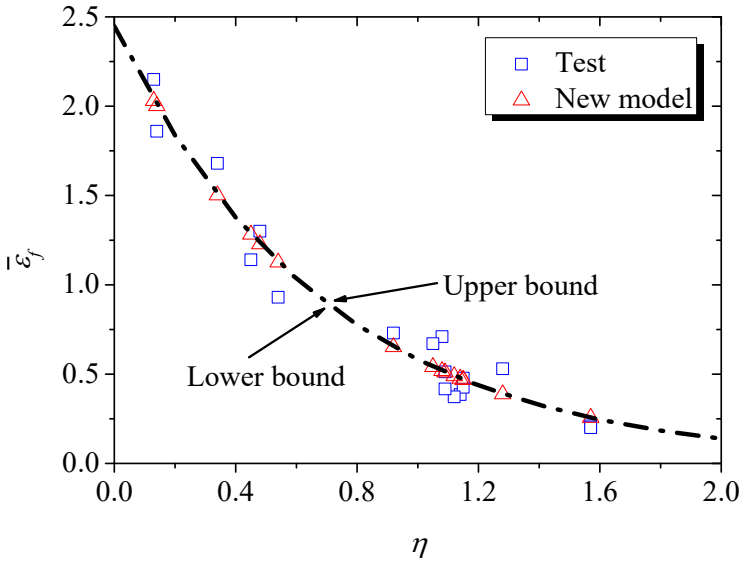

(a)

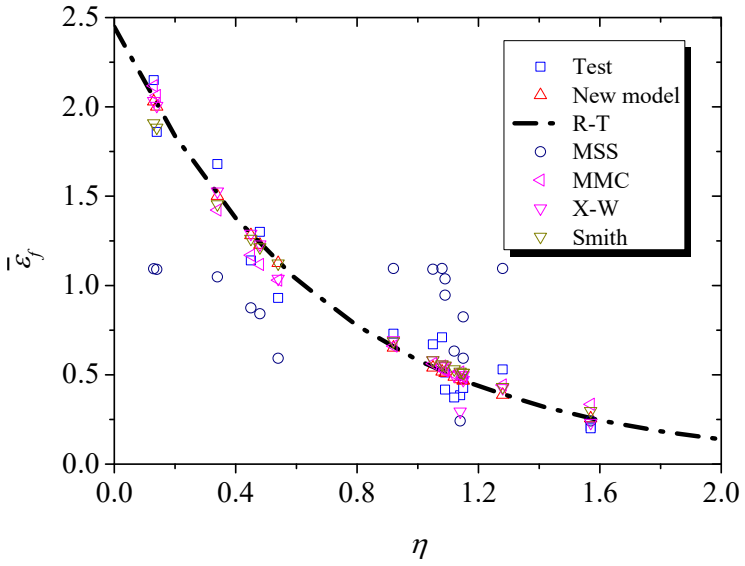

(b)

Fig. 3.12 The predicted fracture locus for A572 steel by various models: (a) prediction by the new fracture criterion; (b) prediction by various models.

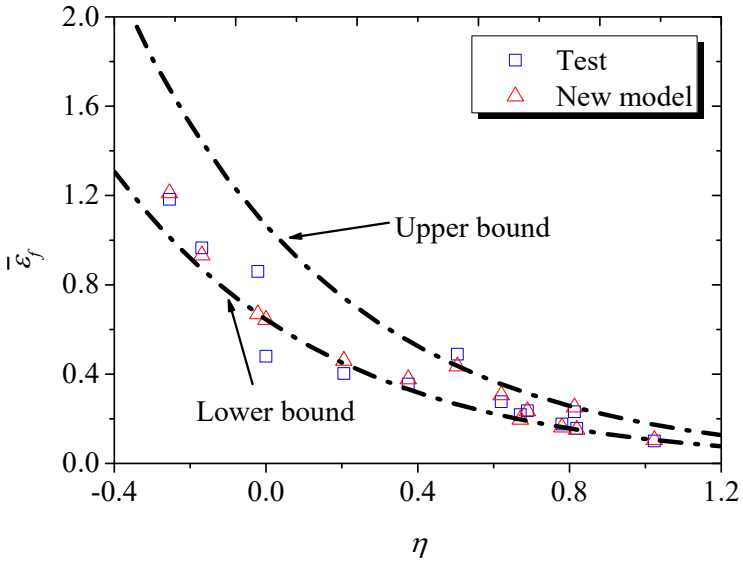

(a)

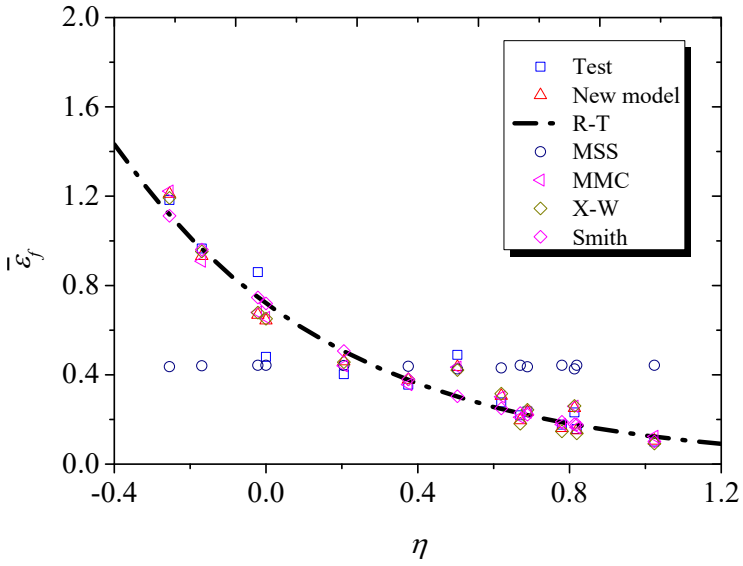

(b)

Fig. 3.13 The predicted fracture locus for steel 1045 by various models: (a) prediction by the new fracture criterion; (b) prediction by various models.

3.5.3 Comparison of predicted fracture loci

In the interest of covering a wide range of stress states and different shear stress sensitivities, the fracture locus for two types of structural steel are considered to compare the performance of the fracture criteria. To simplify the discussion, the relative fracture locus is defined as $\bar{\varepsilon}_f^{predicted} \big/ \bar{\varepsilon}_f^{test}$. The predicted results for each model are plotted in Fig. 3.14. The performances of the MMC and the Smith model are highly dependent on the material and specimen types. While the R-T model provides acceptable prediction for the shear stress insensitive A572 steel, the proposed model, the MMC and the X-W model are more accurate in the shear stress sensitive steel 1045 due to their shear stress related feature. Since the triaxiality and the shear stress parameter in the MMC model have a constrained relationship, it is more likely that MMC is better at predicting shear sensitive fractures than shear insensitive ones. In terms of the MSS model, it is only capable of capturing the fracture locus for plane stress cases. Moreover, the new model and the X-W model show good flexibility in the transition of triaxiality and shear stress dependent criteria.

As discussed above, the fracture locus in different types of metal alloys exhibit different shear stress sensitivities. To evaluate the effect of shear stress, the ratio of upper limit and lower limit of fracture locus is introduced

$$\lambda_\phi = \frac{\bar{\varepsilon}_f\left(\eta, 0.5\right)}{\bar{\varepsilon}_f\left(\eta, \frac{1}{\sqrt{3}}\right)} \tag{3.31}$$

Obviously, the ratio λ_ϕ is no less than 1. A larger λ_ϕ denotes a greater sensitivity of the ϕ factor. The λ_ϕ-η curves for different types of metal alloys are plotted in Fig. 3.15(a). This shows that the curves for different varieties of metal alloys have various shapes and heights. Compared to steel A572, the other two materials have quite larger λ_ϕ values. Even though

steel 1045 has a λ_ϕ-η curve close to Al 2024-T351, its λ_ϕ value keeps constant. This implies that the ϕ factor has a uniform contribution to the fracture locus in steel 1045 regardless of the triaxiality. In contrast, the λ_ϕ for Al 2024-T351 decreases with triaxiality indicating the effect of the ϕ factor depends on the stress triaxiality. In other words, the interaction of triaxiality and shear stress for Al 2024-T351 is more significant than the other two structural steels. Three separated lines in Fig. 3.15(a) demonstrates the roles of the ϕ factor in the ductile fracture process of metal alloys are significant.

On the other hand, the triaxiality dependency of the fracture strain also varies with materials. To make a comparison, the index λ_η is introduced as

$$\lambda_\eta = \frac{\bar{\varepsilon}_f(\eta, 0.5)}{\bar{\varepsilon}_f(1, 0.5)} \tag{3.32}$$

where λ_η is the ratio of the fracture strain at a certain triaxiality and at the triaxiality η=1 for the axisymmetric loading case, i.e., ϕ=0.5. As shown in Fig. 3.15(b), Al 2024-T351 has the least sensitivity of triaxiality among three types of metals while steel 1045 has the greatest. This trend can be also implied by the model parameter β, where the fracture locus of three different materials have the absolute values of β ordered as $|\beta|_{\text{steel 1045}} > |\beta|_{\text{steel A572}} > |\beta|_{\text{Al 2024-T351}}$. Since there exists significant interaction of triaxiality and shear stress in Al 2024-T351, the sensitivity of triaxiality is reduced by the ϕ factor. This is one reason that the ductility of Al 2024-T351 has relatively little dependency on triaxiality.

There are some uncertainties in the validation studies discussed above. One is from the experimental results reported by other references. Even for tests on the same type of metals, the fracture locus reported by different authors show discrepancies. This may be due to the differences in the tested materials, different test procedures and different stress and strain parameters obtained from different numerical simulations. In terms of the

numerical modeling, the results also depend on the accuracy of the material calibration, mesh sensitivity and analysis methodology. On the other hand, due to the fact that fracture is dependent on both stress triaxiality and shear stress, the determination of fracture initiation and critical location is not an easy process. Unlike those for the triaxiality-dependent models, the fracture strains are not necessarily monotonic functions of the two stress state variables for the triaxiality and shear stress dependent criteria. In-depth analysis on the strain gradient as well as the stress state for different types of materials and components is required to investigate the characterization of shear stress sensitive ductile fracture in future studies. However, regardless of these limitations, the proposed criterion achieves good correlations with the test data and shows significant potential for ductile fracture prediction.

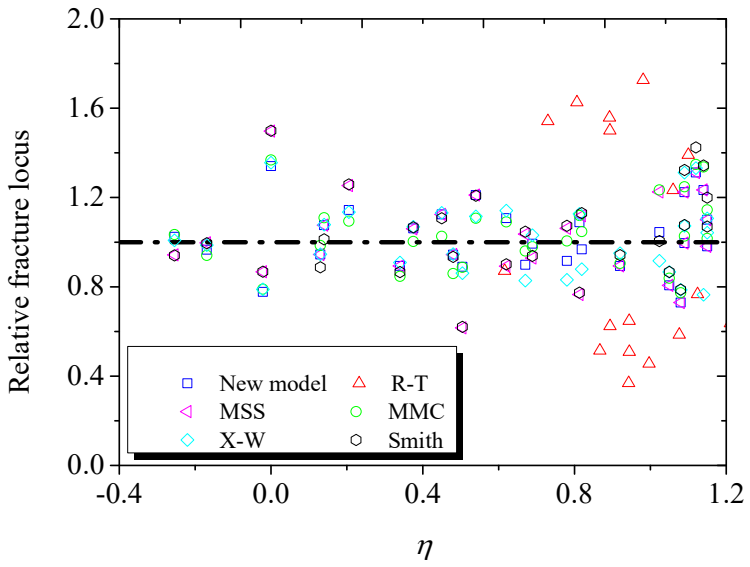

Fig. 3.14 Relative fracture locus for A572 and 1045 steels.

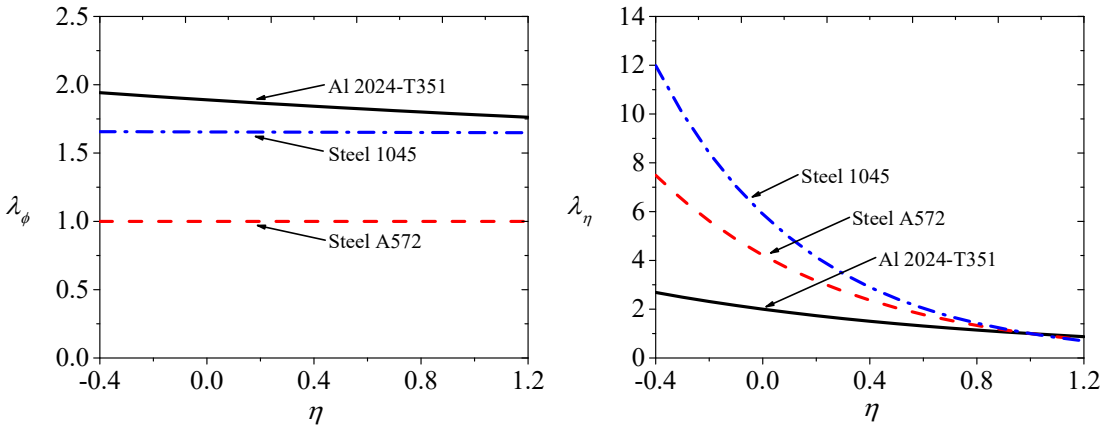

(a) (b)

Fig. 3.15 Effect of shear stress and triaxiality for various metal alloys: (a) index of shear stress dependency; (b) index of triaxiality dependency.

3.6 SUMMARY AND CONCLUSIONS

In this chapter, a new ductile fracture model coupling both triaxiality and the shear stress parameter was proposed. The model was developed based on the evaluation of the roles of triaxiality and shear stress in ductile fracture mechanisms. These two stress states act together over a wide range of triaxiality. The contribution of each stress state to the fracture locus varies with triaxiality. The stress triaxiality, in terms of hydrostatic stress, dominates the damage evolution at the high range of triaxiality with an outcome of tensile-type fracture. Whereas, shear stress has a dominant effect on fracture in the low range of triaxiality, which results in the shear-type fracture.

The R-T and modified maximum shear stress models were employed to construct the new model, wherein the interaction of two stress state parameters is emphasized. Two stress state variables in the new model compete, as increasing the value of one will suppress the effect of the other on the fracture locus. Parametric studies on each of the four model

parameters were carried out. The results indicate that the parameter α acts as the amplification of the fracture strain without any influence on the shape of fracture locus map. Furthermore, the parameter β directly effects the stress triaxiality sensitivity of the fracture locus, and the effect of stress triaxiality increases with the absolute value of β. Additionally, parameters γ and k work together to characterize the fracture strain dependency on the stress triaxiality and shear stress. Thus, the shear stress sensitivity is determined by the parameters γ, k and the amount of stress triaxiality. Also, the parametric studies confirm the upper and lower bounds. These two bounds represent the fracture locus for the axisymmetric and the plane strain cases, respectively. The correlation between the proposed model and the physical observations were also investigated. Comparison of the strain at microvoid failure predicted by micromechanical modeling and the proposed model demonstrates the link of the new criterion to the microscopic phenomena.

The proposed model was then applied to construct fracture loci of Al 2024-T351, steel A572 and steel 1045. The predicted results show good agreement with experimental data in a range of triaxiality from negative to positive. Comparison among several popular ductile fracture criteria demonstrates the proposed model has good performance for all series of fracture locus predictions. The validation analysis also shows that the shear stress sensitivity of the fracture locus varies among three types of metal alloys. The structural steel A572 is less sensitive to shear stress than steel 1045 and 2024-T351 aluminum alloy. The fracture locus of A572 predicted by the triaxiality dependent models had acceptable accuracy. Generally, the numerical results demonstrate the potential of the proposed model for ductile fracture prediction in engineering applications.

CHAPTER 4

Simulation of Ductile Fracture in Structural Steels by a Stress Triaxiality and Shear Stress Coupled Model

4.1 INTRODUCTION

Ductile fracture is an important failure mode in structural steel components, and the accurate assessment of ductile fracture is of practical significance for structural safety design. Ductile fracture has been explored by various approaches, including micro-mechanical analyses (Rice and Tracey, 1969; McClintock, 1968; Hancock and Mackenzie, 1976; Oyane, 1972; Gurson, 1977; Bandstra et al., 2004; Benzerga et al., 2004; Barsoum and Faleskog, 2007b; Brünig et al., 2008), experimental investigations (Bao and Wierzbicki, 2004; Barsoum and Faleskog, 2007a; Weck and Wilkinson, 2008; Bai, 2008; Li et al., 2011; Smith et al., 2014; Kiran and Khandelwal, 2013a) and computational simulations (Dos Santos and Ruggieri, 2003; Pardoen and Hutchinson, 2000; Ristinmaa, 1997; Kiran and Khandelwal, 2013b; 2015; Barsoum and Faleskog, 2007b). Each method contributes to the understanding of ductile fracture and each method helps support development of the other methods. Experimental observations provide fundamental information to support micromechanical studies. Further, numerical computation has been a key tool in the development and implementation of micromechanics-based models.

From the micro-mechanical point of view, ductile fracture initiation involves the steps of microvoid nucleation, growth and coalescence (Kuwamura and Yamamoto, 1997; Anderson, 2005). McClintock (1968) and Rice and Tracey (1969) suggested that void growth was dominated by two main quantities, which are the accumulated plastic strains and the hydrostatic stress, and further developed micromechanics-based models with

respect to these two variables. Freudenthal (1950), Cockroft and Latham (1968), Brozzo et al. (1972), Ayada et al. (1987), Oyane (1972) and Wierzbicki and Xue (2005) proposed similar models that have been used to predict fracture in various ductile materials. In these studies, fracture initiation is described as a critical condition rather than the outcome of internal damage accumulation. In contrast, another kind of coupled damage-plasticity models takes account continuous strength degradation due to void growth (Gurson, 1977; Tvergaard and Needleman, 1984; Zhang et al., 2000; Lemaitre, 1985; Chaboche, 1988, 2008; Brünig et al., 2008; Xue, 2007b; Kiran and Khandelwal, 2014). Even though the damage coupled models have better physical descriptions of the ductile fracture process, they require extensive calibration of model parameters, which can be very difficult and costly. However, the existing damage-uncoupled constitutive models may often be of acceptable accuracy in many engineering applications. For example, two popular uncoupled models, the void growth model (VGM) and the stress modified critical strain criterion (SMCS), have gained success in a wide range of applications of fracture prediction (Chi et al., 2006; Kanvinde and Deierlein, 2004, 2006, 2007; Kiran and Khandelwal, 2013b).

In parallel with the analytical studies, ductile fracture experiments are also conducted to explore ductile fracture at both qualitative and quantitative levels. Hancock and Mackenzie (1976), Mackenzie et al. (1977), Hancock and Brown (1983), Marini et al. (1985) and Panontin and Sheppard (1995) tested axisymmetric notched specimens to investigate the effect of stress triaxiality on fracture strain in various steels. Bao (2003), Bai (2008), Barsoum and Faleskog (2007a), Smith et al. (2014) and Li et al. (2011) carried out tests on various specimens including axisymmetric tension, plane strain tension, and combined shear and tension or compression, to identify the roles of the stress states on

fracture initiation over a wide range of triaxiality. With the triaxiality varying from negative to positive, fracture modes including shear, mixed shear-dimple and cup-cone types have been observed in the tests. In addition, microscopic studies are preformed to analyze the characteristics of microvoids and the fracture initiation mechanisms (Bandstra et al., 2004; Benzerga et al., 2004; Kiran and Khandelwal, 2013b; Li et al., 2011; Weck et al., 2008; Weck and Wilkinson, 2008). These results provide insights into the nature of void shape, spacing and orientation as well as microvoid coalescence modes and fracture surfaces under various loading conditions. While the qualitative studies provide basic insight of void growth mechanisms and fracture initiation phenomena, the quantitative studies facilitate development of numerical relationships between stress state and plastic strain at initiation of ductile fracture.

In recent years, the effect of shear stress on ductile fracture mechanisms has received attention in both experimental and micromechanical studies (Pardoen and Brechet, 2004; Barsoum and Faleskog, 2007b; Besson, 2010; Li et al., 2011). In addition to void necking and dilation, the modes of the microvoid growth and coalescence stages, including void elongation and shear-linkup in the ligaments between voids, were observed by Bai and Wierzbicki (2008), Nahshon and Hutchinson (2008), Zhang et al. (2001), Kim et al. (2004), Gao and Kim (2006) and Xue (2007a). These new-found modes are prominent in the low stress triaxiality range and are sensitive to shear stress. Subsequently, micromechanics-based models were improved based on these physical evidences. Xue (2007a) introduced another parameter, Lode angle, to the fracture criterion accounting for the shear stress effect. Bai and Wierzbicki (2010) modified Mohr-Coulomb fracture criterion (MMC) by extending the Mohr-Coulomb model to a new function with respect to triaxiality and Lode parameter. Xue (2008) and Malcher et al. (2014) modified the Gurson-

Tvergaard-Needleman (GTN) model by incorporating the Lode angle to consider microvoid elongation and further shearing damage effects. Lou et al. (2012) proposed a new ductile fracture criterion to couple the internal necking and shear linking effects on microvoid coalescence.

FE simulation is now widely used in ductile fracture investigations, both for micromechanical modeling of microvoid evolution and for macroscopic simulations for quantitative determination of stress and strain states. Barsoum and Faleskog (2007b) developed a finite-element model consisting of a planar band with a square array of cells and a spherical void to analyze two different modes of void coalescence. Gao and Kim (2006) modeled a cubic block with a void at the center and found void coalescence depends on material flow properties and stress states in terms of stress triaxiality and Lode angle. Kiran and Khandelwal (2013b) conducted numerical analysis on a cylindrical cell with a spherical microvoid to investigate the influence of stress states and material properties on the process of microvoid growth. At the macroscopic level, FE simulation has advantages of monitoring complex stress and strain states and damage evolution during the deformation history, which usually cannot be achieved by experimental measurements. Li et al. (2011) performed FE simulations of both tensile and compression tests to evaluate the accuracy of two categories of ductile fracture criteria in predicting the time and location of fracture initiation. Kiran and Khandelwal (2014) carried out a series of FE analysis to study the triaxiality and plastic strain evolutions in different cylindrical notched specimens. Kiran and Khandelwal (2015) proposed a numerical model to study the load displacement response, fracture initiation and damage mechanism in ASTM A992 structural steel.

Though the development and the application of micromechanics-based fracture models to structural steels are encouraging (Kanvinde and Deierlein, 2007; Kiran and

Khandelwal, 2013a), further work is still needed, particularly in regard to shear stress effect on the ductile fracture in structural steel. The available evidence suggests that stress triaxiality alone is insufficient to represent the stress states that influence fracture initiation in structural steels (Smith et al., 2014; Kiran and Khandelwal, 2015). In this chapter, the micro-mechanisms of ductile fracture are briefly reviewed to provide the basis of micromechanics-based models. A new fracture criterion introduced in the previous chapter, which couples the stress triaxiality and shear stress factor, is then reviewed. Finite-element simulations of two series of tests on A992 and 1045 steels are performed. The methodology of fracture locus determination based on the stress and strain profiles is discussed. Both the proposed model and the VGM are calibrated and validated by experimental observations. The performance and applicability of these two models in predicting fracture of two structural steels are discussed. This chapter aims to verify the role of shear stress in ductile fracture initiation in structural steels and validate the proposed model for its future application in structural steel components.

4.2 MICROMECHANICS-BASED FRACTURE MODELS

4.2.1 Micro-mechanisms of ductile fracture

As discussed in chapter 2, it is well established that ductile fracture initiation follows the process composed of micro-void nucleation, growth, and coalescence. The void forms around a second-phase particle or inclusion at the interfaces between the particles and the matrices. As previously discussed, there are two modes of void growth identified by previous investigators. Microvoid dilation was the first mode of void growth investigated (McClintock, 1968; Rice and Tracey, 1969; Gurson, 1977; Tvergaard, 1982; Tvergaard and Needleman, 1984). Investigators showed that the hydrostatic stress

dominates this mode of void volumetric growth. The other mode of void growth, microvoid elongation involving void shape change and rotation is found to be prominent at low triaxiality (Xue and Wierzbicki, 2007; Barsoum and Faleskog, 2007a, b; Bai and Wierzbicki, 2010; Malcher et al., 2014; Kiran and Khandelwal, 2014; Kiran and Khandelwal, 2015). Compared to microvoid dilation, this mode with little volumetric variation is controlled by the deviatoric stress components. With continuous loading and deformation, the nearby voids coalesce to form the macroscopic fracture surface. Two modes of coalescence, including intervoid ligament necking and void shearing, have been extensively investigated by Rice and Tracey (1969), Brown and Embury (1973), Le Roy et al. (1981), Weck and Wilkinson (2008) and Weck et al. (2008). In ligament necking, the ligaments between voids break perpendicular to the loading direction, facilitating the void coalescence process. In void shearing, shear-linking up of voids facilitates the void coalescence process, and occurs in the localized shear direction due to the intrinsic slip-based deformation.

Through systematic studies in mechanics and experiments, shear stress is believed to be a significant variable affecting the process of void growth and coalescence. While the role of stress triaxiality is fairly clear, further investigation is needed to better define the combined effects of shear stress and triaxiality on ductile fracture. Previous models proposed by McClintock (1968), Rice and Tracey (1969) and Hancock and Mackenzie (1976) are only applicable for high stress triaxiality cases where shear type fracture is negligible. Work is needed on the role of shear stress on ductile fracture mechanisms and in developing models for the cases where the shear stress effect is significant.

4.2.2 Void growth model (VGM)

The VGM is based on the investigation by Rice and Tracey (1969), where void growth was studied using an analytical model involving a single spherical void in an unbounded solid of a perfectly plastic material. The growth rate was correlated with the applied high stress triaxiality and strain rate field. The basic function to quantify the void growth can be expressed as $\dot{R}/R = 0.283\exp(\lambda\eta)\dot{\varepsilon}_{eff}^{\infty}$, where R and $\dot{R}$ are the radius of the void as well as its change rate, respectively; η is the stress triaxiality; and $\dot{\varepsilon}_{eff}^{\infty}$ is the remote strain rate field. Herein, the stress triaxiality η is defined as the ratio of the hydrostatic stress and the Von Mises stress. As the voids grow large enough to exceed a critical size, the material among voids breaks and neighboring voids coalesce. The initiation of ductile fracture is then considered to occur when the void growth index reaches its critical value, i.e., $VGI_{critical}$. The basic VGM function can be expressed as

$$VGI = \int_0^{\bar{\varepsilon}_f} \frac{d\varepsilon_p}{\exp(-\lambda\eta)} \geq VGI_{critical} \tag{4.1}$$

As can be seen, the VGM model has two parameters including the critical void growth index $VGI_{critical}$ and the exponential constant λ that need to be calibrated. The inability to describe the shear stress effect on ductile fracture initiation limits the application of the VGM. The shortcomings of this model will be discussed in the following sections.

4.2.3 Review of the proposed model

Based on the observations of experimental and micro-mechanics studies, a new ductile fracture criterion was proposed in chapter 3 that employs a coupled treatment of stress triaxiality and shear stress. The model is developed based on the VGM and maximum shear stress models (MSS), where the VGM model is triaxiality dependent and the MSS

model is shear stress dependent. The MSS model is found to be robust in predicting shear-type ductile fractures (Wierzbicki et al., 2005; Bai and Wierzbicki, 2015; Li et al., 2011). Assuming a power hardening material law, i.e., $\sigma=K\varepsilon^{n}$, the MSS model can be expressed as $\bar{\varepsilon}_f = \left(K\phi\right)^{-1/n}$. K and n are two power hardening material constants. The shear stress factor ϕ represents the normalized maximum shear stress and is defined as the ratio of maximum shear stress and the Mises stress $\phi=\tau_{max}/\sigma_e$, and is in to limited range of 0.5 and $1/\sqrt{3}$. Another feature of the MSS model is it couples the effect of the strain hardening property of the steel matrix, which also influences the process of microvoid evolution. Furthermore, the MSS model is modified before being introduced into the new fracture criterion to take account of the interaction between two stress states (η, ϕ) and their effects on material plasticity. Combining the VGM and the modified MSS models leads to the proposed new fracture criterion, which can be expressed as:

$$\bar{\varepsilon}_f\left(\eta,\phi\right) = \alpha \exp\left(\beta\eta\right)\phi^{\frac{\gamma}{\eta+k}} \tag{4.2}$$

where, α, β, γ and k are four parameters of the new criterion that need to be calibrated.

To describe the characteristics of the new criterion, a sample group of parameters (α=0.05, β=-0.5, γ=-20 and k=5) is chosen and the corresponding geometrical representation of the 3D fracture surface is constructed and plotted in Fig. 4.1. This plot shows the equivalent strain to fracture $\bar{\varepsilon}_f$ as a function of the triaxiality η, and the shear stress factor ϕ. It can be observed that the three-dimensional surface has upper and lower bounds, at ϕ=0.5 and $\phi=1/\sqrt{3}$, respectively. At a given stress triaxiality, a greater value of the ϕ factor reduces the fracture strain. Similarly, increasing the triaxiality decreases the equivalent plastic strain to fracture under a constant ϕ factor. When compared to the 2D curve of the VGM, the 3D surface in Fig. 4.1 is more flexible in considering complex stress

state effects on fracture. However, the shape and the dimension of the surface depends on factors such as the material properties and loading conditions, and requires further study.

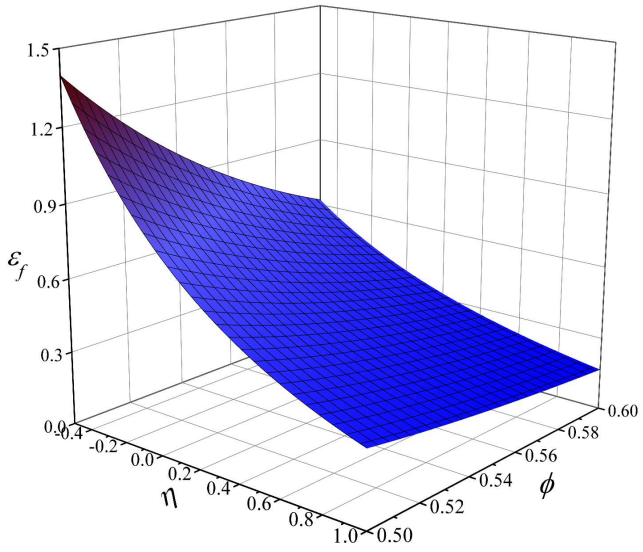

Fig. 4.1 A representative 3D fracture locus by the new ductile fracture model.

4.2.4 Damage evolution rule

Instead of a sudden event, ductile fracture initiation is generally considered as the state when the internal damage accumulates to a critical point. This approach, which is adopted by VGM, takes the stress history into account. It is reasonable to assume that the stress state remains relatively constant in a small strain increment, so that the incremental damage accumulation is defined as $dw_D = d\varepsilon_p / \bar{\varepsilon}_f(\eta,\phi)$, where w_D is the damage index. The damage accumulation integrated over the plastic strain history is then expressed as:

$$w_D = \int_0^{\bar{\varepsilon}_f} dw_D = \int_0^{\bar{\varepsilon}_f} \frac{1}{\bar{\varepsilon}_f(\eta,\phi)} d\varepsilon_p \tag{4.3}$$

When the condition w_D=1 is reached, the material element is considered to reach its

ductility limit and ductile fracture initiates. The corresponding equivalent plastic strain is known as the plastic strain to fracture $\varepsilon_p = \bar{\varepsilon}_f$.

For engineering applications, a straightforward parameter calibration process is needed. If calibration can be conducted for a case where the stress states (η, ϕ) remain constant, the fracture locus simplifies to a function of stress state written as $\bar{\varepsilon}_f = \bar{\varepsilon}_f(\eta, \phi)$. More generally, variations of triaxiality and ϕ factor during a calibration test give rise to difficulties in constructing the fracture locus map. Alternatively, the first mean value theorem for integrals is introduced into the calibration process. This method involves the determination of fracture locus using strain-weighted average parameters (η, ϕ), which are expressed as:

$$\eta_{avg} = \frac{1}{\bar{\varepsilon}_f}\int_0^{\bar{\varepsilon}_f} \eta(\varepsilon_p)\, d\varepsilon_p, \qquad \phi_{avg} = \frac{1}{\bar{\varepsilon}_f}\int_0^{\bar{\varepsilon}_f} \phi(\varepsilon_p)\, d\varepsilon_p \tag{4.4}$$

where $\bar{\varepsilon}_f$ is the estimated plastic strain to fracture and the average stress state parameters are measured from the beginning of the plastic range to fracture initiation. Once the fracture locus is established, fracture initiation when $\varepsilon_p = \bar{\varepsilon}_f$ can be predicted by Eq. (4.2). Since the strain-weighted average method is essentially an estimation of stress state parameters, its accuracy needs to be examined by comparing the fracture plastic strain $\bar{\varepsilon}_f$ from fracture locus maps obtained by the damage accumulation rule.

4.3 PREDICTION OF DUCTILE FRACTURE IN ASTM A992 STEEL

Kiran and Khandelwal (2013a) carried out a series of uniaxial tension tests to investigate ductile fracture in ASTM A992 structural steels at high triaxialities. The specimens were axisymmetric notched bars with various geometries and dimensions. The notched specimens can be classified as C-notched, V-notched and U-notched types, and

are shown in Fig. 4.2. In the current study, four representative specimens with different notched shapes and dimensions are selected, including two C-notched and one each V-notched and U-notched bars, to analyze the effect of stress triaxiality, shear stress and plastic strain on the ductile fracture initiation of axisymmetric tension specimens, and to calibrate the fracture model parameters for A992 steel.

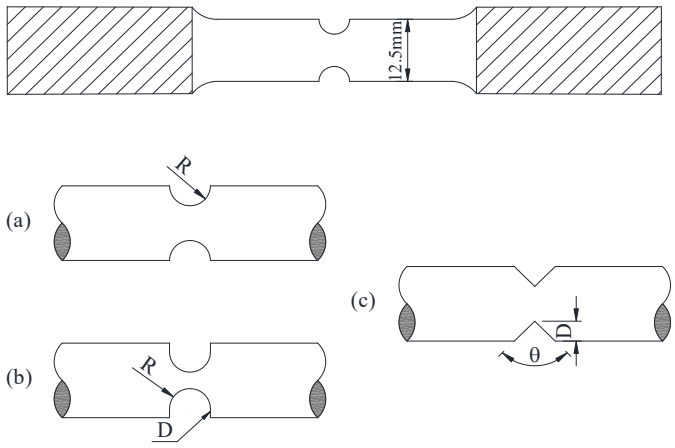

Fig. 4.2 Geometry of notched specimens tested by Kiran and Khandelwal (2013a): (a) C-notch, C1: R=0.5mm, C2: R=2.0mm, (b) U-notch, R=1mm, D=0.75mm, (c) V-notch, D=1mm, θ=90°.

Both mechanical testing and scanning electron microscopy (SEM) analysis on specimens were carried out by Kiran and Khandelwal (2013a). The former was to determine the material behavior in terms of the stress-strain curve as well as the load-displacement response of each notched bar, and the latter focused on identifying the fracture surface, the locations of fracture initiation and the fracture propagation modes. Based on the SEM studies, it was observed that the fracture surface consists of three distinct zones, including the microvoid coalescence zone (MVC), the cleavage fracture zone and

the shear lip zone. Previous work has shown that the MVC zone is the location where ductile fracture initiates (Toribio, 1997). According to Li et al. (2011), the MVC zone can show either as cup and cone type or as a shear-plane type fracture surface. Both were captured by Kiran and Khandelwal (2013a) that the MVC zone of specimen C2 was attributed to the cup and cone type and was at the center of fracture surface. Meanwhile, specimens C1, U1 and V1 with shear-plane fractures showed MVC zones at their peripheries.

4.3.1 Finite element analysis

Before being used to predict fracture initiation, the proposed model requires calibration of its model parameters. Finite element simulations were therefore carried out to analyze the evolution of the stress and strain states in terms of stress triaxiality, ϕ factor and equivalent plastic strain during the entire loading history for different specimens. Prior to that, the numerical results need to be validated by comparing the predicted load-displacement curves with experimental data. The parameter calibration process requires information of stress and strain states at critical points. The critical point refers to not only the instant but also the location of fracture initiation. The stress and strain states at fracture initiation obtained from numerical analysis are then used to determine the model parameters. The effectiveness of the model is first evaluated by calculating the fracture initiation for the specimens used for parameter calibration. The necessity of such an evaluation process will be discussed later.

Nonlinear finite-element simulation was carried out using the FE platform ABAQUS/Explicit for the implementation of ductile fracture models. Taking advantage of symmetry, a 2D axisymmetric model with the solid element CAX4R, which is a bilinear

axisymmetric element with reduced integration, was employed to represent the cylindrical notched specimen. Geometric and material nonlinearity was considered throughout the analysis. The true stress-plastic strain curve obtained from a uniaxial smooth bar test by Kiran and Khandelwal (2013a) was adopted in the current study, and is shown in Fig. 4.3. According to Kiran and Khandelwal (2013a), the model was meshed with 0.08mm size for accurately capturing stress and strain fields in the critical region.

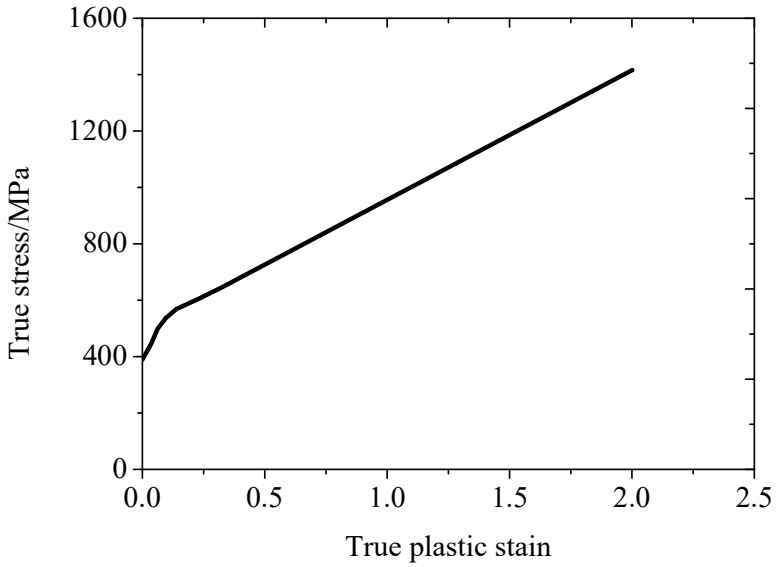

Fig. 4.3 Strain hardening curve for A992 steel. (after Kiran and Khandelwal, 2013a)

Furthermore, a user-defined subroutine VUMAT was developed for the implementation of the fracture criterion coupled material law. Analysis with both fracture criterion deactivated and activated material laws were conducted successively. The former was to achieve the load-displacement curve, update the stress and strain states at the end of each increment and determine the location and instant of fracture initiation. The second run was to calculate the damage index accumulation at the end of each increment and predict

fracture initiation by the proposed criterion. Since no damage evolution was considered in the current analysis, the material point is removed immediately after it meets the criterion given by Eq. (4.3). This simplification is adopted since the focus of the present study is on prediction of ductile fracture initiation. Prediction of fracture propagation is beyond the scope of this study.

The load-displacement curves for different specimens obtained from FE simulations excluding the fracture criterion are plotted and compared with experimental results in Fig. 4.8. These plots show that the numerical results have good correlation with the experimental results up to fracture initiation. However, there are discrepancies between simulation and experiment at the latter part of the curves. These discrepancies can be attributed to two factors: One is that the J_2 plasticity model employed in the simulation neglects the stress degradation caused by the internal damage accumulation due to the micro-void growth. The other factor is that the numerical results plotted in Fig. 4.8 are obtained through the analysis using fracture criterion deactivated material law while the actual fracture initiation influences the load-displacement response. On the other hand, since the coalescence of microvoids at the fracture initiation point will rapidly spread to a large amount of material resulting in a significant strength degradation, the point where the load-carrying capacity suddenly drop is considered to be the instant ductile fracture initiates (MacKenzie et al., 1977; Kanvinde and Deierlein, 2006; Kiran and Khandelwal, 2013a). However, this may not be true for cases other than uniaxial tension, since for such cases the load capacity does not necessarily steeply fall off after fracture initiation. Many factors, such as strain gradient, stress concentration, crack propagation mode, material properties and loading conditions, influence the global load-displacement response after crack initiation. Therefore, the determination of displacement to fracture requires careful

treatment for different cases. The experimental displacements to fracture for all the current four specimens are highlighted in Fig. 4.8.

Stress and strain states history

The stress triaxiality distribution over the critical cross section of the notched bar under different plastic strain levels are plotted in Fig. 4.4(a-d). The normalized distance in the Fig. 4.4(a-d) represents the distance measured from the center of the cross section. Thus, a normalized distance of zero corresponds to the center of the cross section and a normalized distance of 1.0 corresponds to the surface of the notch. In the elastic range, the peak of the stress triaxiality curve appears near the notch surface because of the existence of high constraint at that region. With plastic strain increasing, the shape of the triaxiality distribution curve changes. The peak of the triaxiality curve moves towards the center of cross section for C2 and U1. However, for C1 and V1, the point of maximum triaxiality remains near the notch surface. It is also observed that the triaxiality near the center increases with plastic strain while it decreases around the periphery of the cross section for most cases. This is due to changes in the notch geometry during the loading process, which influences the level of constraint and stress flow over the entire cross section. Fig. 4.4(e, f) show the evolution of triaxiality at the locations of the center and the surface. It is clearly seen that the triaxiality varies significantly during the loading history. While it tends to decrease at the notch surface, the triaxiality increases at the center.

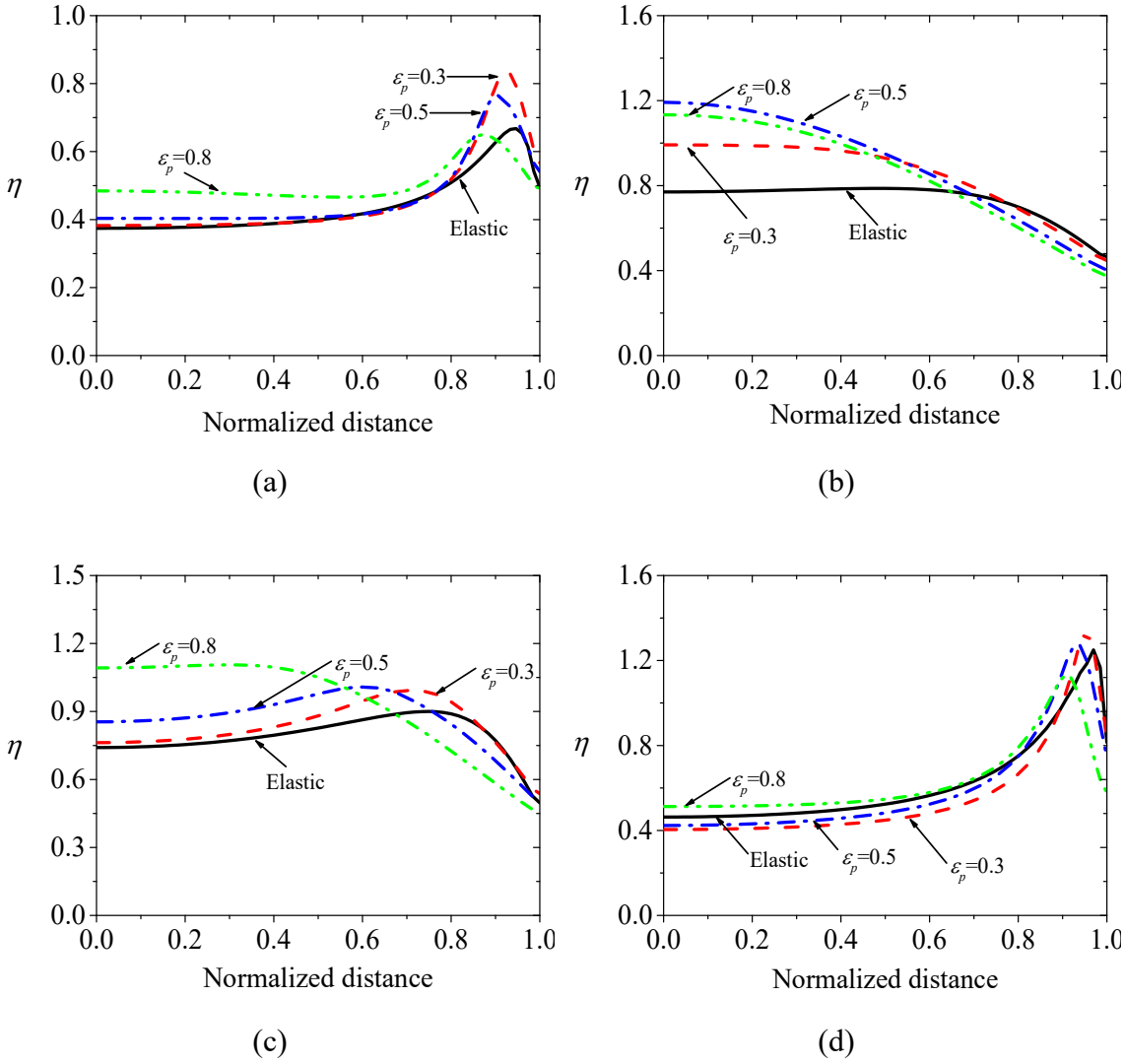

Fig. 4.4 Stress triaxiality distributions under different plastic strain levels: (a) C1; (b) C2; (c) U1; (d) V1; (e) center; (f) surface.

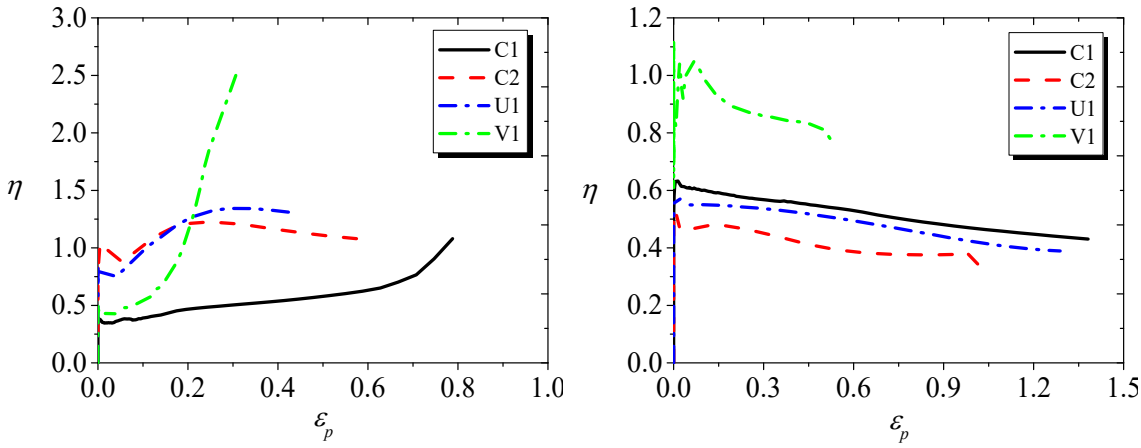

(e) (f)

Fig. 4.4, cont.

In terms of the ϕ factor, its distribution along the cross section at a given plastic strain of ε_p=0.6 is shown in Fig. 4.5(a). Because the specimens are axisymmetric, the ϕ factor at the center of each specimen keeps constant at 0.5 throughout the loading history. This is because the two principal stresses at the geometric center have identical values, i.e., σ_2=σ_3, both of which are in the plane perpendicular to the loading direction. The Von Mises stress is therefore equal to (σ_1-σ_3), which is twice of the maximum shear stress (σ_1-σ_3)/2. Away from the center, the ϕ factor gradually increases and reaches its peak at the surface of the notch. The peak value varies with the notch shape and dimension. Fracture initiation at the surface is more likely to be controlled by the combination of triaxiality and ϕ factor than that at the center, which is strongly dependent on the triaxiality. Therefore, contrary to previous finding that the ϕ factor is constant as 0.5, the fact is it varies from 0.5 to $1/\sqrt{3}$ in a circumferentially notched bar. Based on fracture surface observations by Kiran and Khandelwal (2013a), fracture initiation in specimens U1 and V1 occurred at the peripheries of the specimens where the triaxialities are relatively small and the ϕ factors are at their

peak values. This suggests that the role of shear stress on the ductile fracture of notched bars needs further investigation.

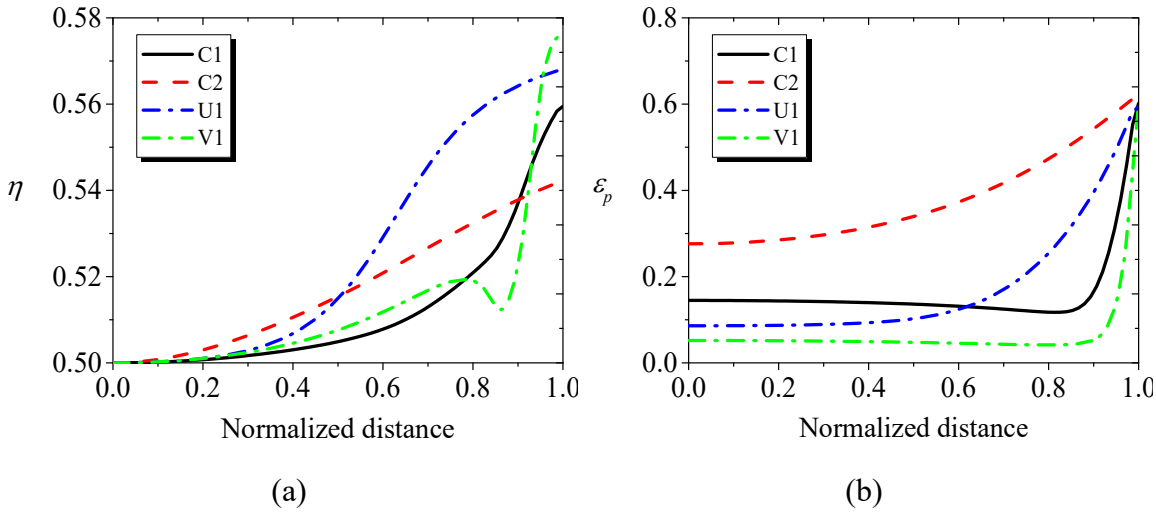

Fig. 4.5 ϕ factor and plastic strain distributions for different specimens: (a) ϕ factor at a plastic strain of 0.6; (b) plastic strain distribution over cross section.

The plastic strain distributions for different specimens in Fig. 4.5(b) are intended to illustrate basic characteristics of these distributions. With the same plastic strain ε_p=0.6 at the notch surface, there are a variety of plastic strain distributions for the different specimens. For C1 and V1, the minimum ε_p occurs a short distance from the notch surface. It is contrast, for specimens C2 and U1, ε_p has its minimum value at the center of notched bars. Moreover, C2 has quite a flat strain gradient when compared to the other specimens. For V1, owing to its sharp notch, the plastic strain at the notch root is significantly higher than the rest of the cross section.

Determination of fracture initiation

The instant of fracture initiation can be determined from the experimental load-displacement curves. However, the location of fracture initiation in the numerical simulations is uncertain, since it involves complex stress and strain distributions over the cross section. The plastic strain profile at the instant of fracture initiation is plotted in Fig. 4.6(a). All the specimens have their maximum ε_p at the notch surface. Specimens C2 and U1 with deeper notches have flat strain gradients, while C1 and V1 has relatively steep strain distributions. As previously mentioned, contrary to the other notched bars, C2 had fracture initiation at the surface. This indicates that the site with peak plastic strain will not necessarily be the critical point where fracture initiates.

It can be observed in Fig. 4.4(e, f) that the triaxiality varies significantly with the applied strains. Therefore, the fracture locus established based on either the initial triaxiality or the triaxiality at fracture initiation will lead to a significant deviation. In this case, the average triaxiality calculated by Eq. (4.4) was alternatively introduced for fracture locus determination. As the process of fracture initiation prediction involves damage accumulation, the average triaxiality can quantitatively reflect the triaxiality evolution during the strain history. The average triaxiality measured up to fracture initiation is plotted in Fig. 4.6(b). Note that the location of peak average triaxiality is not necessarily the fracture initiation point. For U1 and V1, fracture initiates at the point with the smallest average triaxiality. The distribution of average ϕ factor is plotted in Fig. 4.6(c). The contribution of the ϕ factor in axisymmetric tension cases cannot be simply ignored. The estimation of fracture initiation must be based on the supply and demand of fracture strain. For instance, though the required plastic strain to fracture is high because of the low triaxiality and ϕ factor at a certain point, the actual plastic strain is great enough to meet

the fracture criterion earlier than any other material points. Consequently, fracture initiation occurs at the point with low triaxiality and ϕ factor. In general, the cross section with a relatively uniform triaxiality distribution would possibly have fracture initiation at the point with high plastic strain and ϕ factor, whereas the critical point is likely to occur at the locations with extremely high triaxiality and ϕ factor where the strain gradient is relatively flat.

For a few ductile fracture experiments, the location of fracture initiation has been determined by approaches such as SEM. More generally, the determination of fracture initiation is not an easy process in the common fracture tests and engineering practice. Therefore, it must be estimated using numerical approaches based on computed stress and strain fields. For axisymmetric tension cases, the potential fracture initiation would be at the point with peak plastic strain or stress triaxiality. The determination of fracture initiation also involves an inverse analysis procedure. The fracture criterion parameters are calculated upon the assumed fracture initiation point. Once the criterion is established, it is necessary to reversely verify that the predicted fracture initiation corresponds to the assumed point. An example of fracture initiation prediction for specimen C1 is given to illustrate the importance of this verification process. As plotted in Fig. 4.7, two series of fracture criteria were developed based on the assumption that the notch surface is the fracture initiation point. These plots show that the plastic strain profile is below the fracture locus predicted by criterion *A* except for the expected critical point, which implies the predicted fracture initiation coincides with the assumed point. While for criterion *B*, the fracture locus is lower than the present strain for a large portion of the cross section. This means fracture initiates somewhere away from the notch rather than the notch surface and the predicted critical point is incorrect. It is therefore important to conduct this type of

verification analysis to confirm that the predicted location of fracture initiation matches the assumed location used in the model parameter calibration process. More detailed verification studies will be discussed in the following section.

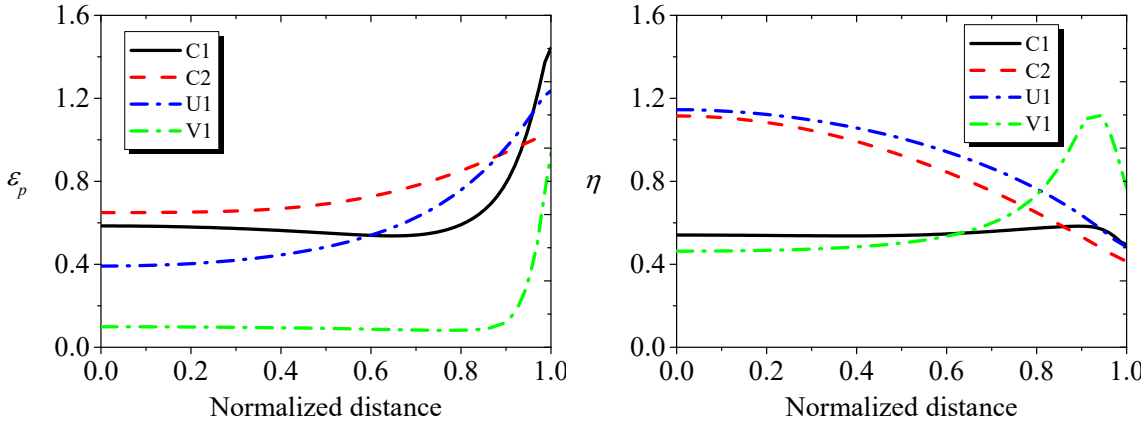

(a) (b)

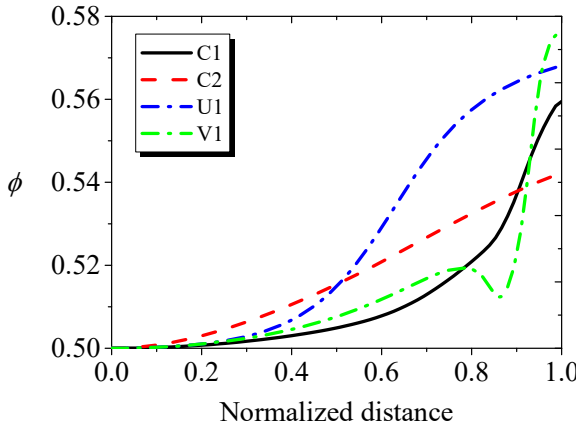

(c)

Fig. 4.6 Average stress triaxiality, ϕ factor and plastic strain at fracture initiation: (a) plastic strain; (b) average triaxiality; (c) average ϕ factor.

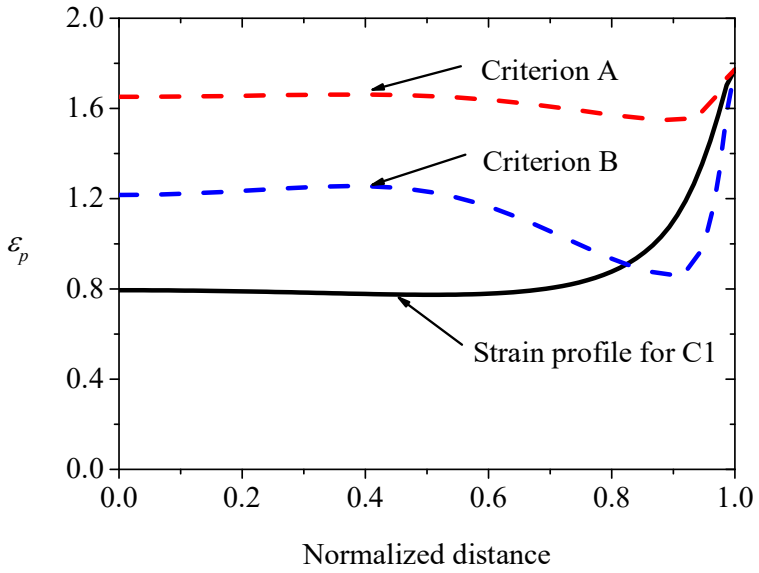

Fig. 4.7 Example of fracture location evaluation.

Parameter calibration

Once the critical fracture initiation point is determined, the corresponding average stress triaxiality, ϕ factor and plastic strain at fracture initiation can be computed using Eq. (4.4). The information regarding fracture initiation points of all four specimens, as determined by SEM examinations of fracture surfaces by Kiran and Khandelwal (2013a), are listed in Table 4.1. The calibration process results in a group of model parameters (α = 1.68, β = -1.07, γ = -0.46, k = 0.24) for A992 steel ductile fracture prediction. For comparison purposes, VGM is also applied to predict fracture initiation. With only two model parameters, VGM is calibrated by C1 and C2, resulting in $VGI_{critical}$ = 2.97 and λ = 1.417. The other two specimens are used for VGM model validation.

As shown earlier (Fig. 4.5(a)), the value of the ϕ factor at fracture initiation in a notched round bar varies with its location. Only for the case with fracture initiating at the center of round bar does the ϕ factor equal to 0.5 at fracture initiation. Therefore,

construction of a fracture locus map for the circumferentially notched bars also needs to consider the ϕ factor as of one variable.

Table 4.1 Locations of fracture initiation and corresponding stress and strain states for specimens by Kiran and Khandelwal (2013a).

Specimen	η_{avg}	ϕ_{avg}	$\overline{\varepsilon}_f$	Location of fracture initiation
C1	0.50	0.56	1.45	surface
C2	1.12	0.5	0.65	center
U1	0.48	0.55	1.24	surface
V1	0.77	0.57	0.94	surface

4.3.2 Simulation with fracture criterion

Once the fracture criterion has been established, it is activated in the FE model to investigate damage indicator evolution and to predict fracture initiation. The load-displacement curves achieved using the proposed new fracture criterion coupled simulations are plotted in Fig. 4.8. These plots identify the point on the computed load-displacement curves identified as fracture refer to the point the first element is removed. These plots show that the predicted fracture initiation points match well with the experimental results. Note that even though the predicted fracture initiation point for V1 matches the experiment well, the post-fracture initiation load-displacement response shows a considerable deviation. According to Kiran and Khandelwal (2013a), the propagation mode for V1 was cleavage fracture due to its sharp tip notch. The sudden drop of the load-displacement curve after fracture initiation is attributed to shear tearing of the lip at the surface of notch. However, both the fracture initiation and propagation modes considered in FE study assume ductile fracture. This is the reason that the numerical analysis was incapable of capturing the load-displacement behavior after fracture initiation for specimen

V1. This also demonstrates a basic limitation of ductile fracture models in cases where brittle fracture occurs.

The damage index (w_D) distribution at the instant of fracture initiation was calculated by Eq. (4.3), and is plotted in Fig. 4.9. The plot is an indicator of the location of fracture initiation where the index is most close to 1. It is observed that C1, U1 and V1 have fracture initiation at the surface of the notches, while C2 has fracture initiation located at the center. All the predicted fracture initiation locations coincide with the experimental observations. Also, C2 and U1 are most likely to have very rapid crack propagation following fracture initiation since the damage index gradients over their cross sections are relatively flat. This is supported by the experimental load-displacement curves in which the load capacity suddenly drops after fracture initiation. Specimen V1 has a steep damage contour over the cross section, where the notch tip has an extremely higher damage index. As noted earlier, fracture initiation of V1 was followed by cleavage fracture propagation. Contrary to the slow split predicted by FE simulation, a rapid fracture propagation was observed in the test. For comparative purposes, the void growth index VGI for VGM is normalized by $VGI_{critical}$ and is also plotted in Fig. 4.9. Note that the damage index distributions predicted by VGM agree well with the proposed model except for U1, which has predicted fracture initiating at the center. This corresponds to the concern discussed above, where the predicted fracture location is away from the estimated site, and highlights the necessity of back-evaluation process for fracture sites.

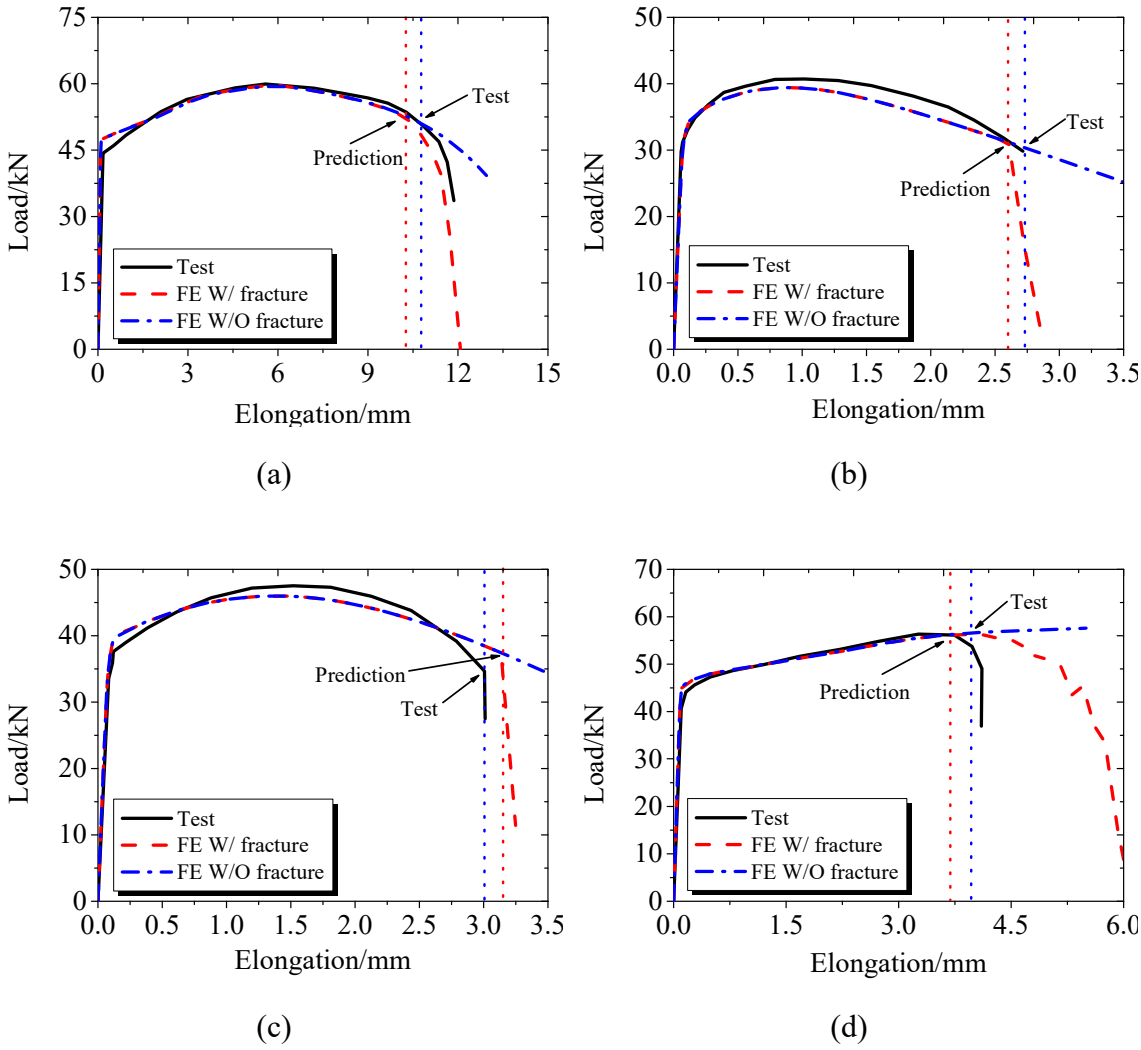

Fig. 4.8 Load-displacement curves from tests by Kiran and Khandelwal (2013a) and from numerical simulations: (a) C1; (b) C2; (c) U1; (d) V1.

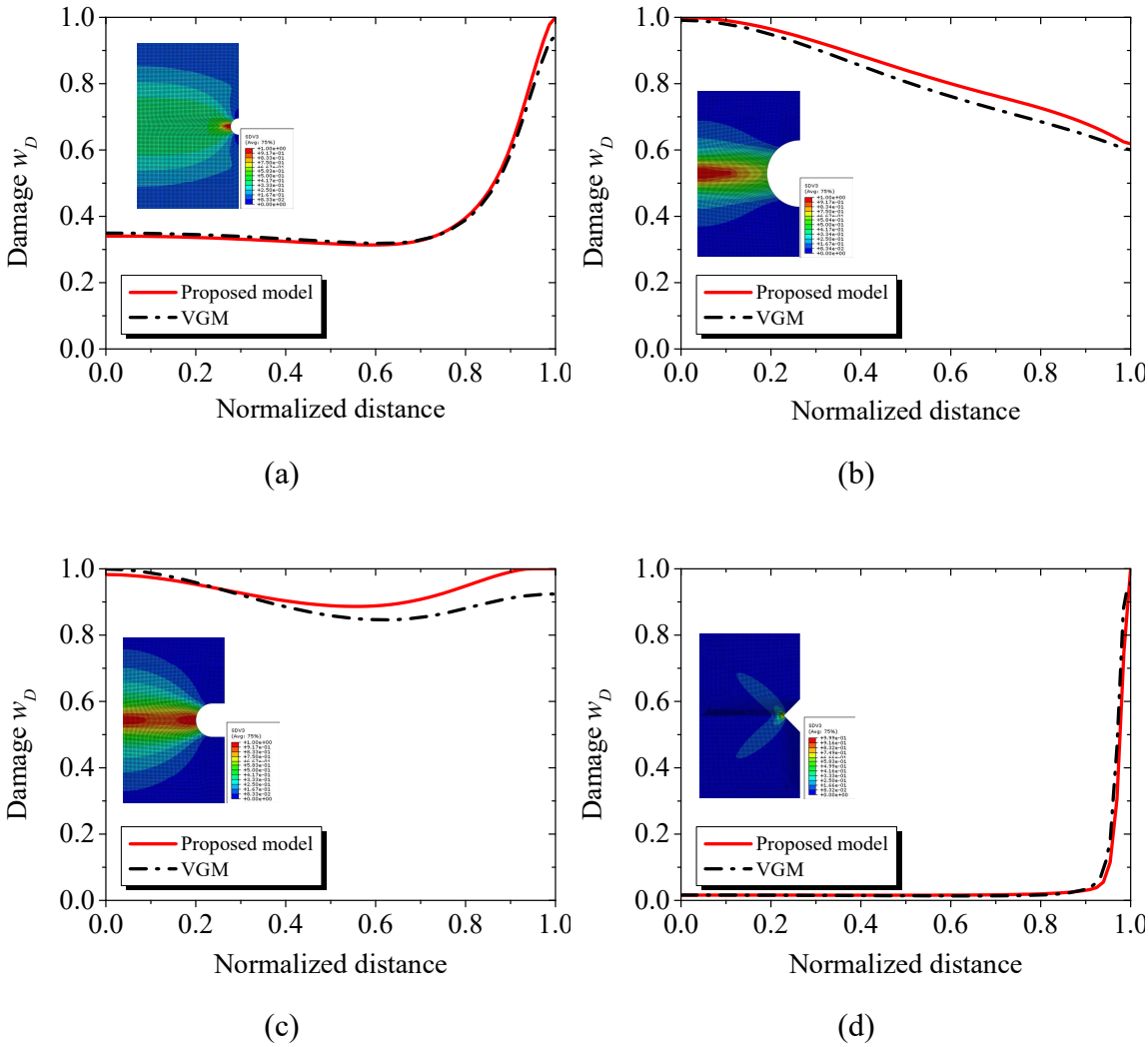

Fig. 4.9 Damage index distribution at fracture initiation for specimens by Kiran and Khandelwal (2013a): (a) C1; (b) C2; (c) U1; (d) V1.

The accuracy of the strain weighted-average stress parameter method was evaluated by comparing the analytical fracture strain calculated by Eq. (4.2) and (4.3) to the solution obtained from FE analysis. Both the analytical and numerical fracture strains for each specimen are plotted in Fig. 4.10. This shows that the two categories of fracture strains agree well with each other and indicates that the strain-weighted average stress parameter

is an effective indicator to estimate the quantities of the stress parameters. It therefore appears reasonable to build the fracture locus based the strain-weighted average method. Comparison of analytical fracture strain between the proposed model and VGM is also shown in Fig. 4.10. This shows that there is little discrepancy between the two criteria. The triaxiality-dependent VGM is applicable to capture fracture initiation in each specimen. The reason is ductile fracture in these four specimens is relatively insensitive to shear stress and is largely governed by stress triaxiality. This may be relevant to the material property and the stress triaxiality range at which fracture initiates. Further discussion regarding the shear stress sensitivity in A992 steel will be discussed later.

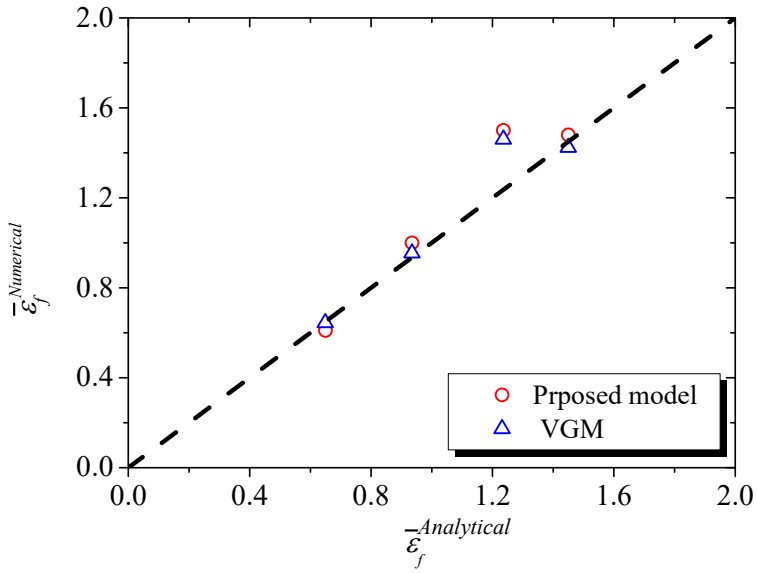

Fig. 4.10 Comparison of fracture strain from analytical and numerical solutions.

4.3.3 Model validation using non-axisymmetric specimens

To further examine the capabilities and limitations of the proposed model, it is instructive to use the model to predict fracture initiations of specimens other than those

used for model parameter calibration. Arasaratnam et al. (2011) carried out a series of plate tensile tests on ASTM A992 steel. The specimens are 9.1mm thickness dog-bones with through-thickness holes at the center. The width of the reduced section of the specimens is 40mm width. Two specimens, with either a 4mm or 8mm diameter hole, are considered in this section. Load is applied to one end while a fixed boundary condition is applied to the other end.

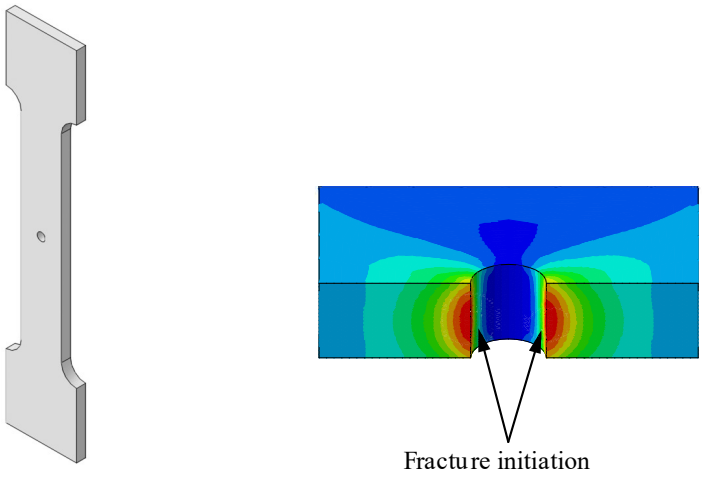

Fig. 4.11 FE model of non-axisymmetric specimen with an 8mm diameter hole.

The geometry as well as the damage contour for the critical region are illustrated in Fig. 4.11. A fine mesh with a size of 0.3mm was used around the hole to capture the strain and stress gradients and a relatively coarse mesh size of 2mm was used for the remaining parts of the model. The global load-elongation behavior from FE analysis is plotted in Fig. 4.12 and compared to the experimental results, and shows reasonably good agreement. The FE analysis overestimates the displacement to fracture of the small-hole and big-hole specimens by 8.4% and 13.9% for the proposed model, 13.6% and 14.5% for VGM, respectively. The discrepancy is attributed, in part, to the fact that even though these

specimens are A992 steel, they are a different heat than the A992 steel specimens used for calibration. Furthermore, the load-elongation relationship, in terms of average stress versus average strain curve, demonstrates the global behavior of a structural component. When compared to the global response, the behavior in a strain localization region, i.e., net section, is more sensitive to the strain hardening property. The material properties not only affect the stress distribution, but also significantly influence the strain history in the localized region. As fracture initiation occurs within the strain localized region, a slight change in the strain hardening property will result in a considerable variation in material ductility. In other words, the accuracy of the fracture initiation prediction depends on whether the model parameters are established using the actual material.

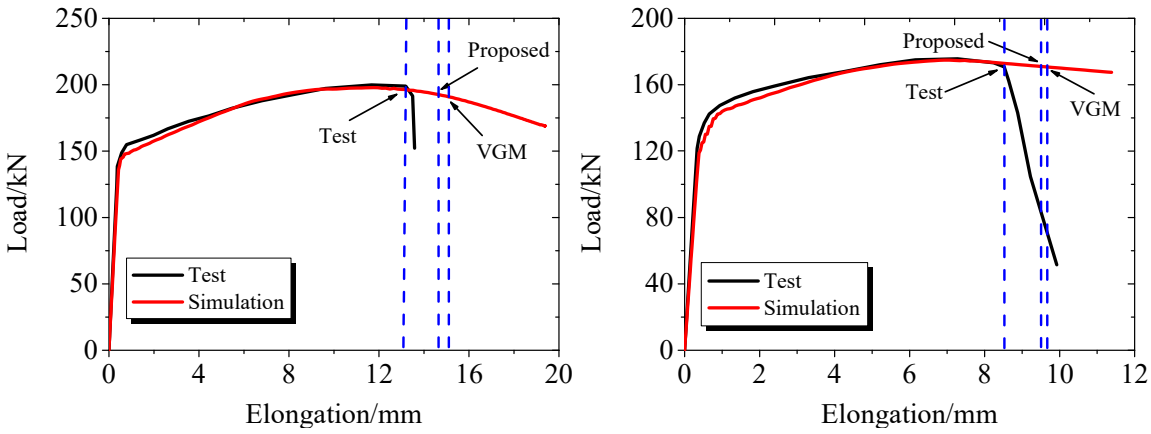

Fig. 4.12 Comparison of analysis versus test results for pull-plate specimens: (a) 4mm hole; (b) 8mm hole.

The predicted fracture initiation location is the mid-thickness of the necking region, and at the edge of the hole. Owing to the steep strain gradient, the fracture point

corresponds to the site with peak plastic strain. The stress and strain fields were monitored over the net-section region. The average stress triaxiality for the small-hole and large-hole specimens were 0.54 and 0.48, and the average ϕ factor were 0.52 and 0.53, respectively. Both the stress triaxialities are comparable with those of the notched-bar specimens, where the lowest triaxiality was 0.48. For the pull-plate specimens, strain localization occurs with necking around the bolt hole.

4.4 PREDICTION OF DUCTILE FRACTURE IN AISI 1045 STEEL

Bai (2008) carried out a series of fracture tests on specimens with various geometries and dimensions made of AISI 1045 steel. The tests achieved not only the axisymmetric tension cases but also plane strain and combined tension and shear cases, which covers a wide range of stress triaxialities and ϕ factors. The objective of this section to use data from this series of tests is to investigate ductile fracture with different levels of triaxiality and ϕ factor, and verify the proposed model for another variety of structural steel. In this section, in addition to the smooth (SR) and the notched round bars (NR) specimens, flat-grooved plate (GP) and the butterfly specimens with loading angles of 0° (B-0), 10° (B-10), 22° (B-22), 30° (B-30), 90° (B-90) are employed to perform analysis. The geometries of the specimens are shown in Fig. 4.13. Loadings with various angles applied to butterfly specimens are to achieve pure shear and combined shear and tension loading cases. For instance, the 0° butterfly denotes the pure shear test on the butterfly, whereas the 30° butterfly refers to the combined shear and tension test where the loading direction is at a 30° angle with the shear plane. While the plane strain cases of the flat-grooved plate and 0° butterfly have the identical ϕ factor of $1/\sqrt{3}$, 10°, 22° and 30° butterfly specimens would achieve ϕ factors between 0.5 and $1/\sqrt{3}$. Moreover, all the specimens have

triaxialities between 0 and 1.

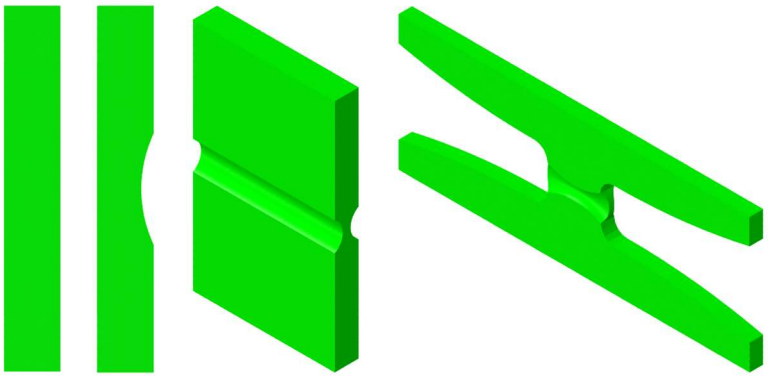

Fig. 4.13 Geometry of four specimens: smooth round bar; notched round bar; grooved plate; butterfly plate (Bai 2008).

4.4.1 Fracture initiation locus and model parameter calibration

Except for two smooth and notched round bars, all the other specimens are of non-axisymmetric geometries, which give rise to complexity in fracture initiation locus determination. First, strain and stress states of the critical cross section, where the strain concentration as well as the fracture initiation takes place, are monitored. It is confirmed that both the increasing stress triaxiality and ϕ factor reduce the strain to fracture. The case for which the peak triaxiality, ϕ factor and plastic strain coincide at a single point can be easily determined as the fracture initiation site. Such cases occur for the grooved plate and the butterfly specimens with 30° and 90°loading angles. The profile of strain and stress states for the grooved plate at fracture initiation is plotted in Fig. 4.14. It is observed that the triaxiality, ϕ factor and plastic strain are relatively uniform in the main plane except for the edge of the plate where there are very low triaxialities and plastic strains. In contrast, the triaxiality and plastic strain in the direction of thickness have larger gradients, with

their maximum values at the center. This indicates that the point at the center of the thickness will be the site where fracture initiates. For other cases such as the butterfly with 10° loading angle shown in Fig. 4.15, the peak triaxiality and ϕ factor are not coincident with the maximum plastic strain. Maximum triaxiality and minimum plastic strain occur at the center of the thickness. While the difference of the stress triaxialities between the middle and the edge of the thickness is about 100%, the strain gradient in the thickness direction is relatively flat. Therefore, it is likely that the middle of the thickness is the location of fracture initiation because of its highest stress triaxiality. The same situation is observed in two axisymmetric specimens, which have flat plastic strain and ϕ factor gradients and peak stress triaxialities at the center. In addition, the ϕ factors at the center for both two specimens are identical at 0.5.

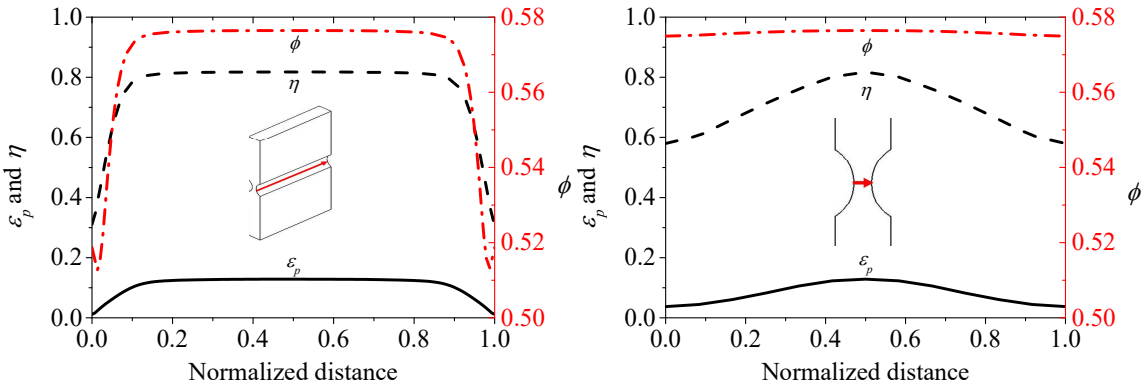

Fig. 4.14 Stress variables and plastic strain distributions for grooved plate at fracture initiation: (a) main plane; (b) thickness direction.

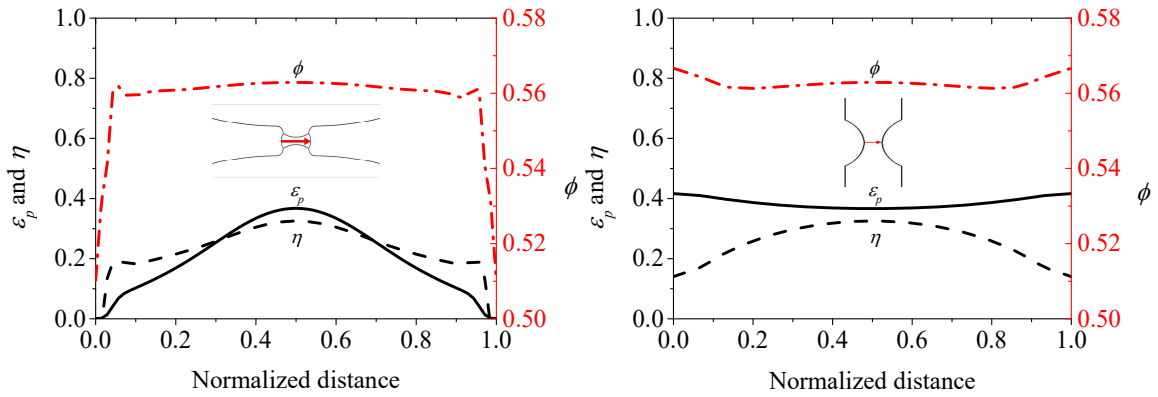

Fig. 4.15 Stress variables and plastic strain distributions for 10° butterfly at fracture initiation: (a) main plane; (b) thickness direction.

Table 4.2 Locations fracture initiation and corresponding displacement, stress and strain parameters.

Specimen	Displacement to fracture u_f (mm)	η_{avg}	ϕ_{avg}	$\overline{\varepsilon}_f$	Location of fracture initiation	
					Main plane	Thickness direction
SR	3.09	0.49	0.5	0.439	center	
NR	0.68	0.78	0.5	0.2	center	
GP	0.15	0.82	0.577	0.129	center	center
B-0	1.03	0.02	0.577	0.877	center	surface
B-10	0.42	0.32	0.563	0.367	center	center
B-22	0.29	0.59	0.51	0.283	center	center
B-30	0.22	0.71	0.536	0.282	center	center
B-90	0.1	0.88	0.576	0.115	center	center

The fracture initiation location for each specimen as well as its corresponding displacement to fracture, and the stress and strain parameters are listed in Table 4.2. It can be observed that the ϕ factor is in the range of 0.5 to 0.577 and the triaxiality varies from 0 and 0.9. Four specimens with the upper and lower limits of ϕ factor are utilized for the parameter calibration, i.e., SR, NR, GP and B-0. The remaining four specimens are used

for validation analysis of the proposed model. The parameter calibration process resulted in α = 0.0182, β = -0.1619, γ = -6.564 and k = 0.9094. Further, the parameter calibration for the VGM was based on the smooth and notched bars, leading to the parameters $VGI_{critical}$ = 1.596, and λ = 2.656.

4.4.2 Simulation with fracture criterion

Numerous ductile fracture tests focus on the axisymmetric tension cases where the triaxialities are greater than 0.33. This results in some limitations for studying ductile fracture at low triaxialities. The numerical analysis investigates the role of shear stress in ductile fracture and validate the applicability of the proposed model at not only a high range but also at a low range of triaxiality. The relative accuracy of fracture models can be evaluated based on comparison of the predicted fracture displacement by the proposed model and VGM with the experimental value, which is plotted in Fig. 4.16. This plot shows that the fracture displacements predicted by the proposed model are accurate within 7% for B-10, B-22, B-30 and B-90 specimens, while the VGM have relative errors from 9.05% to 82.3% for GP and all of the butterfly specimens. For GP, B-0, B-10 and B-90 specimens, which have ϕ factors greater than 0.56, the VGM overestimates the displacements by more than 20%. Particularly, for B-0 and B-10, which have triaxialities lower than 0.33, the over-prediction of fracture displacements is more than 72%.

The contours shown in Fig. 4.17 are the damage index (w_D) distributions at fracture initiation calculated by the proposed model. All the specimens have maximum damage index at their geometric center except the 0° butterfly, for which the critical point is at the surface of the main plane. All the predicted fracture initiation locations coincide with previous estimations. The curves shown in Fig. 4.17 are the damage accumulation evolving

with plastic strain for both models. The vertical dashed-lines indicate the plastic strain to fracture from the tests, and the predicted fracture strain occurs where the damage reaches 1. For the proposed model, all the specimens have predicted fracture strains that agree well with the experimental results. The predicted fracture strains by VGM have at least 15.1% differences from the experimental fracture strain for all the specimens except those two used for model parameter calibration. The reason that the VGM overestimates the fracture strain is an increasing ϕ factor reduces the fracture strain while VGM is calibrated by two cases with the lowest ϕ factor. The performance of VGM herein indicates the triaxiality variable alone is incapable to accurately capture ductile fracture at low triaxialities and/or high ϕ factors.

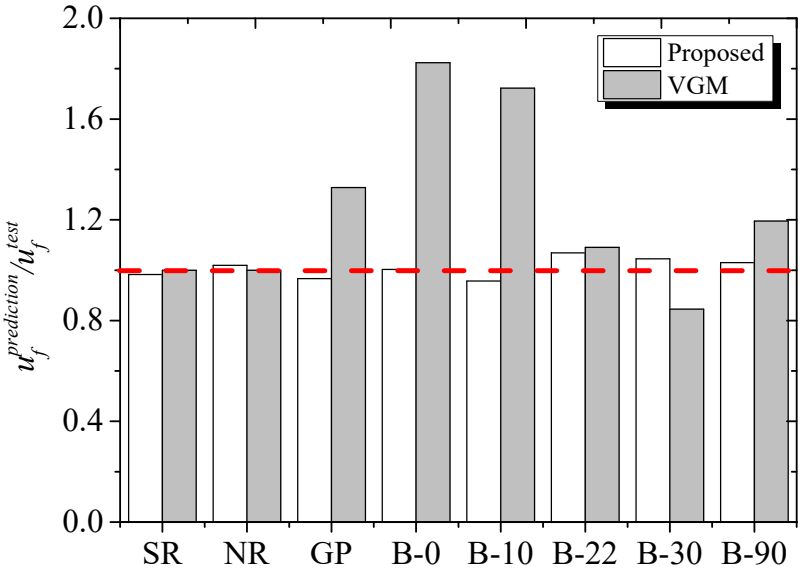

Fig. 4.16 Comparison of relative accuracy for the proposed model and VGM.

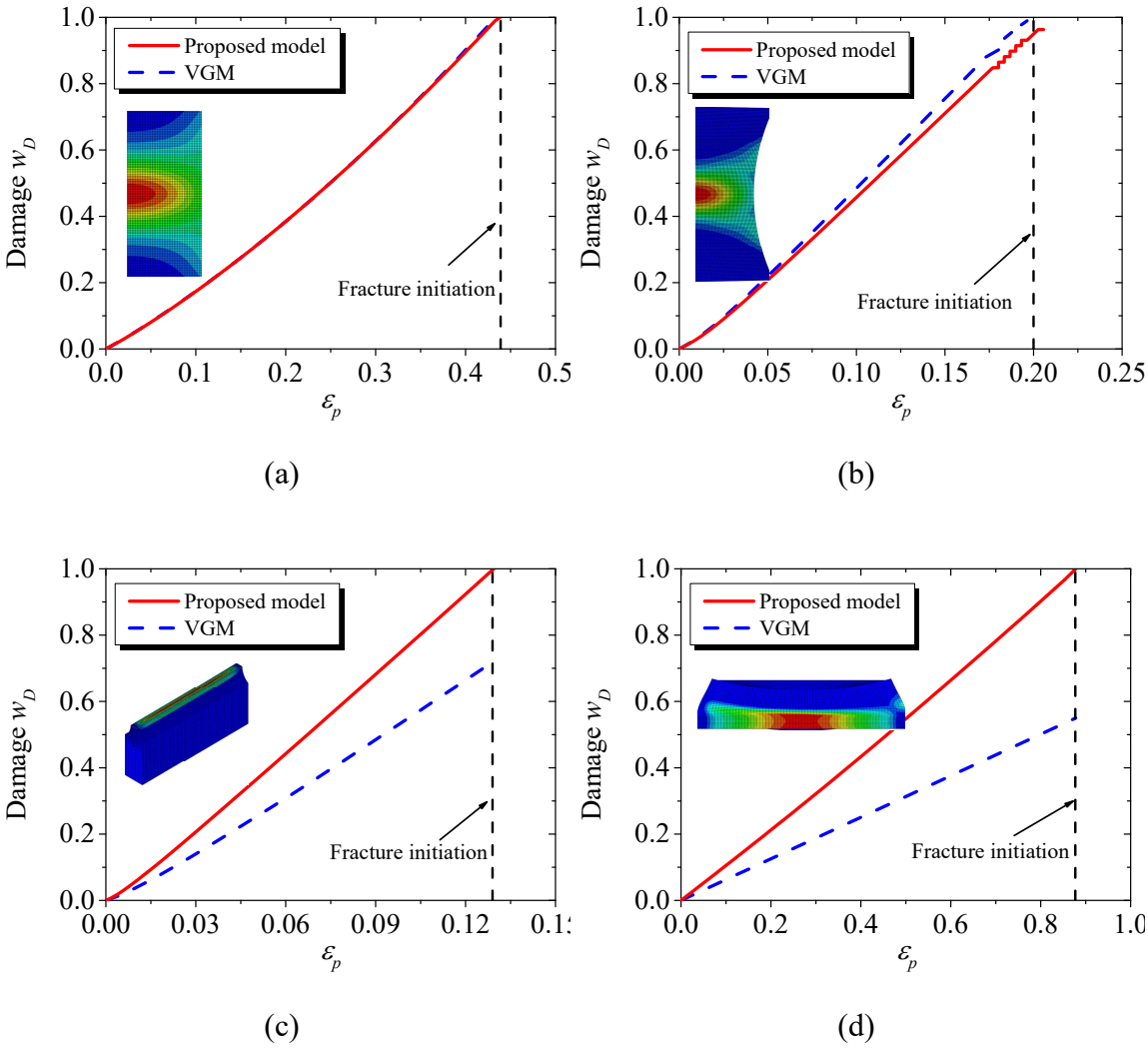

Fig. 4.17 Damage accumulation at critical points: (a) smooth bar; (b) notched bar; (c) grooved plate; (d) 0° butterfly; (e) 10° butterfly; (f) 22° butterfly; (g) 30° butterfly; (h) 90° butterfly.

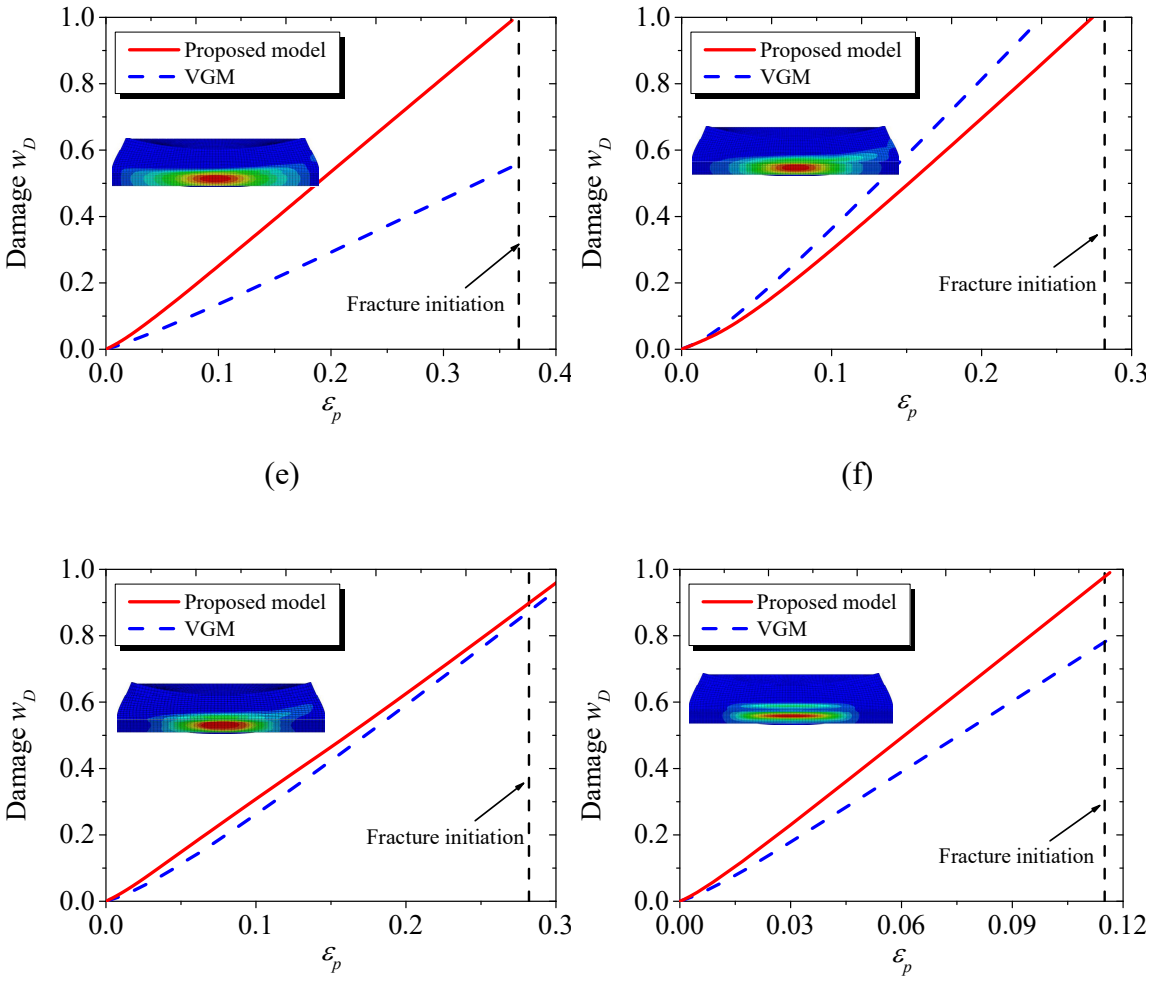

Fig. 4.17, cont.

Comparison of the fracture strain predicted by the proposed model and the experimental results is plotted in Fig. 4.18. The two dashed lines represent the fracture locus for the cases with ϕ factors equal to 0.5 and $1/\sqrt{3}$, which are the lower and upper bounds of the fracture locus. At a given stress triaxiality, the fracture strain monotonically decreases with increasing ϕ factor. The influence of ϕ factor on the fracture locus decreases as triaxiality increases since the two bounds tend to converge. Conversely, these two lines

gradually move apart from each other as triaxiality decreases. The fracture strain will exponentially increase with decreasing triaxiality if the fracture locus is independent on the ϕ factor. Comparison of predicted and experimentally determined fracture strains illustrates that the stress triaxiality and shear stress coupled model with four parameters has predicted ductile fracture initiation all the specimens with reasonable accuracy. Therefore, the proposed model provides accurate predictions not only for global displacement to fracture but also from local strain perspectives.

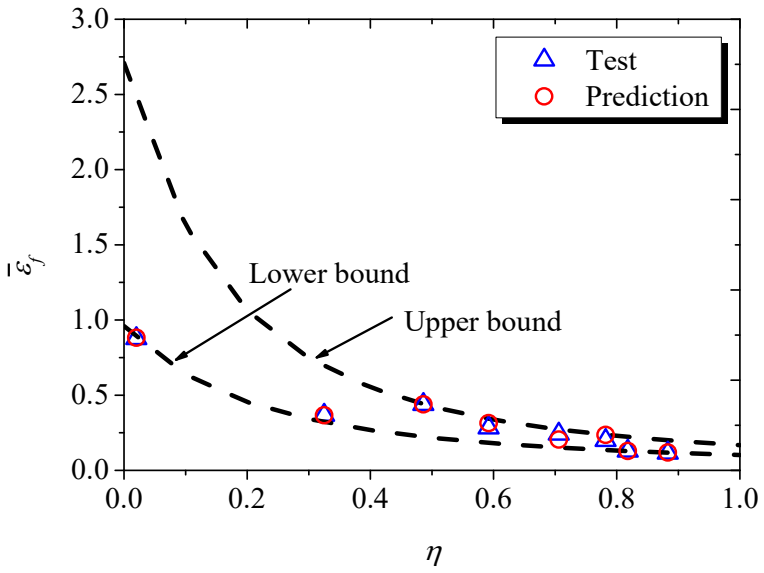

Fig. 4.18 The predicted fracture locus for AISI 1045 steel by the proposed model.

4.5 DISCUSSION ON THE DUCTILE FRACTURE PREDICTION IN STRUCTURAL STEELS

4.5.1 Comparison of ductile fracture in A992 and 1045 steels

Through FE analysis of ductile fracture in A992 and 1045 structural steels, it was seen that fracture initiation in these two varieties of steel exhibit different shear stress

sensitivities. To quantify the effect of the ϕ factor, the parameter λ_ϕ is defined as the ratio of fracture strain for ϕ=0.5 and ϕ=1/√3 at a given stress triaxiality, and is written as:

$$\lambda_\phi = \frac{\bar{\varepsilon}_f\left(\eta, 0.5\right)}{\bar{\varepsilon}_f\left(\eta, 1/\sqrt{3}\right)} \tag{4.5}$$

This parameter reflects the ratio of upper limit and lower limit of fracture strain for a given value of triaxiality. It is clearly that λ_ϕ is no less than 1, and a larger value of λ_ϕ indicates a greater shear stress sensitivity. As can be seen in Fig. 4.19, λ_ϕ gradually decreases with increasing triaxiality. As previously discussed, shear stress has greater influence on fracture initiation at low triaxialities than at high triaxialities. For A992 steel, λ_ϕ decreases from 1.32 to 1.04 as the triaxiality increases from 0 to 1.2. The lowest triaxiality in the A992 steel fracture tests by Kiran and Khandelwal (2013a) is 0.48, where λ_ϕ is 1.09. The difference in fracture strain predicted by shear stress coupled and uncoupled models is within 10% at a triaxiality greater than 0.33. Since the value of 0.33 is the lowest triaxiality for axisymmetric tensile tests, the effect of shear stress in smooth-notched specimens is negligible. A 30% difference between the shear stress coupled and uncoupled models appears at the triaxiality of 0, which emphasizes the contribution of shear stress at low triaxialities. For 1045 steel, even though values of λ_ϕ at high triaxialities are significantly lower than at low triaxialities, it exhibits a fairly high level in the entire range of triaxiality from 0 to 1.2, with λ_ϕ varying between 1.56 and 2.82.

Comparison of λ_ϕ between these two types of structural steels implies that the effect of shear stress on the fracture strain varies with material even though it has the same general tendency with triaxiality. As for VGM, the ratio λ_ϕ is constant at 1 corresponding to the dashed line in Fig. 4.19. The VGM predicted fracture in A992 steel with good accuracy because (1) ductile fracture in A992 steel is relatively insensitive to shear stress and (2) all

the cases are for fracture at high triaxialities. Similarly, the VGM shows its insufficiency in predicting fracture of 1045 steel, since this type of steel appears to be more shear stress sensitive and some cases involve the fracture at low triaxialities. When compared to VGM, the proposed model is more reliable in fracture prediction for both varieties of structural steels. This is due to its stress triaxiality and shear stress coupled feature. The new model can capture the effect of shear stress at different ranges of triaxialities, and can be adopted for fracture prediction in both shear stress sensitive and insensitive steel materials.

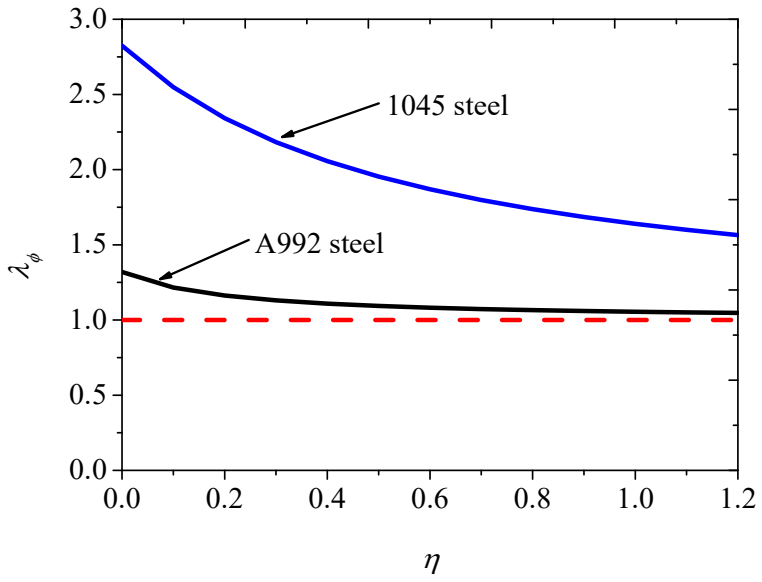

Fig. 4.19 The ratio of upper and lower bounds of fracture locus for ASTM A992 and AISI 1045 steels.

4.5.2 Application to structural engineering practice

The micromechanics-based models, such as VGM and SMCS, have many benefits over traditional fracture models and toughness criteria. They do not require the assumption of an initial macro-flaw and are able to capture the effects of stress triaxialities and plastic

strains. However, the applicability of these models is limited due to the shortcomings of their underlying micro-mechanism assumptions. With recent findings on the shear stress effect on ductile fracture, the reliability of the triaxiality-dependent models is being challenged. The accuracy of the VGM is diminished when it is adopted for predicting fracture in shear stress sensitive steels and/or at low triaxialities. While the fracture modes vary with triaxiality from dimple fracture, to mixed dimple shear fracture, to shear fracture, the governing domain for triaxiality is restricted to the regime with high values. This results in a gap between the applicability of triaxiality dependent models and structural engineering applications.

Many practical engineering situations have the possibility of fracture initiating at low triaxialities induced by the combined effects of triaxiality and shear stress. Examples include bolt shear fracture, block shear fracture, and bearing tear-out fractures in bolted connections. In such cases, the effect of shear stress completely dominates over triaxiality. Other examples are fracture in regions of strain concentration in braces that have experienced global and local buckling, and fracture in welded connections under combined shear and tension. Fracture in these cases can be controlled by a variety of stress states, where both triaxiality and the shear stress effect play significant roles. Fracture in these, and many other examples with practical importance cannot be reliably predicted by triaxiality-only dependent models. The role of shear stress in fracture initiation is likely important in many structural engineering applications.

While the triaxiality dependent models, i.e. VGM and SMCS, offer convenient implementation for structural engineering practice, their deficiencies in low triaxialities and shear stress sensitive cases significantly affect their accuracy. Though the proposed model needs more validation before being applied to steel structural components and large-

scale structures, it provides an alternative to triaxiality dependent models for describing the shear stress effect on ductile fracture in structural steels. The current study suggests that the proposed model has significant potential to predict ductile fracture initiation both for a wide range of stress states and in shear stress sensitive type steels. Further model validation would extend its range of applicability to more samples of structural steels and to more complex loading conditions.

More in-depth studies are also needed to address common drawback of damage uncoupled fracture criteria, including the proposed model and VGM, to improve fracture prediction performance. Due to the existence of micro-void growth followed by continuous damage accumulation before fracture initiation, the material will undergo gradual strength degradation. More significantly, the stress states in terms of the triaxiality and the ϕ factor influence not only damage evolution but also material plastic behavior. In this case, actual plasticity responses under different loading conditions may be different from the responses obtained from the standard material calibration tests, i.e., ordinary tensile tests. Such issues require exploration at the microstructural level to identify the interplay among the strain hardening properties, stress and strain states and micro-void evolutions before fracture initiation. Additional work is also needed to clarify the correlation of the proposed model with the micro-mechanisms of ductile fracture, to enhance the physical interpretation of the model.

4.6 SUMMARY AND CONCLUSIONS

A new micromechanics-based ductile fracture model, which focuses on ductile fracture not only at high triaxialities but also low triaxialities, is reviewed in this chapter. The void growth model (VGM) and the maximum shear stress model (MSS), which have

gained success in predicting fracture at their respective applicable domains, provide the basis for developing the new triaxiality and shear stress coupled model. The proposed model offers a uniform criterion to describe the interplay of stress triaxiality, shear stress and plastic strain, to establish a 3D space of fracture locus and to extend the application of fracture prediction to a wider range of triaxialities.

Detailed numerical analyses on two varieties of structural steels, i.e., ASTM A992 and AISI 1045 steel, were carried out to study the evolution of stress and strain states and to investigate the robustness of the proposed model. Two series of tests reported in the literature generated ductile fracture covering a wide range of triaxiality and ϕ factor. Prior to constructing the fracture locus, the methodology in determining the location of fracture initiation was discussed. Either the plastic strain or the stress triaxiality alone is insufficient to estimate the fracture initiation site. Both the triaxiality and ϕ factor determine the criterion of plastic strain to fracture, while the actual plastic strain provides the supply. The point that first meets the criterion of strain to fracture corresponds to the location where fracture initiates. For comparison, the VGM was also implemented for both steels, to compare the performance of fracture prediction with the proposed model. The results illustrate that the new model and the VGM model have comparative accuracy for A992 steel, while the proposed model has better agreement with the experimental results than VGM for 1045 steel. Comparison of ductile fracture between the two structural steels indicates that the fracture in 1045 steel is more sensitive to shear stress than in A992 steel, and the fracture at low triaxialities has greater shear stress sensitivity than at high triaxialities for both steels. Although the proposed model offers accurate prediction in two varieties of steels, validation studies using a wider spectrum of structural steels are needed.

Shear stress induced fracture appears in many situations, such as in bolted

connections, and this increases the practical value of the proposed model in structural engineering. Even though introducing one more variable is associated with more expensive implementation, the proposed model has a benefit over the VGM. The VGM performs poorly in predicting shear type fracture, whereas the proposed model provides relative better correlation with ductile facture in the perspective of micro-mechanisms due to the important role of shear stress in the micro-void evolution. However, further work is needed to clarify issues in ductile facture, such as the interaction of stress triaxiality and shear stress in micro-void growth and coalescence, and the relationship between material microstructure, stress states and their influences on the ductility of metals. Further investigation by micromechanical studies is required to address these issues.

CHAPTER 5

Modeling of Void Growth and Coalescence in Ductile Fracture: Effects of Normal and Shear Stresses

5.1 INTRODUCTION

Micromechanics-based modeling is a powerful tool to provide insights into the underlying physics of ductile fracture. It is well established that ductile fracture involves the steps of void nucleation, growth, and coalescence. In metallic alloys, the nucleation of microvoids is achieved by particle interface debonding or inclusions and second-phase particles cracking in the material matrix. Void nucleation is followed by void volumetric growth, which is influenced by the stress states and material strain hardening. As the void grows, localization of plastic flow occurs between neighboring voids, and the space between them reduces. Further intense strain localization leads to the ligament between neighboring voids necking and finally tearing. However, it has been recognized that void growth is delayed and the voids gradually flatten into micro-cracks at low triaxialities. This is due to the shearing effect wherein the deformation becomes localized into a narrow shear band between neighboring voids. The shear band facilitates the interaction of neighboring voids, which gives rise to void coalescence after the material reaches its maximum load carrying capacity.

There has been a long history in investigating the void volumetric growth and necking-type coalescence mechanism. Early studies on void growth considered the plastic material containing cylindrical spherical voids and suggesting the growth process was dominated by two main variables, which were the equivalent plastic strain and the stress triaxiality. Further efforts were devoted to developing the void growth models to quantify

the microstructural behavior by these two variables. Meanwhile, several constitutive models for porous materials were proposed by coupling the material constitutive behaviors with the void growth evolution laws (Gurson, 1977; Gologanu et al., 1993). Among those, the Gurson model is the most widely known. This model introduced a single variable, the void volume fraction, into the macroscopic yield criterion. The Gurson model was modified by Tvergaard (1981, 1982, 1990) and Tvergaard and Needleman (1984) to account for the effects of void interaction and material strain hardening. The limitations remaining in the Gurson model and its extensions are that they fail to take account for the initially non-spherical void and the void shape evolution during the course of deformation. Meanwhile, the Gologanu-Leblond-Devaux model initially developed by Gologanu et al. (1994) addresses this shortcoming by introducing void shape effects. In terms of the void coalescence induced by internal necking, contributions have been made by Gologanu (1997), Benzerga and Besson (2001), Pardoen and Hutchinson (2000) and Gologanu et al. (2001) to the modeling of the last stage of void evolution before final failure in porous ductile materials. The necking-type void coalescence is treated as a plastic flow localization phenomenon occurring within layers of thickness comparable to the void size. A sudden shift from a homogeneous deformation state to a localized state is assumed to occur at the onset of void coalescence. The shift was fundamentally discussed in numerical unit-cell analysis by Koplik and Needleman (1988). To mimic the post-shift micro-deformation, Thomason (1985) modeled the unit cell consisting of porous and rigid regions. According to Thomason's work, the onset of void coalescence relies on the current geometry of the voids and the main axial stress. Based on the notation of Thomason's (Thomason, 1985) studies, Benzerga et al. (1999) proposed a closed form of Thomason's criterion. More details were provided in the extensions of Thomason's criterion in recent years (Benzerga,

2002; Benzerga and Leblond, 2014; Morin et al., 2015; Torki et al., 2015).

More recently, the shearing-dominated void evolution has drawn increasing attention. Fleck and Hutchinson (1986) modeled an initially spherical void under remote shearing and found that the void gradually experiences shape evolution towards a penny-shaped crack. Other numerical investigations on shearing-dominated void evolution, e.g., Tvergaard (1989, 2015), McVeigh et al. (2007), Nielsen and Tvergaard (2011), show contact pressure arises between the particle and the void surface under intense shearing that plays an important role on the void as well as overall material behavior. Cox and Low (1974) and Van Stone et al. (1985) studied the materials containing multi-scale voids or inclusions, and observed that plastic flow localized between two larger voids. On the other hand, the final failure under intense shear deformation always follows a shear band instability (Rice, 1976; Needleman and Rice, 1978; Anderson et al., 1990), which leads the failure to a void sheet mechanism. Fleck et al. (1989) modeled the shear specimen of Cowie et al. (1989), by developing a cell containing a row of cylindrical voids. They applied combined shear and tension or compression and has found void sheet failure occurs in the direction parallel to the shear loading. In predicting shear-type fracture, the Gurson-type models exhibit limitations. In the Gurson-family of models, the damage parameter increases with void volume fraction and finally reaches a criterion of material failure. Nahshon and Hutchinson (2008) recently proposed an extension to the Gurson models to capture the loss of load carrying capacity and further material failure at low triaxialities. The extended model is phenomenological in which the void volume fraction is an effective indicator to keep the damage parameter increasing while the void volume fraction decreases under intense shearing.

Early micromechanical investigations of ductile fracture treated triaxiality as the

sole parameter to characterize the effects of stress states on ductile fracture (McClintock, 1968; Rice and Tracey, 1969). In recent years, the stress triaxiality alone has been found to be incapable of predicting ductile fracture under various loading conditions other than axisymmetric tension. Besides, multiple stress states can result in the same triaxiality. The micromechanical unit cell modeled by Kim et al. (2003, 2004), Gao et al. (2005) and Gao and Kim (2006) provides insights into various macroscopic material response and void behavior with the same triaxiality with different stress states. Another parameter, i.e., the Lode parameter, was recently introduced to work with triaxiality to identify the triaxial stress state. While adding a shear stress component to the triaxial stress states, the stress state cannot be unambiguously described by triaxiality and Lode parameter. For a given value of triaxiality and Lode parameter, there exists infinite combined normal and shear stress states. In this case, it gives rise to uncertainty in material response as well as void growth and coalescence behavior. It has been recognized there exists a diversity of critical strains for void coalescence induced by multiple stress states at a prescribed triaxiality and Lode parameter (Barsoum and Faleskog, 2011; Tekoglu, 2014; Bomarito and Warner, 2015; Wong and Guo, 2015). Only the minimum critical strain for a certain stress state was the focus of most micromechanical investigations of ductile fracture.

In this chapter, a void-contained unit cell model will be developed to study the dependency of void growth and coalescence behavior on the stress states. The roles of triaxial stresses and the shear stress component on the void growth and the critical strain for the onset of void coalescence at a given triaxiality and Lode parameter will be considered first. Subsequently, the combined influences of triaxiality, Lode parameter and shear stress component on void evolution and overall material response of the cell will be examined. The void coalescence mechanisms of the cell subjected to both shear coupled

and uncoupled stress states will be introduced. As mentioned above, the characteristics of void coalescence at low triaxialities are quite different from those at high and intermediate triaxialities. Void coalescence mechanisms at different triaxiality ranges will be investigated.

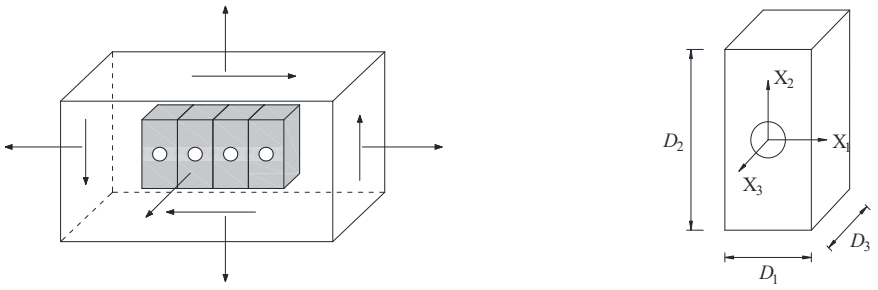

(a) (b)

Fig. 5.1 Micromechanics model: (a) homogeneous material with a layer of voided unit cells; (b) dimensions of the unit cell.

5.2 MICROMECHANICAL MODELING

5.2.1 3D unit cell model

To study void evolution under different stress states, the material is assumed to contain a regular square array of unit cells containing pre-existing voids as shown in Fig. 5.1(a). Each cell with the void at its center denotes a representative volume element (RVE), which constitutes the basis of the micromechanical model. By applying fully periodic boundary conditions, i.e., point-to-point constraints, the single cell can be studied instead of an array of voids. The representative 3D unit cell with a spherical void is studied in this chapter and is shown in Fig. 5.1(b). The dimensions of the unit cell are D_1, D_2 and $2D_3$ in

a Cartesian coordinate system (X_1, X_2, X_3). The initial size of the cell is given as $D_1=D_2/2=2D_3=D_0$, and the radius of the void is $R_0=0.2D_0$. The initial void volume fraction in the cell is defined as $f_0 = 2\pi R_0^3 / 3D_0^3$, which is equal to 0.0168 in the present case.

5.2.2 Loading and boundary conditions

The macroscopic stress state applied to the unit cell is a triaxial stress state combined with a shear stress component and is shown in Fig. 5.2(a). The macroscopic Cauchy stresses Σ_{ij} acting upon the unit cell in terms of the stress ratios are given as

$$\rho_1 = \frac{\Sigma_{11}}{\Sigma_{22}}, \quad \rho_2 = \frac{\Sigma_{12}}{\Sigma_{22}}, \quad \rho_3 = \frac{\Sigma_{33}}{\Sigma_{22}} \tag{5.1}$$

The macroscopic hydrostatic stress as well as the macroscopic effective stress are then defined as

$$\Sigma_h = \frac{\Sigma_{11} + \Sigma_{22} + \Sigma_{33}}{3} \tag{5.2}$$

$$\Sigma_e = \frac{1}{\sqrt{2}} \sqrt{(\Sigma_{11} - \Sigma_{22})^2 + (\Sigma_{11} - \Sigma_{22})^2 + (\Sigma_{11} - \Sigma_{22})^2 + 6\Sigma_{12}^2} \tag{5.3}$$

The stress triaxiality η and Lode parameter L are given as

$$\begin{aligned} \eta &= \frac{\Sigma_h}{\Sigma_e} = \frac{(1+\rho_1+\rho_3)\,\mathrm{sgn}\,\Sigma_{22}}{3\sqrt{1+\rho_1^2+3\rho_2^2+\rho_3^2-\rho_1-\rho_3(\rho_1+1)}} \\ L &= \frac{2\Sigma_{\mathrm{II}} - \Sigma_{\mathrm{I}} - \Sigma_{\mathrm{III}}}{\Sigma_{\mathrm{I}} - \Sigma_{\mathrm{III}}} \end{aligned} \tag{5.4}$$

The macroscopic principal stresses $\Sigma_{\mathrm{I}} \geq \Sigma_{\mathrm{II}} \geq \Sigma_{\mathrm{III}}$ and thus the Lode parameter are given as

$$\Sigma_{\mathrm{I}} = \frac{\Sigma_{11}+\Sigma_{22}}{2} + \sqrt{\frac{(\Sigma_{11}-\Sigma_{22})^2}{4} + \Sigma_{12}^2}$$

$$\begin{cases} \Sigma_{\mathrm{II}} = \Sigma_{33} \\ \Sigma_{\mathrm{III}} = \dfrac{\Sigma_{11}+\Sigma_{22}}{2} - \sqrt{\dfrac{(\Sigma_{11}-\Sigma_{22})^2}{4} + \Sigma_{12}^2} \end{cases} \quad \text{if} \quad \Sigma_{\mathrm{II}} \geq \Sigma_{\mathrm{III}} \tag{5.5}$$

$$\begin{cases} \Sigma_{\mathrm{II}} = \dfrac{\Sigma_{11}+\Sigma_{22}}{2} - \sqrt{\dfrac{(\Sigma_{11}-\Sigma_{22})^2}{4} + \Sigma_{12}^2} \\ \Sigma_{\mathrm{III}} = \Sigma_{33} \end{cases} \quad \text{else}$$

$$\begin{cases} L = \dfrac{(2\rho_3 - \rho_1 - 1)\,\mathrm{sgn}\,\Sigma_{22}}{2\sqrt{\dfrac{(\rho_1-1)^2+4\rho_2^2}{4}}} & \text{if} \quad \Sigma_{33} \geq \dfrac{\Sigma_{11}+\Sigma_{22}}{2} - \sqrt{\dfrac{(\Sigma_{11}-\Sigma_{22})^2}{4} + \Sigma_{12}^2} \\ L = \dfrac{\rho_1 + 1 - 6\sqrt{\dfrac{(\rho_1-1)^2+4\rho_2^2}{4}} - 2\rho_3}{\rho_1 + 1 + 2\sqrt{\dfrac{(\rho_1-1)^2+4\rho_2^2}{4}} - 2\rho_3} & \text{if} \quad \Sigma_{33} < \dfrac{\Sigma_{11}+\Sigma_{22}}{2} - \sqrt{\dfrac{(\Sigma_{11}-\Sigma_{22})^2}{4} + \Sigma_{12}^2} \end{cases} \tag{5.6}$$

Due to the symmetry of the stress state applied to the cell, only half of the unit cell ($-D_0 \leq X_3 \leq 0$) is modeled. Corresponding to the combined normal and shear stress state, the displacements U_1, U_T, U_2, U_3 are imposed to the boundaries of the unit cell, where U_1, U_2 and U_3 are three normal displacements and U_T denotes the tangential displacement parallel to X_1, which is shown in Fig. 5.2(b). Then, the average of the deformation gradient over the unit cell volume is defined as

$$\overline{\mathbf{F}} = \begin{pmatrix} \dfrac{D_1}{D_0} & 0 & 0 \\ \dfrac{U_T}{2D_0} & \dfrac{D_2}{2D_0} & 0 \\ 0 & 0 & \dfrac{2D_3}{D_0} \end{pmatrix} \tag{5.7}$$

where $D_1 = D_0 + U_1$, $D_2 = 2D_0 + U_2$ and $D_3 = D_0/2 + U_3$ are the current dimensions of the unit cell. Furthermore, the rate of deformation gradient is defined as the symmetric part of the velocity gradient given as

$$\mathbf{D} = sym(\dot{\overline{\mathbf{F}}}\overline{\mathbf{F}}^{-1}) = \begin{pmatrix} \frac{\dot{U}_1}{D_1} & \frac{1}{2}(\frac{\dot{U}_T}{D_2} - \frac{U_T\dot{U}_1}{D_1D_2}) & 0 \\ \frac{1}{2}(\frac{\dot{U}_T}{D_2} - \frac{U_T\dot{U}_1}{D_1D_2}) & \frac{\dot{U}_2}{D_2} & 0 \\ 0 & 0 & \frac{\dot{U}_3}{D_3} \end{pmatrix}, \quad \mathbf{D}' = \mathbf{D} - \frac{\mathrm{tr}(\mathbf{D})}{3}\mathbf{I} \quad (5.8)$$

where $\mathbf{D}'$ denotes the deviatoric strain tensor and $\mathbf{I}$ is the identity matrix. Thus, an effective scalar measure of equivalent strain can be calculated as

$$E_e = \int \sqrt{\frac{2}{3}\mathbf{D}' : \mathbf{D}'}\, dt \quad (5.9)$$

On the other hand, the deformation gradient can be divided into uniform and non-uniform parts as

$$\overline{\mathbf{F}} = \overline{\mathbf{F}}^0 + \overline{\mathbf{F}}^q = \begin{pmatrix} \overline{F}_{11}^0 & 0 & 0 \\ \overline{F}_{12}^0 + q_1 & \overline{F}_{22}^0 + q_2 & 0 \\ 0 & 0 & \overline{F}_{33}^0 \end{pmatrix}, \quad \begin{cases} q_1 = \dfrac{U_T - u_1^0}{2D_0} = \dfrac{u_1^q}{2D_0} \\ q_2 = \dfrac{U_2 - u_2^0}{2D_0} = \dfrac{u_2^q}{2D_0} \end{cases} \quad (5.10)$$

where, u_i^q is the non-uniform part of deformation and is shown in Fig. 5.2(c). Needleman and Tvergaard (1992) defined that the localization of deformation into a narrow planar band occurs when

$$k_\eta = \left\|\dot{\overline{\mathbf{F}}}\right\| / \left\|\dot{\overline{\mathbf{F}}}^0\right\| \gg 1 \quad (5.11)$$

In this chapter, the onset of failure by shear localization is assumed to occur when k_η=10.

Fully periodic boundary conditions are applied on the faces $X_1 = \pm D_0/2$ and $X_2 = \pm D_0$ while the homogeneous boundary condition is assumed on the face X_3=-D_0/2 to keep the surface planar and parallel to X_3 throughout the loading history. The displacement U_1, U_T, U_2 and U_3 are used to describe the periodic boundary conditions as well as the homogeneous boundary condition. Meanwhile, the initial boundary conditions are applied on the edges of $X_1 = D_0/2$, $X_2 = -D_0$ and $X_1 = -D_0/2$, $X_2 = -D_0$ to eliminate the rigid body motion of the cell. All the boundary conditions are formulated as

$$\begin{aligned} &\text{On } X_1 = \pm D_0/2: \\ &u_1(D_0/2, X_2, X_3) = u_1(-D_0/2, X_2, X_3) + U_1 \\ &u_2(D_0/2, X_2, X_3) = u_2(-D_0/2, X_2, X_3) \\ &u_3(D_0/2, X_2, X_3) = u_3(-D_0/2, X_2, X_3) \end{aligned} \tag{5.12}$$

$$\begin{aligned} &\text{On } X_2 = \pm D_0: \\ &u_1(X_1, D_0, X_3) = u_1(X_1, -D_0, X_3) + U_T \\ &u_2(X_1, D_0, X_3) = u_2(X_1, -D_0, X_3) + U_2 \\ &u_3(X_1, D_0, X_3) = u_3(X_1, -D_0, X_3) \end{aligned} \tag{5.13}$$

$$\begin{aligned} &\text{On } X_3 = 0 \text{ and } -D_0/2: \\ &u_3(X_1, X_2, 0) = 0 \\ &u_3(X_1, X_2, -D_0/2) = U_3 \end{aligned} \tag{5.14}$$

$$\begin{aligned} &u_1(-D_0/2, -D_0, X_3) = u_2(-D_0/2, -D_0, X_3) = 0 \\ &u_2(D_0/2, -D_0, X_3) = 0 \end{aligned} \tag{5.15}$$

Moreover, to avoid over-constraint during the analysis, additional treatments are needed for the boundary conditions of common edges and common corners. Independent boundary conditions are thereby applied to such edges and corners while maintaining compatibility with the conditions in Eq. (5.12) -(5.14).

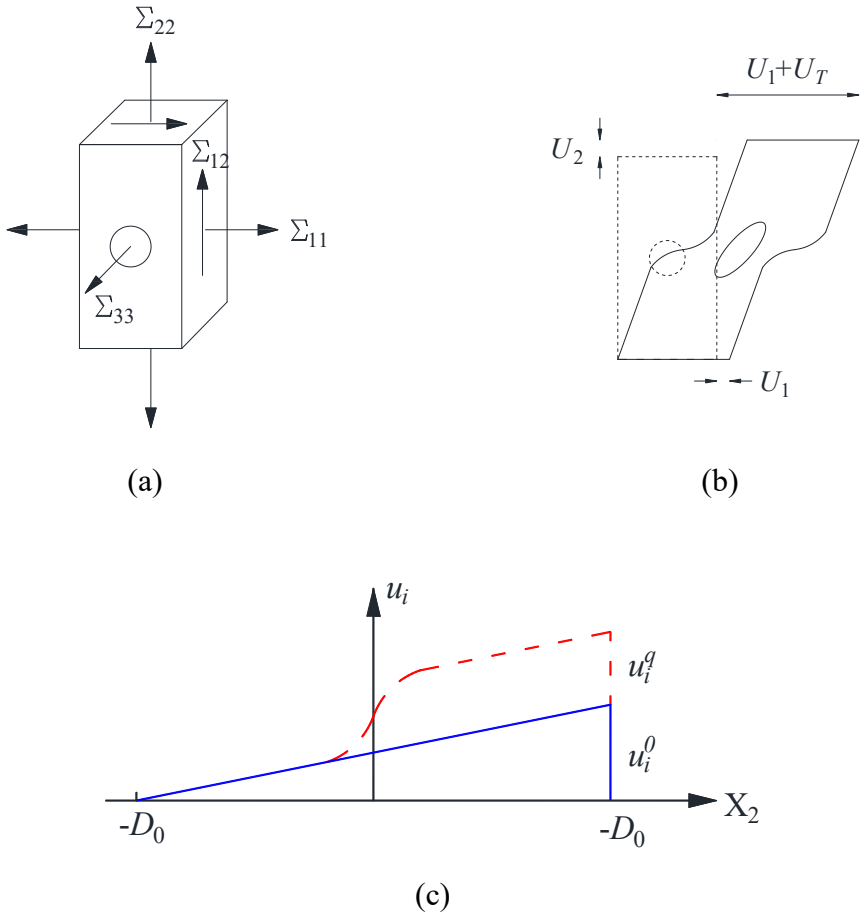

Fig. 5.2 (a) Macroscopic stress state of the unit cell; (b) X_1-X_2 plane displacements (the out-of-plane displacement U_3 is not plotted); (c) uniform and non-uniform deformations due to shear.

5.2.3 Numerical implementation

The 3D unit cell modeling was implemented in the finite element program ABAQUS. Nonlinear analysis was performed using an updated Lagrangian formulation to account for large deformations. The 8-node linear brick element with reduced integration (C3D8R) was used to mesh the unit cell and a total 11984 elements were contained in the

entire model.

Per Hill (1967, 1972), the total work rate of the cell can be determined using the macroscopic deformation rate as well as stress, which is given as

$$\dot{W} = V(\Sigma_{11} D_{11} + \Sigma_{22} D_{22} + \Sigma_{33} D_{33} + 2\Sigma_{12} D_{12}) \tag{5.16}$$

where $V=D_1D_2D_3$ is the current cell volume. Combining Eq. (5.8) and (5.16), the total work is expressed as

$$\dot{W} = V(\frac{\Sigma_{11}}{D_1} - \frac{\Sigma_{12} U_T}{D_1 D_2})\dot{U}_1 + \frac{V\Sigma_{22}}{D_2}\dot{U}_2 + \frac{V\Sigma_{33}}{D_3}\dot{U}_3 + \frac{V\Sigma_{12}}{D_2}\dot{U}_T \tag{5.17}$$

Since all the corner nodes of the unit cell are involved in the periodic boundary conditions, further multi-point constraints are not allowed to be enforced on such nodes in ABAQUS/Standard. Therefore, two spring elements were created to connect the corner nodes with two extra nodes, through which the forces can be applied to the unit cell. As can be seen in Fig. 5.3(a), the spring connected to the corner node ***A*** can transfer forces at three translational degrees of freedom while the other one connected to node ***B*** is used for force transfer at X_1-direction. Thus, a set of generalized forces P_{11}, P_{12}, P_{22} and P_{33} were applied to impose the corresponding displacements U_1, U_T, U_2 and U_3, respectively. The total work rate in terms of the generalized forces is obtained

$$\dot{W} = P_{11}\dot{U}_1 + P_{22}\dot{U}_2 + P_{33}\dot{U}_3 + P_{12}\dot{U}_T \tag{5.18}$$

Combining Eq. (5.17) and (5.18) leads to

$$\{V(\frac{\Sigma_{11}}{D_1} - \frac{\Sigma_{12} U_T}{D_1 D_2}) - P_{11}\}\dot{U}_1 + (\frac{V\Sigma_{22}}{D_2} - P_{22})\dot{U}_2 + (\frac{V\Sigma_{33}}{D_3} - P_{33})\dot{U}_3 + (\frac{V\Sigma_{12}}{D_2} - P_{12})\dot{U}_T = 0 \tag{5.19}$$

Since U_1, U_T, U_2 and U_3 are at independent degrees of freedom, their corresponding change

rates are arbitrary, the coefficient must be vanished and therefore leads to

$$P_{11} = V(\frac{\sum_{11}}{D_1} - \frac{\sum_{12} U_T}{D_1 D_2}), \quad P_{22} = \frac{V \sum_{22}}{D_2}, \quad P_{33} = \frac{V \sum_{33}}{D_3}, \quad P_{12} = \frac{V \sum_{12}}{D_2} \tag{5.20}$$

Substituting Eq. (5.20) by (5.1), the set of generalized forces can be proportional to each other, expressed as

$$P_{11} : P_{22} : P_{33} : P_{12} = (\rho_1 - \rho_2 \frac{U_T}{D_2}) \frac{D_2}{D_1} : 1 : \rho_3 \frac{D_2}{D_3} : \rho_2 \tag{5.21}$$

To realize the proportionality of the generalized forces, a linear multi-point constraint is introduced via a user defined subroutine *MPC. Additionally, a dummy node is created to be the control (master) node of MPC in ABAQUS. The general form of multi-point constraint is written as

$$A_1 u_1 + A_2 u_2 + A_3 u_3 + A_4 u_4 - u_0 = 0 \tag{5.22}$$

where the displacements u_1, u_2. u_3 and u_4 correspond to P_{11}, P_{22}, P_{33} and P_{12}, respectively. By applying an external force P_0 to the master node, constraint forces, e.g. F_{11}, F_{22}, F_{33}, and F_{12}, are generated at all the slave degrees of freedom, as shown in Fig. 5.3(a). These constraint forces are proportional to their respective coefficients. A full derivation of the proportion relationships among constraint forces is given in Appendix A. The coefficients of the MPC equation follow the proportions as

$$A_1 : A_2 : A_3 : A_4 = (\rho_1 - \rho_2 \frac{U_T}{D_2}) \frac{D_2}{D_1} : 1 : \rho_3 \frac{D_2}{D_3} : \rho_2 \tag{5.23}$$

In fact, the coefficients are the functions of current displacements and the MPC applied to the unit cell is not a real linear-constraint for which the coefficients must be constant. Nevertheless, the coefficients are updated at the beginning of each analysis

increment using the displacements at the end of previous increment and remains constant throughout the current increment for approximation. A subroutine *URDFIL that can read the results file during the analysis is introduced and transfers data to the subroutine *MPC via another subroutine *UEXTERNALDB. In this case, the increment size is expected to be small enough to achieve sufficient accuracy. After a process of trial and error, a 0.5% of total analysis time was chosen to be the maximum increment size, and the outcomes of stress states, i.e. triaxiality and Lode parameter, deviated from the targeted values within 0.5%.

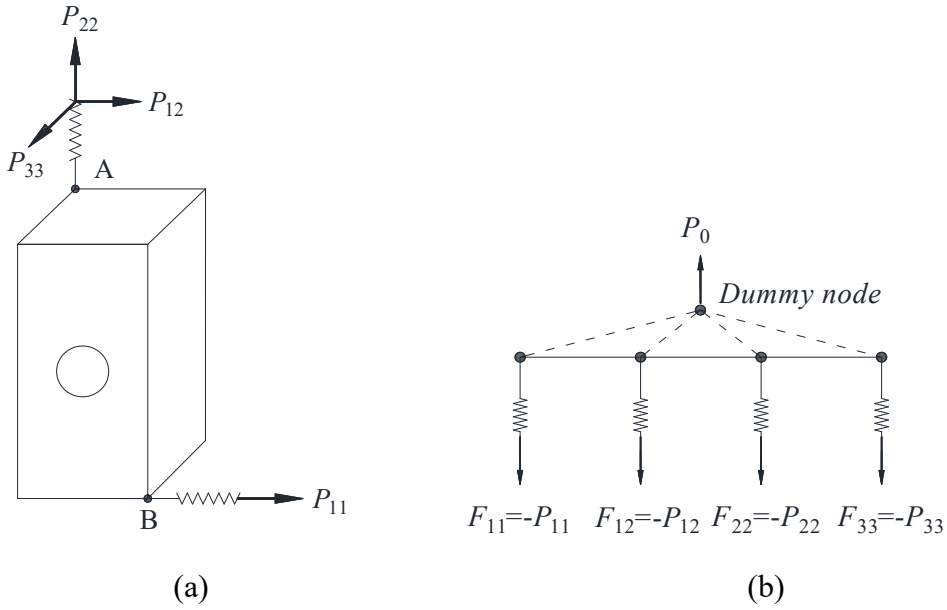

Fig. 5.3 (a) Generalized forces applied to the unit cell; (b) Multi-points constraint to achieve the target loading.

5.2.4 Material model

The matrix material is assumed to be elastic–plastic with isotropic hardening and

is modeled by a finite strain J_2 flow criterion. The power-law rule is employed to represent the hardening property of the material

$$\sigma_y = \sigma_0 (1 + \frac{E\varepsilon_p}{\sigma_0})^n \tag{5.24}$$

where σ_y, σ_0, E, ε_p, n is the current yield stress, initial yield stress, Young's modulus, plastic strain, and strain hardening exponent, respectively. Values of σ_0=400 Mpa, n=0.1 and E/σ_0=300 are used in the present study.

5.3 RESULTS

5.3.1 Effects of stress states on the response of voided cell

For axisymmetric stress cases, where the stress states are the triaxial loading cases and ρ_2=0, the values of ρ_1 and ρ_3 can be determined by the given triaxiality η and Lode parameter L. The deformation pattern is axisymmetric as well. This limits the void evolution to a narrow field. To have a more general understanding of the void evolution mechanism, the in-plane shear stress component is introduced. Due to the existence of shear stress Σ_{12}, there are infinite stress states as well as ρ_1, ρ_2, ρ_3 values to satisfy the given triaxiality and Lode parameter. Among the varieties of combined shear and normal stress cases, those with ρ_2=0, 0.2, 0.4, 0.75 will be covered in this section to study the effect of shear stress on the unit cell response, and the void growth and coalescence behavior.

The cases for triaxiality η=1 and Lode Parameter L=0.5 are first studied and the results of axial stress response as well as void volumetric evolution are plotted in Fig. 5.4. Increasing ρ_2 decreases the load carrying capacity as well as the ductility of the unit cell. The axisymmetric case, where ρ_2=0, with the greatest load carrying capacity and ductility gives rise to a conservative response of the unit cell. The load carrying capacity drops more

significantly for the cases with smaller ρ_2. No sudden drop in load carrying capacity can be clearly observed for the cases with ρ_2=0.4 and ρ_2=0.75. The macroscopic effective strain vs. stress response can be related to the void growth and coalescence. The differences of loading response among various stress cases are owing to the variation of normal and tangent behavior of the cell and different void growth processes. A smaller loading capacity is associated with a faster void growth. As can be observed in Fig. 5.4(b), the void growth rates are larger for the cases with greater ρ_2, and the case for ρ_2=0.75 has extremely high growth rate at the beginning of the void growth stage. For instance, the ratio of current porosity to initial porosity for ρ_2=0.75 is about triple of the axisymmetric case at E_e=0.1. It is clear that the void growth rate depends not only on the triaxiality and Lode parameter, but also on the stress states. Different void growth evolutions result in different inceptions of void coalescence with respect to macroscopic effective strain, which are described in Fig. 5.5. The definition of the onset of void coalescence as well as the corresponding effective strain E_e^c will be given in the following section. Fig. 5.5 shows that E_e^c increases for a decreasing ρ_2 value. A similar trend is seen for cases with different Lode parameter L=-1, -0.75, -0.5, -0.25,0, 0.25, 0.5, 0.75, 1. However, the effect of ρ_2 decreases as the Lode parameter increases. This indicates that E_e^c for the axisymmetric case is the upper limit for the unit cell subjected to various stress states with a given triaxiality and Lode parameter.

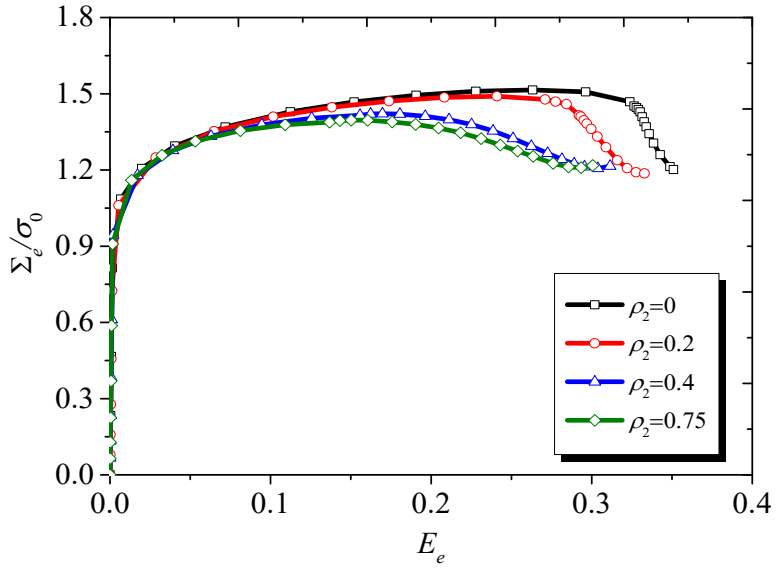

(a)

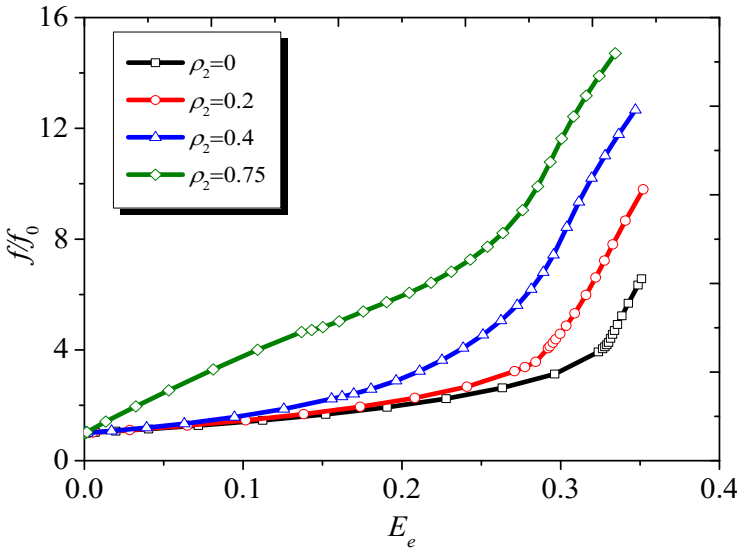

(b)

Fig. 5.4 η=1, L=0.5 with ρ_2=0, 0.2, 0.4, 0.75: (a) Macroscopic effective strain vs. stress; (b) the ratio of current porosity to initial porosity vs. macroscopic effective strain.

Comparison between the axisymmetric and shear coupled stress cases under η=1 and L=0.5 was performed to illustrate the effect of shear stress in detail, and the results are shown in Fig. 5.6. For the axisymmetric case, i.e. ρ_2=0, the localized plastic deformation within the ligament separating two voids is the most common mode of strain localization in the unit cell. With the existence of shear stress, another mode of localized deformation caused by shear appears prominently at the early stage of void growth. For a given value of ρ_2, e.g. 0.2, larger triaxialities give rise to greater Σ_{12}/Σ_e and lower shear localization strains with more open shaped boundaries of the cell, which is consistent with the finding by Barsoum and Faleskog (2011).

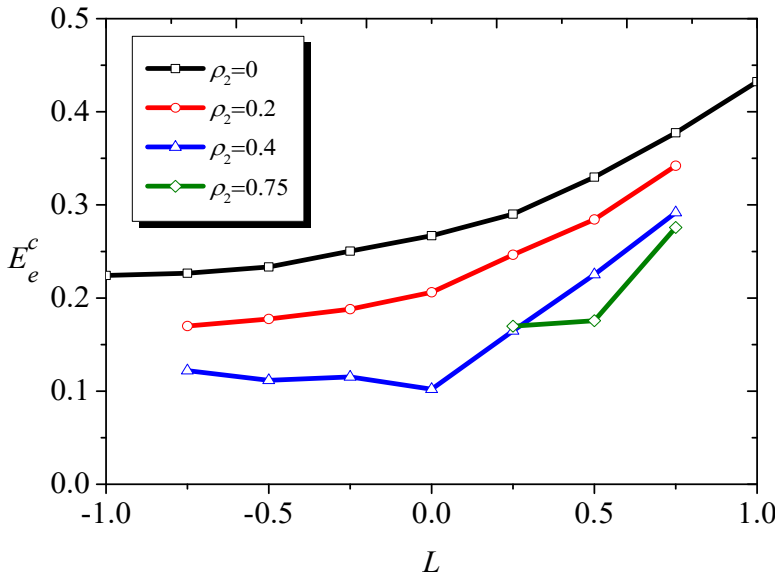

Fig. 5.5 Macroscopic effective strain at the onset of void coalescence for η=1 and L=-1, -0.75, -0.5, -0.25, 0, 0.25, 0.5, 0.75, 1 with ρ_2=0, 0.2, 0.4, 0.75.

The internal necking is believed to be the void coalescence mechanism for this case. In this mode of coalescence, the necking region is involving the ligament between the void

and the outer bound shrinks. The plane in which the necking occurs is perpendicular to the main loading axis. It is observed to be horizontal for the axisymmetric case and inclined from the horizontal plane with a small angle for the combined shear and normal stress case. The relative void spacing parameter χ_1 is defined herein as the ratio of the current smallest space between neighboring voids to the current width of the unit cell. As shown in Fig. 5.6(a), by adding a shear component, the rate of change of the relative spacing ratio χ_1 becomes greater. Both the strain localization due to shear stress and the rotation of the void contribute to a more rapidly increasing χ_1. Similar to the effective stress, the axial stress for the axisymmetric case is greater than for the case with ρ_2=0.2. Per Thomason's coalescence criterion (Thomason, 1985), the main axial stress Σ_{22} directly affects the void coalescence condition. The stress reaches a critical value and this critical value decreases as the void becomes more open and the voids get closer to each other (χ_1 increases). The of sudden decrease in stress corresponds to a rapid increase χ_1 rapid, at which the onset of void coalescence is observed. These two cases presenting different coalescence behaviors is due to the shear stress that affects the axial stress, the χ_1 and W values. One effect of the shear stress on void coalescence at high and intermediate triaxialities is that it makes the void rotate and stretch, leading to a highly-distorted void. As observed in Fig. 5.6(b), compared to the axisymmetric case, even with a smaller axial stress Σ_{22}, the case with ρ_2=0.2 has sufficient W value to compensate for the reduction in axial stress. By affecting the porosity, the relative spacing ratio and the void rotation, the additional shear stress advances the void growth and the initiation of coalescence.

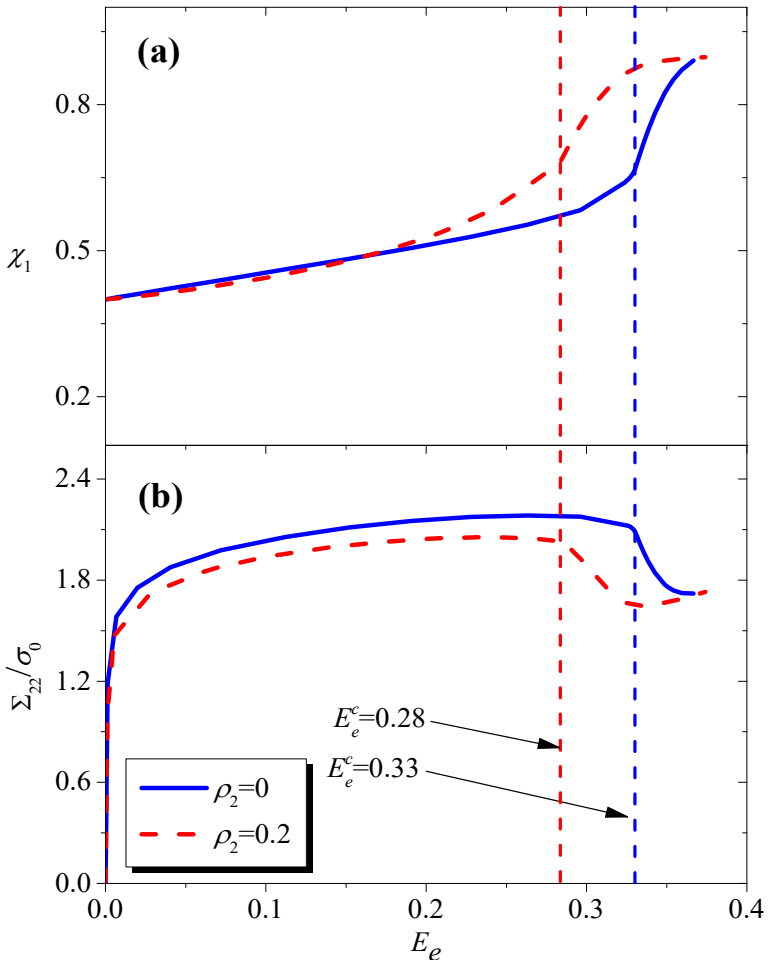

Fig. 5.6 Illustration of void growth and cell response for η=1 and L=0.5: (a) the ligament size ratio χ_1 vs. macroscopic strain; (b) axial stress vs. macroscopic strain.

5.3.2 Effects of triaxiality and Lode parameter on void growth and coalescence

The aim of this section is to investigate the effects of triaxiality and Lode parameter on void growth and coalescence. The combined influence of these two factors and shear stress will also be examined. As such, a constant ρ_2=0.2 is chosen to be the shear stress parameter for comparison with the axisymmetric loading case. Different values of triaxiality and Lode parameter, including η=0.25, 0.5, 0.75, 1, 1.25, 1.5, 1.75, 2 and L=-1,

-0.75, -0.5, -0.25, 0, 0.25, 0.5, 0.75, 1, are considered.

Fig. 5.7 shows the variations of the ratio of axial stress to the current effective stress, the relative spacing ratio, and the relative porosity for cases with ρ_2=0 and ρ_2=0.2. The main axial stress Σ_{22} is found to have a strong effect on void growth as well as on the strain localization process. As can be seen in Fig. 5.7(a), the ratio of axial stress Σ_{22} to Σ_e increases with triaxiality for both the axisymmetric and shear coupled cases. However, the shear stress leads to a decrease of the axial stress ratio at a given triaxiality, and the influence of shear stress on axial stress ratio is more prominent at high triaxiality than at low triaxiality. The rate of change of the relative spacing ratio increases with triaxiality, as shown in Fig. 5.7(b). Also, the effect of shear stress on the relative spacing ratio varies with triaxiality. For the cases with η=1.75 and L=0, the rate of change of the relative spacing ratio for ρ_2=0.2 is greater than that for ρ_2=0 at the early period of void growth. However, things are different for η=1 and 0.25, where the relative spacing ratio for ρ_2=0.2 is smaller than for ρ_2=0. At high triaxialities, the axial stress is dominant in determining the relative spacing ratio and a higher ratio of axial stress to effective stress is related to a greater change rate of χ_1. At intermediate and low triaxialities, shear stress induced uniform and non-uniform shear deformation as well as void rotation have a stronger influence on χ_1. Furthermore, the effect of the shear stress that shrinks the major axis and elongates the minor axis of void makes a significant variation between ρ_2=0.2 and ρ_2=0 at η=0.25.

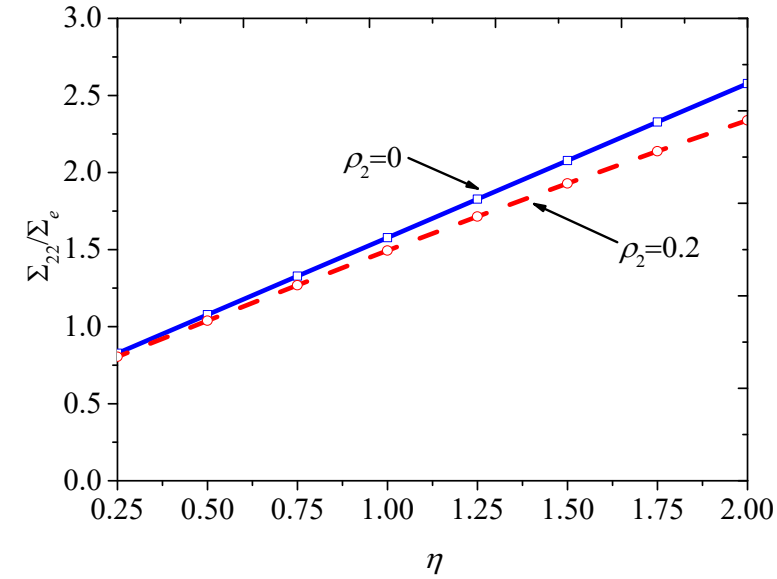

(a)

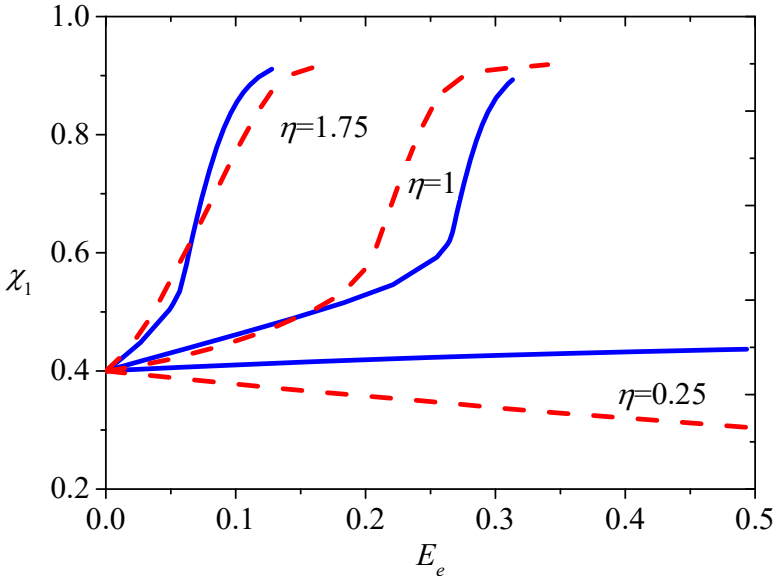

(b)

Fig. 5.7 Effects of triaxiality on void growth for L=0 and ρ_2=0 (blue), 0.2 (red): (a) axial stress vs. triaxiality; (b) the ligament size ratio vs. macroscopic strain; (c) porosity vs. macroscopic strain.

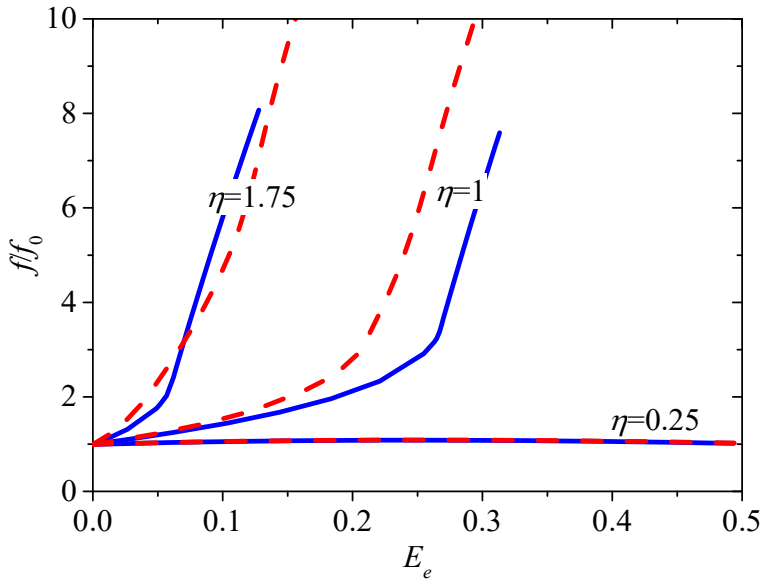

(c)

Fig. 5.7, cont.

As shown in Fig. 5.7(c), the void grows faster as triaxiality increases at the early period of void growth for η=1.75 and 1. In addition, the sudden change of porosity appears earlier for ρ_2=0.2 than in the axisymmetric case. Adding a shear stress component promotes void growth before the onset of void coalescence, while it has no effect on benefit to the change rate of void volume after the onset of void coalescence. Owing to the additional shear stress, the primary reason for the promotion of void growth at high and intermediate triaxialities is that the ratio of axial stress to effective stress increases. Comparing cases for η=1.75 and η=1 demonstrates the consistency of the results in the present study with previous investigations (Kim et al., 2004; Gao et al., 2005) that void growth rate decreases with triaxiality. Furthermore, the porosity at which it suddenly increases becomes smaller as triaxiality increases. It is worth noting that the porosity for η=0.25 keeps constant during the loading history for both ρ_2=0 and 0.2. The slight variation in Σ_{22}/Σ_e between cases for

ρ_2=0 and ρ_2=0.2 closely relates to the small difference in void growth rate. The change rates of porosity and relative spacing ratio indicate that void growth stops for η=0.25, which delays void coalescence.

To illustrate the effect of Lode parameter on the void growth and subsequent coalescence, three different Lode parameters L= -0.5, 0, 0.5 and a constant stress triaxiality η=1 are considered, and the results of axial stress ratio variation, relative spacing ratio as well as porosity are shown in Fig. 5.8. As shown in Fig. 5.8(a), Σ_{22}/Σ_e decreases as Lode parameter increases from -0.75 to 0.75 for both ρ_2=0.2 and ρ_2=0. For all six cases with different Lode parameters and ρ_2, the variations in the plots of relative spacing ratio in Fig. 5.8(b) have little difference before the onset of void coalescence. The sudden change in χ_1 appears earlier with decreasing Lode parameter for the axisymmetric cases. No such rapid increase of χ_1 is seen for the cases with ρ_2=0.2 as for the axisymmetric cases. The influence of Lode parameter on the void growth is shown in Fig. 5.8(c). Among each of the three values for Lode parameter with the same ρ_2 value, little variation can be observed from the porosity evolution curves at the beginning of the loading history. This indicates that Lode parameter has limited effect on the early period of porosity change. It is clear than under the same triaxiality and ρ_2 value, the sudden increase of porosity occurs earlier for the case with lower Lode parameter than with higher Lode parameter. The effective strains at the point where porosity rapidly increases between two cases with the same Lode parameter decreases as Lode parameter increases. This demonstrates that the effect of shear stress on void coalescence also varies with the Lode parameter. The rate of change of porosity with macroscopic strain in the latter portions of the curves in Fig. 5.8(c) quite similar among cases with different Lode parameters. Compared with triaxiality that influences the void porosity evolution in the entire stage of void growth, Lode parameter has a more significant

effect on the effective strain at the onset of void coalescence.

Fig. 5.9(a) shows the critical effective strain at the onset of void coalescence for the unit cell subjected to the same Lode parameter L=0, but different triaxialities η=0.75, 1, 1.25, 1.5, 1.75 and for cases where ρ_2=0 and 0.2. In Fig. 5.9(a), E_e^c increases with decreasing η. There is no void coalescence preceded by void dilation at triaxialities lower than 0.75. The change rate of critical strain is more significant at lower triaxialities than at higher triaxialities. Adding a shear stress component lowers the critical effective strain for various triaxialities. Fig. 5.9(b) shows the critical effective strain variations as a function of Lode parameter for an intermediate stress triaxiality level η=1 and a high triaxiality level η=2. E_e^c increases with L and reaches a maximum value when L=1. The change rate of critical effective strain is more significant as Lode parameter approaches 1.

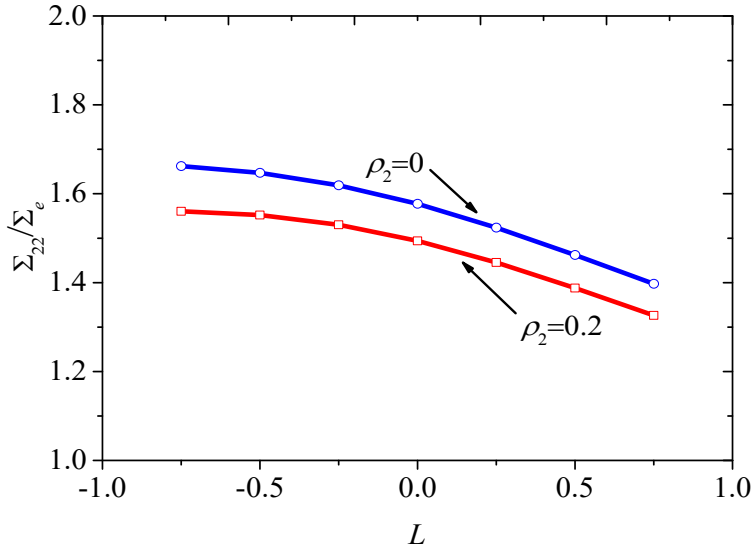

(a)

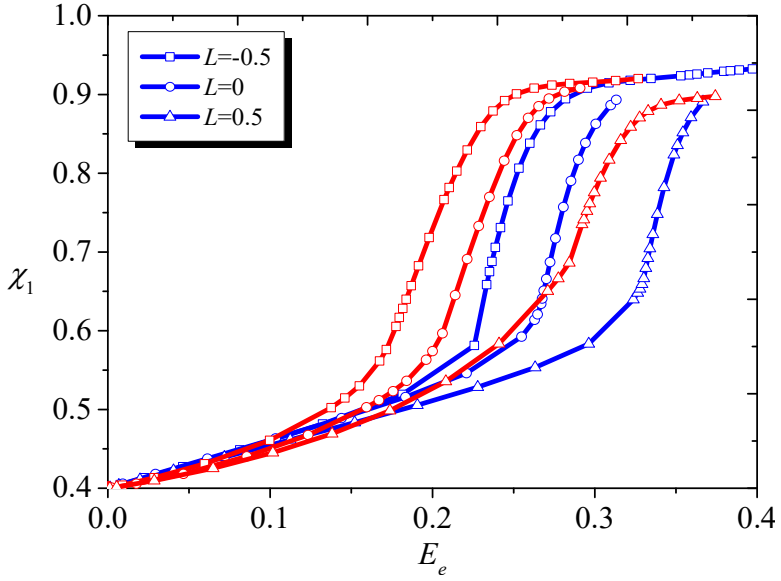

(b)

Fig. 5.8 Effects of Lode parameter on the void growth for η=1: (a) axial stress vs. triaxiality for ρ_2=0 (blue), 0.2 (red); (b) the ligament size ratio vs. macroscopic strain; (c) porosity vs. macroscopic strain.

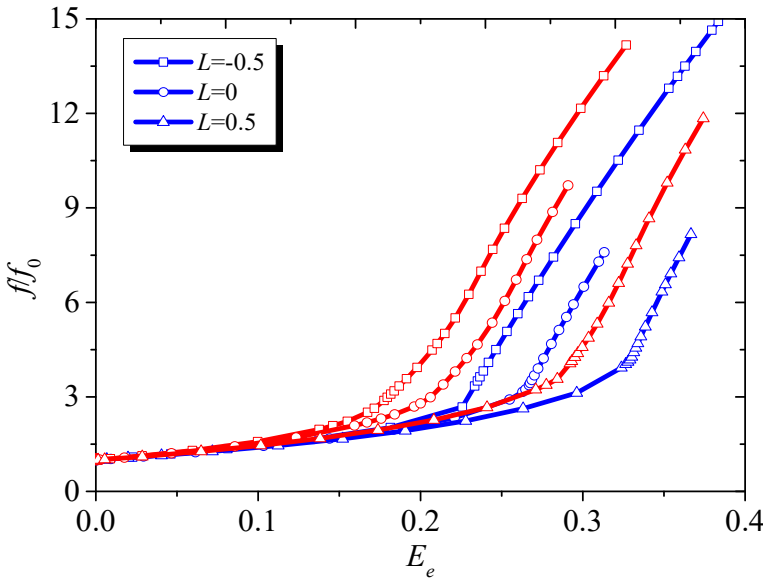

(c)

Fig. 5.8, cont.

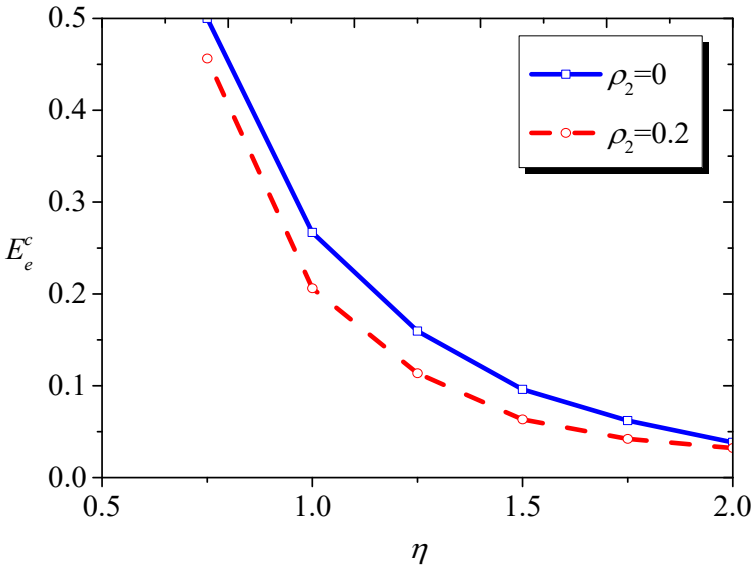

(a)

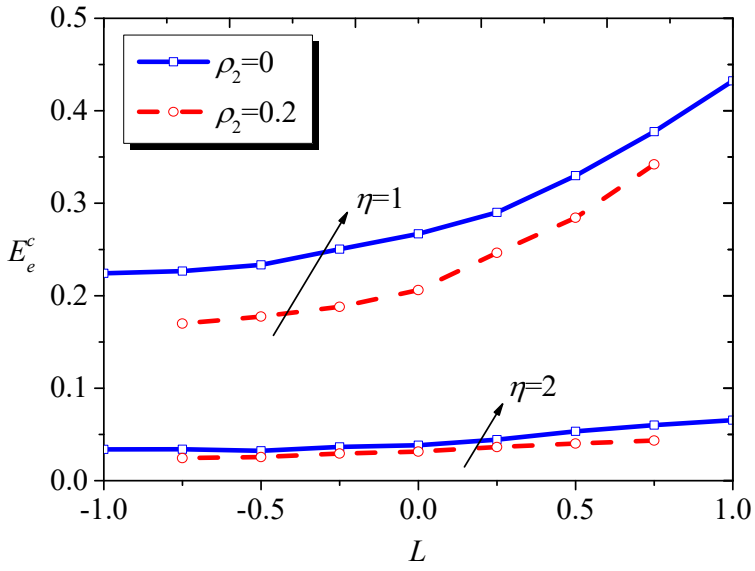

(b)

Fig. 5.9 Influence of triaxiality and Lode parameter on the critical effective strain at the onset of void coalescence: (a) η=0.75, 1, 1.25, 1.5, 1.75, 2 and L=0; (b) η=1, 2 and L=-1, -0.75, -0.5, -0.25, 0, 0.25, 0.5, 0.75, 1.

5.3.3 Void coalescence mechanisms at high and intermediate triaxialities

As the last stage of void evolution, void coalescence serves as the precursor to the initiation of ductile fracture. The onset of void coalescence can be treated as a practical indicator of final material failure for engineering purposes since very limited macroscopic strain can be further imposed on the material, which loses load carrying capacity rapidly. Although ductile fracture has been widely studied for many years, void coalescence has not seen as much attention as the void growth process. As the bridge between microscopic void growth and macroscopic crack formation, void coalescence plays an important role in the entire void evolution and material failure process. Void coalescence can be treated as the continuation of void growth and determines the failure modes. Void coalescence depends strongly on factors such as porosity, void shape, void spacing, stress triaxiality, Lode parameter, stress state, strain hardening and so on. In this section, the effects of triaxiality, Lode parameter as well as shear stress component will be examined. Though the effect of initial void shape is not considered, the void shape evolution under various stress states that influence void coalescence behavior will be discussed.

The mechanisms of void coalescence at high and intermediate triaxialities will be first discussed. As mentioned above, the void volume fraction grows rapidly at high and intermediate triaxiality levels and is followed by a significant reduction in intervoid ligament areas. As void growth continues, macroscopic effective stress reaches a maximum value when the reduction in ligament area is sufficient to overcome the strain-hardening of the matrix material. Further void growth results in a smooth drop of macroscopic effective stress, which is often followed by a sudden decrease of effective stress. and the corresponding E_c at that instant is defined as the macroscopic effective strain E_e^c at the onset of void coalescence. To illustrate the response of the unit cell at the onset of void

coalescence, the axisymmetric case with η=2 and L=0.5 is considered. The deformation gradient history as well as the relative spacing ratio versus macroscopic effective strain are given in Fig. 5.10. As shown in Fig. 5.10(a), the deformation gradient components in all three directions gradually vary with effective strain at the beginning of the loading history. As macroscopic effective strain reaches E_e^c, X_1 and X_3 components of the deformation gradient stop changing and the X_2 component, which coincides with the main loading axis, increases more dramatically. This indicates the deformation mode shifts from a triaxial straining mode to a uniaxial one at the onset of void coalescence, which corresponds to the transition from a uniform pattern to flow localization in the ligament between adjacent voids. In Fig. 5.10(b) the relative spacing ratio rapidly increases at the onset of void coalescence. The relative spacing ratio curves at X_1 and X_2 directions coincide with each other during the entire course of the loading history and implies that the flow localization occurs in both directions. The localization caused by internal necking of the intervoid ligament occurs in the plane perpendicular to the main loading axis.

Another example to illustrate the effect of shear stress on the void coalescence mechanisms will be considered by introducing the shear stress component while keeping triaxiality as η=2 and Lode parameter as L=0.5. As additional shear deformation is imposed to the cell, the deformation is characterized as a combination of asymmetric and anti-symmetric modes. The resulting localization is in a shear mode or in a combination of symmetric and shear modes depending on the stress state. For the present case with η=2 and L=0.5, the shear localized deformation arises before the localization caused by internal necking. Prior to the onset of void coalescence, shear localization occurs as a shear band across the void. The deformation gradient is homogeneous outside the band and varies with position across the band. The parameter $q_1 / \bar{F}_{12}$ in Fig. 5.11(a), covering the range of 0 and

1, reveals the degree of non-uniform deformation gradient across the band. The parameter equals to 0 represents the case where there is no shear localized deformation whereas when it is equal to 1, all the shear deformation applied to the cell is localized into the shear band and there is no uniform shear deformation outside the shear band. Besides for η=2, the parameters for η=1.25 and 0.75 are also plotted in Fig. 5.11(a) for comparison. For these three cases with a certain Lode parameter and ρ_2 value, shear localization is more prominent at higher triaxiality. The parameter $q_1 / \bar{F}_{12}$ increases before the onset of void coalescence. As the void grows, internal necking dominated localization develops and leads to the onset of void coalescence inside the shear band. The onset of void coalescence coincides with a sudden growth of the parameter $q_1 / \bar{F}_{12}$, which is marked in Fig. 5.11(a). The onset of void coalescence is also shown in the plots of the deformation gradient curves in Fig. 5.11(b), which refer to the deformation gradients of the case with ρ_2=0.2. As can be seen in Fig. 5.11(b), the deformation gradient of the X_1 component stops while that of the X_3 component is unstable with a small fluctuation after the onset of void coalescence (U_2 drastically increases and is not included in the plot). Hence, due to the shear deformation, the localization in the present case can also be characterized as an axial mode, which is distinguished from the uniaxial mode for the axisymmetric stress case. Moreover, owing to shear stress, the localization plane at the onset of void coalescence is no longer perpendicular to the X_2 direction as it is for the axisymmetric stress cases. Given the critical strain, the localization plane with a certain inclination with respect to the X_1 direction is where void coalescence begins. Fig. 5.11(c) depicts the orientations of localization planes as well as the void shapes for cases of ρ_2=0, 0.1, 0.2, 0.3. The inclination angle of the plane increases with ρ_2. Relating to the critical strain, the increasing inclination angle is associated with decreasing effective strain at the onset of void coalescence. This again

demonstrates the effect of shear stress on void coalescence. The contribution of shear localization on material failure can be evaluated by the localization indicator k_η shown in Fig. 5.11(d). Prior to the onset of void coalescence, the localization indicator increases for all three cases and never reaches the criterion of k_η=10, at which the shear band localizes into a narrow planar band that results in a drop of load carrying capacity. The rapidly growing k_η is interrupted by the void coalescence at about k_η=2 for η=2, k_η=1.8 for η=1.25 and k_η=1.2 for η=0.75. Therefore, internal necking rather than shear localization induces strain softening for three cases. Though the shear localization influences both the orientation of the localization plane and the critical strain significantly, the mechanisms of void coalescence for the cases investigated herein are dominated by internal necking.

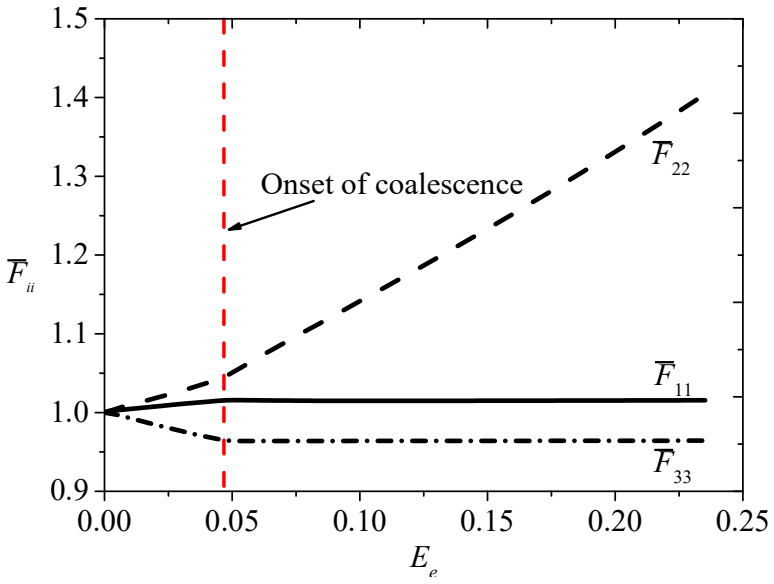

(a)

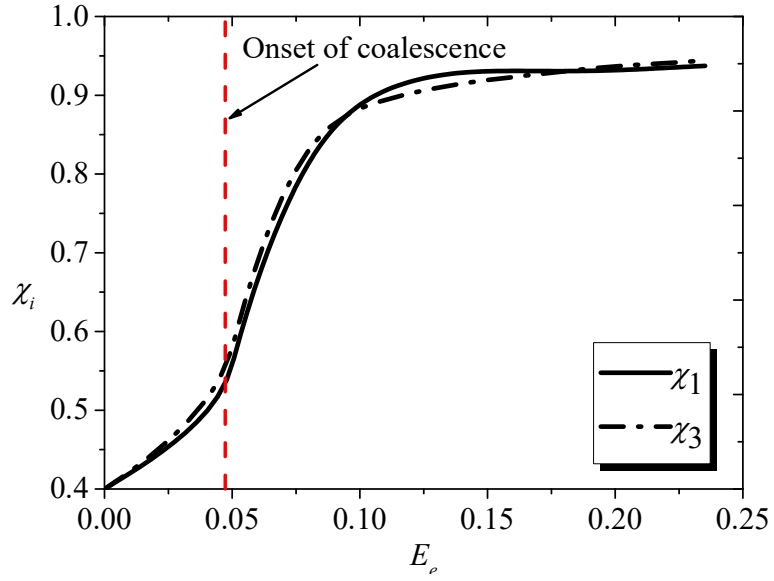

(b)

Fig. 5.10 Illustration of void coalescence for η=2, L=0.5 and ρ_2=0: (a) deformation gradient evolution; (b) relative spacing ratio vs. macroscopic effective strain.

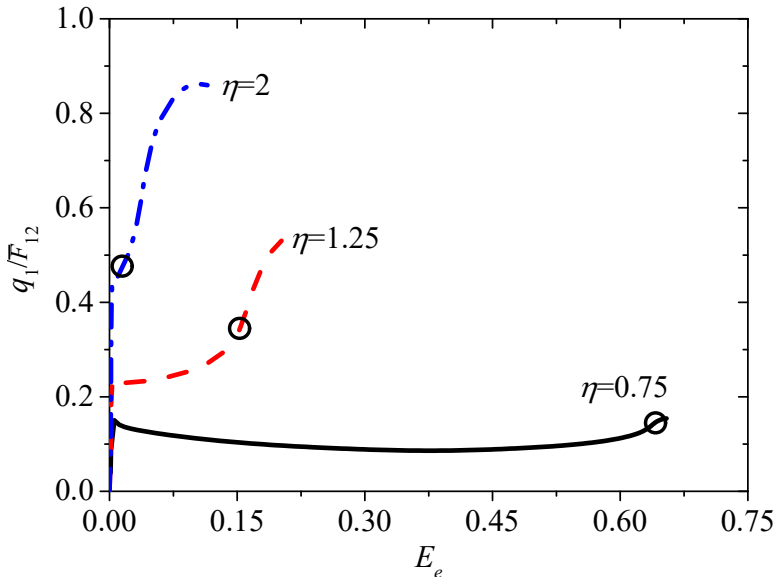

(a)

Fig. 5.11 Illustration of shear stress effect on the void coalescence for L=0.5: (a) Comparison of parameter $q_1 / \bar{F}_{12}$ for ρ_2=0.2 and various η=0.75, 1.25, 2; (b) Deformation gradients for η=2; (c) Void shapes and band orientations at the onset of void coalescence for η=2 and ρ_2=0, 0.1, 0.2, 0.3; (d) Comparison of parameter k_η for ρ_2=0.2 and various η=0.75, 1.25, 2. The black circle indicates the onset of void coalescence.

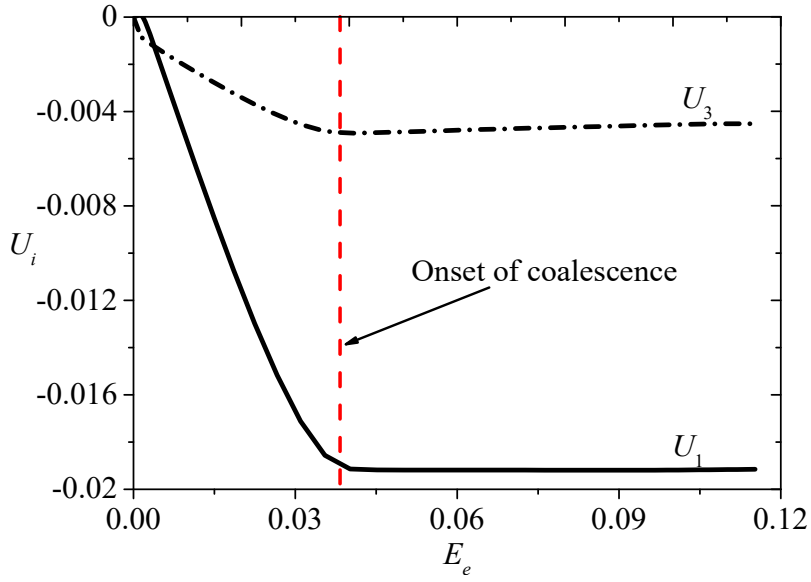

(b)

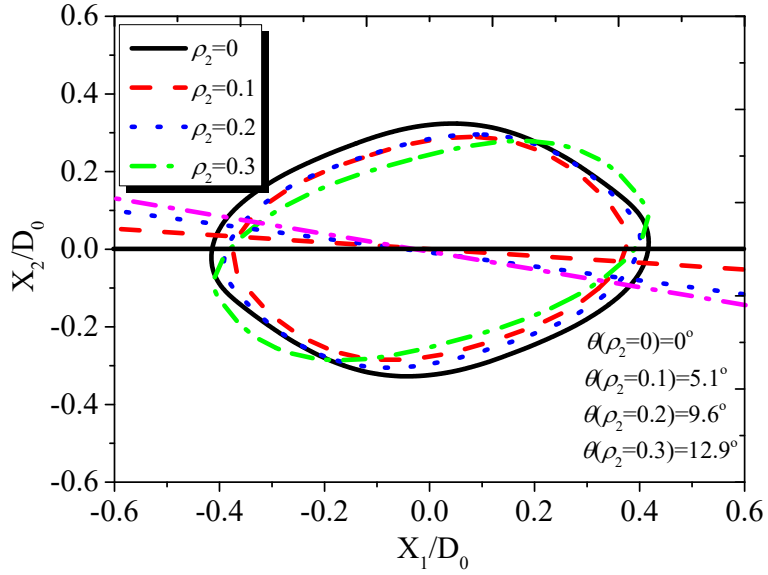

(c)

Fig. 5.11, cont.

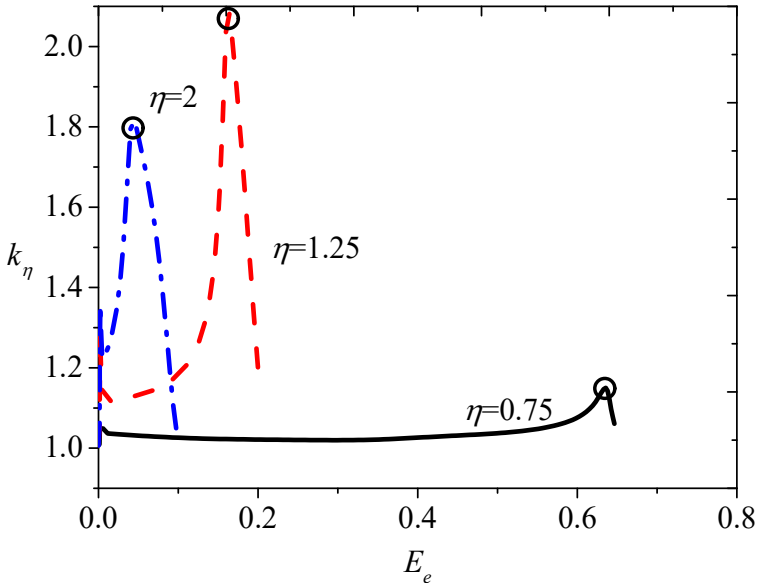

(d)

Fig. 5.11, cont.

5.3.4 Void coalescence mechanisms at low triaxialities

As discussed above, internal necking caused by void growth leads to void coalescence and subsequent material failure at high and intermediate triaxialities. The evolutions of void volumetric fraction for the axisymmetric cases with L=0.5 and various triaxialities η=0, 0.25, 0.5, 0.75 are shown in Fig. 5.12. At triaxiality η=0.75, the void grows large enough and the onset of void coalescence occurs at E_e=0.63. The void volumetric fraction remains for η=0.5 and decreases for both η=0.25 and 0. At low triaxialities, the delayed void growth does not contribute to the void coalescence process, and this leads to a mechanism quite different from that at high and intermediate triaxialities. To illustrate the void coalescence behavior at low triaxiality, the axisymmetric cases for η=0 and various L=-1, -0.5, 0, 0.5, 1 are first considered. At such low triaxiality as η=0,

the X_1 axis of the void elongates while the X_2 axis shortens under continuous loading and the void subsequently flattens and collapses into a penny-like shape. On the other hand, large plastic straining occurs along the rim of the voids. As shown in Fig. 5.13, the maximum plastic strain appears on the void surface for cases with various Lode parameters. For the cases with $L \leq 0$ shown in Fig. 5.13(a)-(c), X-shaped narrow zones with highly concentrated plastic strain form across the void. Subsequent deformation will be strongly localized into the narrow region, i.e. shear band. At a given triaxiality, the orientation and shape of the shear band varies during the course of deformation and are depending on Lode parameter. Even though a bifurcation into a shear band was not observed in this study, introducing an initial imperfection would trigger the shear band instability. Further non-uniform deformation following the shear band makes the ligaments between neighbor microcracks thinner and facilitates the interaction between microvoids that results in final void coalescence. Different from the internal necking mechanism at high and intermediate triaxialities, the coalescence mechanism herein is characterized as shearing-type coalescence mechanism. However, highly-concentrated plastic strain only occurs surrounding the voids for cases with Lode parameter greater than 0 (Fig. 5.13(d)-(e)). No such localized strain region is observed in the cases with $L > 0$. The mechanisms of neighboring void interaction for these cases and further void coalescence as well as failure modes are not clear and need further investigation.

Even for the axisymmetric stress cases without shear stress component, the void coalescence mechanism at low triaxialities is dominated by shearing. Nevertheless, the effect of shear stress on the shearing mechanism can be promoted by adding a shear stress component to the unit cell. The primary effects of shear stress on the void coalescence process are on the void rotation, elongation, and the shear band orientation. The effect on

the shear band orientation can be observed from the cases for η=0 and L=-0.5 with ρ_2=0.2, 0.4 and 0.6, shown in Fig. 5.14. For the cases with small shear stress components, there is no non-uniform shear deformation across the void at the early stages of the loading history. At the same macroscopic effective strain E_e=0.5, the X-shaped high strain concentration zone rotates along with the void and the rotational angle increases with ρ_2. The X-shaped region is no longer axisymmetric and variation of strain concentration between two bands is more distinct as ρ_2 increases. The effective strain at which the void collapses into a micro-crack becomes smaller as ρ_2 increases at a given triaxiality and Lode parameter.

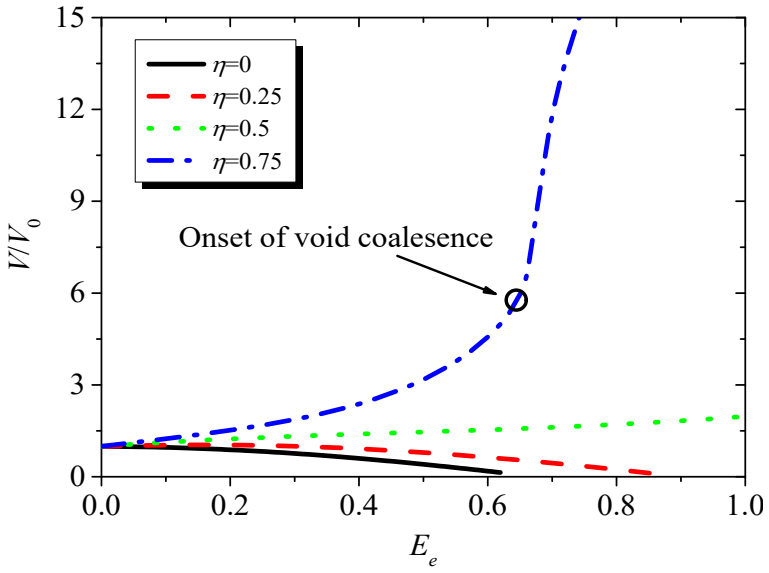

Fig. 5.12 The void volumetric fraction for L=0.5, ρ_2=0 and various η=0, 0.25, 0.5, 0.75.

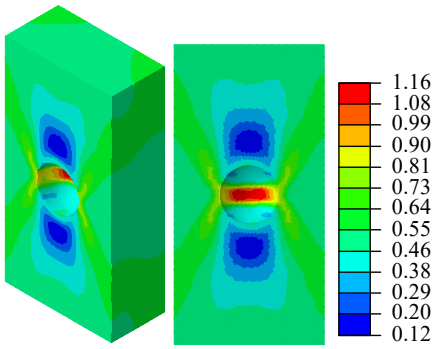

(a)

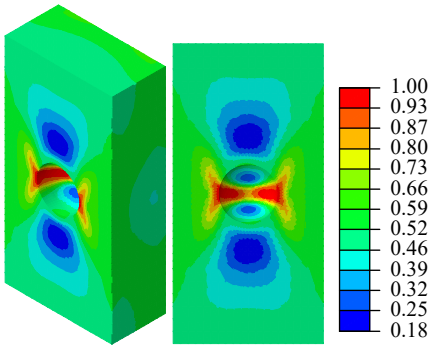

(b)

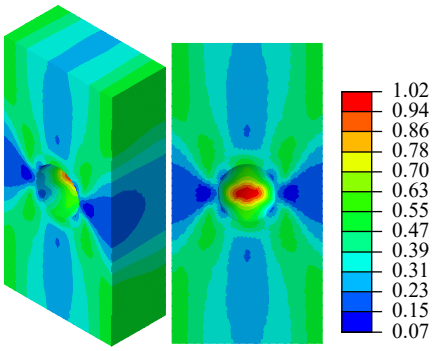

(c)

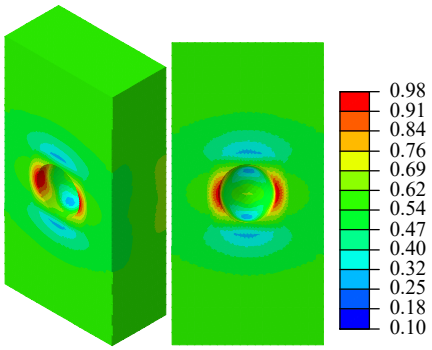

(d)

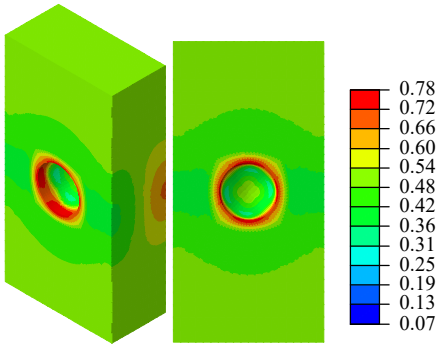

(e)

Fig. 5.13 Equivalent plastic strain distribution at E_e=0.5 in the current deformed configuration for η=0, ρ_2=0 and (a) L=-1; (b) L=-0.5; (c) L=0; (d) L=0.5; (e) L=1.

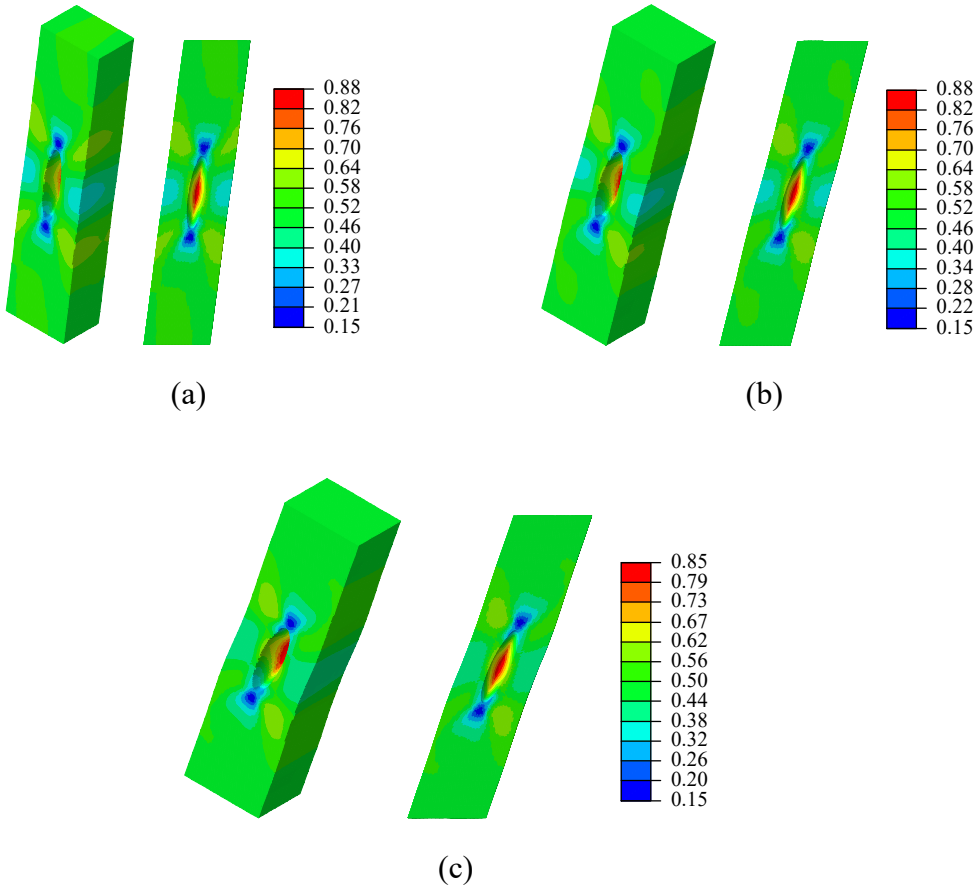

Fig. 5.14 Equivalent plastic strain distribution at E_e=0.5 in the current deformed configuration for η=0, L=-0.5: (a) ρ_2=0.2; (b) ρ_2=0.4; (c) ρ_2=0.6.

Herein, a special case, i.e. the simple shear case, is studied to investigate the unit cell subjected to intense shearing. As shown in Fig. 5.15, the plastic strain for the simple shear case is highly localized at an almost horizontal band across the void. Before the onset of strain softening, the void has collapsed into a microcrack and the ligaments between neighboring microcracks are thick enough to be visible. After the onset of strain softening, the ligaments are thinner, indicating a higher strain localization. Very high strain is concentrated on the side that the void-tip rotates towards. In contrast, strain on the other

side remains small from the beginning of the loading history to the occurrence of failure. The material response in Fig. 5.16(a) illustrates that the onset of strain softening is rapidly followed by the occurrence of the onset of material failure. The non-uniform deformation gradient, shown in Fig. 5.16(b), remains at a low level before the onset of strain softening, and suddenly increases at the onset of strain softening. The same situation can be observed from the evolution of the localization indicator k_η, which is plotted in Fig. 5.16(c). To quantify the shear deformation, the shear angle ψ, defined by $\psi=\arctan(U_T/(2D_0+U_2))$, is introduced. Moreover, the orientation of the void is specified as the angle between the major axis of void and the X_1 axis, where the major axis is determined by linking two nodes on the void edge at X_1-X_2 plane with the largest distance, which is defined as R_1. The void orientation as a function of shear angle is plotted in Fig. 5.16(d). The direction of the void is linearly decreasing as the shear angle increases. At E_e=0.97, the void orientation is less than 10° and the void lays almost horizontally.

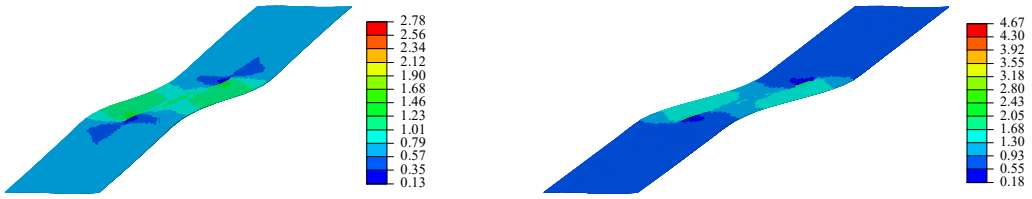

(a) (b)

Fig. 5.15 Equivalent plastic strain distribution in the current deformed configuration for simple shear case: (a) at E_e=0.68 before the onset the of strain softening; (b) at E_e=0.97 after the strain softening.

Whiles holding constant the triaxiality at η=0 and the Lode parameter at L=0, the pure shear case and the simple shear case show variations in void orientation, evolution of

void elongation and shear band orientation. The shear band for the pure shear case has an approximately 45° inclination angle with respect to the X_1 direction, which is different from the horizontal shear band for the simple shear case. Meanwhile, it is observed that the rate of deformation of the void axis R_1 for the simple shear case is greater than for the pure shear case, as shown in Fig. 5.17. The rate of void elongation for the simple shear case becomes even more rapid after the onset of strain softening. Factors such as the inclination of the shear band, the length of the void major axis and the orientation of the void strongly influence the ligament spacing and interaction between neighboring voids inside the shear band. Therefore, it is expected that both the strain to failure and the orientation of void coalescence for the simple shear and pure shear cases will be different.

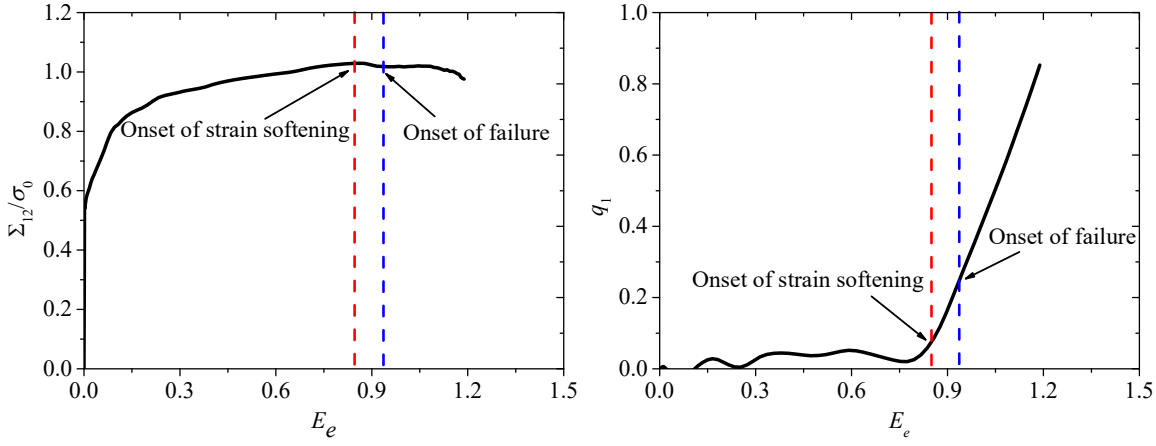

Fig. 5.16 Illustration of void coalescence by internal shearing in simple shear case: (a) Macroscopic effective stress; (b) the parameter q_1 vs. macroscopic effective strain E_e; (c) the parameter k_η vs. macroscopic effective strain E_e; (d) the void orientation θ vs. shear angle ψ.

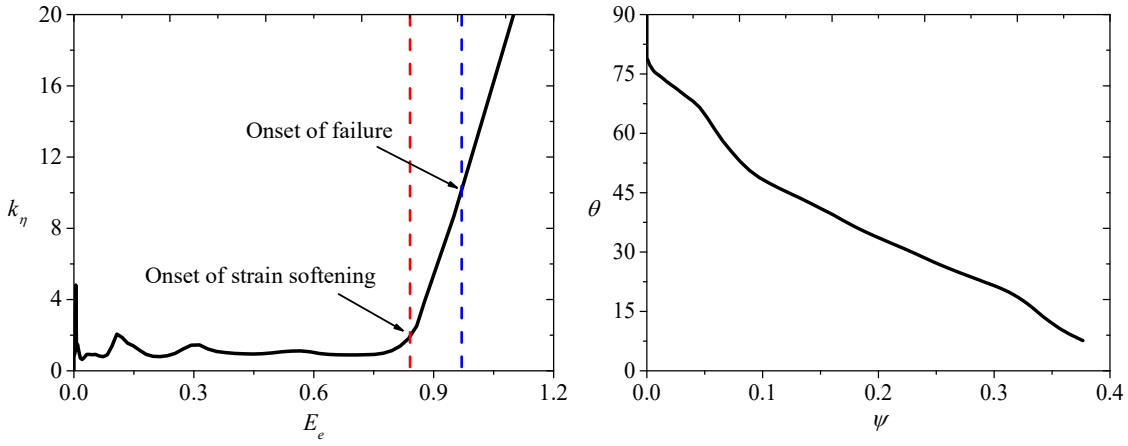

Fig. 5.16, cont.

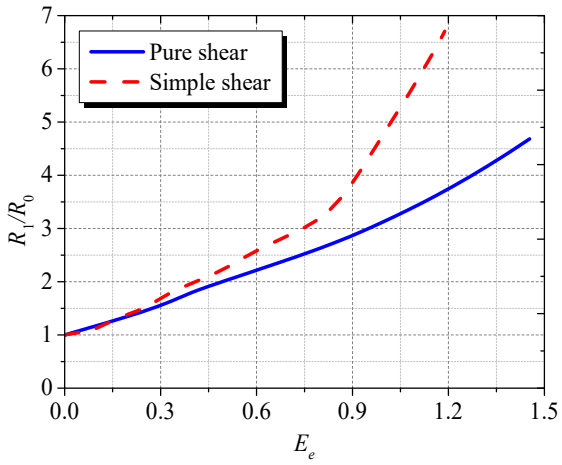

Fig. 5.17 Comparison of void elongations between simple shear and pure shear cases.

5.4 CONCLUSIONS

By adding the shear stress component to the triaxial stress states, the combined influences of stress triaxiality, Lode parameter and shear stress on the process of void growth and coalescence as well as on the macroscopic material response were investigated

in this chapter. For the combined normal and shear stress cases, various stress states with different stress ratios ρ_1, ρ_2 and ρ_3, can achieve the same stress triaxiality and Lode parameter. Thus, the additional shear stress component shifts the deformation mode of the unit cell from axisymmetric type to shearing type. The results show strong dependency of the voided cell behavior on both stress states and deformation modes.

For a given triaxiality and Lode parameter, an increasing shear stress ratio ρ_2 increases the ratio of the main normal stress to macroscopic effective stress, and is associated with a higher void growth rate. Due to the shearing effect, the rotation of the void and the shearing deformation of the unit cell decreases the distance between ligaments of neighboring microvoids. At high and intermediate triaxiality ranges, the greater void growth rate as well as the reduced ligament distance lead to an earlier loss of load carrying capacity and a smaller macroscopic effective strain at the onset of void coalescence. At low triaxiality, though the shear stress facilitates the process of void growth, void volume fraction remains small and is incapable of inducing internal necking dominated void coalescence. Important effects of shear stress at low triaxialities are that it leads to void rotation and accelerates the void flattening and elongation.

Void coalescence mechanisms are classified as internal-necking and shearing types based on the triaxiality. At high and intermediate triaxialities, the orientation of the localization band and the void shapes at the onset of void coalescence for combined normal and shear stresses cases are different from those for axisymmetric stress cases. Meanwhile, the onset of void coalescence is denoted by a shift in the cell deformation to a uniaxial mode for the axisymmetric case and to a biaxial mode for the shear coupled stress case. At low triaxialities, where shear bands develop, the shearing localization induces void coalescence. For the axisymmetric stress cases, the orientation of shear band is greatly

influenced by the Lode parameter. Comparison between simple shear and pure shear cases illustrates the effects of shear stress on the orientation of the shear band and void shape evolution. The shear stress contributes to void elongation and rotation and affects the interaction of neighboring voids and the subsequent shearing dominated void coalescence. Additionally, the orientation of the localization band coincides with the direction of maximum shear stress for these two cases. Further studies can explore the correlation between maximum shear stress and void coalescence behavior.

While this chapter concentrated on the singly spherical voided cell, other factors such as void initial shape and multi-population of voids would also affect the interaction of voids and the subsequent onset of void coalescence. Many popular void growth and coalescence models for the cases with high and intermediate triaxialities rarely take into account void rotation and shear induced localized deformation. Further modifications of such models to accurately capture shear effect are needed. Meanwhile, there is currently no simple model to predict the onset of the micro-crack, which is common at low triaxiality ranges. Further detailed studies of micro-crack based void coalescence are needed. Another significant issue that remains is the length effect on ductile material at such microscopic scales. Studies by Liu et al. (2003), Zhang et al. (2004), Zybell et al. (2014) have found the significant effects of material size on properties of strain localization as well as on void growth rate. A possible approach to addressing this issue would be modeling material behavior using strain gradient plasticity instead of classical plasticity theories and introducing adaptive remeshing technology to the finite element analysis. Careful treatments on the size-scale effects are required for the micromechanical modeling of void growth and coalescence.

CHAPTER 6

A One-Dimensional Nonlocal Model for Analysis of Post-Necking Behavior in Structural Metals

6.1 INTRODUCTION

Strain localization is a common phenomenon in a wide range of materials from soil and rock to concrete and metal alloys. The key feature of this occurrence is a rapid transition in either the displacement field or the strain field from a homogenous to a discontinuous pattern, followed by the occurrence of intense straining within a narrow region. Another consequence of strain localization is reflected in the mechanical behavior, wherein the global stress increases with strain up to a peak point and then decreases with increasing strain. The behaviors before and after the peak point are known as strain hardening and strain softening, respectively, and the latter results in a negative tangent modulus. Such a drop in loading capacity can be treated as a precursor of final material failure. Consequently, strain localization plays an important role in the mechanical behavior and engineering applications of many materials, including ductile metals.

A common example of strain localization in ductile metals is seen in a uniaxial tension testing. At a certain point in the loading history, there is a change from a uniform distribution of strain along the tensile specimen to a localized concentration of strain in a small region associated with the physical appearance of a neck. This necking type of instability is essentially the consequence of the competition between the deformation of the material and the level of the applied stress. Structural metals generally show continuous strain hardening where the rate of stress increase decreases with increasing strain. As a result of this reduced rate of strain hardening, it is possible that the incremental rate of the

applied load and the decreasing rate of cross-sectional area achieve balance at a point during the deformation history. Beyond this point, an arbitrary small imperfection can trigger localized deformation. Subsequent deformation is concentrated into the necked region until final fracture of the material.

A problem in mathematically describing the strain softening phenomenon in ductile metals is that the material stiffness matrix is no longer positive definite and the governing equation becomes ill-posed within the framework of classical (local) constitutive law, which has been confirmed by De Borst et al. (1993) and Bažant and Jirásek (2002). This leads to infinitely many solutions of the strain localization distribution and energy dissipation for a single case. Consequently, finite element simulations become intrinsically mesh sensitive, wherein the solution does not converge with increasing mesh refinement. Factors contributing to this mesh dependency include that the fact that the size of localization zone can become arbitrarily small and the load-displacement response beyond the peak point drops rapidly upon mesh refinement.

The motivation to study strain localization in ductile metals is its important effects on the strain softening behavior as well as on the ductile fracture and damage processes. As a special case of strain localization, necking in tensile testing gives rise to more complexity in determining the strain hardening properties of a ductile metal with respect to the true stress vs. strain curve, which is fundamental for the investigation of ductile fracture. Maintaining a well-posed boundary value problem after the onset of necking in a tensile test may not be possible by local continuum approaches. This mesh sensitivity problem is discussed by Mikkelsen (1997).

To remedy this problem exhibited in both analytical and numerical solutions, regularization treatment is needed by incorporating a length scale into the constitutive law.

Approaches based on this idea can be generally divided into three categories: the micropolar (cosserat) continuum models, the high order of strain gradient models and the nonlocal models. In cosserat theory, additional rotational degrees of freedom are introduced into the framework of the continuum model. Though this approach has shown effectiveness in modeling problems involving size effects and strain localization, its robustness reduces in the pure tension case because of small curvatures within the necking zone (Fleck and Hutchinson, 1993). The enhanced strain gradient models (Fleck and Hutchinson, 1997; Mikkelsen, 1999) provide continuum descriptions by coupling plastic strain as well as its gradients into the yield function. For these type of approaches, the plastic strain and its gradients are considered as the unknowns, and have similar roles as the displacements in finite element formulations.

The nonlocal family of regularization approaches are now widely used to capture strain softening as well as the ductile fracture behavior in metals, and numerous nonlocal models have been proposed (Belnoue et al., 2007; Belnoue and Korsunsky, 2012; Abiri and Lindgren, 2015; Nguyen et al., 2015; Chow et al., 2011; Wcisło and Pamin, 2017). Even though the basic mechanical behavior of ductile solids exhibits strain hardening up to ductile fracture, strain softening can be induced by factors as continuum damage, temperature, and geometric effect. On the other hand, strain hardening cannot be the immediate cause of the strain localization. Considering a typical tensile test of a structural metal, even though damage and temperature can be two factors influencing the process of necking, a primary reason the material undergoes strain softening is the geometry evolution in the necked region. While most of the nonlocal models concentrate on the damage effect that directly leads the strain hardening properties of metals to be the strain softening type, less attention has been paid to the geometry triggered strain softening. Examining the

geometry effect can lead to a better understanding and characterization of the necking phenomenon.

The objective of this chapter is to deal with the geometry effect in strain localization. First, the role of necking in causing strain softening will be identified. The geometry factor will be directly coupled into the material behavior in the form of a one-dimensional model. Analytical solutions will be derived to investigate the cause of mesh dependency in a numerical context. A one-dimensional model by nonlocal formulation will be proposed. Analytical investigations will be performed to study the regularization effect on the localization problem. A numerical example will be given to confirm the mesh insensitivity of the finite element solutions. The application details as well as the limitations of the proposed one-dimensional model will also be discussed.

6.2 PROBLEM FORMULATION

For the sake of simplicity and generality, an exponential relationship of true stress-strain, which is also a common approximation for the strain hardening properties of structural metals, is taken as

$$\sigma = K\varepsilon^n \tag{6.1}$$

where K is the strength coefficient and n is the strain hardening exponent. On the other hand, the material response obtained from a tensile test is determined from the applied load and deflection using the original specimen geometry, and is given in the form of engineering stress and strain

$$\sigma_{eng} = \frac{P}{A_0}, \qquad \varepsilon_{eng} = \frac{L - L_0}{L_0} \tag{6.2}$$

where A_0 is the original area of cross section and L_0 is the original gauge length. Taking

the incremental strain to be the ratio of the incremental length and the current length results in

$$d\varepsilon = \frac{dL}{L} \rightarrow \varepsilon = \int_{L_0}^{L} \frac{dL}{L} = \ln\left(1 + \frac{L - L_0}{L_0}\right) \tag{6.3}$$

Eq. (6.2) and (6.3) provide a relationship between true strain and engineering strain. An assumption is made that plastic deformation does not change the volume and the elastic volume change is neglectable during the deformation. The zero-volume change leads to

$$dV = 0 \rightarrow \frac{A}{A_0} = \frac{L_0}{L} \tag{6.4}$$

Therefore, the current area of the cross section can be calculated by the initial area of cross section and the current true strain measurement as

$$A = A_0 e^{-\varepsilon} \tag{6.5}$$

The relation above is valid for the regime prior to necking where the cross-sectional area remains uniform along the gauge length. For the post-necking range, the strain distribution is non-uniform both longitudinally and transversely. Herein, a simplification is made that the area variation relates to the average longitudinal strain, which is the tensile strain at a certain point in the one-dimensional model. This is equivalent to the assumption that the cross-sections remain planar and are perpendicular to the centerline, which is also the starting point of necking analysis by Antman and Carbone (1977) and Coleman and Newman (1988). The applied load in Eq. (6.2) can be formulated using the initial area of the cross section, the true stress and the true strain as follows

$$P = A\sigma = A_0 \sigma e^{-\varepsilon} \tag{6.6}$$

Combining Eq. (6.1) and (6.6) leads to the relationship between the true strain and the engineering stress in terms of the applied load. The rate of change of engineering stress with respect to the true strain, i.e., the tangent modulus, E_t, can be derived as

$$\frac{dP}{A_0 d\varepsilon} = E_t = K\varepsilon^{n-1}e^{-\varepsilon}\left(n-\varepsilon\right) \tag{6.7}$$

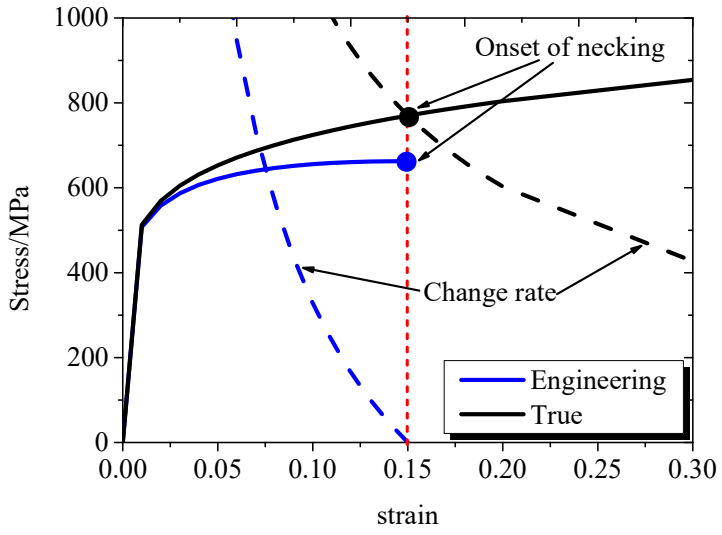

Fig. 6.1 Illustration of engineering and true stress vs. strain and their change rates in a tensile test.

Consider a numerical example by taking K=1023.5 MPa and n=0.15. Fig. 6.1 compares the variations of the true and engineering stress and their change rates. Contrary to the continuous strain hardening trend of the true stress, the engineering stress exhibits strain hardening before the onset of necking, which is followed by strain softening after the necking point. Regarding the change rate of engineering stress, it gradually decreases from positive to negative. A similar tendency can be found in the change rate of the true

stress, but the difference is that it keeps positive as the strain increases. The necking point corresponds to the moment when the change rate of engineering stress equals zero and the change rate of true stress equals to the true stress itself.

6.2.1 One-dimensional model

As discussed above, strain softening is the outcome of interaction between the geometry effect (area change) and the strain hardening (true stress). To combine these two effects, a one-dimensional model is proposed in the current study. This one-dimensional consideration considers as constant cross-sectional area. Even though such a simplification from three dimensions to one dimension does not ensure completely consistent, physically and mathematically equivalent conversions, the drawbacks of which will be discussed later, it is quite a popular formulation due to its ability to reveal the essence of the strain localization problem and leads to useful analytical solutions. With this one-dimensional model, the strain hardening followed by strain softening behavior is completely accomplished by the material property, which is expressed as

$$\sigma = K\varepsilon^{n}e^{-\varepsilon} \tag{6.8}$$

In addition, to characterize the geometry effect during the deformation, a geometry parameter is introduced as

$$\omega_g = 1 - e^{-\varepsilon} \tag{6.9}$$

The geometry parameter ω_g varies from 0 to 1, where the lower and upper bound represents areas of the cross-section equal to its initial value and equal to zero, respectively. Also, the incremental rate of the geometry parameter is given as

$$\Delta\omega_g = (1-\omega_g)\Delta\varepsilon \tag{6.10}$$

Next, the governing partial differential equation prior to and after necking will be examined for both static and dynamic cases. First, in terms of the static problems, the equilibrium equation has the form of

$$\frac{\partial\sigma}{\partial x} = f \rightarrow E_t \frac{\partial\varepsilon}{\partial x} = f \tag{6.11}$$

where f refers to the external force. When the tangent modulus is positive, say, $\varepsilon < n$, the partial differential equation is an elliptic type. As E_t decreasing to 0 and the critical condition is achieved, a bifurcation of deformation from a homogeneous mode to a discontinuous state occurs. Once the strain exceeds n, the equation in Eq. (6.11) loses its ellipticity and the static problem is therefore no longer well posed.

In the dynamic application, the stress wave propagation is explored to analyze the necking instability. The equation of momentum balance satisfies

$$\frac{\partial\sigma}{\partial x} = \rho\frac{\partial^2 u}{\partial t^2} \tag{6.12}$$

where ρ is the material density and u is the displacement. The incremental first derivative of the displacement field with respect to both time and spatial coordinate can be given as

$$\begin{cases} d\left(\dfrac{\partial u}{\partial t}\right) = \dfrac{\partial^2 u}{\partial t^2}dt + \dfrac{\partial^2 u}{\partial x\partial t}dx \\ d\left(\dfrac{\partial u}{\partial x}\right) = \dfrac{\partial^2 u}{\partial x^2}dx + \dfrac{\partial^2 u}{\partial x\partial t}dt \end{cases} \tag{6.13}$$

Combining Eq. (6.12) and (6.13) leads to a system of quasilinear equations, which is written as

$$\begin{bmatrix} E_t & 0 & -\rho \\ 0 & dx & dt \\ dx & dt & 0 \end{bmatrix} \begin{Bmatrix} \partial^2 u/\partial x^2 \\ \partial^2 u/\partial x \partial t \\ \partial^2 u/\partial t^2 \end{Bmatrix} = \mathbf{AX} = \begin{Bmatrix} 0 \\ d\left(\partial u/\partial t\right) \\ d\left(\partial u/\partial x\right) \end{Bmatrix} \tag{6.14}$$

with the characteristic determinant det(**A**)=0. This leads to the expression of wave speed v_p and is given by

$$v_p = \frac{dx}{dt} = \pm\sqrt{\frac{E_t}{\rho}} \tag{6.15}$$

Similar to the static cases, a positive value of E_t keeps the characteristics in Eq. (6.14) real and distinct, maintaining the system hyperbolic and ensures the solution to the system is unique. When the tangent modulus decreases to zero and becomes negative, the characteristics are complex, the system becomes elliptic and the wave speed in Eq. (6.15) is imaginary. In this case, the initial value problem is ill-posed and leads to numerical instabilities when solved by the finite element method.

The analysis for both the static and dynamic cases indicate the governing equations change their types due to strain softening, and giving rise to numerical difficulties. As soon as the material enters the strain softening range, the computational solution exhibit nonphysical meanings in energy dissipation and strain distribution in the localized zone, both of which are expected to occur over a region tending to a zero measurement.

6.2.2 Mesh dependency

A finite element model is developed to provide numerical evidence corresponding to the analytical solutions discussed above. The example is a one-dimensional truss model, which only resists uniaxial tension. The initial length of the bar is assumed to be L_0=10mm, and the area of cross section is constant to be a unit one, i.e., A=1 mm^2. The configuration

of the model is shown in Fig. 6.2. The same displacement is applied to both ends. The shaded region in Fig. 6.2 refers to the localization zone, the width of which needs to be further investigated. The same material properties as used in the previous example (K=1023.5 MPa and n=0.15) are also applied to this model. The corresponding stress-strain curve is shown in Fig. 6.3. The modulus of elasticity for the elastic loading and unloading assumed to be E=210GPa.

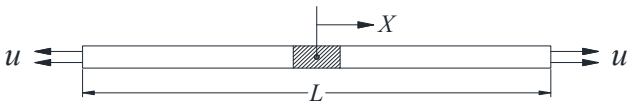

Fig. 6.2 One-dimensional truss model.

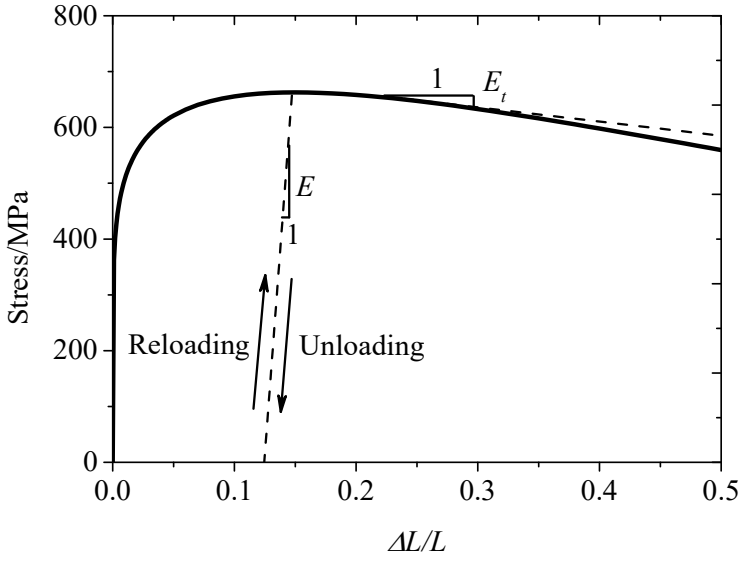

Fig. 6.3 Constitutive relation for the truss model.

The truss model is discretized by four different mesh refinements, using 25, 51, 101, 201 elements. The engineering stress-strain responses using four different spatial

discretizations are shown in Fig. 6.4, where the engineering strain is measured by the ratio of elongation to the initial length and the engineering stress is the force on the bar divided by the initial unit area. The solid line in Fig. 6.4 refers to the response where no strain localization occurs, which means softening occurs uniformly over the entire bar beyond the instability point. Before the maximum stress point, the results for different mesh refinements coincide with each other. The maximum stress is equal to 662.8MPa at $\Delta L/L_0$=0.162. Comparison among the uniform and localization responses indicate that bifurcation occurs instantaneously beyond the peak point. After this peak point, the material undergoes strain softening within the localization zone with elastic unloading outside the localization region. The finer the mesh is, the more dramatic the stress drops.

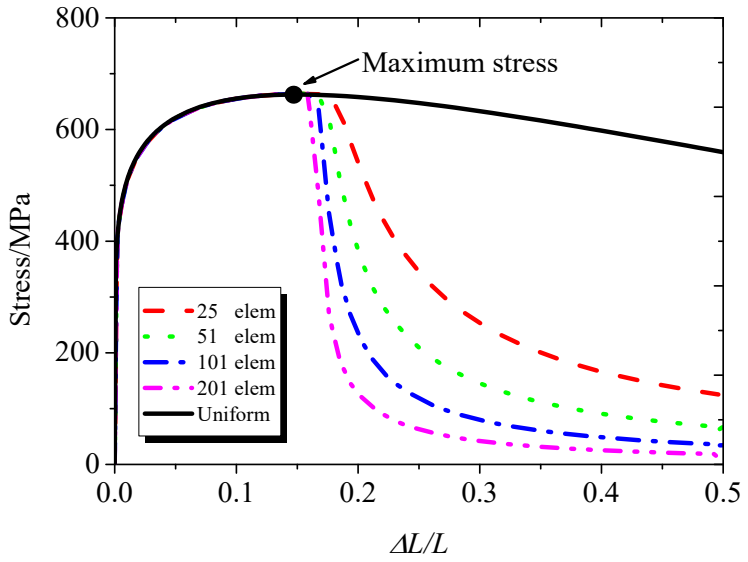

Fig. 6.4 Engineering stress vs. engineering strain response for several mesh refinements using local approach.

The strain distribution along the length of the bar for the four different meshes is

shown in Fig. 6.5. For each mesh h, strain localized into the middle of the bar model. For the region outside the localization zone, the strain magnitudes are almost the same. The strain is concentrated in the single element for each mesh refinement. As the mesh becomes finer, the magnitude of the localized strain increases. When localization takes place, material within the shaded zone shown in Fig. 6.1 follows the strain softening path as the strain increases. The remaining material experiences elastic unloading, and the elastic deformation of this material decreases. Since the elastic modulus is much greater than the tangent modulus of strain softening, decreasing a certain applied load does not significantly change the strain outside the localization zone but significantly influences the strain within the localization region. The length of localization zone and the internal strain are dependent on the size of the single element in the middle of the bar. As the element size becomes infinitesimal, the length of localization region also become infinitesimal.

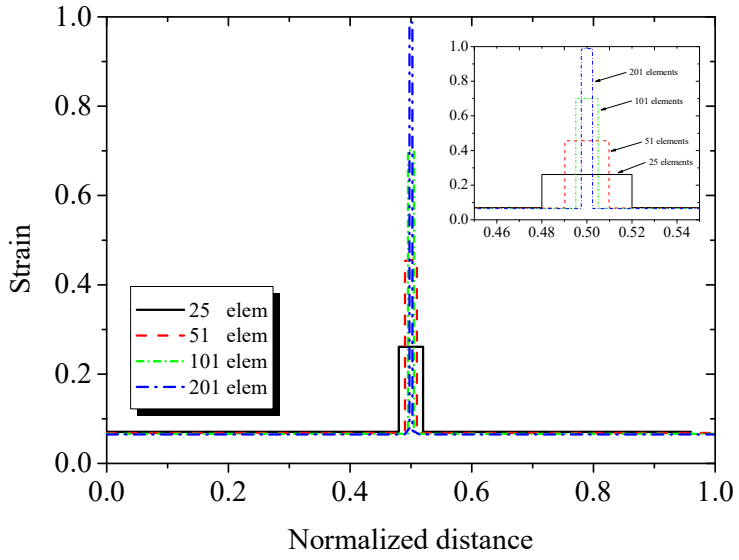

Fig. 6.5 Strain distribution for several mesh refinements using local approach.

It is unrealistic that the length of the localization zone as well as the strain distribution follow not the physical facts but the mesh refinement. Furthermore, if a numerical imperfection is introduced into the FE model, the results will strongly depend on the numerical disturbance (Wu and Wang, 2010). The numerical results correspond to the analytical solutions that the strain softening problems show difficulties within the framework of classical continuum model. This is also the case in the three-dimensional necking problem. It is the strain softening related variable, i.e., the geometry parameter ω_g in Eq. (6.9), that results in spurious localization as well as mesh dependency during the deformation. The strain softening is essentially material property induced, since if the strain hardening exponent is greater than the strain at fracture, necking would never occur up to material failure. The material requires a localization limiter to ensure the strain localizes into a finite and determined region at an arbitrary mesh refinement. The localization limiter partly requires that a material characteristic length be appropriately introduced into standard constitutive laws to regularize the boundary value problem and to obtain numerical solutions with physical meaning.

6.3 NONLOCAL APPROACH

The nonlocal approach can provide an effective regularized effect on the boundary value problem. The basic idea of the nonlocal family of models is replacing the local material internal variables by their nonlocal counterparts, which are obtained by the variables of material points within a certain domain. In contrast to the standard constitutive theories that the mechanical behavior of a material point is only related to the point itself, the nonlocal approach allows the state of each material point to be evaluated by its surrounding materials. The limitation of local constitutive models disappears as the

material behaves as a continuous medium. However, once the discontinuity resulting from either material heterogeneity or mechanical instability enters the problem, deviation of the response obtained by the local continuum models from the actual behavior is observed (Bažant and Jirásek, 2002). This, in turn, highlights the importance of the nonlocal effects. From the physical point of view, such nonlocality may be due to nonuniformity of the strain field on a small scale and to the interactions of microcracks and microvoids during the course of their growth, both of which exhibit strong size effects at the microstructural level. In terms of a mathematical meaning, both strong and weak discontinuities associated with singularity and negative definiteness of the tangent stiffness matrix result in numerical instabilities that require an additional characteristic length to serve for regularization.

Early developments in the nonlocal theories can be traced back to 1970s, when the nonlocal treatments were applied to many complicated fields, e.g., force and energy. Subsequent simplifications led to the use of the nonlocal models in several practical implementations, most of which were attributed to elastic problems at that time (Edelen et al., 1971; Eringen and Kim, 1974; Eringen et al., 1977). In the early 1980s, the nonlocal formulations began to address the plastic range, in which the nonlocal approach was formulated in the stress field (Eringen, 1981). Unfortunately, it did not achieve a regularization effect for strain localization problems since the stress is uniform due to the equilibrium condition it satisfies. More recently, Bažant and Lin (1988) replaced either the plastic strain or plastic multiplier or its rate by their nonlocal averages to formulate another version of nonlocal plasticity theory. The numerical solutions indicate these nonlocal plastic variables can be effective localization limiters. In terms of the nonlocal applications to continuum damage mechanics, early attempts can be found from Lemaitre and Chaboche (1994), where the nonlocality is with respect to the damage variable. Other formulations

of nonlocal damage theories regarding the damage energy release rate, the softening related strain, the damaged stiffness matrix, and the inelastic stress were applied and compared by Jirásek (1998). Different responses were observed and the results indicate only the formulations on the damage energy release rate lead to a reasonable behavior.

The fundamental operation of nonlocality is to calculate the spatial average of a certain variable that is used as the localization limiter, which has the form

$$\bar{g}(x) = \frac{1}{\int_\Omega \alpha(x,y)\,dy} \int_\Omega \alpha(x,y)\, g(y)\, dy \tag{6.16}$$

where g is the local variable and $\bar{g}$ is its nonlocal counterpart. The material at x is the host point that will interact with its surrounding points at y. Ω is the volume of the structure. The term $\alpha(x,y)$ is the nonlocal weight operator, which is a function of characteristic length and the distance from the host to the receiver point. A popular form of the weight function is the bilateral exponential function, which will also be adopted in the current study and is taken as

$$\alpha(x,y) = \exp\left(-\frac{|x-y|}{l}\right) \tag{6.17}$$

where l is the material characteristic length. The nonlocal operator gradually degrades from the host point to the remote point, and the weight at its center x has the greatest value $\alpha(x,x)=1$. This is physically reasonable in that the greater the distance between two points, the weaker the interaction will be. For an unbounded problem, the exponential function gives rise to the relation that $\int_{-\infty}^{+\infty} \alpha(x,y)\,dy = 2l$. To ensure a consistent nonlocality, the denominator of the right-hand expression in Eq. (6.16) is applied to calculate the nonlocal variable. The reason is that the term $\int_\Omega \alpha(x,y)dy$ is constant if the material point x is far from

the boundary while for the material close to the boundary, only part of the domain of influence participates in the averaging so that the term $\int_{\Omega}\alpha(x,y)dy$ will deviate from the one sufficiently remote from the boundary.

By expanding into a Taylor series, the integral form of the nonlocal variable in Eq. (6.16) can be converted into the differential form involving the gradient of the local variable

$$\bar{g} = g + c\nabla^2 g \tag{6.18}$$

where c is a material constant related to the characteristic length l. Using the explicit gradient formulation, the nonlocal approach can be interpreted in a more physical way. Within a uniform material, the higher order term in Eq. (6.18) is negligible and there is little difference between local and nonlocal variable. For a material that contains strong discontinuous regions, e.g., a localization zone, the local variable at the peak level will keep a negative second derivative so that its nonlocal counterpart will be reduced by the influence of the neighboring material. Otherwise, the nonlocal variable will be increased. The contribution of the gradient of the local variable is significant in dealing with the highly nonlinear discontinuity issue, and it also overcomes the shortcomings of standard continuum models, which determine the state of a material point only by the local variable of the current point.

6.3.1 Nonlocal model for post-necking analysis

Regarding the choice of the variable to be nonlocal, Bažant and Jirásek (2002) suggested that formulations of different variables would result in quite different responses and nonlocal effectiveness. Considering the case of necking in the present study, the strain localization is dominated by the longitudinal strain and the geometry parameter, both of

which are good candidates for nonlocality. Furthermore, since the longitudinal strain is a determinative variable of both the stress field and the geometry parameter, it is reasonable to treat the longitudinal strain instead of the geometry effect as nonlocality. However, this nonlocal formulation essentially regularizes the mechanical field so that the deformation, in other words, the area of cross section still needs to be calculated by the local longitudinal strain.

Before formulating the nonlocal model for post-necking analysis, some assumptions are needed. First, note that the longitudinal strain can be divided into an elastic and a plastic part, i.e., $\varepsilon=\varepsilon_e+\varepsilon_p$. The focus of this study is on the material behavior at the onset of and after necking, where the elastic strain is negligible when compared to the plastic strain. By ignoring the elastic strain increment after yielding, the strain hardening law in Eq. (6.1) can be simplified as

$$\sigma = K\left(\frac{\sigma_0}{E}+\varepsilon_p\right)^n \rightarrow \sigma = K\left(\frac{\sigma_0}{E}\right)^n\left(1+\frac{E}{\sigma_0}\varepsilon_p\right)^n \tag{6.19}$$

where σ_0 is the initial yield stress. Although this modification will would lead to deviation from actual behavior at early stages of plasticity, only a very minor is expected in post-necking regime, which is attractive for this investigation. The cross-sectional area reduction is mainly due to the plastic deformation and this decrease is irreversible. For the material that undergoes elastic unloading, the cross-sectional geometry remains unchanged. In this case, the geometry parameter is obtained by the maximum equivalent plastic strain during the deformation history, which is given as

$$-\ln\left(1-\omega_g\right) = \max\left(\varepsilon_p\right) \tag{6.20}$$

Consequently, the local material behavior for the one-dimensional model can be re-

organized in terms of accumulated plastic strain and is expressed as

$$\sigma = K\left(\frac{\sigma_0}{E}\right)^n \left(1+\frac{E}{\sigma_0}\varepsilon_p\right)^n e^{-\varepsilon_p} \rightarrow \sigma = \sigma_0\left(1+\frac{E}{\sigma_0}\varepsilon_p\right)^n e^{-\varepsilon_p} \tag{6.21}$$

The above conversion is based for two reasons. One is to facilitate the elastic predictor-plastic corrector algorithm in the numerical implementation. This is of great importance when dealing with the elastic loading/unloading and plastic strain hardening/softening issues. The other reason is the fact that the total strain formulated by the nonlocal approach cannot be an effective localization limiter. Preventing instability modes requires that the nonlocal treatment is applied to variables that will never decrease, e.g., accumulated plastic strain.

Thus, according to Vermeer and Brinkgreve (1994) and Jirásek and Rolshoven (2003), a complete avoidance of spurious mesh dependency for the localization problem induced by plastic strain softening requires a refinement of the standard nonlocal formation. Known as the over-nonlocal formulation, this modification involves the definition of the over-nonlocal cumulative plastic strain using a linear combination of its local variable and nonlocal averaging counterpart

$$\hat{\varepsilon}_p = (1-m)\varepsilon_p + m\bar{\varepsilon}_p \tag{6.22}$$

where $\hat{\varepsilon}_p$ is the over-nonlocal equivalent plastic strain, $\bar{\varepsilon}_p$ is the nonlocal average of ε_p calculated by Eq. (6.16), and m is the over-nonlocal parameter. Two special values of m=0, 1 reduce the over-nonlocal model to the local plasticity model and standard nonlocal formulation, respectively. It is also observed that only when m>1 will the plastic localization region have a nonzero length, which will be discussed later in this study.

6.3.2 Characteristic length

One of the most important aspects of applying the nonlocal approach is to identify the characteristic length. The concept of the characteristic length in nonlocal formulation has meanings at two different levels, including the regularization parameter in a mathematical and numerical sense, and the length scale to describe the size effect in accordance with physical facts. It should be noted that the nonlocal characteristic length is not necessarily equivalent to the notion of intrinsic material length, which is adopted by many other enhanced continuum theories. The relation between the nonlocal length parameter and other length parameters is not well established, but they are likely strongly linked with each other.

Among various reasons to explain such a close relation, the size effect is the dominant one, since most of the theories that incorporate the characteristic length are motivated by the scale dependent phenomena observed in experiments and numerical simulations. In the field of ductile metals, due to their microstructure and mechanical behavior, the characteristic length can be generally related with either the grain size or the inclusion spacing. Panontin and Sheppard (1995) suggested the characteristic length was proportional to the grain diameter, although the underlying physical explanation for this relationship is not clear. In terms of the inclusion spacing-based characteristic length, it is more likely appropriate for the ultimate behavior of metals, and their quantitative relations proposed by various researchers (Ritchie et. al., 1979; Panontin and Sheppard, 1995) deviate one from another significantly. This implies the characteristic length inferred by physical features need further exploration.

The experimental determination of characteristic length, though indirect, is of great importance and is the most popular tool to identify the nonlocal parameter. The procedure

involving inverse analysis of test results requires a nonlocal sensitive experimental setup. Previously, the global load-displacement response was the unique item used for length parameter calibration, in other words, determining the parameter by fitting the load-displacement curve. Subsequent analysis pointed out the inadequacy of this approach. Estimating the nonlocal parameter based on the global response should also be verified by the local field, e.g., the strain field in the localization zone for the plasticity model and the damage field for the continuum damage model. By paying attention to the local behaviors, which is more relevant to size effect, the identification strategy provides a more accurate and rigorous determination of the nonlocal characteristic length (Geers et al., 1999a; 1999b; Belnoue and Korsunsky, 2012).

The scope of this study will not cover any experimental calibration of the nonlocal length for a specific material. The characteristic length is considered as a numerical parameter rather than a material constant. In this case, the effects of such nonlocal length on the material response, including the appearance of the necking region, and the material response will be investigated. In addition, more than reflecting the size effect in the small-scale problem, the nonlocal length in this paper is likely related to the regularization effect and to the localization distribution. Therefore, the length adopted for the numerical modeling needs to be compatible with computational considerations, e.g., the nonlocal length is required to be greater than the maximum size of the elements and significantly smaller than the entire length of the numerical model.

6.4 ANALYTICAL SOLUTIONS

In this section, the simplicity of a one-dimensional model will be used to analytically study the behavior of the material with the nonlocal formulation specified in

this study. Noting the strain hardening/softening law in Eq. (6.21) and its nonlocality in Eq. (6.22), the local plastic variable in the plasticity model is replaced by its nonlocal counterpart, and the corresponding yield function can be given as

$$F\left(\sigma,\hat{\varepsilon}_p\right)=\sigma-\sigma_0\left(1+\frac{E}{\sigma_0}\hat{\varepsilon}_p\right)^n e^{-\hat{\varepsilon}_p} \tag{6.23}$$

where σ is the current stress and is calculated by its local quantity

$$\sigma=E\left(\varepsilon-\varepsilon_p\right) \tag{6.24}$$

Defining a plastic multiplier $\dot{\gamma}=\dot{\varepsilon}_p$, the plastic flow is required to satisfy the Kuhn-Tucker loading-unloading condition and the plastic consistency condition

$$\dot{\gamma}\geq 0,\quad F\leq 0,\quad \dot{\gamma}F=0 \text{ and } \dot{\gamma}\dot{F}=0 \tag{6.25}$$

6.4.1 Spectral analysis of localization

Herein, the capacity of this nonlocal plasticity model will be examined in the dynamic context. Following the approach by Borino et al. (2003) and Di Luzio and Bažant (2005), the localization analysis will focus on the exact solution of the propagation speed of stress acceleration waves. In contrast to the results of the local model, a real propagation speed is expected within the framework of nonlocality. The one-dimensional bar is adopted again, the length of which is assumed to be infinite to eliminate the boundary effect. Considering the bar initially in a homogenous state of strain, i.e., $\hat{\varepsilon}\left(x\right)=\varepsilon\left(x\right)=\varepsilon_0$ and $\hat{\varepsilon}_p\left(x\right)=\varepsilon_p\left(x\right)=\varepsilon_{p0}$, the stress-strain relation of Eq. (6.24) can be written in rate form as

$$\dot{\sigma}=E\left(\dot{\varepsilon}-\dot{\varepsilon}_p\right) \tag{6.26}$$

Accordingly, the rate form of the yield function of Eq. (6.23) in this initially uniform state

need also satisfy

$$\dot{F} = E\left(\dot{\varepsilon} - \dot{\varepsilon}_p\right) - \sigma_0\left(1 + \frac{E}{\sigma_0}\hat{\varepsilon}_p\right)^{n-1}\left(\frac{nE}{\sigma_0} - 1 - \frac{E}{\sigma_0}\hat{\varepsilon}_p\right)e^{-\hat{\varepsilon}_p}\dot{\hat{\varepsilon}}_p = 0 \tag{6.27}$$

For the sake of simplicity, the nonlocal tangent modulus with respect to the plastic strain is defined as

$$\hat{E}_{tp} = \sigma_0\left(1 + \frac{E}{\sigma_0}\hat{\varepsilon}_p\right)^{n-1}\left(\frac{nE}{\sigma_0} - 1 - \frac{E}{\sigma_0}\hat{\varepsilon}_p\right)e^{-\hat{\varepsilon}_p} \tag{6.28}$$

and the uniform property leads to $\hat{E}_{tp}\left(x\right) = E_{tp}\left(x\right) = E_{tp0}$. Recall the equation of motion in Eq. (6.12), the rate form of which reads

$$\frac{\partial\dot{\sigma}}{\partial x} = \rho\frac{\partial^2\dot{u}}{\partial t^2} \tag{6.29}$$

The harmonic wave solutions with respect to the angular frequency ω and the wave number *k* are assumed to follow the form

$$\dot{u}\left(x,t\right) = \dot{u}_0 e^{i(kx-\omega t)}, \qquad \dot{\varepsilon}_p\left(x,t\right) = \dot{\varepsilon}_{p0}e^{i(kx-\omega t)} \tag{6.30}$$

Note the relation $\dot{\varepsilon}\left(x,t\right) = \partial\dot{u}\left(x,t\right)/\partial x$, and substituting the harmonic solutions into Eq. (6.26), (6.27) and (6.29), a system of linear equations is obtained

$$\begin{cases} \left\{\left(Ek^2 - \rho\omega^2\right)\dot{u}_0 + Eik\dot{\varepsilon}_{p0}\right\}e^{i(kx-\omega t)} = 0 \\ \left\{Eik\dot{u}_0 - \left[E + E_{tp0}\left(1 - m + \frac{m}{2l}A\left(k\right)\right)\right]\dot{\varepsilon}_{p0}\right\}e^{i(kx-\omega t)} = 0 \end{cases} \tag{6.31}$$

where $A\left(k\right) = \int_{-\infty}^{+\infty}\alpha\left(z\right)e^{ikz}dz = 2l/\left(1 + k^2l^2\right)$ is the Fourier transform of weight function. To ensure non-zero solutions of $\dot{u}_0$ and $\dot{\varepsilon}_{p0}$, the determinant of the coefficient matrix for the linear system in Eq. (6.31) must equal to zero, leading to

$$-\left(Ek^2-\rho\omega^2\right)\left[E+E_{tp0}\left(1-m+\frac{m}{2l}A\left(k\right)\right)\right]+E^2k^2=0 \tag{6.32}$$

Consequently, the angular frequency ω can be expressed as

$$\omega=kC_e\sqrt{\frac{E_{tp0}\left(1-m+\frac{m}{2l}A\left(k\right)\right)}{E+E_{tp0}\left(1-m+\frac{m}{2l}A\left(k\right)\right)}} \tag{6.33}$$

where $C_e=\sqrt{\frac{E}{\rho}}$ is the elastic propagation velocity. The corresponding phase velocity can be given as

$$v_p=\frac{\omega}{k}=C_e\sqrt{\frac{E_{tp0}\left(1-m+\frac{m}{2l}A\left(k\right)\right)}{E+E_{tp0}\left(1-m+\frac{m}{2l}A\left(k\right)\right)}} \tag{6.34}$$

A special case of l=0 eliminates the dependency of the phase velocity on the nonlocal parameter m, which reduce the model to the local type and the phase velocity becomes imaginary. Otherwise, the following condition needs to be maintained to ensure the velocity never becomes imaginary when the tangent modulus becomes negative,

$$1-m+\frac{m}{l}A\left(k\right)\le 0\ \Rightarrow\ m\ge\frac{k^2l^2+1}{k^2l^2}>1 \tag{6.35}$$

According to Eq. (6.35), the basic requirement is m>1. More strictly, the requirement is related to the wave number k and the characteristic length l. Even for the standard nonlocal formulation, m=1, a real velocity is not achieved. Moreover, for m < 1, the term within the square root of Eq. (6.34) is negative, which implies the non-dispersion of the phase velocity.

Next, considering the critical condition (v_p=ω=0) that leading to a static bifurcation, the corresponding critical wave number is obtained

$$k_{cr} = \frac{1}{l}\sqrt{\frac{1}{m-1}} \tag{6.36}$$

And the critical wave length is

$$\lambda_{cr} = \frac{2\pi}{k_{cr}} = 2\pi l\sqrt{m-1} \tag{6.37}$$

The critical value in Eq. (6.37) is the upper limit of wave length, and only below this limit can the wave propagate. If $\lambda>\lambda_{cr}$, only a small disturbance of $\dot{u}$ will result in an unbounded response, which is not a stable state. It is clearly seen that the critical wave length is a function of the nonlocal parameter and the characteristic length. For this quasi-static case, where $\lambda=\lambda_{cr}$, the length of the localization region is proportional to the length parameter with a given m. Furthermore, $0\leq m\leq 1$ gives an imaginary value of wave length as well as the wave number. In other words, only when $m>1$ will the nonlocal model achieve a complete regularization effect on the localization problem. The dimensionless critical wave length λ_{cr}/l increases with the nonlocal parameter m, which is shown in Fig. 6.6. With both the nonlocal parameter and the characteristic length being determined, the wave length will also be constant.

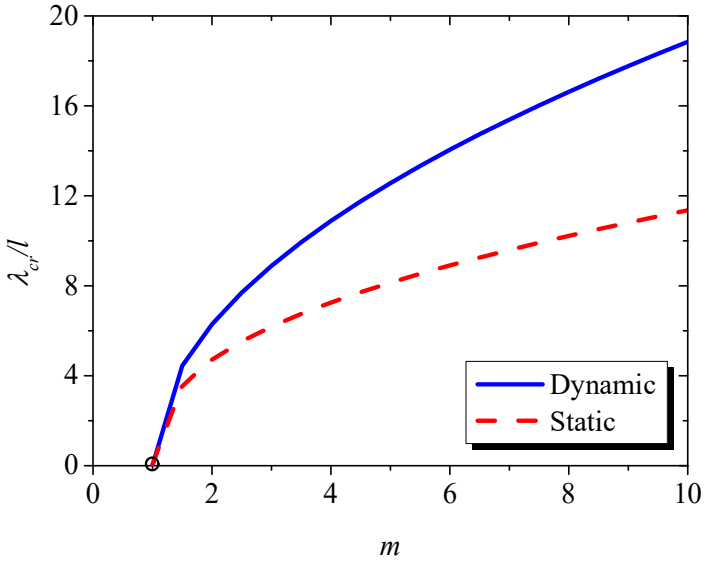

Fig. 6.6 The dimensionless critical wave length λcr/l vs. the over-nonlocal parameter m.

6.4.2 Analytical solution of localization for the static case

This section will focus the behavior of the nonlocal model in the static context. The same one-dimensional truss model is adopted. The basic idea is to obtain the stress and the plastic strain distribution along the entire truss member after the onset of necking. The main objective is to examine if the plastic strain increment takes place within a fixed length of the localization region to reflect the regularization of this nonlocal model in the static case, as is in the dynamic case. First, considering the yield function at the *i*th loading increment

$$F_i = \sigma_i - \sigma_0 \left(1 + \frac{E}{\sigma_0}\hat{\varepsilon}_{p,i}\right)^n e^{-\hat{\varepsilon}_{p,i}} = 0 \tag{6.38}$$

and the yield function at the (*i*+1)th loading increment

$$
\begin{aligned}
F_{i+1} &= \sigma_{i+1} - \sigma_0 \left(1 + \frac{E}{\sigma_0} \hat{\varepsilon}_{p,i+1} \right)^n e^{-\hat{\varepsilon}_{p,i+1}} = 0 \\
&= \sigma_{i+1} - \sigma_0 \left(1 + \frac{E}{\sigma_0} \hat{\varepsilon}_{p,i} + \frac{E}{\sigma_0} \Delta\hat{\varepsilon}_p \right)^n e^{-\hat{\varepsilon}_{p,i} + \Delta\hat{\varepsilon}_p} = 0
\end{aligned}
\tag{6.39}
$$

Combining Eq. (6.38) and (6.39), the stress increment at the current loading step can be obtained as

$$
\Delta\sigma = \sigma_0 \left(1 + \frac{E}{\sigma_0} \hat{\varepsilon}_{p,i} \right)^{n-1} \left(\frac{nE}{\sigma_0} - 1 - \frac{E}{\sigma_0} \hat{\varepsilon}_{p,i} \right) e^{-\hat{\varepsilon}_{p,i}} \Delta\hat{\varepsilon}_p \tag{6.40}
$$

Since the nonlocal tangent modulus is only related to the stress and strain states of the previous loading increment, it can be treated as a constant value at the current loading step. Together with the over-nonlocal plastic multiplier expression in Eq. (6.22), the stress increment can be expressed as

$$
\Delta\sigma(x) = \hat{E}_{tp,i}(x) \left[(1-m)\Delta\varepsilon_p(x) + \frac{m}{l} \int_{-\infty}^{+\infty} \alpha(x,y) \Delta\varepsilon_p(y)\, dy \right] \tag{6.41}
$$

Moreover, the equilibrium condition of the one-dimensional truss member results in the requirement that $\Delta\sigma(x)=\Delta\sigma$=constant. The analysis herein just considers the case at the onset of necking, and gives an infinitesimal tangent modulus $\hat{E}_{tp,i}(x) = E_{tp,i}(x) = \overline{E}_{tp,i}$, which is assumed to be uniform. Hence, only the plastic multiplier is a function of the spatial coordinate. The underlying assumption of over-nonlocal formulation in Eq. (6.41) is that localization occurs at the location far from the boundary and the length of the truss member can be considered as infinite when compared to the localization length. To solve this equation, it is also necessary to specify the boundary conditions

$$
\Delta\varepsilon_p = 0, \quad \Delta\varepsilon_{p,x} = \mp \frac{\Delta\sigma}{l(1-m)\hat{E}_{tp,i}} \quad \text{for} \quad x = \pm\frac{w}{2} \tag{6.42}
$$

where w is the assumed length of the localization region. The material within the localization region continues strain softening and the remaining material undergoes elastic unloading. Through some algebraic manipulations (Lu et al., 2010), the plastic multiplier is obtained as

$$\Delta\varepsilon_p = \frac{\Delta\sigma}{\bar{E}_{tp,i}}\left[1+\frac{1}{\sin C}\cos\left(\frac{x}{l\sqrt{m-1}}\right)\right], \qquad -\frac{w}{2}\le x\le\frac{w}{2} \tag{6.43}$$

where C is a constant defined as $C=\tan^{-1}\left(1/\sqrt{m-1}\right)$, and the explicit expression for w is then given as

$$w = l\sqrt{m-1}\left(\pi+2C\right) \tag{6.44}$$

Comparison of the localization region length between static and dynamic cases is shown in Fig. 6.6. Obviously, as m > 1 tends to 1, the analytical solution for the static case is identical to that for the dynamic case. Otherwise, the length for the static case is smaller. Analysis of both cases indicates the length of the localization zone is not a solution dependent parameter and can only be determined by the nonlocal parameter and the characteristic length. It is worth noting that as the strain softening becomes more intensive, the tangent modulus cannot be viewed as a uniform parameter in that it is also a function of spatial coordinate. This makes it impossible to obtain the analytical solution to the plastic multiplier distribution at an arbitrary loading step of post-necking range. However, at the onset of localization, the length of strain softening determines the boundary conditions of the tangent modulus, i.e., $\hat{E}_{tp,i}\left(\pm w/2\right)=0$. One can imagine that for the subsequent loading step, the variation of the nonlocal tangent modulus influences the magnitude of the plastic multiplier rather than the boundaries of the strain softening evolution, i.e., the localization length w will keep constant. The same behavior has been obtained by Bažant

and Jirásek (2002) that the strain softening region does not change during the localization process while the shape of the plastic strain profile is related to the tangent modulus. To provide further insight into the localization region, the finite element method is considered in the next section.

6.5 FINITE-ELEMENT SOLUTION

The analysis presented above demonstrates the regularization effect of the nonlocal approach on the one-dimensional localization problem. However, analytical solutions are not easily obtained for all problems, especially for 2D and 3D cases. Finite element modeling can be employed to deal with such problems. An issue that must be investigated is the mesh dependency of the numerical solution within the framework of the nonlocal constitutive law, application of the finite element methods the necking type of strain softening problem as well as to their extensions to other localization simulations.

6.5.1 Numerical implementation

Start with the weak form of the equilibrium equation, which is given as

$$\int_{\Omega} \sigma \delta w d\Omega = \int_{\Gamma} f \delta w d\Gamma \tag{6.45}$$

where δw is a test function, and Γ is the boundary to the domain Ω, and f is the external force applied to the boundary. Considering the current case, the body force is neglected. Subjected to time discretization, Eq. (6.45) can also be written in the incremental form

$$\int_{\Omega} \Delta\sigma \delta w d\Omega = \int_{\Gamma} f_{i+1} \delta w d\Gamma - \int_{\Omega} \sigma_i \delta w d\Omega \tag{6.46}$$

where $\Delta\sigma=\sigma_{i+1}-\sigma_i$ is the stress increment from the ith to the $(i+1)$th time increment. The stress increment can be linked to the strain increment and displacement field through the

tangent modulus

$$\Delta\boldsymbol{\sigma} = \boldsymbol{C}_{ep}\Delta\boldsymbol{\varepsilon} = \boldsymbol{C}_{ep}\frac{d\Delta\boldsymbol{u}}{dx} \tag{6.47}$$

The displacement field $\Delta\boldsymbol{u}$ is discretized to nodal displacements $\Delta\boldsymbol{u}_N$ as

$$\Delta\boldsymbol{u} = \boldsymbol{N}\Delta\boldsymbol{u}_N \tag{6.48}$$

where $\boldsymbol{N}$ is the shape function for displacement. Consequently, the strain increment can be expressed by the nodal displacement field

$$\Delta\boldsymbol{\varepsilon} = \frac{d\Delta\boldsymbol{u}}{dx} = \frac{d\boldsymbol{N}}{dx}\Delta\boldsymbol{u}_N = \boldsymbol{B}\Delta\boldsymbol{u}_N \tag{6.49}$$

Assuming the test function w is related to the nodal displacement variation, Eq. (6.46) can be converted into

$$\begin{aligned}\Delta\boldsymbol{u}_N\int_\Omega \boldsymbol{B}^{\mathrm{T}}\boldsymbol{C}_{ep,i+1}\boldsymbol{B}d\Omega &= \int_\Gamma f_{i+1}\boldsymbol{N}d\Gamma - \int_\Omega K_i u_{N,i}d\Omega - \int_\Omega \boldsymbol{B}^{\mathrm{T}}\boldsymbol{\sigma}_i d\Omega \\ \Rightarrow \boldsymbol{K}_{i+1}\Delta\boldsymbol{u}_N &= \boldsymbol{f}_{i+1}^{ext} - \boldsymbol{f}_i^{\mathrm{int}} = \Delta\boldsymbol{R}_{i+1}\end{aligned} \tag{6.50}$$

where $\boldsymbol{K}$ is the element stiffness matrix, $\boldsymbol{f}^{\mathrm{int}}$ is the internal force vector, and $\Delta\boldsymbol{R}$ is the unbalanced force vector. Given a linear shape function for this one-dimensional truss member, the strain matrix is

$$\boldsymbol{B} = \left\{-\frac{1}{L^e}, \frac{1}{L^e}\right\} \tag{6.51}$$

where L^e is the current length of the element. The element stiffness matrix is formulated as

$$\boldsymbol{K}_{i+1}^e = \frac{A_0 C_{ep,i+1}^e}{L_i^e}\begin{bmatrix} 1 & -1 \\ -1 & 1 \end{bmatrix} \tag{6.52}$$

The current length of the element can be calculated by $L_i^e = L_0^e + \Delta L_i^e$, i.e., the initial length

plus the elongation at the end of the *i*th time increment. The tangent modulus calculation involves the return-mapping algorithm for the plasticity model. In this case, an elastic state is assumed for the current increment, which means

$$\sigma_{i+1}^{trial} = E\left(\varepsilon_i + \Delta\varepsilon - \varepsilon_{p,i}\right) \tag{6.53}$$

Next, check the trial state for plastic behavior

$$F_{i+1}^{trial} = \sigma_{i+1}^{trial} - \sigma_0\left(1 + \frac{E}{\sigma_0}\hat{\varepsilon}_{p,i}\right)^n e^{-\hat{\varepsilon}_{p,i}} \tag{6.54}$$

If $F_{i+1}^{trial} \le 0$, then the trial state is purely elastic and the increment of the plastic multiplier $\Delta\gamma$=0, otherwise, a plastic corrector needs to be applied to the current state to satisfy

$$F_{i+1}^{trial} = \sigma_{i+1}^{trial} - E\Delta\gamma - \sigma_0\left[1 + \frac{E}{\sigma_0}\left(\hat{\varepsilon}_{p,i} + \Delta\hat{\gamma}\right)\right]^n e^{-\hat{\varepsilon}_{p,i}+\Delta\hat{\gamma}} = 0 \tag{6.55}$$

The Newton-Raphson method is employed to obtain the plastic multiplier increment and then the accumulated plastic strain is updated as

$$\varepsilon_{p,i+1} = \varepsilon_{p,i} + \Delta\gamma \tag{6.56}$$

Note that the strain increment can be split into elastic and plastic parts

$$\Delta\varepsilon = \Delta\varepsilon_e + \Delta\varepsilon_p \tag{6.57}$$

and the corresponding stress increment can be written as

$$\Delta\sigma = E\left(\Delta\varepsilon - \Delta\varepsilon_p\right) \tag{6.58}$$

Substituting the relation between the stress increment and the plastic multiplier increment in Eq. (6.43) into Eq. (6.58), the tangent modulus for strain softening can be obtained as

$$C^e_{ep,i+1} = \frac{E\hat{E}^e_{tp,i} q(x^e)}{E + \hat{E}^e_{tp,i} q(x^e)} \tag{6.59}$$

where $q(x) = 1 + \cos\left(2\pi x / w\right)$ and x^e is the current coordinate of the gauss point of the element. For the strain hardening case, the tangent modulus can be expressed as

$$C^e_{ep,i+1} = \frac{E\hat{E}^e_{tp,i}}{E + \hat{E}^e_{tp,i}} \tag{6.60}$$

In summary, the tangent modulus for the element stiffness matrix can be given as

$$C^e_{ep,i+1} = \begin{cases} E & \text{if } \Delta\gamma = 0 \\ \dfrac{E\hat{E}^e_{tp,i}}{E + \hat{E}^e_{tp,i}} & \text{if } \Delta\gamma > 0 \text{ and } \varepsilon_p \le n - \dfrac{\sigma_0}{E} \\ \dfrac{E\hat{E}^e_{tp,i} q(x^e)}{E + \hat{E}^e_{tp,i} q(x^e)} & \text{if } \Delta\gamma > 0 \text{ and } \varepsilon_p > n - \dfrac{\sigma_0}{E} \end{cases} \tag{6.61}$$

6.5.2 Numerical example

For purposes of comparison, the geometry and mesh refinements for the truss member with the nonlocal formulation is the same as those with the local formulation. The initial yield stress is assumed to be σ_0=400MPa, which is also the same as the numerical example for the local constitutive law. The characteristic length l and nonlocal parameter m are initially given as l=1mm and m=1.1 to demonstrate the regularization effect provided by the nonlocal formulation. Parametric studies on these two parameters will be carried out to show their effects on the post-necking behavior.

The engineering stress-strain response using different mesh refinements is shown in Fig. 6.7. Other than result for the very coarse mesh (with 25 elements), which gives the

least ductile material behavior, all the others (with 51, 101 and 201 elements) have a very similar post-necking response. Comparison of engineering stress-strain results between local and nonlocal formulations demonstrates the effect of nonlocality on eliminating mesh dependency with respect to global response. The other aspect of the analysis results to be examined is the plastic strain profile after necking. The distributions of the plastic strain at $\Delta L/L$=0.25 using different mesh refinements is shown in Fig. 6.8. This indicates both the length of the localization region and the shape of plastic strain profile are largely independent of the mesh. Contrary to the results obtained by the standard constitutive law, which shows a mesh size sensitive localization length, the nonlocal approach mesh size insensitive shape of the localization region. The finite element solution exhibits the same behavior as obtained by the analytical solution. The length of the localization region from numerical analysis is comparable to the length from the analytical solution, which gives a value equal to 1.145mm. In contrast to the sudden change in strain distribution at localization region predicted by the local formulation, a gradual increase in plastic strain entering the strain localized region is observed in Fig. 6.8. The edge of the necking region cannot be determined from the numerical analysis in a straightforward way. Any deviation of the length of the necking region between the numerical and the analytical solutions computed by Eq. (6.44), if it exists, is due to the boundary effect. The analytical solution assumed a bar of infinite length, whereas the numerical solution was for a bar of finite length. Such a difference is also reported by Di Luzio and Bažant (2005).

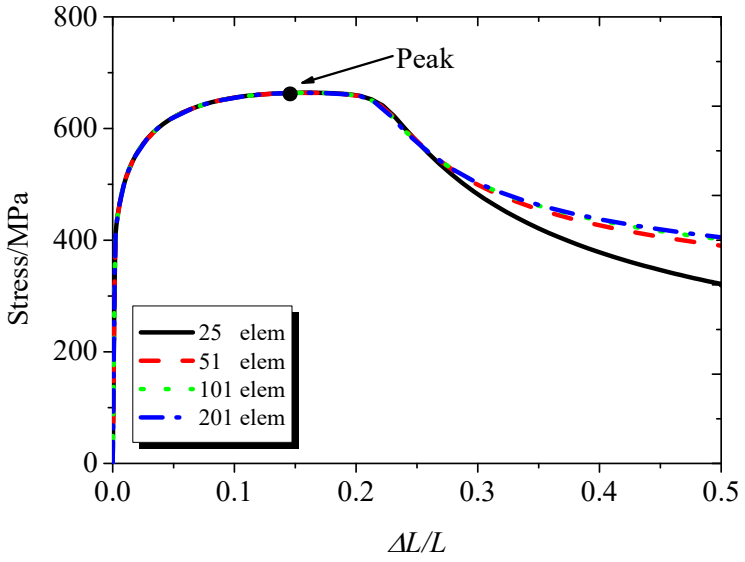

Fig. 6.7 Engineering stress vs. engineering strain response by nonlocal formulation (l=1.0mm, m=1.1).

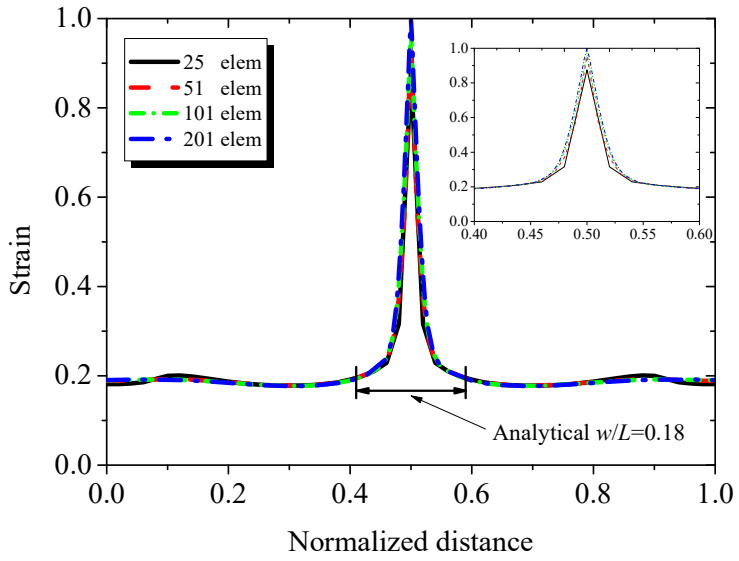

Fig. 6.8 Plastic strain profile for different mesh refinements at ΔL/L=0.25.

To recover the geometry profile for a uniaxial tension test, a round bar is assumed in this study. In this case, a relation can be established between the radius of the specimen r and the geometry parameter ω_g, which is expressed as

$$\frac{R}{R_0} = \sqrt{\left(1-\omega_g\right)} \tag{6.62}$$

where R_0 is the initial radius. While nonlocality is adopted to the material behavior, the geometry profile is obtained based on the local plastic strain, since the transverse geometry evolution is only related to the local axial elongation of the specimen in this example. The geometry evolution with elongations is plotted in Fig. 6.9. This plot shows that the necking corresponding to three different elongations (ΔL=2mm, 2.3mm, 2.5mm) occurs within a fixed region. It exhibits the same behavior as that obtained by analytical solutions, which show the length of the necked region keeps constant throughout the course of deformation. For a given m and l, the length of necked zone is determined while the depth of necking is dependent on the stress and strain history.

The effect of the nonlocal parameter m on the stress-elongation response as well as on the plastic strain distribution within the localization zone is investigated by performing parametric studies. The global response for four different values of m is shown in Fig. 6.10. The higher the value of m, the greater the post-necking strength the material exhibits. The influence of m on the plastic strain profile and necking shape is presented in Fig. 6.11. Similar to the analytical derivation in Eq. (6.44), an increasing m increases the length of the necking zone while it weakens the strain localization. A greater m provides a stronger strain distribution effect to the localization region, one evidence of which is the smoother plastic strain distribution given by the larger m. This can be interpreted that the effect of the nonlocal parameter on the global material response delays re-distribution of the plastic

strain during the strain softening process.

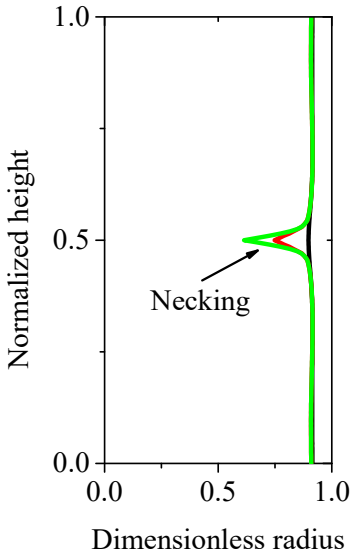

Fig. 6.9 Geometry evolution after necking (at ΔL/L=0.2, 0.23, 0.25).

The characteristic length l has a similar role as the nonlocal parameter in influencing the global response and the plastic strain distribution. As can be seen in Fig. 6.12, enlarging the length parameter increases the strength of the material after necking. Contrary to the sudden drop of the loading capacity for the smaller characteristic length case, the stress decreases in a milder way with a large characteristic length. The effect on the strain localization, as shown in Fig. 6.13, is that a greater characteristic length gives rise to a wider localization region, which corresponding to less pronounced necking.

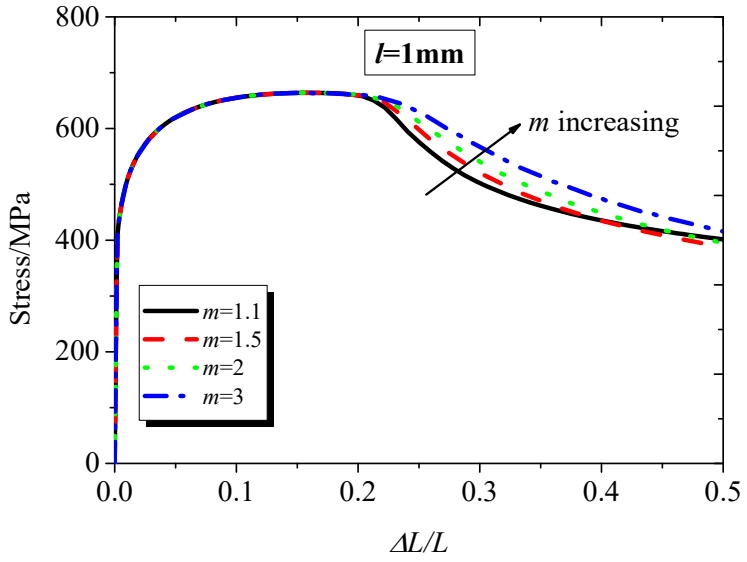

Fig. 6.10 The stress-elongation response upon different nonlocal parameters (m=1.1, 1.5, 2, 3).

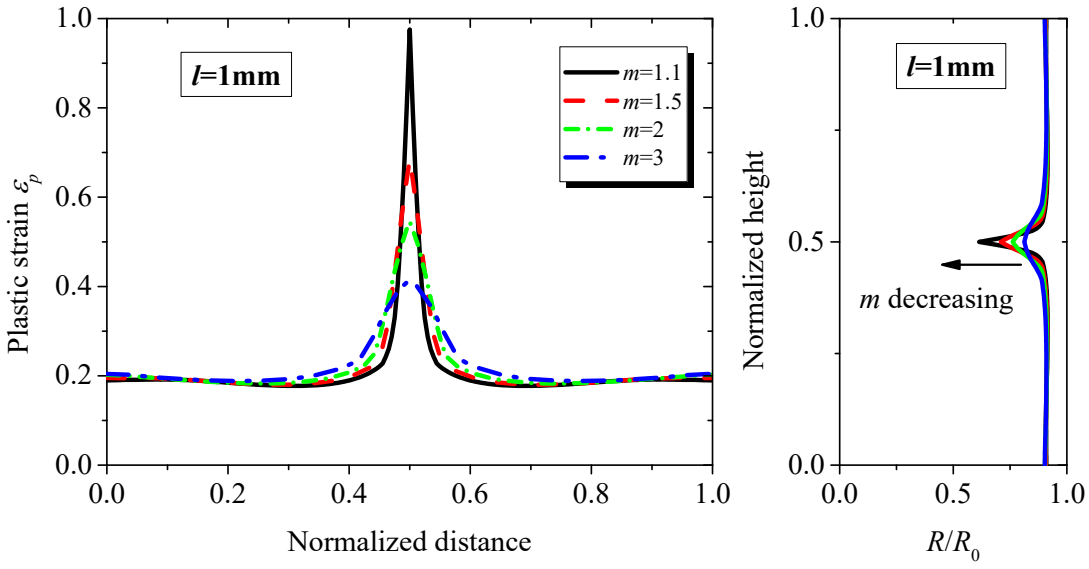

Fig. 6.11 The plastic strain profiles and necking shapes upon different nonlocal parameters at ΔL/L=0.25 (m=1.1, 1.5, 2, 3).

The purpose of the parametric studies is not only to investigate the effect of the characteristic length l and the nonlocal parameter m on the material behavior, but also to provide insight for material property measurement, e.g., the strain hardening behavior, and material parameter calibration. As previously mentioned, the global load-deformation response is the primary evidence typically used for the material calibration process. Since there generally exists three parameters for this over-nonlocal formulation, numerous combinations can replicate the post-necking portion of load-displacement curve that reasonably fits experimental observations. This emphasizes the importance of local measurement, i.e., the profile of the localization region, in the calibration process. In other words, the experimental measurements are needed of the geometry of the necked region, including the length of the necked zone, the depth of the necking as well as its curvature.

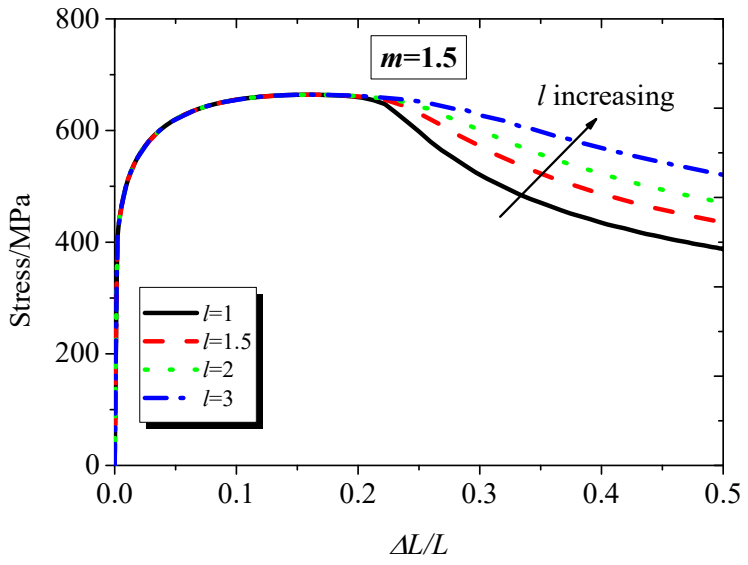

Fig. 6.12 The stress-elongation response upon different characteristic lengths (l=1mm, 1.5mm, 2mm, 3mm).

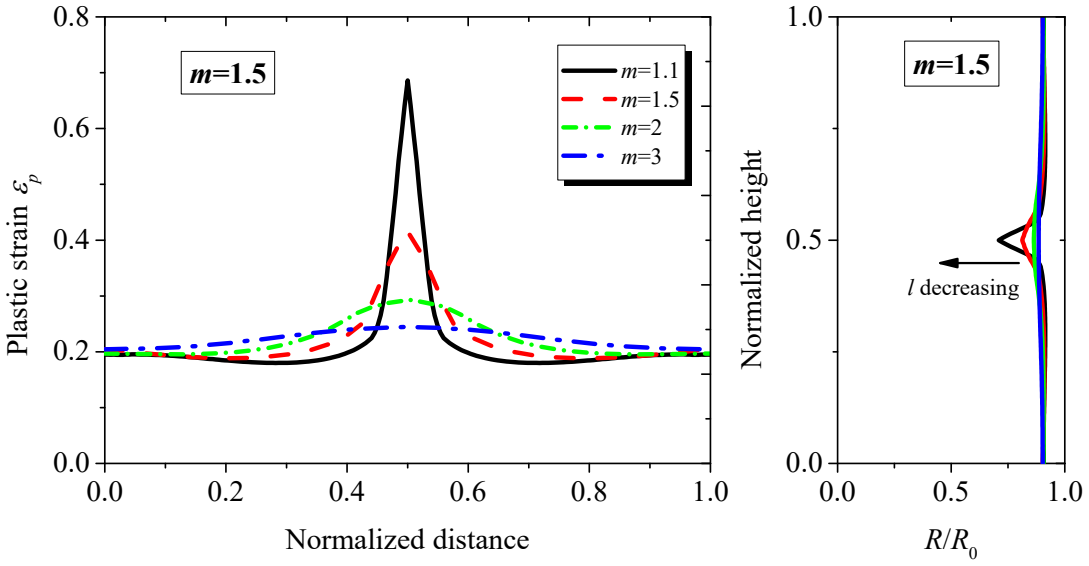

Fig. 6.13 The plastic strain profiles and necking shapes upon different characteristic lengths at ΔL/L=0.25 (l=1mm, 1.5mm, 2mm, 3mm).

6.6 APPLICATION OF THE ONE-DIMENSIONAL MODEL

The performance of the one-dimensional model with nonlocal formulation is based on tacit assumption that the one-dimensional case is equivalent to the full three-dimensional model. However, such a reduced dimensional configuration cannot completely reproduce all of the conditions in 3D cases. The most noteworthy limitation of this model is its lack of compatibility condition for the kinematic formulation. One remarkable evidence of this shortcoming is the sudden change in uniaxial strain, i.e., the geometric parameter, from the uniform region to the necking zone, which can be observed in Fig. 6.5. This is due to the fact that it is just the equilibrium equation, without the assistance of compatibility, that determines the uniaxial strain as well as the variation of area of the cross section. This limitation is highlighted in the local one-dimensional model. However, the model with nonlocal formulation partly remedies this drawback. But the

nonlocality is still incapable of ensuring the longitudinal area variation totally follows the compatibility condition. This suggests the necessity that the nonlocal parameter and characteristic length to be calibrated based on a geometric basis. Once the predicted geometric parameter variation by the nonlocal model coincides with the experimental facts, the compatibility condition is satisfied automatically.

Assuming a circular cross section, the geometry with respect to the radius variation can be evaluated using Eq. (6.62). In many cases, the uniaxial tension test is on a specimen with rectangular cross section. In this case, the extent of shrinkage in one direction is not necessarily equal to that in the other direction, so that the necking shape in either direction cannot be determined by the square root of the geometric parameter. From the experimental operation point of view, it is more practical to measure the width of cross section than directly measure the area of cross section. In the case of where information the necking relation between two sides is lacking, the assumption that both sides of the cross section have the same necking process would simplify the procedure of establishing the geometric profile in numerical modeling. The validation of the hypothesis can be performed during the parameter identification process if experimental evidence is sufficient.

Regarding the nonlocal treatment employed in the current study, replacing the plastic variable in the current yield stress by its nonlocal counterpart is not the only option. In fact, the geometry parameter, which induces strain softening, has a very similar role as the damage variable in a damage plasticity coupled model. For some nonlocal damage models, only the damage variables are considered for nonlocality treatment. In this case, the alternative to the present nonlocal formulation is just replacing the geometry parameter related plastic strain by its nonlocal quantity while keeping the strain hardening related plastic strain as the local variable. More simply, this kind of nonlocal model only requires

a standard nonlocality, i.e., m=1, which is confirmed by Rolshoven (2003) and Di Luzio and Bažant (2005). By reducing the number of parameters, the model would somehow lose part of its flexibility, especially in reproducing the geometric characters of the problem. In all, this potential nonlocal model needs further investigation to confirm its regularization effect, and robustness in predicting material properties.

With cautious manipulation of this one-dimensional nonlocal model, it is expected to provide a valuable tool to calibrate material behavior for the post-necking regime without encountering the numerical dilemma of spurious mesh dependency. Besides, the present model is capable to partly recover the longitudinal geometry. Beyond that, it is impossible to capture any information regarding transverse distributions of strain or stress since the model is established based the simplified average strain at a given cross section. In addition, this model is only applicable to the uniaxial tension case while the geometry induced localization problem is common in situations other than ordinary tensile testing for structural metals. Considering these limitations, extending the present model to a 2D or full 3D model is preferred when one is interested in studying more detailed mechanical behavior than the true stress-strain curve representing the actual material when such necking like localization occurs.

6.7 CONCLUSIONS

Much attention has been drawn to the mesh dependency problem when calibrating the post-necking material behavior for structural metals by numerical simulations. This problem is confirmed to be inevitable within the framework of the standard constitutive law. In this case, to explore the essence of this spurious mesh sensitivity in modeling post-necking behavior and to handle this issue, a one-dimensional model as well as its nonlocal

formulation is proposed in this chapter.

Necking, known as a strain localization phenomenon in uniaxial tension specimen, is caused by nonlinear geometry. This geometry effect is converted to the material effect in the one-dimensional case as a factor contributing to strain softening. Behavior of this model in both the static and the dynamic context was studied analytically. The results demonstrate the initial boundary value problem is ill-posed when the material transitions from strain hardening to softening, which causes the singularity of numerical solutions that is as mesh dependency.

The nonlocal constitutive law, which is believed to provide regularization to the localization problem, was adopted to investigate the necking phenomenon in structural metals. The fundamental approach was to substitute the local plastic strain in the current yield surface by its nonlocal counterpart. The analytical solutions for the nonlocal model is well-posed and gives a constant length of the localization region. Numerical investigation was also performed and the mesh insensitivity in the numerical solutions was demonstrated.

The length, the plastic strain distribution as well as the geometric profile of the necked region are strongly dependent on the nonlocal parameter and the characteristic length, which also determine the accuracy and robustness of this one-dimensional nonlocal model in evaluating material behavior. Consequently, the identification procedure for these two parameters need focus not only on the global material response, but also on the local measurement, i.e., the details of localization geometry. Shortcomings of this one-dimensional model limit its application to calibration of post-necking material behavior to the uniaxial tension case. Geometry induced localization in other situations than that of necking requires the extensions of current model to 2D and full 3D models. Nonlocal

approaches offer an encouraging direction to deal with the localization issue in structural metals.

CHAPTER 7

A Nonlocal Triaxiality and Shear Dependent Continuum Damage Model for Finite Strain Elastoplasticity

7.1 INTRODUCTION

Strain localization is a common phenomenon in a material undergoing large plastic deformation. With this phenomenon, the mode of deformation transitions from a homogenous to a discontinuous pattern, with intense straining occurring in a narrow region. Some well-known manifestations of strain localization are necking in ordinary tensile testing of ductile metals and shear banding of soils and rocks subject to compression or shear. This plastic instability condition is caused by either mechanical, geometrical, microstructural, or thermal effects or combination of these, and is often a precursor to a complete failure, since the localized deformations significantly increase the cumulative damage. Other than the strain softening models used to represent strain localization of geotechnical materials, strain hardening material models are often adopted to simulate plastic behavior of metals. In contrast to strain softening materials, the loss of material stability in metals is dependent on the strain hardening process and accumulation of internal damage within the material as well as on the geometric evolution of the structure.

It is widely accepted that ductile failure in metals results from the microscopic process of the void nucleation, growth and coalescence (Rice and Tracy, 1968; Anderson and Anderson, 2005). Many physics-based models have been developed to describe the micromechanical process of ductile fracture. Among those, the Gurson model and its extensions have been widely used to predict void volume fraction evolution and its effect on plastic yield and flow rules during the ductile fracture process. The Gologanu–Leblond–

Devaux model improved the Gurson-type models by coupling the void shape effect with material behavior. A more phenomenological group of approaches is attributed to continuum damage mechanics (CDM) models. In these approaches, a damage variable, defined at the macro-scale, is introduced to represent the influence of micro-cracks and micro-void growth on degradation of material properties. This category of models is essentially established based on macroscopic considerations. The internal damage is further incorporated into constitutive equations representing the continuous deterioration of elastic properties and the yield stress using the notion of effective stress. Some key contributions of CDM model development and application includes work by Kachanov (1978), Saanouni et al. (1994), Germain et al. (1983), Lemaitre (1985), Lemaitre and Desmorat (2005) and Rousselier (1987; 2001). Among these, the Lemaitre damage model (Lemaitre, 1985) is popular and provides a basis for many other damage-coupled yield criteria. Its underlying function relates the damage increment to the equivalent plastic strain increment and the strain energy density release rate, which facilitates description of stress triaxiality dependency of the damage process. This allows the Lemaitre model to well describe the characteristics of ductile fracture. In general, the evolution of the damage variable leads to strain softening in structural metals, and is one important source that induces bifurcation and the strain and damage localization phenomena. This chapter will focus on such damage-dominated strain softening and localization modeling.

As discussed in the previous chapter, once the classical continuum approach is adopted to describe the bifurcation problem, the analytical solution of the governing equations of equilibrium losses its ellipticity and becomes physically meaningless. In this case, finite element results show an inextricable mesh dependency where reducing the mesh size does not lead to convergence. With increasing mesh refinement, the damage and

strain tend to localize into a band with zero thickness and with zero energy dissipation. To overcome these shortcomings, many enhanced continuum models and numerical solution strategies have been proposed. A common idea behind these approaches is to consider the stress at a material point depending on the strain field of the point itself as well as its neighborhood by introducing a characteristic or intrinsic length scale. Some typical formulations following this idea are cosserat, strain gradient and nonlocal theories. An early approach is provided by Cosserat and Cosserat (1909), who treated the material particle with rotational degrees of freedom in addition to the displacement degrees of freedom in the continuum description. Further, the development of cosserat continua to the couple-stress and the micropolar theories facilitates this family of approaches to regularize the momentum balance equations for strain localization cases. Another group of methods incorporate the higher gradients of displacements (the gradients of strains) into the material constitutive model and into the finite element formulation as additional degrees of freedom (Fleck and Hutchinson, 1993, 1997).

The last family of approaches is known as nonlocal models of the integral type. These enriched continuum models are based on a spatial smoothing of certain variables at a point over its surrounding volume. Some early studies of nonlocal approaches applied to elastic problems include Eringen (1966) and Eringen and Edelen (1972). These attempts, which considered the stress as a function of spatial averaged strain, aimed at describing interaction of crystal defects at small scales. Further development of nonlocal models extended to inelastic materials. Among these, Eringen (1981) and Eringen (1983) developed a nonlocal formulation for isotropic hardening and perfect plasticity, where the nonlocal variable is the elastic stress. Bažant et al. (1984) introduced the nonlocal total strain tensor to a strain softening damage model to recover a well-posed boundary value

problem. Bažant and Lin (1988) proposed nonlocal plasticity models, in which the variables subjected to nonlocal spatial integration are either the plastic strain or the rate of the plastic multiplier while the elastic part of the strain remains unchanged. Nonlocal formations were coupled with continuum damage mechanics to describe quasi-brittle materials, which show strong strain softening behaviors (Bažant and Pijaudier-Cabot,1988; Jirásek and Rolshoven, 2003; Bažant and Jirásek, 2002; Borino et al, 2003; Peerlings et al.,1996; Grassl and Jirásek, 2006). The application of nonlocal approaches to describe softening and fracture phenomena of ductile materials is relatively recent (Tvergaard and Needleman, 1995; Brunet et al., 2004; Andrade et al., 2009; Belnoue et al., 2009; Chow et al., 2011). Nonlocal averaging treatments were introduced into either continuum damage models for macroscopic fracture problem (Belnoue and Korsunsky, 2012; Belnoue et al., 2010; Korsunsky et al., 2005) or micromechanics based material constitutive equations to study response of metal matrix composites (Drabek and Böhm, 2005; 2006; Brunet et al., 2005). Other studies showed the numerical validity and efficiency of nonlocal approaches applied to ductile metals (Andrade et al., 2011; Belnoue et al., 2007; Poh and Swaddiwudhipong, 2009; Peerlings et al., 2012). With its ability to overcome numerical instability resulting from strain softening, to avoid nonconvergent mesh sensitivity, and to capture size effects, the nonlocal approach becomes a valuable tool to describe ductile fracture.

Even though regularization approaches are adopted in numerical modeling, highly distorted elements in the localization region is sometimes inevitable. This issue is more prominent for strain localization of metal materials characterized as highly ductile, e.g. structural steels. The localized effect leads the elements to have unexpected shapes and aspect ratios in narrow zones under large deformations. This will in turn affect the

effectiveness of the nonlocal treatment and mesh dependency issues. Therefore, a sufficient numerical grid consisting of appropriately shaped elements is needed during the deformation history. In contrast to the Lagrangian framework that cannot deal with the element distortion issue, the adaptive remeshing strategy based on arbitrary Lagrangian-Eulerian (ALE) formulations provide a useful strategy to maintain high-quality in the spatial mesh and trace the boundary. The idea of the ALE approach is to allow the mesh movement independent of material flow, which circumvents the limitation of the Lagrangian approach by taking advantage of the Eulerian approach. Early applications of the ALE technique to one and two-dimensional localization problems includes work by Huerta et al. (1992), Pijaudier-Cabot et al. (1995) and Askes et al. (1998). Though the spatial discretization of the localization zone is improved through ALE remeshing optimization, the governing equation of equilibrium is still ill-posed. With the ALE framework, the connectivity as well as the number of the elements remain unchanged. Consequently, it is possible to apply this method to a nonlocal-coupled finite element formulation for the localization problem. The motivation to pursue this approach is to avoid an unreasonable numerical solution caused by spurious localization and element distortion, and to achieve numerical convergence to the physically realistic point.

In a Lagrangian formulation, the average operator of the nonlocal model is evaluated at either the deformed configuration, i.e. Eulerian-type, or the undeformed configuration, i.e. Lagrangian-type. For small strains, these two averaging strategies lead to negligible differences. This may not be true in a finite strain case. This is not only related to the averaging weight factor of each material point, but also because the number of material points that account for the nonlocal influence would be dramatically changed. As the ALE approach is adopted to the finite strain formulation, it gives rise to a more complex

comparison between the two strategies. Besides, these two averaging strategies have significant effect on the computational efficiency. The Lagrangian-type allows the averaging computation to be carried out only at the beginning of each analysis, while for the Eulerian-type, the averaging operator needs to be updated at every time increment. Considering their performances in both computational cost and numerical accuracy, it is necessary to evaluate and compare these two strategies within the combined nonlocal model and ALE framework.

The objective of this chapter is to propose a shear stress and triaxiality dependent nonlocal continuum damage model to deal with strain softening. For numerical modeling, the ALE approach is coupled with nonlocal treatment. The combination of these two strategies is aimed to eliminate spurious mesh sensitivity for the strain localization problem completely. The mixed explicit and implicit scheme is adopted for numerical implementation. Evaluation of the proposed method will be performed based on a comparison of ALE and nonlocal model in terms of damage and strain localization zone length and load-displacement response. Two numerical examples will be carried out to illustrate the performance of the proposed nonlocal model, the validation of the ALE remapping strategy, and the efficiency of the numerical algorithm.

7.2 LOCAL CONTINUUM DAMAGE

7.2.1 Kinematics

In the framework of continuum mechanics, deformations or strains are arbitrarily large. In this case, it is preferred to describe the deformation by finite strain theory. The large strain is evaluated using the approach of polar decomposition. The deformation gradient $\boldsymbol{F}$ can be given as

$$\boldsymbol{F} = \boldsymbol{F}^e \boldsymbol{F}^p \tag{7.1}$$

where $\boldsymbol{F}^e$ and $\boldsymbol{F}^p$ are the elastic and plastic deformation gradients, respectively. While the plastic deformation $\boldsymbol{F}^p(\mathbf{x})$ involves the history of plastic flow at material point $\mathbf{x}$, the elastic counterpart $\boldsymbol{F}^e(\mathbf{x})$ is a function of the current stress and plastic deformation gradient $\boldsymbol{F}^p(\mathbf{x})$, which represents the stretching and rotation of the microstructure that leads to the elastic distortion in an infinitesimal neighborhood of $\mathbf{x}$. In this case, $\boldsymbol{F}^e$ and $\boldsymbol{F}^p$ can be further expressed using the right and left polar decompositions:

$$\begin{aligned} \boldsymbol{F}^e &= \boldsymbol{R}^e \boldsymbol{U}^e = \boldsymbol{V}^e \boldsymbol{R}^e \\ \boldsymbol{F}^p &= \boldsymbol{R}^p \boldsymbol{U}^p = \boldsymbol{V}^p \boldsymbol{R}^p \end{aligned} \tag{7.2}$$

Regarding the elastic portion, $\boldsymbol{R}^e$ is a rotation, while $\boldsymbol{U}^e$ and $\boldsymbol{V}^e$ are symmetric, positive-definite right and left elastic stretch tensors, respectively. Likewise, $\boldsymbol{R}^p$, $\boldsymbol{U}^p$ and $\boldsymbol{V}^p$ are the plastic counterparts. The elastic stretch tensors subsequently give

$$\begin{aligned} \boldsymbol{b}^e &= \boldsymbol{F}^e \boldsymbol{F}^{e\mathrm{T}} = \left(\boldsymbol{V}^e\right)^2 \\ \boldsymbol{C}^p &= \boldsymbol{F}^{p\mathrm{T}} \boldsymbol{F}^p = \left(\boldsymbol{U}^p\right)^2 \end{aligned} \tag{7.3}$$

where $\boldsymbol{b}^e$ is the elastic left Cauchy-Green tensor and $\boldsymbol{C}^p$ is the plastic right Cauchy-Green tensor.

7.2.2 Finite strain elastoplasticity

The relation between the elastic stretch tensor and the logarithmic measure of elastic strain can be expressed as

$$\varepsilon^e = \ln(\boldsymbol{V}^e) = \frac{1}{2}\ln(\boldsymbol{B}^e) \tag{7.4}$$

The effective Kirchhoff stress tensor can be calculated using the linear elasticity

fourth-order tensor

$$\begin{aligned} \hat{\boldsymbol{\tau}} &= {}^4\boldsymbol{H} : \varepsilon^e \\ {}^4\boldsymbol{H} &= \kappa \boldsymbol{I} \otimes \boldsymbol{I} + 2\mu({}^4\boldsymbol{I}^s - \frac{1}{3}\boldsymbol{I} \otimes \boldsymbol{I}) \end{aligned} \tag{7.5}$$

where κ and μ denote the bulk and shear modulus, respectively. $\boldsymbol{I}$ and ${}^4\boldsymbol{I}^s$ are the 3×3 identity matrix and fourth-order identity tensor. Note that the Kirchhoff stress has a simple relation with the Cauchy stress given as

$$\hat{\boldsymbol{\tau}} = J\hat{\boldsymbol{\sigma}} \tag{7.6}$$

where J is the volume change ratio and is calculated by the determinant of the deformation gradient, det$\boldsymbol{F}$. Following the J_2 criterion, a plastic potential function is given in terms of the effective Kirchhoff stress $\hat{\tau}_{eq}$

$$\hat{\phi}(\hat{\boldsymbol{\tau}}, \tau_y) = \hat{\tau}_{eq} - \tau_y(\gamma) = \sqrt{\frac{3}{2}\hat{\boldsymbol{\tau}}^d : \hat{\boldsymbol{\tau}}^d} - \tau_y(\gamma) \tag{7.7}$$

where τ_y is the current yield stress and is determined by the current equivalent plastic strain γ. $\hat{\boldsymbol{\tau}}^d$ is the deviatoric component of Kirchhoff stress. Given a plastic multiplier $\dot{\gamma}$, the equation above must also satisfy the Kuhn–Tucker loading-unloading condition and the plastic consistency condition

$$\dot{\gamma} \geq 0, \quad \hat{\phi} \leq 0, \quad \dot{\gamma}\hat{\phi} = 0 \text{ and } \dot{\gamma}\dot{\hat{\phi}} = 0 \tag{7.8}$$

7.2.3 Continuum damage model

Due to nucleation and growth of micro-voids or micro-cracks in ductile metals, the material strength on a micro-mechanical scale gradually degrades, which may lead to final macroscopic failure. To have a continuous description of this deterioration, damage

variables are introduced into continuum constitutive equations within the framework of continuum mechanics. Such damage coupled constitutive models, which are capable of capturing the progressive increments of damage and the evolution of material deterioration, are essentially macroscopic measurement and phenomenological in nature. The basic hypothesis of continuum damage mechanics is strain equivalence, where the strain at a damage state is equivalent to that at its undamaged state. The effective Kirchhoff stress $\hat{\boldsymbol{\tau}}$ at an undamaged state can be related to the applied stress $\boldsymbol{\tau}$ at a damage state given as:

$$\hat{\boldsymbol{\tau}} = \frac{\boldsymbol{\tau}}{1-D} \tag{7.9}$$

where D is a scalar damage variable such that D=0, 1 are the lower and upper bounds representing undamaged and complete failure states, respectively. With the strain equivalence and effective stress principles, the constitutive law for a damaged material can be easily formulated using the equations referred to the undamaged material, by replacing the applied stress $\boldsymbol{\tau}$ by the effective stress $\hat{\boldsymbol{\tau}}$. Considering an isotropic material, the Helmholtz's free energy form of thermodynamic potential ψ is given as

$$\psi = \psi(\varepsilon^e, \gamma, D) \tag{7.10}$$

Assuming the contributions of the elasticity-damage and the plasticity to the free energy are decoupled, the thermodynamic potential can be written as

$$\psi = \psi^{ed}(\varepsilon^e, D) + \psi^p(\gamma) \tag{7.11}$$

According to Lemaitre's model, the elasticity-damage part of the thermodynamic potential ψ^{ed} is assumed as

$$\rho\psi^{ed} = \frac{1}{2}\varepsilon^e : (1-D)^4 \boldsymbol{H} : \varepsilon^e \tag{7.12}$$

The corresponding state laws follow as

$$\boldsymbol{\tau} = \rho \frac{\partial \psi}{\partial \varepsilon^e} = \rho \frac{\partial \psi^{ed}}{\partial \varepsilon^e}; \quad -Y = -\rho \frac{\partial \psi}{\partial D} = -\rho \frac{\partial \psi^{ed}}{\partial D} \tag{7.13}$$

where ρ is the constant material density and -Y represents the energy release rate. Combining Eq. (7.12) and the second term of (13) leads to

$$Y = \frac{-\tau_{eq}^2}{2E(1-D)^2}\left[\frac{2}{3}(1+\upsilon) + 3(1-2\upsilon)\left(\frac{\tau_h}{\tau_{eq}}\right)^2\right] \tag{7.14}$$

where E is Young's modulus, υ is Poisson's ratio, τ_h and τ_{eq} are the hydrostatic pressure and the von Mises equivalent stress, respectively, both of which are calculated by the Kirchhoff stress tensor. In addition, the term τ_h/τ_{eq} denotes the triaxiality, which significantly influences the ductile fracture process. By introducing the concept of triaxiality

$$R_v = \frac{2}{3}(1+\upsilon) + 3(1-2\upsilon)\left(\frac{\tau_h}{\tau_{eq}}\right)^2 \tag{7.15}$$

the energy release rate can be treated as the product of the stress related term and triaxiality function. On the other hand, the dissipation potential, complementary to the thermodynamic potential, is defined as the sum of the damage part ${}^*\psi^d$ and the plastic part ${}^*\psi^p$

$${}^*\psi = {}^*\psi^d + {}^*\psi^p \tag{7.16}$$

Regarding the dissipation potential due to the damage, a function proposed by Lemaitre (1985) is introduced in terms of the damage variable and energy release rate as follows

$$^{*}\psi^{d} = \frac{r}{(1-D)(s+1)}\left(\frac{-Y}{r}\right)^{s+1} \tag{7.17}$$

where r represents the energy strength of damage, and s is a temperature-dependent material parameter. The underlying principles for developing this damage potential include the ideas that the damage rate remains proportional to the plastic multiplier and it increases with the energy release rate, both of which are based on micromechanics-based observations.

In this chapter, the temperature is assumed to be room temperature and its effect on the damage evolution will not be considered. As reported by Andrade et al. (2009), the parameter s is treated as s=1. On the other hand, the original version of Lemaitre's damage model considered that ductile damage results from microvoid nucleation and enlargement, both of which have strong links with the triaxiality. The effect of this stress related quantity has been included in the factor R_v. However, this may not be true when ductile facture occurs at low triaxialities or under loading cases such as plane strain, for which the effect of shear stress overwhelms the triaxiality. The physical manifestation of this effect is the prominent elongation of microvoids or microcavities, and the final void coalescence and material failure is driven by shear localization. A generalized damage model needs to couple such the shear stress effect into the damage dissipation potential. Noting that this effect is measured by the Lode parameter or the maximum shear stress ratio, the variable $\bar{\phi}$ factor is introduced to quantify the shear stress effect and is given as

$$\bar{\phi} = 2\frac{\tau_1 - \tau_3}{\tau_{eq}} \tag{7.18}$$

where τ_1 and τ_3 are two of the three principal stresses with the order of $\tau_1 \geq \tau_2 \geq \tau_3$. Owing to the relation between the equivalent stress τ_{eq} and the principal stresses, the upper and lower

bounds of the $\bar{\phi}$ factor are directly determined as $2/\sqrt{3}$ and 1. The case with the lower bound of the $\bar{\phi}$ factor refers to the axisymmetric loading case whereas the upper bound is attributed to the plane strain case. Considering the shear stress effect on both micromechanical behavior and macroscopic damage evolution, the damage energy strength is further given as

$$r = \frac{r_0}{1 + A\bar{\phi}^m} \tag{7.19}$$

where r_0, A and m are material parameters. The combination of A and m determines the effect of shear stress on the damage evolution process. Both A and m must be non-negative, ensuring that higher values of $\bar{\phi}$ lead to a greater potential of damage dissipation. A=0 reduces the damage dissipation potential to a shear stress independent function.

The dissipation potential due to plasticity, adopting the von Mises yield function and the Kirchhoff stress measurement, takes the form

$${}^{*}\psi^{p} = \frac{\sqrt{3J_2}}{(1-D)} - \tau_y(\gamma) = \frac{q}{(1-D)} - \tau_y(\gamma) \tag{7.20}$$

Combining Eq. (7.17), (7.19) and (7.20), the evolution rates of the damage variable and the plastic strain are given as

$$\dot{D} = \dot{\gamma}\frac{\partial^{*}\psi}{\partial(-Y)} = \frac{\dot{\gamma}}{(1-D)}\left(\frac{-Y}{r}\right)^{s}; \quad \dot{\varepsilon}^{p} = \dot{\gamma}\frac{\partial^{*}\psi}{\partial\boldsymbol{\tau}} = \dot{\gamma}\sqrt{\frac{3}{2}}\frac{\boldsymbol{\tau}^{d}}{(1-D)\left\|\boldsymbol{\tau}^{d}\right\|} \tag{7.21}$$

where $\boldsymbol{\tau}^{d}$ is the deviatoric component of the Kirchhoff stress tensor.

7.3 NONLOCAL APPROACH

The standard (local) continuum theories show their robustness in modeling material

behavior within a considerable range of applications. However, their inability is noteworthy in some areas such as obtaining objective and mesh insensitive numerical solutions for localized softening and damage problems, describing microstructural heterogeneity at small scales, and capturing size effects. Regarding the first point, the drawback of the local approach can be interpreted by two aspects. First, as the tangential stiffness of a material becomes negative, the stress waves would be neither propagating in an arbitrary direction nor completely stationary. Second, for the static boundary value problem, the governing differential equation changes its type from elliptic to hyperbolic and becomes ill-posed, by which an infinitesimal change in the initial conditions can lead the numerical solution to be unstable. To deal with the numerical instability issue in modeling the behavior of a softening material, the development of the constitutive models is indispensable to regularize the boundary value problem. Other physical reasons necessitating an improvement of local continuum theories is, for instance, for the microstructure on a small scale, the strain that matters for the macroscopic stress is not a point-based value but the spatial integrated strain value within a volumetric domain. These facts motivate the development of constitutive models that couple the nonlocality of material into their general equations. The basic idea of the nonlocal treatment is to substitute a certain variable in the constitutive model by its nonlocal counterpart. The nonlocal variable $\tilde{f}(x)$ is defined as a spatial integration of the local quantity $f(x)$ in the entire domain Ω.

$$\tilde{f}(x) = \frac{1}{\int_{\Omega} \alpha(x,\xi)\, d\xi} \int_{\Omega} \alpha(x,\xi)\, f(\xi)\, d\xi \tag{7.22}$$

where $\alpha(x,\xi)$ is the non-negative weight function selected for nonlocal integration. For the sake of simplicity, the normalized version of the weight function is always adopted and can

be defined as

$$\alpha^{*}\left(x,\xi\right)=\frac{\alpha\left(x,\xi\right)}{\int_{\Omega}\alpha\left(x,\xi\right)d\xi} \tag{7.23}$$

The function $\alpha(x,\xi)$ must be symmetric about the host point at x and monotonically decreasing with the distance $\|x-\xi\|$ from the point $\xi=x$, where there is a maximum $\alpha(x,x)$. Many functions can fulfil these required characteristics, for instance, the Gauss-error function and the bell-shaped function. As is widely adopted in nonlocal approaches, the bell-shaped function is also applied in this chapter, and is given as

$$\alpha\left(x,\xi\right)=\begin{cases}\left(1-\left\|x-\xi\right\|^{2}/l^{2}\right)^{2} & \text{if} \quad \left\|x-\xi\right\|\le l\\ 0 & \text{if} \quad \left\|x-\xi\right\|>l\end{cases} \tag{7.24}$$

where l is a characteristic length parameter. This length parameter, or in other words, the nonlocal interaction radius, does not necessarily equal to but relies only on the material intrinsic length. The determination of the weight function is seemingly based on mathematical considerations. In fact, the function has its physical linking with microcracks as well as their surrounding boundaries. It can be treated as a material property and is dependent on the stress field in a neighborhood of the point. The contained length parameter serves to partially reflect these behaviors of the weight function of spatial integration.

7.3.1 Characteristic length

The physical interpretation of the length parameter in metal materials can be linked to microstructural features such as the void spacing and the density of geometrically necessary dislocations. The length parameter in a nonlocal continuum can be determined

using a combination of experiments and FEM inverse analysis. Experimental investigations of characteristic length are required to focus on the micromechanical response or macroscopic material behavior of region in which damage or strain is localized. For instance, this may involve measuring the energy dissipation and plastic strain distribution in softening or damage localized regions. In terms of FEM analysis for the nonlocal interaction prediction, examinations of both global and local mechanical responses are needed to identify an accurate nonlocal length. While fitting the global load-displacement curve is a prerequisite, the analysis of the local strain fields provides deeper insights into the information which is more relevant to the strain and damage localizations. However, to the author's knowledge, the precise determination of nonlocal length parameter is complex and is indirectly based on experimental evidence and numerical solution until now. Moreover, the proposed values of internal length for metals are quite varied, from a few nanometers to a few centimeters, and there is no widely accepted value. The characteristic length and the nonlocal interaction radius in this chapter are simply considered as a numerical parameter. In the FE computational viewpoint, this characteristic length l requires a compromise on the FE modeling in that it needs to be greater than the maximum mesh size in the region of interest, ensuring that the interaction volume of a material point covers at least a few neighboring points. The present study is not intended to compare the results of simulation to any experimental observations. The effect of the length parameter on the global and local responses will be investigated to further demonstrate the ability of the nonlocal approach to avoid mesh dependency and the ability be an effective localization limiter.

7.3.2 Nonlocal variable selection

The basis of the nonlocal continuum damage model is to define damage in a nonlocal manner. This can be done by several possible formulations, which, for instance, involve the nonlocal damage energy release rate, nonlocal strain tensor, nonlocal plastic multiplier, inelastic stress, or inelastic stress increment. Evaluations and comparisons of these approaches by Jirásek (1998) show that different types of nonlocal averaging lead to different computational costs and material responses. Thus, some nonlocal formulations give rise to unreasonable behavior and are inherently flawed. Micromechanical investigations on the interactions among microcracks also suggest that variables such as stress and elastic strain tensors are local (Bažant, 1991). The principle for nonlocal variable selection suggested by Bažant and Jirásek (2002) is that the candidate variable never decreases and relates to the dissipative mechanism. In this case, the damage energy release rate and the damage variable appear to be most appropriate to describe the localization problem properly in the framework of CDM. A simple nonlocal formulation of damage coupled plasticity is obtained if the local damage variable is replaced by its nonlocal quantity. Note that if the nonlocal averaging is directly applied to the damage variable itself, the quantities from the elastic loading/unloading regions can influence the nonlocal algorithm in a physically unreasonable manner. Consequently, it is necessary to take the increment of the damage variable for averaging treatment, expressed as

$$\tilde{\dot{D}}(x) = \int_{\Omega} \alpha^{*}(x,\xi)\,\dot{D}(x)\,d\Omega \tag{7.25}$$

where $\dot{D}(x)$ and $\tilde{\dot{D}}(x)$ are the local and nonlocal increment of damage variable, respectively.

7.3.3 Lagrangian vs. Eulerian non-locality

There exist two types of non-locality, i.e. Lagrangian and Eulerian, to evaluate the nonlocal kernel in Eq. (7.23). As noted above, if both the interactive volume and the weight function are computed in the undeformed configuration and are not updated during the deformation history, such treatment is called Lagrangian or material non-locality. Conversely, the Eulerian or spatial nonlocality refers to the case where the domain and the weight function are evaluated in the deformed configuration. In the Lagrangian type of formulation, the nonlocal domain for a point undergoes deformation with the entire material. The nonlocal kernel for each material point, which is initially within the interactive volume, remains unchanged. In this case, the length parameter, i.e. the interactive radius, is essentially non-constant and is heavily dependent on the deformation. Whereas, the interactive domain for the Eulerian formulation will keep its geometry, and just move with its host material point. Due to the deformation of the material, the material points that are within the domain during the deformation will not necessarily be those that initially belong to the domain. In the special case of tension, material particles tend to leave the interactive volume with the continuous deformation so that the solution becomes more likely local. The opposite situation will be found in compression, where the interactive domain will include an increasing number of material particles, which leads to a more nonlocal outcome. Consequently, the weight factor in Eq. (7.23) may evolve significantly within the framework of finite strain elastoplasticity.

On the other hand, physical evidence to determine the best approach for non-locality is not well established. Further investigation is needed to establish whether the nonlocal kernel is dependent on deformation or not. The current study mainly concentrates on the computational efficiency of these two approaches. Obviously, the Eulerian approach

is significantly more expensive than the Lagrangian approach in numerical implementation. The assessment of their performance will also be based on the comparison of numerical results by these two types of non-locality using numerical examples.

7.4 ARBITRARY LAGRANGIAN-EULERIAN APPROACH

Even though the nonlocal treatment avoids zero global dissipation of energy and remains well-posed for the strain localization problem, its drawback emerges at the ultimate stages of the material failure, where strain localized into one or two layers of elements with large distortions. One remedy is to refine the mesh of the critical zone at the beginning of the analysis, ensuring that the numerical grid can capture the large strain gradients to the greatest possible. However, the inability of this approach to prevent element distortion and excessive computational cost caused by extra degrees of freedom lead to the need for a remeshing strategy. The motivations of introducing such spatial discretization adaptivity are to provide a less expensive alternative to initial mesh refinement that achieves a well-defined interpolation of strain localization without unnecessarily increasing mesh quantities.

The ALE approach involves three main stages including the updated Lagrangian phase, the smoothing phase, and the advection phase. In the Lagrangian step, equilibrium is achieved by solving the governing equation in a pure Lagrangian form, i.e., keeping the spatial map moving along with the material map. The subsequent smoothing and advection phases are not necessarily performed at every time increment, but are activated either at the end of every few increments or once the element quality meets a certain criterion. Once an unacceptable distortion is detected, the smoothing step is activated to determine a new mesh by pulling the nodes towards the locations with less distortion. This is performed

based on the strategy of redefining the spatial maps while keeping the material map fixed. The third phase of adaptive remeshing is following with the accomplishment of mesh sweeps when the targeted mesh quality is obtained. This operation is due to independent mesh and material motion in the smoothing phase and remaps solution variables from previous Lagrangian mesh to the new mesh. The new quantities are computed by evaluating the momentum balance and mass conservation equations, into which the advective terms, reflecting the relative motion between the material and the mesh, are introduced. Herein, even though all the node and element variables are remapped separately through the advection strategy, equilibrium and consistencies among variables are not guaranteed. Accordingly, the plastic internal variables, the damage variables and stress tensors at the quadrature points and the spatial positions, and velocities and accelerations at the nodes are selected to be re-evaluated. All other variables are reconstructed by enforcing the constitutive equations. The yield surface will also be updated after the transfer of all solution variables to re-satisfy the loading-unloading conditions. All the convergences and consistencies need to be achieved before the following updated Lagrangian procedure, ensuring a robust, accurate and stable numerical treatment of adaptive remeshing.

Once remeshing occurs, a material point that coincides with a gauss integration point of an element at the beginning of the analysis may not remain coincident with the same gauss point during the deformation history. On the other hand, the nonlocal evaluation is a material point based operation. To avoid numerical instability, the nonlocal integration and the adaptive meshing are performed at different time points, i.e., the former one is done right after the updated Lagrangian step has completed and the latter one takes place at the beginning of each time increment. This is to guarantee that the nonlocal

variables of a specific material point are computed based on the material map instead of the spatial map and to track the histories of nonlocal variables in a physical and consistent manner. However, transferring the nonlocal variables during the advection phase is in the same as transferring other local state variables. Circumventing any disturbance caused by the deviation of mesh and material points, the adopted strategy provides numerical accuracy for the nonlocal and ALE coupled computation in the current study.

7.5 NUMERICAL IMPLEMENTATION

The analysis procedure in the present study is globally based on the explicit integration scheme. The computational efficiency of this algorithm results from having no iterations and no need for a tangent stiffness matrix. As an essentially dynamic procedure, it requires an extensive number of time step, and sufficiently small time increments to achieve conditional stability and represent a quasi-static process. On the other hand, the constitutive equation is highly non-linear since it contains the continuum damage representation and the nonlocality so that it requires additional computational treatment. To describe the behavior of the material subjected to a given deformation gradient, a fully implicit predictor-corrector algorithm is employed using classical Newton-Raphson iteration to give accurate material response at each time interval. Therefore, the strategy adopted in the present study is a mixed explicit-implicit type, which achieves an inexpensive numerical implementation while still providing accuracy.

7.5.1 Time discretization

The primary unknown variables are the displacement field as well as the deformation gradient tensor. To solve this, the second-order central-difference time integration scheme is applied. The entry point of the time discretization can be the dynamic

equilibrium equations, from which there is easy access to the accelerations at time t_{n}.

$$\ddot{u}_{(n)} = \mathbf{M}^{-1}\left(\boldsymbol{P}_{(n)} - \boldsymbol{R}_{(n)}\right) \tag{7.26}$$

where $\mathbf{M}$ is the mass matrix, $\boldsymbol{P}$ and $\boldsymbol{R}$ are the applied load vector and the internal force vector, respectively. The subscript n denotes the number of the time increment. Due to its simple inverse counterpart, the diagonal mass matrix is used in this equation, which significantly contributes to the computational efficiency of the explicit procedure. Besides, the internal force vector is attributed to the individual elements. Without assembling a global stiffness matrix, it is quite straightforward to calculate the accelerations at time t_{n}, which can then be used to derive the velocity and the displacement solutions at the following time increment n+1 given as

$$\dot{u}_{(n+1/2)} = \dot{u}_{(n-1/2)} + \frac{\Delta t_{(n+1)} + \Delta t_{(n)}}{2}\ddot{u}_{(n)} \tag{7.27}$$

$$u_{(n+1)} = u_{(n)} + \Delta t_{(n+1)}\dot{u}_{(n+1/2)} \tag{7.28}$$

where $\Delta t_{(\mathrm{n+1})}$ is the time increment from time t_{n} to time $t_{\mathrm{n+1}}$, and the subscripts n-1/2 and n+1/2 refer to mid-increment values. The variable $\dot{u}_{(n-1/2)}$ is calculated from the previous increment. Additional consideration is required to define the starting values of the mean velocities $\dot{u}_{(-1/2)}$ and $\dot{u}_{(+1/2)}$, both of which are specified as

$$\begin{aligned} \dot{u}_{(+1/2)} &= \dot{u}_{(0)} + \frac{\Delta t_{(1)}}{2}\ddot{u}_{(0)} \\ \dot{u}_{(-1/2)} &= \dot{u}_{(0)} - \frac{\Delta t_{(0)}}{2}\ddot{u}_{(0)} \end{aligned} \tag{7.29}$$

With the displacement field calculated by Eq. (7.28), the conversion from the gradient of displacements to the targeted deformation gradient is expressed as

$$\boldsymbol{F}_{(n+1)} = \nabla \boldsymbol{u}_{(n+1)} + \boldsymbol{I} \tag{7.30}$$

7.5.2 Elastic predictor-plastic corrector algorithm

Despite the additional complexity of the constitutive equations resulting from inclusion of the continuum damage, it is still efficient to adopt the conventional implicit elastic predictor/ returning mapping algorithm to the present plasticity model. To start with this scheme, a time increment from t_{n} to $t_{\mathrm{n+1}}$ is considered, upon which the items including the deformation gradient tensor at $t_{\mathrm{n+1}}$, $\boldsymbol{F}_{\mathrm{n+1}}$, the plastic deformation gradient tensor at t_{n}, $\boldsymbol{F}_n^p$, and the plastic internal variable at $t_{\mathrm{n+1}}$, ε_n^p are all known. Within the framework of the elastic predictor, the material is assumed to be purely elastic in the present time interval so that the incremental deformation tensor completely contributes to the elastic deformation leading to

$$^{\star}\boldsymbol{F}_{i,n+1}^{e} = \boldsymbol{F}_{i,n+1}\boldsymbol{F}_{i,n}^{p-1} \tag{7.31}$$

Herein, the subscript i denotes the material point number that is under processing. The asterisk * is to indicate that the corresponding quantity is under its elastic trial state. The trial elastic left Cauchy-Green deformation tensor can then be obtained as

$$^{\star}\boldsymbol{b}_{i,n+1}^{e} = \boldsymbol{F}_{i,n+1}\boldsymbol{C}^{p-1}\boldsymbol{F}_{i,n+1}^{\mathrm{T}} \quad \text{and} \quad ^{\star}\varepsilon_{i,n+1}^{p} = \varepsilon_{i,n}^{p} \tag{7.32}$$

from which the effective elastic trial stress tensor can be calculated using Eq. (7.4) and (7.5) as

$$^{\star}\hat{\boldsymbol{\tau}}_{i,n+1} = \frac{1}{2}\,{}^{4}\boldsymbol{H} : \ln(^{\star}\boldsymbol{b}_{i,n+1}^{e}) \tag{7.33}$$

The yield function is therefore evaluated based on the undamaged effective elastic stress and the yield stress from previous time increment t_{n}

$$^{\star}\hat{\phi}(\hat{\boldsymbol{\tau}},\tau_y) = {}^{\star}\left(\hat{\tau}_{eq}\right)_{i,n+1} - \tau_y\left({}^{\star}\gamma_{i,n}\right) \tag{7.34}$$

A negative value of this trial yield function indicates a completely elastic state for the current increment, and no further modification on the trial stress and strain tensors are needed. Otherwise, the plastic corrector using the return mapping scheme must be employed to update the plastic variable. Before that, the plastic flow at the current time interval is given as

$$^{\star}\boldsymbol{\eta}_{i,n+1} = \sqrt{\frac{3}{2}}\frac{^{\star}\hat{\boldsymbol{\tau}}^{d}_{i,n+1}}{\left\|^{\star}\hat{\boldsymbol{\tau}}^{d}_{i,n+1}\right\|} \tag{7.35}$$

The corrected stress tensor and equivalent plastic strain are obtained as

$$^{\star}\left(\hat{\tau}_{eq}\right)_{i,n+1} = \left(\hat{\tau}_{eq}\right)_{i,n+1} - 3\mu\Delta\gamma_{i,n+1} \tag{7.36}$$

$$\hat{\boldsymbol{\tau}}_{i,n+1} = {}^{\star}\hat{\boldsymbol{\tau}}_{i,n+1} - 2\mu\Delta\gamma_{i,n+1}\,{}^{\star}\boldsymbol{\eta}_{i,n+1} \tag{7.37}$$

$$\varepsilon^{p}_{i,n+1} = \varepsilon^{p}_{i,n} + \Delta\gamma_{i,n+1} \tag{7.38}$$

Given the explicit expressions above, the problem is to obtain the increment of the plastic multiplier $\Delta\gamma$, which is strongly related to the damage variable. The basic equations of the damage variable evolution can be written as

$$D_{n+1} = D_n + \Delta D_{n+1} \quad \text{and} \quad D_{n+1} = \frac{3\mu\Delta\gamma}{^{\star}\left(\hat{\tau}_{eq}\right)_{i,n+1} - \tau_y(\gamma_{i,n+1})} \tag{7.39}$$

Combining Eq. (7.39) and (7.21), a single residual equation as the function of the plastic variable increment can be given as

$$F\left(\Delta\gamma'\right) \equiv \frac{3\mu}{{}^{\star}\left(\hat{\tau}_{eq}\right)_{i,n+1} - \tau_y(\gamma_{i,n} + \Delta\gamma')} - \left(1 - D_{i,n}^{NL}\right) + \frac{{}^{\star}\left(\hat{\tau}_{eq}\right)_{i,n+1} - \tau_y(\gamma_{i,n} + \Delta\gamma')}{3\mu}\left(\frac{-Y}{r}\right)^s = 0$$

(7.40)

where the quantities D^{NL} and $\Delta\gamma'$ are the nonlocal damage variable and local plastic multiplier increment. The Newton-Raphson iteration algorithm is an effective approach to solve for the unknown variable $\Delta\gamma'$ from

$$\Delta\gamma'^{k+1} = \Delta\gamma'^{k} - \left(\frac{\partial F\left(\Delta\gamma'^{k}\right)}{\Delta\gamma'}\right)^{-1} F\left(\Delta\gamma'^{k}\right) \tag{7.41}$$

where the superscript k represents the number of Newton-Raphson iteration.

7.5.3 Nonlocal damage update

The increments of the damage variable and the plastic multiplier obtained by Eq. (7.39), (7.40) and (7.41) are essentially local variables since the residual equation for a point in Eq. (7.40) is solved independent on other material points. Once all the material points have been processed by the elastic predictor-plastic corrector algorithm, the local damage variable rates can be collected to compute their nonlocal counterparts by Eq. (7.25). Then the nonlocal damage variable at time t_{n+1} can be updated by

$$D_{i,n+1}^{NL} = D_{i,n}^{NL} + \dot{D}_{i,n+1}^{NL} \tag{7.42}$$

With the given nonlocal damage variable $D_{i,n+1}^{NL}$, the corresponding internal plastic variable $\Delta\gamma_{i,n+1}$ is then evaluated by the second term of Eq. (7.39). The plastic deformation gradient also needs to be updated as a known variable for the following time increment, which is obtained by

$$\boldsymbol{F}_{i,n+1}^{p} = \boldsymbol{F}_{i,n}^{p} + \Delta\gamma_{i,n+1}\boldsymbol{F}_{i,n}^{p} {}^{\star}\boldsymbol{\eta}_{i,n+1} \tag{7.43}$$

The strategy for the nonlocal treatment is relatively efficient, since neither iteration nor a global stiffness matrix is needed to obtain the nonlocal variable. This is the benefit of the explicit algorithm adopted in the present study. The nonlocal integration is only applied to the point that is plastic at time t_{n+1}. In other words, the material point without any local damage variable increment would occupy a zero value for its nonlocal damage variable increment.

7.6 NUMERICAL EXAMPLES

To illustrate the behavior of the proposed nonlocal continuum damage model and the computational efficiency of numerical treatments, two examples including the necking of a plane strain bar and tension applied to an axisymmetric cylindrical bar will be investigated. The items such as the mesh dependency, the contribution of adaptive remeshing, triaxiality dependency and shear stress ratio dependency will also be analyzed. Considering the objective of this chapter is to describe the numerical implementation of the proposed model without providing any parameter calibration procedure or experimental validation, the same damage related material parameters reported by Andrade et al. (2011) are employed in the present study. Regarding the strain hardening property of structural metals, a commonly used relation is employed and is given as

$$\sigma_y\left(\varepsilon_p\right) = \sigma_0\left(1 + \frac{E}{\sigma_0}\varepsilon_p\right)^n \tag{7.44}$$

where σ_0 is the initial yield stress and E is the elastic modulus. All the material parameters are listed in Table 7.1. Both example use the same material properties for comparison purposes.

Table 7.1 Material properties for numerical examples.

Elastic modulus, E	210GPa
Poisson's ratio, ν	0.3
Initial yield stress, σ_0	400MPa
Hardening exponent, n	0.15
Damage exponent, s	1.0
Damage denominator, r_0	5MPa
Damage shear-dependent exponent, m	2
Damage shear-dependent factor, A	0.21
characteristic length, l	0.63mm

7.6.1 Tension of a rectangular bar under plane strain

The example employed in this section is a two-dimensional plane strain case. The plate has a geometry with 20mm height and 5mm width. The bottom of the plate is subject to a fixed constraint and the top of the bar is subject to uniaxial tension. In order to keep strain localized into the central region of the plate and necking occurring at the same place, an imperfection is introduced wherein the width at mid-height is reduced by 0.8%. Three different mesh refinements have been considered to evaluate the effectiveness of the nonlocal model in overcoming the spurious mesh sensitivity problem. The model is discretized by bilinear plane strain elements with reduced integration. That means each element holds only one integration point and one material point. The FE discretizations shown in Fig. 7.1 with 400, 1122 and 4556 elements, respectively. The coarse mesh shown on the left of Fig. 7.1 has a uniform element size of 0.5mm, which is smaller than the characteristic length (0.63mm), indicating the nonlocal interactive circle could cover several elements at the beginning of deformation.

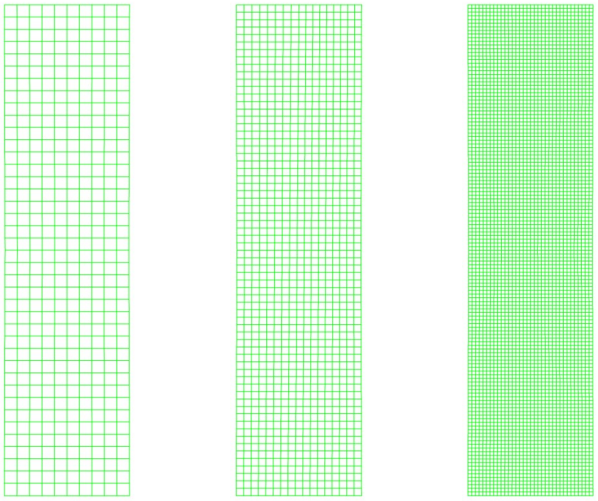

Fig. 7.1 Geometry and mesh refinements of the tension plate representing 400, 1122 and 4556 elements.

A straightforward way to illustrate the mesh sensitivity of the analysis is to compare the load-displacement curves resulting from different mesh refinements. The results with the local model, i.e. l=0, are shown in Fig. 7.2. The horizontal axis refers to relative displacement, which equals the ratio of the elongation to the initial height of the plate. For the results with and without the ALE adaptive remeshing, the force-relative displacement curves for the different discretizations are all deviating from each other, which clearly demonstrates a mesh dependency. The result implies the peak load with 3772 kN occurs at strain equal to 0.18, at which point the necking starts. The point at which the load-displacement curves diverge upon mesh refinement coincides to a strain equal to 0.24 for both cases. As is expected, the local damage model has no effect on eliminating spurious mesh sensitivity. Thus, the adaptive remeshing strategy along with the local model seems not to be an effective approach to achieve the convergence upon mesh refinement. Comparison of the load-displacement curves between the remeshing coupled and

uncoupled cases illustrates that the ALE remeshing leads to a more rapid load drop and a less ductile material behavior.

The contribution of the ALE approach can be clarified by comparing the deformed grids from the analysis with and without adaptive remeshing, which are depicted in Fig. 7.3. The elements from the remapping coupled analysis have more favorable aspect ratios than the normal analysis, especially for those elements within the necked region. The elements become increasingly distorted from the edge towards the center if no remeshing treatment is employed, as shown in Fig. 7.3(a). Examining Fig. 7.3(b), the discretizations throughout the central cross section have quite a uniform shape. Such unreasonable element distortion as shown in Fig. 7.3(a) will no doubt influence the accuracy of numerical results. By improving the aspect ratio of the elements, the ALE remeshing can make the necking zone consist of more elements to reproduce the geometry of the deformed plate in a more physically realistic manner. This remapping approach also has the benefit of improving the concave boundary curvature in the necking region. For this highly curved boundary, it is necessary to keep sufficient mesh refinement to obtain a smooth curvature. However, the validation of ALE approach needs to be further supported by experimental evidence such as the measured shape of the boundary and other measurements of the mechanical response of the material. The approach adopted in the current study shows its robustness in improving numerical grid quality for the necking type of strain localization case.

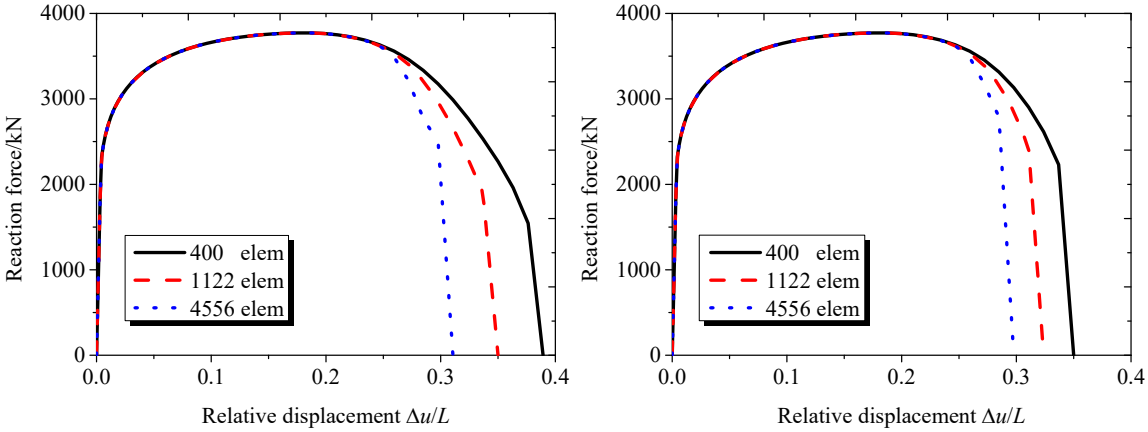

Fig. 7.2 Force-displacement curves for three mesh refinements for the local damage case (l=0): (a) without adaptive remeshing; (b) with adaptive remeshing.

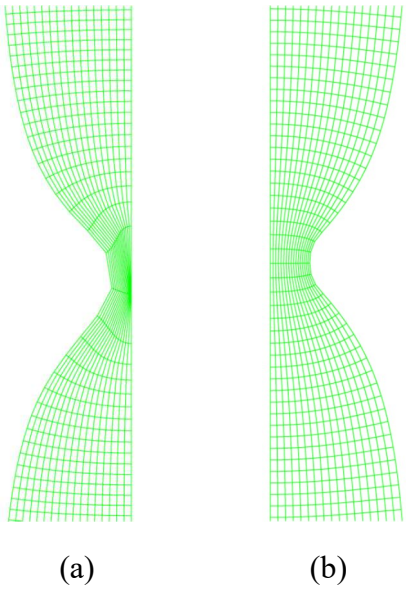

Fig. 7.3 Comparison of element shapes at Δu/L=0.3 with and without ALE remapping: (a) without ALE; (b) with ALE.

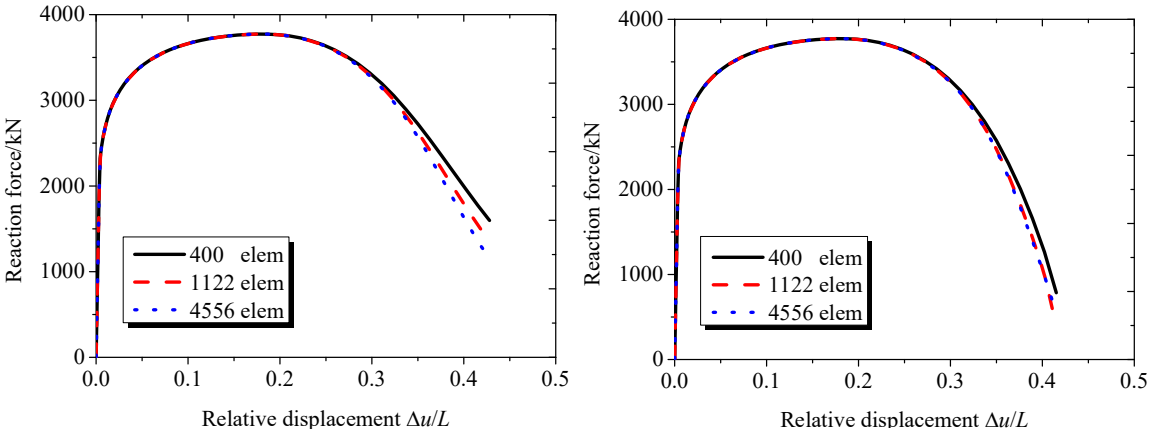

Fig. 7.4 Force-displacement curves for three mesh refinements for nonlocal damage case (l=0.63mm): (a) without adaptive remeshing; (b) with adaptive remeshing.

The load-displacement curves for the nonlocal damage model are shown in Fig. 7.4. When compared to the results of the local model, these curves show significantly less mesh dependency for the post-necking region of response. Without impacting the load-displacement response before necking, the non-locality approach has quite a significant effect on the material response for the post-necking range. This indicates that the regularized model proposed in this chapter significantly alleviates mesh sensitivity. However, without including the ALE remapping approach, the analysis still shows a slight mesh dependency in Fig. 7.4(a). The small deviations among different mesh refinements initiates at a strain equal to 0.29. Results shown in Fig. 7.4(b) for the nonlocal formulation coupled with the adaptive meshing approach exhibit very similar load-deformation curves in the post-necking range for the different meshes, other than the coarse mesh, indicating the response predictions converge with increasing mesh refinement. As the deformation is highly localized into the necking zone, the mesh distortion is inevitable if ALE remapping

is deactivated, which further influences the accuracy of numerical computation. The results highlight the necessity of combining the ALE adaptive remeshing and the nonlocal treatment in addressing the mesh dependency issue.

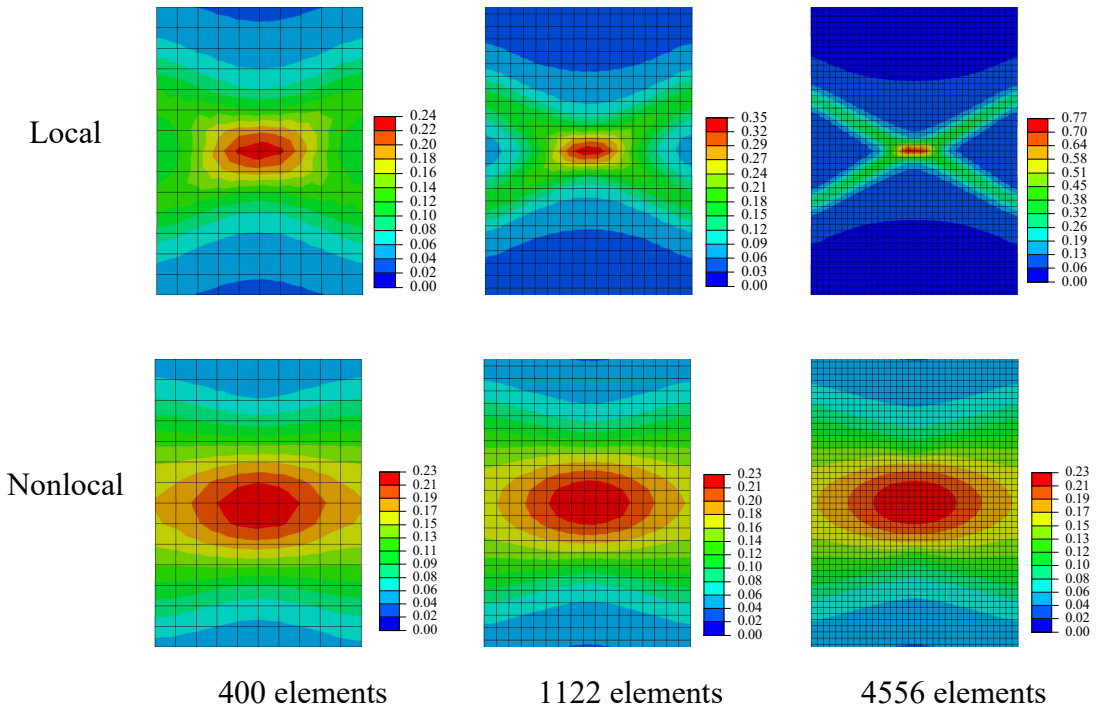

Fig. 7.5 Comparison of damage contours at Δu/L=0.32 for local and nonlocal models.

Another way to examine the effects of the non-locality approach is to inspect the damage distributions for different mesh refinements. As shown in Fig. 7.5, all the plotted damage contours are for the plate under the same elongation at $\Delta u/L$=0.32. Note that only the damage at the critical region is presented in Fig. 7.5. The damage results by the local model, shown in Fig. 7.5(a), (b) and (c), exhibit the tendency to concentrate into an infinitely small region upon mesh refinement. Thus, the maximum damage variable significantly increases with a finer mesh. Conversely, the damage distributions for the

nonlocal model show only small differences for the three different meshes. The damage is concentrated towards the center of the necked region but over a relatively large zone.

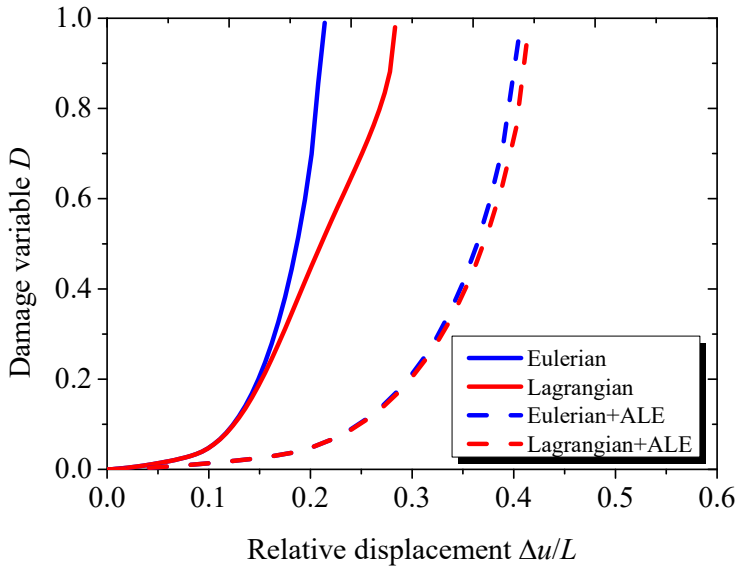

Fig. 7.6 The evolution of the nonlocal damage variable at the center of the necked zone for Eulerian vs. Lagrangian non-locality.

To investigate the Lagrangian and Eulerian types of non-locality, analysis using the numerical model with the medium mesh (1122 elements) was also carried out. The results of the damage variable evolution at the center of the necked zone are shown in Fig. 7.6. Comparison between the two approaches without adaptive remeshing indicates greater differences of damage evolution. The deviations are negligible at the early stages of deformation. However, the situation is completely different once necking taking place, corresponding to $\Delta u/L$=0.18. As is expected, the Eulerian nonlocal case has damage increasing more rapidly than the Lagrangian case, which leads to a more brittle material behavior. The Eulerian case reaches failure at $\Delta u/L$=0.21 while the Lagrangian case reaches

failure at $\Delta u/L$=0.28. As explained above, for this tension case the number of material points within the interactive volume decreases under the Eulerian formulation, which drives the nonlocal model more locally.

The results in Fig. 7.6 that include adaptive remeshing coupled demonstrate a more ductile material response when compared to the cases without adaptive remeshing. With adaptive remeshing, only small differences can be observed between the Eulerian and Lagrangian cases. Even though the damage from the Eulerian approach grows a little more rapidly, the ALE remapping strategy diminishes the differences between Eulerian and Lagrangian non-locality. Considering both the numerical outcomes and the computational costs, it is clear that the Lagrangian nonlocal approach associated with the ALE adaptive meshing is the preferred choice for nonlocal numerical implementation.

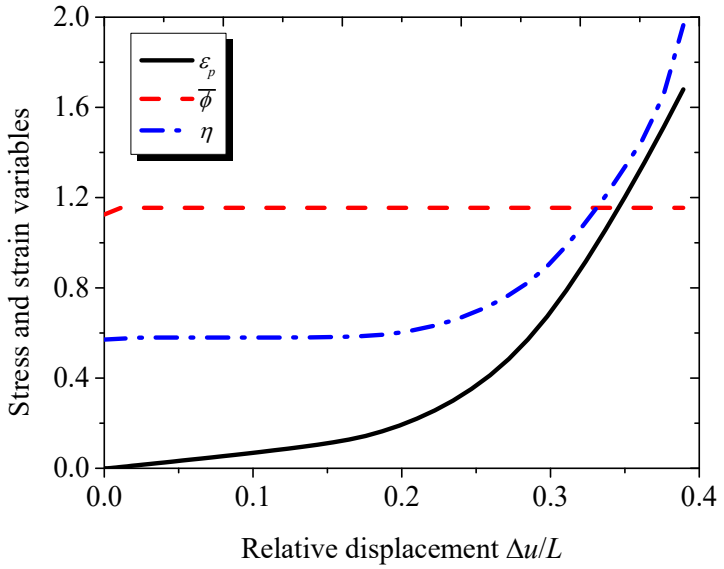

Fig. 7.7 The stress and strain variables at the center of the necked zone.

Note that the critical location of the tension plate is at the center of the necked zone,

where the failure initiates. Consequently, the following analysis will focus on the material point at that location. The evolutions of triaxiality, $\overline{\phi}$ factor and equivalent plastic strain are depicted in Fig. 7.7. The $\overline{\phi}$ factor almost remains constant at 1.15, which is close to the theoretical value for this plane strain case, i.e. $2/\sqrt{3}$. The other stress variable, triaxiality, grows dramatically from 0.57 to 1.97. From Eq. (7.14), (7.19) and (7.21), the damage variable is explicitly dependent on the triaxiality and $\overline{\phi}$ factor. As the latter remains unchanged, the variation of damage rate completely follows the plastic internal variable and the triaxiality. Nevertheless, since the shear-dependent factor A is greater than 0, the $\overline{\phi}$ factor has a contribution to the increment of the damage variable.

7.6.2 Tension of an axisymmetric bar

The second numerical example involves tension applied to an axisymmetric bar. This example is adopted because the stress state can achieve quite different $\overline{\phi}$ factor values from the first example, which facilitates examination of the shear stress dependency of the damage model. As confirmed previously, the nonlocal damage model coupled with ALE adaptive remeshing provides efficiency in obtaining mesh insensitive numerical results. Herein, a single mesh refinement will be applied to the model, for which the critical region is meshed by a relatively small element with about 0.1mm size and the rest of the cylindrical bar is discretized by 0.3mm elements, as shown in Fig. 7.8. Both mesh sizes are based on the mesh dependency studies of the previous example. The bar with 20mm height and 2.5mm radius has a half circle notch at mid-height. Taking advantage of symmetry, only half of the bar is modeled.

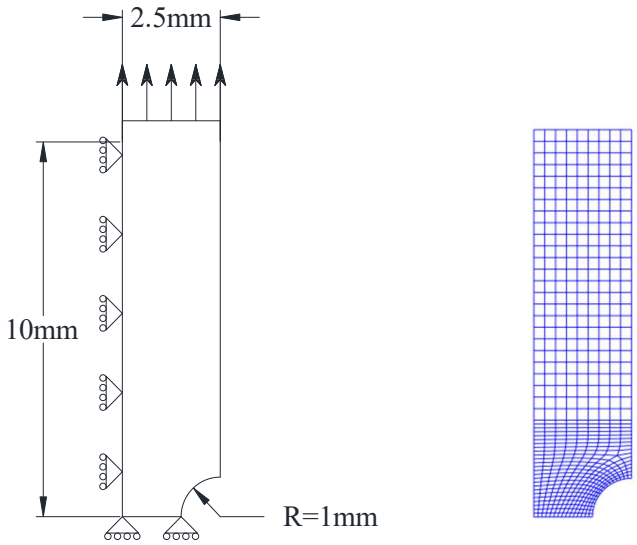

Fig. 7.8 The geometry, boundary condition and mesh of the axisymmetric bar.

Comparison between the axisymmetric and plane strain case is illustrated in Fig. 7.9 The damage in the plane strain case grows much faster than the axisymmetric case. Even though the triaxiality level for the plane strain case is lower than for the axisymmetric case during the early stages of deformation, its damage rate is greater. This is attributed to the high value of the $\overline{\phi}$ factor for the plane strain case, whereas the value is constant at 1 for this axisymmetric case. As the equivalent plastic strain exceeds 1.4, the triaxiality increases significantly for the plane strain case, which leads the more rapid damage accumulation. This demonstrates that the combination of shear stress and triaxiality influences the damage evolution. Additionally, the $\overline{\phi}$ factor does not change the rate of damage variable since it keeps constant throughout the deformation history. Many experimental observations and micromechanics based investigations indicate similar material behavior (Bao 2003; Bao and Wierzbicki 2004; Smith et al. 2014; Nahshon and Hutchinson, 2008). However, the contribution of each variable varies and is dependent on

many factors such as the material behavior, the loading condition, the temperature, and the strain rate. Further study is needed to calibrate the triaxiality and shear stress related parameters to provide a more accurate solution in describing and predicting damage of ductile solids.

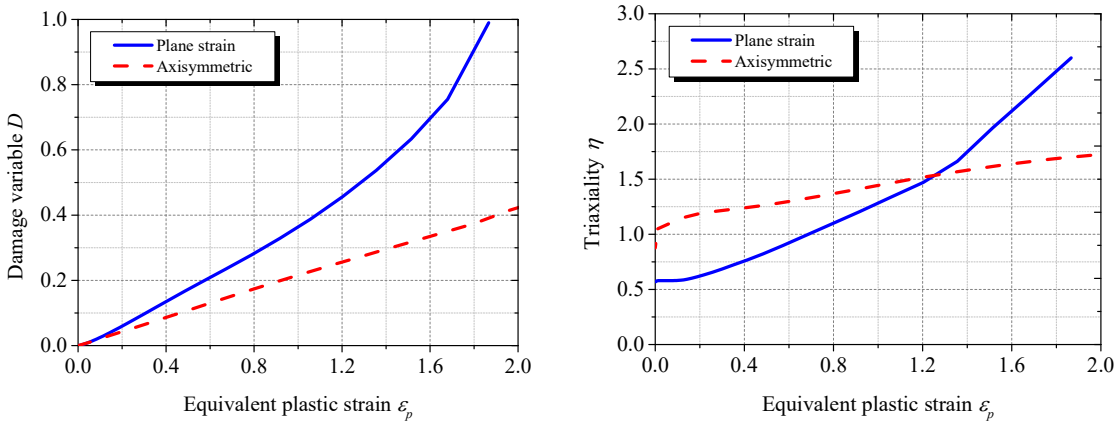

(a) (b)

Fig. 7.9 Comparison of damage and triaxiality between the two examples: (a) damage variable; (b) triaxiality.

The equivalent plastic strain and damage evolution are shown in Fig. 7.10(a) and (b), respectively. The maximum value of equivalent plastic strain occurs at the edge of the critical cross section, and becomes uniform as elongation increases. The opposite phenomenon can be observed from the damage contours at Fig. 7.10(b). The maximum damage appears at the center of the critical cross section. This is due to the high level of triaxiality at this location. As the cylindrical bar continues to be stretched, the damage tends to be more localized into the center. In this numerical example, the triaxiality overwhelms the equivalent plastic strain in determining the damage distribution. However, the

maximum damage point is not always at the center of a notched bar. The shape of notch and the material behavior will influence the levels of the triaxiality, the $\overline{\phi}$ factor and the plastic strain, and their effects on the damage evolution.

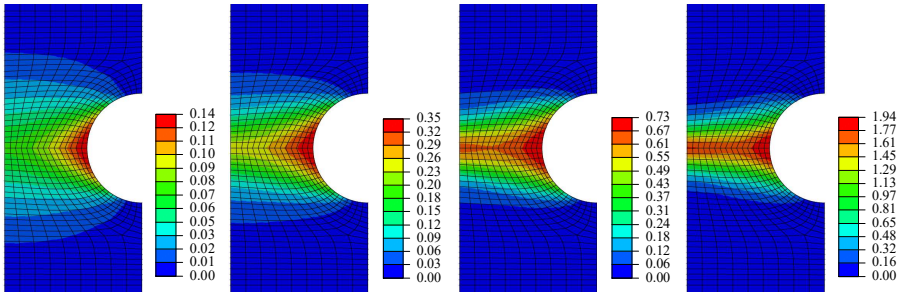

(a)

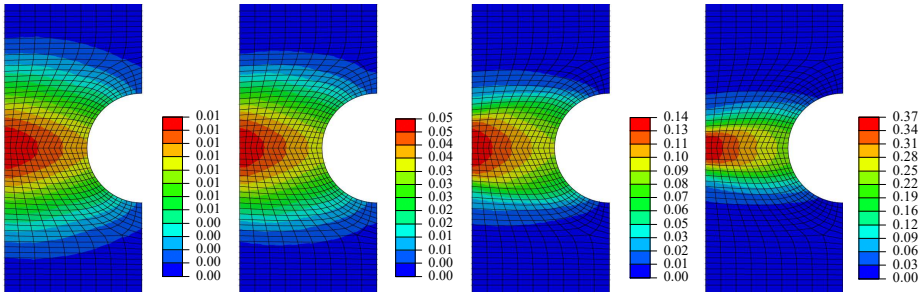

(b)

Fig. 7.10 Equivalent plastic strain and damage contours at elongation equals to 0.19mm, 0.4mm, 0.72mm and 1.33mm: (a) equivalent plastic strain; (b) damage variable.

7.7 CONCLUSIONS

This chapter presented the development of a continuum damage model coupling triaxiality and shear stress effects within the framework of nonlocal finite strain elastoplasticity. The proposed model is useful for strain softening and damage localization

problems in structural metals. The model is established based on thermodynamic principles and micromechanics-based observations. Considering the important role of shear stress in microvoid growth and coalescence, which results in the final failure of structural metals, a maximum shear stress related factor is introduced into the damage model. This model extends the continuum damage approach to include more factors that will influence ductile damage.

A non-local approach was employed to deal with the mesh dependency problems exhibited in the numerical application of the damage model. Some details of the nonlocal approach with respect to the characteristic length, the nonlocal variable and the nonlocal kernel were discussed. Besides their underlying physical meaning, the importance of these details for numerical implementation was also investigated. Both aspects influence the robustness and accuracy of the nonlocal strategy.

In FE analysis, the quality of mesh is crucial for achieving a reasonable outcome. To overcome the element distortion problem in modeling strain localization of ductile materials, the arbitrary Lagrangian and Eulerian adaptive remeshing approach was adopted. With this numerical strategy, it is expected that the elements will maintain favorable aspect ratios throughout the loading history, even for material that experiences excessive deformation. Combined with the ALE approach, the Lagrangian and Eulerian treatments for non-locality were considered to compare and evaluate their respective behaviors in numerical implementation.

A mixed explicit and implicit algorithm was applied to the nonlocal damage model. The benefits of this method are that it allows the computations to advance without performing iterations or calculating tangent stiffness matrixes. It is even more encouraging for the nonlocal type of damage model, since extra stiffness matrixes for the non-locality

are needed if the fully implicit scheme is adopted. A limitation of this method is that it is essentially an approximation for the nonlocal variable since the nonlocality proceeds only after equilibrium has been achieved. However, the use of very small time increment remedies this drawback.

Two numerical examples, including the plane strain tension and axisymmetric tension cases, are carried out. The results demonstrate that the nonlocal damage model together with the ALE remeshing strategy significantly alleviates the mesh sensitivity problem. The combination of these two approaches overcomes the unrealistic energy dissipation and mesh distortion that develop with more conventional FE approaches. There were only slight differences in numerical results by treating the nonlocal kernel as Lagrangian and Eulerian type. From the computational cost viewpoint, the Lagrangian non-locality is a better choice. Comparisons between the two examples emphasize the contribution of shear stress in accelerating damage accumulation. Further experimental investigations are needed to quantitatively identify material parameters such as the characteristic length, the triaxiality and the shear stress related parameters. It is also necessary to establish a more direct relation between the micromechanical mechanisms of ductile failure and this phenomenological nonlocal damage model.

CHAPTER 8

Conclusions and Future Work

8.1 SUMMARY AND CONCLUSIONS

The research reported in this dissertation focused on the initiation of ductile fracture in structural metals from both microscopic and macroscopic perspectives. The research was divided into three main parts: micromechanical modeling of ductile fracture, the development of a micromechanics-based ductile fracture model and its numerical implementation, and a numerical investigation of geometry and damage induced strain localization based on a nonlocal formulation. A summary of the primary research activities and associated observations and conclusions are described below.

The micro-mechanisms of ductile fracture involve micro-void nucleation, growth, and coalescence. To better understand microvoid evolution as well as material response under the mechanical field, micromechanics-based modeling was adopted. The objective of the micro-mechanics based studies was to investigate the role of the shear stress component on the ductile fracture process. The results indicate that with concurrent normal and shear stress components, the previously well recognized stress parameters affecting ductile fracture (triaxiality and Lode parameter) cannot completely characterize void growth and coalescence. For constant values of triaxiality and Lode parameter, increasing the shear stress component leads to the growth of microvoids and facilitates the fracture process.

Observations on microvoid evolution and the corresponding material behavior from the micromechanical studies completed in this research were used to develop a new ductile fracture initiation criterion. This portion of the research derived a local approach for

fracture initiation prediction based on both microscopic and macroscopic considerations. The form of this new model is a multiplicative combination of the void growth model and the modified maximum shear stress model, with the resulting new model being a triaxiality and shear stress factor dependent function of the fracture strain. The new model proposed in this study was then compared with other present models to demonstrate the benefits of this model both in computational efficiency and predictive accuracy.

Numerical implementation of the new model was illustrated by evaluating ductile fracture initiation in two different kinds of structural steels. The details of implementation, including the determination of specimen fracture initiation, model parameter calibration, and the evaluation of predictive accuracy were investigated. The proposed model showed the capability to predict ductile fracture initiation over a wide range of triaxialities. The predicted results also suggested that the sensitivity of the shear stress factor in ductile fracture initiation varies with the type of structural steel.

Strain localization is an important issue in studying the ultimate behavior of ductile metals, since this unstable phenomenon is a precursor to final material failure. The ductile fracture process is driven by strain localization at either the microscopic or macroscopic level or both. Most of the current standard constitutive theories are unable to characterize this phenomenon. Consequently, the third part of this research concentrated on capturing strain localization phenomena induced by geometric nonlinearity and ductile damage accumulation using the nonlocal theory. The primary aim of this portion of the research was to overcome numerical difficulties in modeling macroscopic strain localization, e.g. the ill-posed governing equation and the inextricable mesh sensitivity. The nonlocal approach introduced in this research showed significant potential for overcoming these difficulties, and the potential for successfully modeling strain localization in ductile metals.

8.2 RECOMMENDATIONS FOR FUTURE WORK

Observations from the current study suggest several next steps to further advance capabilities to predict the initiation of ductile fracture. Broadly, future research needs include further study of the shear related mechanisms of ductile fracture, developing a better understanding of micromechanical material behavior, and further developments in the computational mechanics of strain localization modeling. More detailed recommendations are as follows:

- The mechanisms of ductile fracture cannot be well established without accurately describing strain localization. In contrast to instability in some softening materials, strain localization in ductile solids is not directly triggered by its material constitutive behavior, but by geometry (necking and shear band), damage (strength degradation), or thermal effects. This gives rise to challenges in understanding and modeling strain localization. Currently, the nonlocal theory and peridynamic theory are two popular constitutive formulations that can regularize the boundary value problem when strain localization takes place. However, improvements to these approaches or the development of alternative modeling approaches are needed to achieve this research target. Attention is needed to both the macroscopic and microscopic strain localization. It is worth mentioning that microscopic strain localization is a primary driver of void growth, coalescence, and ultimate material failure. Hence, further work on strain localization is needed to advance understanding of ductile fracture.
- In terms of the mechanisms of ductile fracture, the microvoid enlargement mode has been extensively studies. However, the other primary mechanism of ductile fracture concerning the shearing mode has seen far less attention. The roles of the

shear stress component as well as the shearing band (strain localization) in microvoid evolution merits further exploration. Work is needed on numerical simulations to reproduce the shear dominated process and on analytical derivations to mathematically characterize this mechanism.

- Most of current micromechanical investigations of ductile fracture disregard some important aspects of how the evolution of microvoids and microstructures under the mechanical field will affect the plastic strain hardening material behavior. The size effect is quite prominent at the micro-scale. It is unclear how the microvoids and microstructures of the material interact and how the microvoids affect dislocations (strain hardening). It would be valuable to explore the interaction between plastic behavior and the ductile fracture process. It is not certain whether existing theories such as strain-gradient theory are suitable to deal with these issues or if new formulations are required.

Appendix A

Enforcing Proportional Loading via Linear Multi-Point Constraints

A.1 Multi-point Constraints (MPC) Derivation

A general form of the linear multi-point constraint is considered to apply to the multi-point system (N_0, N_1, N_2, N_3, N_4)

$$A_1u_1 + A_2u_2 + A_3u_3 + A_4u_4 - u_0 = 0 \tag{A.1}$$

where the displacements u_0, u_1, u_2. u_3 and u_4 are imposed to N_0, N_1, N_2, N_3, N_4, respectively. N_0 is the control point of the system, and the remainder are the slave nodes. Based on virtual displacements, the constraint equation can also be expressed as

$$A_1\delta u_1 + A_2\delta u_2 + A_3\delta u_3 + A_4\delta u_4 - \delta u_0 = 0 \tag{A.2}$$

The virtual work of the kinetic constraint following the principle of virtual work is given as

$$\delta W = P_0\delta u_0 + \sum_{i=1}^{4}\{(-F_i)\delta u_i\} = 0 \tag{A.3}$$

where F_i is the constraint force applied to the corresponding slave point, and P_0 and -F_i are the loads acting upon the master and slave nodes, respectively. Combining Eq. (A.2) and (A.3) leads to

$$A_1\delta u_1 + A_2\delta u_2 + A_3\delta u_3 + A_4\delta u_4 - (\sum_{i=1}^{4} F_i\delta u_i)/P_0 = 0 \tag{A.4}$$

Re-arranging Eq. (A.4) leads to

$$\sum_{i=1}^{4}(A_i - \frac{F_i}{P_0})\delta u_i = 0 \tag{A.5}$$

Since each virtual displacement δu_i is independent of the others and is arbitrary, its corresponding coefficient must satisfy

$$A_i - \frac{F_i}{P_0} = 0 \quad \forall i \tag{A.6}$$

The proportional relation of the coefficients can therefore be written as

$$A_1 : A_2 : A_3 : A_4 = F_1 : F_2 : F_3 : F_4 \tag{A.7}$$

Note that all the nodes involved in the multi-point constraint must be with nonzero displacements. Various slave node symbols can refer to the same node but with different degrees of freedom. The proportional loading relation is also applicable to the cases with an arbitrary number of slave nodes rather than four slave nodes.

A.2 ABAQUS SUBROUTINE CODE

Subroutine URDFIL: read the model information from the result file

```
      SUBROUTINE URDFIL(LSTOP,LOVRWRT,KSTEP,KINC,DTIME,TIME)
!
      INCLUDE 'ABA_PARAM.INC'
!
      DIMENSION ARRAY(513),JRRAY(NPRECD,513),TIME(2),LRUNIT(2,1)
      EQUIVALENCE(ARRAY(1),JRRAY(1,1))
      PARAMETER(CX=1.D0, CY=2.D0, CZ=5.D-1)
      CALL POSFIL(KSTEP,KINC,ARRAY,JRCD)
```

```
      OPEN(UNIT=17,FILE='!:\XXX.TXT',STATUS='REPLACE')
      LOVRWRT=1
      DO  K1=1,99999
!
        CALL DBFILE(0,ARRAY,JRCD)
        IF(JRCD.NE.0) GOTO 110
          KEY=JRRAY(1,2)
!
!       KEY IS THE NUMBER OF NODE TO BE APPLIED BY MPC
          IF(KEY.EQ.101) THEN
            KEL=JRRAY(1,3)
            IF (KEL .EQ. 22) THEN
              UX=ARRAY(4)
              D1=CX + UX
!       WRITE THE CURRENT DIMENSION OF THE CELL TO THE EXTERNAL FILE
              WRITE(17,120) D1
 120          FORMAT(5X,F20.14,5X)
            ELSEIF (KEL .EQ. 29) THEN
              U12=ARRAY(4)
              UY=ARRAY(5)
              UZ=ARRAY(6)
              D2=CY + UY
              D3=CZ - UZ
              WRITE(17,140) D2,D3,U12
```

```
 140              FORMAT(5X,F20.14,5X,F20.14,5X,F20.14,5X)
               END IF
!
            END IF
!
         END DO
 110     CONTINUE
!
         CLOSE(17)
!
    RETURN
    END
```

Subroutine UEXTERNALDB: exchange information among subroutines

```
   SUBROUTINE UEXTERNALDB(LOP,LRESTART,TIME,DTIME,KSTEP,KINC)
!
      INCLUDE 'ABA_PARAM.INC'
!
      DIMENSION TIME(2)
      COMMON KDX,KDY,KDZ,KUT
      REAL*8 KDX,KDY,KDZ,KUT
!     READ THE DATA OF CURRENT DIMENSION OF CELL FROM
!     EXTERNAL FILE AND TRANSFER THEM TO THE MPC SUBROUTINE
      IF (LOP .EQ. 1) THEN
```

```
      OPEN(17,FILE='!:\XXX.TXT')
      READ(17,*) KDX,KDY,KDZ,KUT
    END IF
!
    REWIND(17)
    CLOSE(17)
!
    RETURN
    END
```

Subroutine MPC: applying user defined multi-points constraints

```
    SUBROUTINE MPC(UE,A,JDOF,MDOF,N,JTYPE,X,U,UINIT,MAXDOF,
   1  LMPC,KSTEP,KINC,TIME,NT,NF,TEMP,FIELD,LTRAN,TRAN)
!
    INCLUDE 'ABA_PARAM.INC'
!
    COMMON KDX,KDY,KDZ,KUT
    REAL*8 KDX,KDY,KDZ,KUT
    DIMENSION A(N),JDOF(N),X(6,N),U(MAXDOF,N),UINIT(MAXDOF,N),
   1          TIME(2),TEMP(NT,N),FIELD(NF,NT,N),LTRAN(N),TRAN(3,3,N)
    PARAMETER( R1 = 0.25D0, R2 = 1.D0, R3 = -1.D0 )
!
    B11 = (R1 - R2 * KUT / KDY) * KDY / KDX
    B22 = R2
```

```
      B33 = R3 * KDY / KDZ
!
!           THE NUMBER OF JTYPE INDICATES THE TYPE OF MPC
!           MULTIPLE MPCS ARE ALLOWED
!           JTYPE IS GIVEN IN ABAQUS INPUT FILE
      IF (JTYPE .EQ. 1) THEN
!           USER CODING TO DEFINE THE MPC RELATION AS IN EQ. (A.1)
*****************************CODING*****************************
      END IF
!
    RETURN
    END
```

Appendix B

ABAQUS Subroutine for the Numerical Implementation of the Nonlocal Model

This appendix provides the main code of the ABAQUS subroutine for the numerical implementation of the nonlocal models proposed in chapter 6 and 7. The numerical modeling is done within ABAQUS/Explicit using the explicit dynamic method. The code consists of the fortran MODULE program unit, the VUMAT user-defined material subroutine, the VEXTERNALDB functional subroutine and the USERHARD user-defined material hardening subroutine.

B. 1 MAIN PROGRAM

Fortran module: Defining global variables that can be available within any defined routines

```
      MODULE VARIABLE_NL
!           THE NUMBER OF MATERIAL POINT THAT IS BEING PROCESSING
        INTEGER NELEM
!           THE TOTAL NUMBER OF THE MATERIAL POINTS IN THE MODEL
        PARAMETER (NOEL=1106)
!           DEFINING ALL THE GLOBALLY LOCAL AND NONLOCAL VARIABLES
!           AS WELL AS THEIR DATA TYPES
 ****************************CODING*****************************
      END MODULE
```

```
      SUBROUTINE VUMAT (
!   READ ONLY -
     1 JBLOCK, NDIR, NSHR, NSTATEV, NFIELDV, NPROPS, LANNEAL,
     2 STEPTIME, TOTALTIME, DT, CMNAME, COORDMP, CHARLENGTH,
     3 PROPS, DENSITY, STRAININC, RELSPININC,
     4 TEMPOLD, STRETCHOLD, DEFGRADOLD, FIELDOLD,
     5 STRESSOLD, STATEOLD, ENERINTERNOLD, ENERINELASOLD,
     6 TEMPNEW, STRETCHNEW, DEFGRADNEW, FIELDNEW,
!   WRITE ONLY -
     7 STRESSNEW, STATENEW, ENERINTERNNEW, ENERINELASNEW )
!
      USE VARIABLE_NL
      INCLUDE 'VABA_PARAM.INC'
!
      DIMENSION JBLOCK(*), PROPS(NPROPS),DENSITY(*), COORDMP(*),
     1 CHARLENGTH(*), STRAININC(*),
     2 RELSPININC(*), TEMPOLD(*),
     3 STRETCHOLD(*),
     4 DEFGRADOLD(*),
     5 FIELDOLD(*), STRESSOLD(*),
     6 STATEOLD(*), ENERINTERNOLD(*),
     7 ENERINELASOLD(*), TEMPNEW(*),
     8 STRETCHNEW(*),
```

```
     9 DEFGRADNEW(*),
     1 FIELDNEW(*),
     2 STRESSNEW(*), STATENEW(*),
     3 ENERINTERNNEW(*), ENERINELASNEW(*)
!
      PARAMETER (I_UMT_NBLOCK = 1, I_UMT_NOEL = 5 )
!
      CALL VUMATXTRARG ( JBLOCK(I_UMT_NBLOCK),
     1 NDIR, NSHR, NSTATEV, NFIELDV, NPROPS, LANNEAL,
     2 STEPTIME, TOTALTIME, DT, CMNAME, COORDMP, CHARLENGTH,
     3 PROPS, DENSITY, STRAININC, RELSPININC,
     4 TEMPOLD, STRETCHOLD, DEFGRADOLD, FIELDOLD,
     5 STRESSOLD, STATEOLD, ENERINTERNOLD, ENERINELASOLD,
     6 TEMPNEW, STRETCHNEW, DEFGRADNEW, FIELDNEW,
     7 STRESSNEW, STATENEW, ENERINTERNNEW, ENERINELASNEW,
     8 JBLOCK(I_UMT_NOEL))
!
      RETURN
      END
```

Subroutine VUMATXTRARG: Working together with Subroutine VUMAT

```
      SUBROUTINE VUMATXTRARG (
!   READ ONLY -
     1   NBLOCK, NDIR, NSHR, NSTATEV, NFIELDV, NPROPS, LANNEAL,
```

```
     2   STEPTIME, TOTALTIME, DT, CMNAME, COORDMP, CHARLENGTH,
     3   PROPS, DENSITY, STRAININC, RELSPININC,
     4   TEMPOLD, STRETCHOLD, DEFGRADOLD, FIELDOLD,
     5   STRESSOLD, STATEOLD, ENERINTERNOLD, ENERINELASOLD,
     6   TEMPNEW, STRETCHNEW, DEFGRADNEW, FIELDNEW,
!    WRITE ONLY -
     7   STRESSNEW, STATENEW, ENERINTERNNEW, ENERINELASNEW,
!    READ ONLY EXTRA ARGUMENTS -
     8   NELEMENT)
!
      USE VARIABLE _NL
      INCLUDE 'VABA_PARAM.INC'
!
! J2 MISES PLASTICITY WITH PIECEWISE-LINEAR ISOTROPIC HARDENING
! ELASTIC PREDICTOR, RADIAL CORRECTOR ALGORITHM
! NONLOCAL PLASTICITY/DAMAGE THEORY
!
      DIMENSION PROPS(NPROPS), DENSITY(NBLOCK),
     COORDMP(NBLOCK,*),
     1  CHARLENGTH(NBLOCK), STRAININC(NBLOCK,NDIR+NSHR),
     2  RELSPININC(NBLOCK,NSHR), TEMPOLD(NBLOCK),
     3  STRETCHOLD(NBLOCK,NDIR+NSHR),
     4  DEFGRADOLD(NBLOCK,NDIR+NSHR+NSHR),
     5  FIELDOLD(NBLOCK,NFIELDV), STRESSOLD(NBLOCK,NDIR+NSHR),
```

```
     6  STATEOLD(NBLOCK,NSTATEV), ENERINTERNOLD(NBLOCK),
     7  ENERINELASOLD(NBLOCK), TEMPNEW(NBLOCK),
     8  STRETCHNEW(NBLOCK,NDIR+NSHR),
     8  DEFGRADNEW(NBLOCK,NDIR+NSHR+NSHR),
     9  FIELDNEW(NBLOCK,NFIELDV),
     1  STRESSNEW(NBLOCK,NDIR+NSHR), STATENEW(NBLOCK,NSTATEV),
     2  ENERINTERNNEW(NBLOCK), ENERINELASNEW(NBLOCK)
!
!          USING THE NONLOCAL VARIABLE TO CALCULATE THE LOCAL
!          VARIABLES FOR THE CURRENT
!          MATERIAL POINT
**************************CODING*****************************
      RETURN
      END
```

Subroutine VEXTERNALDB: Nonlocal variables processing

```
      SUBROUTINE VEXTERNALDB(LOP, I_ARRAY, NIARRAY, R_ARRAY,
     NRARRAY)
!
      USE VARIABLE_NL
!
      INCLUDE 'VABA_PARAM.INC'
!
!     CONTENTS OF I_ARRAY
```

```
      PARAMETER( I_INT_NTOTALNODES     = 1,
     *           I_INT_NTOTALELEMENTS  = 2,
     *           I_INT_KSTEP           = 3,
     *           I_INT_KINC            = 4,
     *           I_INT_ISTATUS         = 5,
     *           I_INT_LWRITERESTART   = 6  )
!
!     POSSIBLE VALUES FOR THE LOP ARGUMENT
      PARAMETER( J_INT_STARTANALYSIS    = 0,
     *           J_INT_STARTSTEP        = 1,
     *           J_INT_SETUPINCREMENT   = 2,
     *           J_INT_STARTINCREMENT   = 3,
     *           J_INT_ENDINCREMENT     = 4,
     *           J_INT_ENDSTEP          = 5,
     *           J_INT_ENDANALYSIS      = 6 )
!
!     POSSIBLE VALUES FOR I_ARRAY(I_INT_ISTATUS)
      PARAMETER( J_INT_CONTINUE         = 0,
     *           J_INT_TERMINATESTEP    = 1,
     *           J_INT_TERMINATEANALYSIS = 2)
!
!     CONTENTS OF R_ARRAY
      PARAMETER( I_FLT_TOTALTIME   = 1,
     *           I_FLT_STEPTIME    = 2,
```

```
     *          I_FLT_DTIME      = 3 )
!
      PARAMETER (ZERO=0.D0, ONE=1.D0, AAA=1.1D0)
!
      DIMENSION I_ARRAY(NIARRAY),
     *   R_ARRAY(NRARRAY)
!
      KSTEP = I_ARRAY(I_INT_KSTEP)
      KINC = I_ARRAY(I_INT_KINC)
!
!
      IF (LOP .EQ. J_INT_ENDINCREMENT) THEN
       IF (KINC .EQ. 1) THEN
!          CALCULATING THE WEIGHT FACTOR FOR EACH POINT AT THE
!          BEGINNING OF ANALYSIS
*****************************CODING*****************************
       END IF
!
!          CALCULATING THE NONLOCAL VARIABLES BY THE LOCAL
!          COUNTERPART FROM VUMAT
*****************************CODING*****************************
      END IF
!
      RETURN
```

```
      END
```

Subroutine USERHARD: Defining strain hardening

```
      SUBROUTINE USERHARD (SYIELD, HARD, EQPLAS)
!
      INCLUDE 'VABA_PARAM.INC'
!
!         CALCULATING YIELD STRESS USING THE EQUIVALENT PLASTIC STRAIN
****************************CODING*****************************
!
      RETURN
      END
```

Bibliography

Abiri, O., & Lindgren, L. E. (2015). Non-local damage models in manufacturing simulations. *European Journal of Mechanics-A/Solids, 49*, 548-560.

Achouri, M., Germain, G., Dal Santo, P., & Saidane, D. (2013). Experimental characterization and numerical modeling of micromechanical damage under different stress states. *Materials & Design, 50*, 207-222.

Ahn, D. C., Sofronis, P., & Minich, R. (2006). On the micromechanics of void growth by prismatic-dislocation loop emission. *Journal of the Mechanics and Physics of Solids, 54*(4), 735-755.

AIJ (Architectural Institute of Japan). (1995). Fracture in steel structures during a severe earthquake, Tokyo.

Alshibli, K. A., & Akbas, I. S. (2007). Strain localization in clay: plane strain versus triaxial loading conditions. *Geotechnical and Geological Engineering, 25*(1), 45-55.

Anderson, P. M., Fleck, N. A., & Johnson, K. L. (1990). Localization of plastic deformation in shear due to microcracks. *Journal of the Mechanics and Physics of Solids, 38*(5), 681-699.

Anderson, T. L., & Anderson, T. L. (2005). *Fracture mechanics: fundamentals and applications.* CRC press.

Andrade, F. C., Pires, F. A., de Sá, J. M. A., & Malcher, L. (2009). Nonlocal integreal formulation for a plasticity-induced damage model. *Computer Methods in Materials Science, 9*(1), 49-54.

Andrade, F. X. C., César de Sá, J. M. A., & Andrade Pires, F. M. (2011). A ductile damage nonlocal model of integral-type at finite strains: formulation and numerical issues. *International Journal of Damage Mechanics, 20*(4), 515-557.

Antman, S. S., & Carbone, E. R. (1977). Shear and necking instabilities in nonlinear elasticity. Journal of Elasticity, 7(2), 125-151.

Antolovich, S. D., & Armstrong, R. W. (2014). Plastic strain localization in metals: origins and consequences. *Progress in Materials Science, 59*, 1-160.

Arasaratnam, P., Sivakumaran, K. S., & Tait, M. J. (2011). True stress-true strain models for structural steel elements. *ISRN Civil Engineering*, 2011.

Argon, A. S., Im, J., & Safoglu, R. (1975). Cavity formation from inclusions in ductile fracture. *Metallurgical Transactions A, 6*(4), 825-837.

Ashby, M. F. (1966). Work hardening of dispersion-hardened crystals. *Philosophical Magazine, 14*(132), 1157-1178.

Askari, E., Bobaru, F., Lehoucq, R. B., Parks, M. L., Silling, S. A., & Weckner, O. (2008).

Peridynamics for multiscale materials modeling. In *Journal of Physics: Conference Series* (Vol. 125, No. 1, p. 012078). IOP Publishing.

Askes, H., Bodé, L., & Sluys, L. J. (1998). ALE analyses of localization in wave propagation problems. *Mechanics of Cohesive-frictional Materials, 3*(2), 105-125.

Audoly, B., & Hutchinson, J. W. (2016). Analysis of necking based on a one-dimensional model. *Journal of the Mechanics and Physics of Solids, 97*, 68-91.

Ayada, M., Higashino, T., & Mori, K. (1987). Central bursting in extrusion of inhomogeneous materials. *Advanced Technology of Plasticity 1987., 1*, 553-558.

Bai, Y. (2008). *Effect of loading history in necking & fracture*. (Doctoral dissertation). Massachusetts Institute of Technology, Cambridge, MA.

Bai, Y., & Wierzbicki, T. (2008). A new model of metal plasticity and fracture with pressure and Lode dependence. *International journal of plasticity, 24*(6), 1071-1096.

Bai, Y., Teng, X., & Wierzbicki, T. (2009). On the application of stress triaxiality formula for plane strain fracture testing. *Journal of Engineering Materials and technology, 131*(2), 021002.

Bai, Y., & Wierzbicki, T. (2010). Application of extended Mohr–Coulomb criterion to ductile fracture. *International Journal of Fracture, 161*(1), 1-20.

Bai, Y., & Wierzbicki, T. (2015). A comparative study of three groups of ductile fracture loci in the 3D space. *Engineering Fracture Mechanics, 135*, 147-167.

Bandstra, J. P., Koss, D. A., Geltmacher, A., Matic, P., & Everett, R. K. (2004). Modeling void coalescence during ductile fracture of a steel. *Materials Science and Engineering: A, 366*(2), 269-281.

Bao, Y. (2003). *Prediction of ductile crack formation in uncracked bodies.* (Doctoral dissertation). Massachusetts Institute of Technology, Cambridge, MA.

Bao, Y., & Wierzbicki, T. (2004a). On fracture locus in the equivalent strain and stress triaxiality space. *International Journal of Mechanical Sciences, 46*(1), 81-98.

Bao, Y., & Wierzbicki, T. (2004b). A comparative study on various ductile crack formation criteria. *Journal of Engineering Materials and Technology, 126*(3), 314-324.

Bao, Y., & Wierzbicki, T. (2005). On the cut-off value of negative triaxiality for fracture. *Engineering fracture mechanics, 72*(7), 1049-1069.

Bardet, J. P. (1990). A comprehensive review of strain localization in elastoplastic soils. *Computers and geotechnics, 10*(3), 163-188.

Barsoum, I., & Faleskog, J. (2007a). Rupture mechanisms in combined tension and shear-Experiments. *International Journal of Solids and Structures, 44*(6), 1768-1786.

Barsoum, I., & Faleskog, J. (2007b). Rupture mechanisms in combined tension and shear-Micromechanics. *International Journal of Solids and Structures, 44*(17), 5481-5498.

Barsoum, I., & Faleskog, J. (2011). Micromechanical analysis on the influence of the Lode parameter on void growth and coalescence. *International Journal of Solids and Structures, 48(*6), 925-938.

Bažant, Z., & Lin, F. B. (1988). Non-local yield limit degradation. *International Journal for Numerical Methods in Engineering, 26*(8), 1805-1823.

Bažant, Z.P., Pijaudier-Cabot, G. (1988). Nonlocal continuum damage, localization instability and convergence. *Journal of Applied Mechanics, 55*(2), 287-293.

Bažant, Z. P. (1991). Why continuum damage is nonlocal: Micromechanics arguments. *Journal of Engineering Mechanics, 117*(5), 1070-1087. Chicago

Bažant, Z. P., & Jirásek, M. (2002). Nonlocal integral formulations of plasticity and damage: survey of progress. *Journal of Engineering Mechanics, 128*(11), 1119-1149.

Becker, R., Needleman, A., Richmond, O., & Tvergaard, V. (1988). Void growth and failure in notched bars. *Journal of the Mechanics and Physics of Solids, 36*(3), 317-351.

Belnoue, J. P., Nguyen, G. D., & Korsunsky, A. M. (2007). A one-dimensional nonlocal damage-plasticity model for ductile materials. *International Journal of Fracture, 144*(1), 53-60.

Belnoue, J. P., Nguyen, G. D., & Korsunsky, A. M. (2009). Consistent tangent stiffness for local-nonlocal damage modelling of metals. *Procedia Engineering, 1*(1), 177-180.

Belnoue, J. P., Garnham, B., Bache, M., & Korsunsky, A. M. (2010). The use of coupled nonlocal damage-plasticity to predict crack growth in ductile metal plates. *Engineering Fracture Mechanics, 77*(11), 1721-1729.

Belnoue, J. P., & Korsunsky, A. M. (2012). A damage function formulation for nonlocal coupled damage-plasticity model of ductile metal alloys. *European Journal of Mechanics-A/Solids, 34*, 63-77.

Belytschko, T., & Tabbara, M. (1993). H-Adaptive finite element methods for dynamic problems, with emphasis on localization. *International Journal for Numerical Methods in Engineering, 36*(24), 4245-4265.

Benallal, A., & Bigoni, D. (2004). Effects of temperature and thermo-mechanical couplings on material instabilities and strain localization of inelastic materials. *Journal of the Mechanics and Physics of Solids, 52*(3), 725-753.

Benzerga, A. A., Besson, J., & Pineau, A. (1999). Coalescence-controlled anisotropic ductile fracture. *Transactions-American society of mechanical engineers journal of*

engineering materials and technology, 121, 221-229.

Benzerga, A. A., & Besson, J. (2001). Plastic potentials for anisotropic porous solids. *European Journal of Mechanics-A/Solids, 20*(3), 397-434.

Benzerga, A. A. (2002). Micromechanics of coalescence in ductile fracture. *Journal of the Mechanics and Physics of Solids, 50*(6), 1331-1362.

Benzerga, A. A., Besson, J., & Pineau, A. (2004). Anisotropic ductile fracture: Part I: experiments. *Acta Materialia, 52*(15), 4623-4638.

Benzerga, A. A., Besson, J., & Pineau, A. (2005, March). How much input is nedded from the microstructure to model ductile fracture?. In *International conference of fracture* (pp. 6-p). xx.

Benzerga, A. A., & Leblond, J. B. (2010). Ductile fracture by void growth to coalescence. *Advances in Applied Mechanics, 44*, 169-305.

Benzerga, A. A., & Leblond, J. B. (2014). Effective yield criterion accounting for microvoid coalescence. *Journal of Applied Mechanics, 81*(3), 031009.

Beremin, F. M. (1981). Cavity formation from inclusions in ductile fracture of A508 steel. *Metallurgical Transactions A, 12*(5), 723-731.

Besson, J. (2010). Continuum models of ductile fracture: a review. *International Journal of Damage Mechanics, 19(*1), 3-52.

Bomarito, G. F., & Warner, D. H. (2015). Micromechanical investigation of ductile failure in Al 5083-H116 via 3D unit cell modeling. *Journal of the Mechanics and Physics of Solids, 74*, 97-110.

Borino, G., Failla, B., & Parrinello, F. (2003). A symmetric nonlocal damage theory. *International Journal of Solids and Structures, 40*(13), 3621-3645.

Borja, R. I. (2000). A finite element model for strain localization analysis of strongly discontinuous fields based on standard galerkin approximation. *Computer Methods in Applied Mechanics and Engineering, 190*(11), 1529-1549.

Brown, L. M., & Embury, J. D. (1973). Initiation and growth of voids at second-phase particles. In *Proc. Conf. on Microstructure and Design of Alloys, Institute of Metals and Iron and Steel Insitute, London. 1973, 1,* (33), 164-169.

Brozzo, P., Deluca, B., & Rendina, R. (1972). A new method for the prediction of formability in metal sheet, sheet metal forming and formability. In *Proceedings of the Seventh Biennial Conference of the IDDRG*.

Brunet, M., Morestin, F., & Walter, H. (2004). Damage identification for anisotropic sheet-metals using a non-local damage model. *International Journal of Damage Mechanics, 13*(1), 35-57.

Brunet, M., Morestin, F., & Walter-Leberre, H. (2005). Failure analysis of anisotropic sheet-metals using a non-local plastic damage model. *Journal of Materials Processing Technology, 170*(1), 457-470.

Brünig, M., Chyra, O., Albrecht, D., Driemeier, L., & Alves, M. (2008). A ductile damage criterion at various stress triaxialities. *International Journal of Plasticity, 24*(10), 1731-1755.

Campbell, F. C. (Ed.). (2012). *Fatigue and fracture: understanding the basics*. ASM International.

Cazacu, O., Revil-Baudard, B., Chandola, N., & Kondo, D. (2014). New analytical criterion for porous solids with Tresca matrix under axisymmetric loadings. *International Journal of Solids and Structures, 51*(3), 861-874.

Chaboche, J. L. (1981). Continuous damage mechanics-a tool to describe phenomena before crack initiation. *Nuclear Engineering and Design, 64*(2), 233-247.

Chaboche, J. L. (1987). Continuum damage mechanics: present state and future trends. *Nuclear Engineering and Design, 105*(1), 19-33.

Chaboche, J. L. (1988). Continuum damage mechanics: Part II-Damage growth, crack initiation, and crack growth. *Journal of applied mechanics, 55*(1), 65-72.

Chaboche, J. L. (2008). A review of some plasticity and viscoplasticity constitutive theories. *International Journal of Plasticity, 24*(10), 1642-1693.

Chae, D., & Koss, D. A. (2004). Damage accumulation and failure of HSLA-100 steel. *Materials Science and Engineering: A, 366*(2), 299-309.

Chi, W. M., Kanvinde, A. M., & Deierlein, G. G. (2006). Prediction of ductile fracture in steel connections using SMCS criterion. *Journal of structural engineering, 132*(2), 171-181.

Chow, C. L., Mao, J., & Shen, J. (2011). Nonlocal damage gradient model for fracture characterization of aluminum alloy. *International Journal of Damage Mechanics*, 1056789510395364.

Chu, C. C., & Needleman, A. (1980). Void nucleation effects in biaxially stretched sheets. *Journal of Engineering Materials and Technology (Transactions of the ASME), 102*(3), 249-256.

Clifton, C., Bruneau, M., MacRae, G., Leon, R., & Fussell, A. (2011). Steel structures damage from the Christchurch earthquake series of 2010 and 2011. *Bulletin of the New Zealand Society for Earthquake Engineering, 44*(4), 297-318.

Cockcroft, M. G., & Latham, D. J. (1968). Ductility and the workability of metals. *J Inst Metals, 96*(1), 33-39.

Coleman, B. D., & Newman, D. C. (1988). On the rheology of cold drawing. I. Elastic

materials. Journal of Polymer Science Part B: Polymer Physics, 26(9), 1801-1822.

Considère A. (1885) Memoire sur l'emploi du fer et de l'acier dans les constructions (On the use of iron and steel in construction). *Ann Ponts Chauss*, 9, 574-775.

Cosserat, E., & Cosserat, F. (1909). *Théorie des corps déformables*. Paris: Librairie Scientifique A. Hermann et Fils.

Cowie, J. G., Azrin, M., & Olson, G. B. (1989). Microvoid formation during shear deformation of ultrahigh strength steels. *Metallurgical transactions A, 20*(1), 143-153.

Cox, T. B., & Low, J. R. (1974). An investigation of the plastic fracture of AISI 4340 and 18 Nickel-200 grade maraging steels. *Metallurgical Transactions, 5*(6), 1457-1470.

De Borst, R. E. N. É. (1991). Simulation of strain localization: a reappraisal of the Cosserat continuum. *Engineering computations, 8*(4), 317-332.

De Borst, R., Sluys, L. J., Muhlhaus, H. B., & Pamin, J. (1993). Fundamental issues in finite element analyses of localization of deformation. *Engineering computations, 10*(2), 99-121.

De Borst, R., Pamin, J., & Geers, M. G. (1999). On coupled gradient-dependent plasticity and damage theories with a view to localization analysis. *European Journal of Mechanics-A/Solids, 18*(6), 939-962.

Desrues, J., & Viggiani, G. (2004). Strain localization in sand: an overview of the experimental results obtained in Grenoble using stereophotogrammetry. *International Journal for Numerical and Analytical Methods in Geomechanics, 28*(4), 279-321.

Desrues, J., Bésuelle, P., & Lewis, H. (2007). Strain localization in geomaterials. *Geological Society, London, Special Publications, 289*(1), 47-73.

Di Luzio, G., & Bažant, Z. P. (2005). Spectral analysis of localization in nonlocal and over-nonlocal materials with softening plasticity or damage. *International journal of solids and structures, 42*(23), 6071-6100.

Dillamore, I. L., Roberts, J. G., & Bush, A. C. (1979). Occurrence of shear bands in heavily rolled cubic metals. *Metal Science, 13*(2), 73-77.

Dos Santos, F. F., & Ruggieri, C. (2003). Micromechanics modelling of ductile fracture in tensile specimens using computational cells. *Fatigue and Fracture of Engineering Materials and Structures, 26*(2), 173-181.

Drabek, T., & Böhm, H. J. (2005). Damage models for studying ductile matrix failure in composites. *Computational Materials Science, 32*(3), 329-336.

Drabek, T., & Böhm, H. J. (2006). Micromechanical finite element analysis of metal matrix composites using nonlocal ductile failure models. *Computational materials science, 37*(1), 29-36.

Duncombe, E. (1972). Plastic instability and growth of grooves and patches in plates or tubes. *International Journal of Mechanical Sciences, 14*(5), 325-337.

Dyson, B. F., & McLean, D. (1977). Creep of Nimonic 80A in torsion and tension. *Metal science, 11*(2), 37-45.

Edelen, D. G., & Laws, N. (1971). On the thermodynamics of systems with nonlocality. *Archive for Rational Mechanics and Analysis, 43*(1), 24-35.

Enakoutsa, K., Leblond, J. B., & Perrin, G. (2007). Numerical implementation and assessment of a phenomenological nonlocal model of ductile rupture. *Computer Methods in Applied Mechanics and Engineering, 196*(13), 1946-1957.

Engelen, R. A., Geers, M. G., & Baaijens, F. P. (2003). Nonlocal implicit gradient-enhanced elasto-plasticity for the modelling of softening behaviour. *International journal of Plasticity, 19*(4), 403-433.

Engelhardt, M., Venti, M., Fry, G., Jones, S., and Holliday, S. (2000). Behavior and Design of Radiu Cut Reduced Beam Section Connections. Report No. SAC/BD-00/17, SAC Joint Venture, Sacramento, California.

Eringen, A. C. (1966). A unified theory of thermomechanical materials. *International Journal of Engineering Science, 4*(2), 179-202.

Eringen, A.C. (1968). Theory of micropolar elasticity. *In* "Fracture, An Advanced Treatise" (H. Liebowitz, ed.), vol. 2, chapter 7, pp. 621-729. Academic Press, New York.

Eringen, A. C., & Edelen, D. G. B. (1972). On nonlocal elasticity. *International Journal of Engineering Science, 10*(3), 233-248.

Eringen, A. C., & Kim, B. S. (1974). Stress concentration at the tip of crack. *Mechanics Research Communications, 1*(4), 233-237.

Eringen, A. C., Speziale, C. G., & Kim, B. S. (1977). Crack-tip problem in non-local elasticity. *Journal of the Mechanics and Physics of Solids, 25*(5), 339-355.

Eringen, A. C. (1981). On nonlocal plasticity. *International Journal of Engineering Science, 19*(12), 1461-1474.

Eringen, A. C. (1983). Theories of nonlocal plasticity. *International Journal of Engineering Science, 21*(7), 741-751.

Federal Emergency Management Association (FEMA). (2000). Recommended design criteria for new steel moment-frame buildings. *FEMA-350, Prepared by the SAC Joint Venture for FEMA*, Washington, D.C.

Fleck, N. A., & Hutchinson, J. W. (1986, October). Void growth in shear. In *Proceedings of the Royal Society of London A: Mathematical, Physical and Engineering Sciences* (Vol. 407, No. 1833, pp. 435-458). The Royal Society.

Fleck, N. A., Hutchinson, J. W., & Tvergaard, V. (1989). Softening by void nucleation and growth in tension and shear. *Journal of the Mechanics and Physics of Solids, 37*, 515-540.

Fleck, N. A., & Hutchinson, J. W. (1993). A phenomenological theory for strain gradient effects in plasticity. *Journal of the Mechanics and Physics of Solids, 41*(12), 1825-1857.

Fleck, N. A., & Hutchinson, J. W. (1997). Strain gradient plasticity. *Advances in applied mechanics, 33*, 296-361.

Floreen, S., & Hayden, H. W. (1970). Some observations of void growth during the tensile deformation of a high strength steel. *Scripta Metallurgica, 4*(2), 87-94.

Freudenthal, A. M. (1950). The inelastic behavior of solids. *Wiley, New York.*

Fung, Y. C., & Tong, P. (2001). *Classical and computational solid mechanics* (Vol. 1). World scientific.

Gao, X., Faleskog, J., & Shih, C. F. (1998). Cell model for nonlinear fracture analysis-II. Fracture-process calibration and verification. *International Journal of Fracture, 89*(4), 375-398.

Gao, X., Wang, T., & Kim, J. (2005). On ductile fracture initiation toughness: effects of void volume fraction, void shape and void distribution. *International Journal of Solids and Structures, 42*(18), 5097-5117.

Gao, X., & Kim, J. (2006). Modeling of ductile fracture: significance of void coalescence. *International Journal of Solids and Structures, 43*(20), 6277-6293.

Gao, X., Zhang, T., Hayden, M., & Roe, C. (2009). Effects of the stress state on plasticity and ductile failure of an aluminum 5083 alloy. *International Journal of Plasticity, 25*(12), 2366-2382.

Garrison, W. M., & Moody, N. R. (1987). Ductile fracture. *Journal of Physics and Chemistry of Solids, 48*(11), 1035-1074.

Germain, P., Nguyen, Q. S., & Suquet, P. (1983). Continuum thermodynamics. *Journal of Applied Mechanics, 50*(4b), 1010-1020.

Ghosh, S., & Raju, S. (1996). R-S Adapted Arbitrary Lagrangian-Eulerian Finite Element Method for Metal-Forming Problems with Strain Localization. *International journal for numerical methods in engineering, 39*(19), 3247-3272.

Gologanu, M., Leblond, J. B., & Devaux, J. (1993). Approximate models for ductile metals containing non-spherical voids-case of axisymmetric prolate ellipsoidal cavities.

Journal of the Mechanics and Physics of Solids, 41(11), 1723-1754.

Gologanu, M., Leblond, J. B., & Devaux, J. (1994). Approximate models for ductile metals containing nonspherical voids-case of axisymmetric oblate ellipsoidal cavities. *Journal of Engineering Materials and Technology*, 116(3), 290-297.

Gologanu, M., Leblond, J. B., Perrin, G., & Devaux, J. (1997). Recent extensions of Gurson's model for porous ductile metals. In *Continuum micromechanics* (pp. 61-130). Springer Vienna.

Gologanu, M., Leblond, J. B., Perrin, G., & Devaux, J. (2001). Theoretical models for void coalescence in porous ductile solids. I. Coalescence "in layers". *International journal of solids and structures, 38*(32), 5581-5594.

Goods, S. H., & Brown, L. M. (1979). Overview No. 1: The nucleation of cavities by plastic deformation. *Acta Metallurgica, 27*(1), 1-15.

Geers, M. G. D., De Borst, R., & Peijs, T. (1999a). Mixed numerical-experimental identification of non-local characteristics of random-fibre-reinforced composites. *Composites science and technology, 59*(10), 1569-1578.

Geers, M. G. D., De Borst, R., Brekelmans, W. A. M., & Peerlings, R. H. J. (1999b). Validation and internal length scale determination for a gradient damage model: application to short glass-fibre-reinforced polypropylene. *International Journal of Solids and Structures, 36*(17), 2557-2583.

Grassl, P., & Jirásek, M. (2006). Plastic model with non-local damage applied to concrete. *International Journal for Numerical and Analytical Methods in Geomechanics, 30*(1), 71-90.

Griffith, A. A. (1921). The phenomena of rupture and flow in solids. *Philosophical transactions of the royal society of London. Series A, containing papers of a mathematical or physical character, 221*, 163-198.

Gurson, A. L. (1975). *Plastic flow and fracture behavior of ductile materials, incorporating void nucleation, growth, and interaction*. (Doctoral dissertation). Brown University, Providence, RI.

Gurson, A. L. (1977). Continuum theory of ductile rupture by void nucleation and growth: Part I-Yield criteria and flow rules for porous ductile media. *Journal of engineering materials and technology, 99*(1), 2-15.

Ha, P. (1995). A generalized criterion of plastic instabilities and its application to creep damage and superplastic flow. *Acta metallurgica et materialia, 43*(11), 4093-4100.

Ha, Y. D., & Bobaru, F. (2010). Studies of dynamic crack propagation and crack branching with peridynamics. *International Journal of Fracture, 162*(1), 229-244.

Hall, E. O. (1951). The deformation and ageing of mild steel: III discussion of results. *Proceedings of the Physical Society. Section B, 64*(9), 747.

Hancock, J. W., & Mackenzie, A. C. (1976). On the mechanisms of ductile failure in high-strength steels subjected to multi-axial stress-states. *Journal of the Mechanics and Physics of Solids, 24*(2-3), 147-160.

Hancock, J. W., & Brown, D. K. (1983). On the role of strain and stress state in ductile failure. *Journal of the Mechanics and Physics of Solids, 31*(1), 1-24.

Hart, E. W. (1967). Theory of the tensile test. *Acta Metallurgica, 15*(2), 351-355.

Hill, R. (1967). The essential structure of constitutive laws for metal composites and polycrystals. *Journal of the Mechanics and Physics of Solids, 15*(2), 79-95.

Hill, R. (1972, January). On constitutive macro-variables for heterogeneous solids at finite strain. In *Proceedings of the Royal Society of London A: Mathematical, Physical and Engineering Sciences* (Vol. 326, No. 1565, pp. 131-147). The Royal Society.

Hill, R., & Hutchinson, J. W. (1975). Bifurcation phenomena in the plane tension test. *Journal of the Mechanics and Physics of Solids, 23*(4), 239-264.

Hooputra, H., Gese, H., Dell, H., & Werner, H. (2004). A comprehensive failure model for crashworthiness simulation of aluminium extrusions. *International Journal of Crashworthiness, 9*(5), 449-464.

Hu, G. (2011). *Behavior of beam shear connections in steel buildings subject to fire* (Doctoral dissertation). The University of Texas at Austin, Austin, Texas.

Huang, Y., Qu, S., Hwang, K. C., Li, M., & Gao, H. (2004). A conventional theory of mechanism-based strain gradient plasticity. *International Journal of Plasticity, 20*(4), 753-782.

Huerta, A., Pijaudier-Cabot, G., & Bode, L. (1992). ALE formulation in nonlocal strain softening solids. In *Proc. Conf. on Computational Plasticity, Fundamentals and Applications, Parti* (pp. 2249-2268).

Hutchinson, J. W., & Neale, K. W. (1977). Influence of strain-rate sensitivity on necking under uniaxial tension. *Acta Metallurgica, 25*(8), 839-846.

Inglis, C.E. (1913). Stresses in a Plate Due to the Presence of Cracks and Sharp Corners. *Transactions of the Institute of Naval Architects, 55*, 219-241.

Irwin, G.R. (1956). Onset of Fast Crack Propagation in High Strength Steel and Aluminum Alloys. *Sagamore Research Conference Proceedings, 2*, 289-305.

Irwin, G.R. (1957). Analysis of Stresses and Strains near the End of a Crack Traversing a Plate. *Journal of Applied Mechanics, 24*, 361-364.

Jacques, P. J., Furnémont, Q., Lani, F., Pardoen, T., & Delannay, F. (2007). Multiscale mechanics of TRIP-assisted multiphase steels: I. Characterization and mechanical testing. *Acta Materialia, 55*(11), 3681-3693.

Jia, L. J., & Kuwamura, H. (2013). Ductile fracture simulation of structural steels under

monotonic tension. *Journal of Structural Engineering, 140*(5), 04013115.

Jirásek, M. (1998). Nonlocal models for damage and fracture: comparison of approaches. *International Journal of Solids and Structures, 35*(31-32), 4133-4145.

Jirásek, M., & Rolshoven, S. (2003). Comparison of integral-type nonlocal plasticity models for strain-softening materials. *International Journal of Engineering Science, 41*(13), 1553-1602.

Jirásek, M., & Rolshoven, S. (2009). Localization properties of strain-softening gradient plasticity models. Part I: Strain-gradient theories. *International Journal of Solids and Structures, 46*(11), 2225-2238.

Johnson, G. R., & Cook, W. H. (1985). Fracture characteristics of three metals subjected to various strains, strain rates, temperatures and pressures. *Engineering fracture mechanics, 21*(1), 31-48.

Jonas, J. J., & Luton, M. J. (1978). Flow softening at elevated temperatures. In *Advances in Deformation Processing* (pp. 215-243). Springer US.

JSCE (Japan Society of Civil Engineers). (1997). *Report on the Hanshin-Awaji earthquake disaster-Vol. 4: Investigation of causes of damage to civil engineering structures*. Tokyo.

Kachanov, L. M. (1958). Time of the rupture process under creep conditions, Izu. *Akad. Nauk SSR Otd. Tech*, 26-31.

Kachanov, L. M. (1978). On growth of cracks under creep conditions. *International Journal of Fracture, 14*(2), R51-R52.

Kachanov, L. (2013). *Introduction to continuum damage mechanics* (Vol. 10). Springer Science & Business Media.

Kanetake, N., Nomura, M., & Choh, T. (1995). Continuous observation of microstructural degradation during tensile loading of particle reinforced aluminium matrix composites. *Materials science and technology, 11*(12), 1246-1252.

Kanvinde, A. M. (2004). *Micromechanical simulation of earthquake-induced fracture in steel structures*. (Doctoral dissertation). Stanford University, Stanford, CA.

Kanvinde, A. M., & Deierlein, G. G. (2004, August). Prediction of ductile fracture in steel moment connections during earthquakes using micromechanical fracture models. In *13th World Conference on Earthquake Engineering*, (pp. 1-6).

Kanvinde, A. M., & Deierlein, G. G. (2006). The void growth model and the stress modified critical strain model to predict ductile fracture in structural steels. *Journal of Structural Engineering, 132(*12), 1907-1918.

Kanvinde, A. M., & Deierlein, G. G. (2007). Finite-element simulation of ductile fracture in reduced section pull-plates using micromechanics-based fracture models.

Journal of Structural Engineering, 133(5), 656-664.

Kattan, P. I., & Voyiadjis, G. Z. (2012). *Damage mechanics with finite elements: practical applications with computer tools*. Springer Science & Business Media.

Khan, A. S., & Liu, H. (2012). A new approach for ductile fracture prediction on Al 2024-T351 alloy. *International Journal of Plasticity, 35*, 1-12.

Khandelwal, K., & El-Tawil, S. (2014). A finite strain continuum damage model for simulating ductile fracture in steels. *Engineering Fracture Mechanics, 116*, 172-189.

Khoei, A. R., & Bakhshiani, A. (2005). A hypoelasto-viscoplastic endochronic model for numerical simulation of shear band localization. *Finite elements in analysis and design, 41*(14), 1384-1400.

Khoei, A. R., Tabarraie, A. R., & Gharehbaghi, S. A. (2005). H-adaptive mesh refinement for shear band localization in elasto-plasticity Cosserat continuum. *Communications in Nonlinear Science and Numerical Simulation, 10*(3), 253-286.

Khoei, A. R., Yadegari, S., & Biabanaki, S. O. R. (2010). 3D finite element modeling of shear band localization via the micro-polar Cosserat continuum theory. *Computational Materials Science, 49*(4), 720-733.

Kim, J., Gao, X., & Srivatsan, T. S. (2003). Modeling of crack growth in ductile solids: a three-dimensional analysis. *International journal of solids and structures, 40*(26), 7357-7374.

Kim, J., Gao, X., & Srivatsan, T. S. (2004). Modeling of void growth in ductile solids: effects of stress triaxiality and initial porosity. *Engineering Fracture Mechanics, 71*(3), 379-400.

Kiran, R., & Khandelwal, K. (2013a). Experimental studies and models for ductile fracture in ASTM A992 steels at high triaxiality. *Journal of Structural Engineering, 140*(2), 04013044.

Kiran, R., & Khandelwal, K. (2013b). A micromechanical model for ductile fracture prediction in ASTM A992 steels. *Engineering Fracture Mechanics, 102*, 101-117.

Kiran, R., & Khandelwal, K. (2014a). Fast-to-compute weakly coupled ductile fracture model for structural steels. *Journal of Structural Engineering, 140*(6), 04014018.

Kiran, R., & Khandelwal, K. (2014b). A triaxiality and Lode parameter dependent ductile fracture criterion. *Engineering Fracture Mechanics, 128*, 121-138.

Kiran, R., & Khandelwal, K. (2015). A coupled microvoid elongation and dilation based ductile fracture model for structural steels. *Engineering Fracture Mechanics, 145*, 15-42.

Kocks, U. F. (1958). Polyslip in polycrystals. *Acta Metallurgica, 6*(2), 85-94.

Kolwankar, S., Kanvinde, A., Kenawy, M., & Kunnath, S. (2017). Uniaxial Nonlocal Formulation for Geometric Nonlinearity-Induced Necking and Buckling Localization in a Steel Bar. *Journal of Structural Engineering, 143*(9), 04017091.

Koplik, J., & Needleman, A. (1988). Void growth and coalescence in porous plastic solids. *International Journal of Solids and Structures, 24*, 835-853.

Korsunsky, A. M., Nguyen, G. D., & Houlsby, G. T. (2005). Analysis of essential work of rupture using non-local damage-plasticity modelling. *International Journal of Fracture, 135*(1-4), L19-L26.

Krajcinovic, D., & Fonseka, G. U. (1981). The continuous damage theory of brittle materials. *J. appl. Mech, 48*(4), 809-824.

Krajcinovic, D. (1985). Continuous damage mechanics revisited: basic concepts and definitions. *Journal of Applied Mechanics, 52*(4), 829-834.

Kudo, H. (1960). Some analytical and experimental studies of axi-symmetric cold forging and extrusion-I. *International Journal of Mechanical Sciences, 2*, 102-127.

Kuna, K., & Sun, D. Z. (1996). Three-dimensional cell model analyses of void growth in ductile materials. *International Journal of Fracture, 81*, 235-258.

Kuwamura, H., & Yamamoto, K. (1997). Ductile crack as trigger of brittle fracture in steel. *Journal of Structural Engineering, 123*(6), 729-735.

Leblond, J. B., Perrin, G., & Devaux, J. (1995). An improved Gurson-type model for hardenable ductile metals. *European journal of mechanics. A. Solids, 14*(4), 499-527.

Lee, B. J., & Mear, M. E. (1999). Stress concentration induced by an elastic spheroidal particle in a plastically deforming solid. *Journal of the Mechanics and Physics of Solids, 47*(6), 1301-1336.

Lemaitre, J. (1972). Evaluation of dissipation and damage in metals submitted to dynamic loading. *Mechanical behavior of materials*, 540-549.

Lemaitre, J., & Chaboche, J. L. (1978). Aspect phénoménologique de la rupture par endommagement. *J Méc Appl, 2*(3), 317-65.

Lemaitre, J. (1985). A continuous damage mechanics model for ductile fracture. *Transactions of the ASME. Journal of Engineering Materials and Technology, 107*(1), 83-89.

Lemaitre, J., & Chaboche, J. L. (1994). *Mechanics of solid materials*. Cambridge university press.

Lemaitre, J., & Desmorat, R. (2005). *Engineering damage mechanics: ductile, creep, fatigue and brittle failures.* Springer Science & Business Media.

Lemaitre, J. (2012). *A course on damage mechanics*. Springer Science & Business Media.

Lemonds, J., & Needleman, A. (1986). Finite element analyses of shear localization in rate and temperature dependent solids. *Mechanics of Materials, 5*(4), 339-361.

Le Roy, G. (1978). *Large Scale Plastic Deformation and Fracture for Multiaxial Stress States*. (Doctoral dissertation). McMaster University, Hamilton, Ontario.

Le Roy, G., Embury, J. D., Edwards, G., & Ashby, M. F. (1981). A model of ductile fracture based on the nucleation and growth of voids. *Acta Metallurgica, 29*(8), 1509-1522.

Levaillant, C., & Pineau, A. (1982). Assessment of high-temperature low-cycle fatigue life of austenitic stainless steels by using intergranular damage as a correlating parameter. In *Low-Cycle Fatigue and Life Prediction*. ASTM International.

Li, Y., Luo, M., Gerlach, J., & Wierzbicki, T. (2010). Prediction of shear-induced fracture in sheet metal forming. *Journal of Materials Processing Technology, 210*(14), 1858-1869.

Li, H., Fu, M. W., Lu, J., & Yang, H. (2011). Ductile fracture: experiments and computations. *International journal of plasticity, 27*(2), 147-180.

Liao, F., Wang, W., & Chen, Y. (2015). Ductile fracture prediction for welded steel connections under monotonic loading based on micromechanical fracture criteria. *Engineering Structures, 94*, 16-28.

Lin, I. H., Hirth, J. P., & Hart, E. W. (1981). Plastic instability in uniaxial tension tests. *Acta metallurgica, 29*(5), 819-827.

Lin, J., Dunne, F. P. E., & Hayhurst, D. R. (1999). Aspects of testpiece design responsible for errors in cyclic plasticity experiments. *International Journal of Damage Mechanics, 8*(2), 109-137.

Liu, B., Qiu, X., Huang, Y., Hwang, K. C., Li, M., & Liu, C. (2003). The size effect on void growth in ductile materials. *Journal of the Mechanics and Physics of Solids, 51*(7), 1171-1187.

Liu, F., Dan, W. J., & Zhang, W. G. (2017). The Effects of Stress State on the Strain Hardening Behaviors of TWIP Steel. *Journal of Materials Engineering and Performance*, 1-8.

Lou, Y., Huh, H., Lim, S., & Pack, K. (2012). New ductile fracture criterion for prediction of fracture forming limit diagrams of sheet metals. *International Journal of Solids and Structures, 49*(25), 3605-3615.

Lou, Y., & Huh, H. (2013). Extension of a shear-controlled ductile fracture model considering the stress triaxiality and the Lode parameter. *International Journal of Solids and Structures, 50*(2), 447-455.

Lou, Y., Yoon, J. W., & Huh, H. (2014). Modeling of shear ductile fracture considering a changeable cut-off value for stress triaxiality. *International Journal of Plasticity,*

54, 56-80.

Lu, X., Bardet, J. P., & Huang, M. (2010). Length scales interaction in nonlocal plastic strain localization of bars of varying section. *Journal of engineering mechanics, 136*(8), 1036-1042.

Mackenzie, A. C., Hancock, J. W., & Brown, D. K. (1977). On the influence of state of stress on ductile failure initiation in high strength steels. *Engineering fracture mechanics, 9*(1), 167IN13169-168IN14188.

Madou, K., & Leblond, J. B. (2012a). A Gurson-type criterion for porous ductile solids containing arbitrary ellipsoidal voids-I: limit-analysis of some representative cell. *Journal of the Mechanics and Physics of Solids, 60*(5), 1020-1036.

Madou, K., & Leblond, J. B. (2012b). A Gurson-type criterion for porous ductile solids containing arbitrary ellipsoidal voids-II: determination of yield criterion parameters. *Journal of the Mechanics and Physics of Solids, 60*(5), 1037-1058.

Madou, K., & Leblond, J. B. (2013). Numerical studies of porous ductile materials containing arbitrary ellipsoidal voids-I: Yield surfaces of representative cells. *European Journal of Mechanics-A/Solids, 42*, 480-489.

Mahin, S. A. (1998). Lessons from damage to steel buildings during the Northridge earthquake. *Engineering structures, 20*(4), 261-270.

Mahnken, R. (1999). Aspects on the finite-element implementation of the Gurson model including parameter identification. *International Journal of Plasticity, 15*(11), 1111-1137.

Malcher, L., Pires, F. A., & De Sá, J. C. (2014). An extended GTN model for ductile fracture under high and low stress triaxiality. *International Journal of Plasticity, 54*, 193-228.

Marini, B., Mudry, F., & Pineau, A. (1985a). Ductile rupture of A508 steel under nonradial loading. *Engineering Fracture Mechanics, 22*(3), 375-386.

Marini, B., Mudry, F., & Pineau, A. (1985b). Experimental study of cavity growth in ductile rupture. *Engineering Fracture Mechanics, 22*(6), 989-996.

Matsushima, T., Chambon, R., & Caillerie, D. (2002). Large strain finite element analysis of a local second gradient model: application to localization. *International journal for numerical methods in engineering, 54*(4), 499-521.

McClintock, F. A. (1968). A criterion for ductile fracture by the growth of holes. *Journal of applied mechanics, 35*(2), 363-371.

McVeigh, C., Vernerey, F., Liu, W. K., Moran, B., & Olson, G. (2007). An interactive micro-void shear localization mechanism in high strength steels. *Journal of the Mechanics and Physics of Solids, 55*(2), 225-244.

Mear, M. E., & Hutchinson, J. W. (1985). Influence of yield surface curvature on flow localization in dilatant plasticity. *Mechanics of Materials, 4*(3-4), 395-407.

Mikkelsen, L. P. (1997). Post-necking behaviour modelled by a gradient dependent plasticity theory. *International journal of solids and structures, 34*(35-36), 4531-4546.

Mikkelsen, L. P. (1999). Necking in rectangular tensile bars approximated by a 2-D gradient dependent plasticity model. *European Journal of Mechanics-A/Solids, 18*(5), 805-818.

Mindlin, R. D. (1964). Micro-structure in linear elasticity. *Archive for Rational Mechanics and Analysis, 16*(1), 51-78.

Morin, L., Leblond, J. B., & Benzerga, A. A. (2015). Coalescence of voids by internal necking: theoretical estimates and numerical results. *Journal of the Mechanics and Physics of Solids, 75*, 140-158.

Mott, N. F. (1948). Fracture of metals: theoretical considerations. *Engineering, 165*(4275), 16-18.

Nahshon, K., & Hutchinson, J. W. (2008). Modification of the Gurson model for shear failure. *European Journal of Mechanics-A/Solids, 27*(1), 1-17.

NIST. 2005. *Final Report on the Collapse of the World Trade Center Towers*. Report NIST NCSTAR 1, National Institute of Standards and Technology, Gaithersburg, MD.

Needleman, A., & Tvergaard, V. (1977). Necking of biaxially stretched elastic-plastic circular plates. *Journal of the Mechanics and Physics of Solids, 25*(3), 159-183.

Needleman, A., & Rice, J. R. (1978). Limits to ductility set by plastic flow localization. In *Mechanics of sheet metal forming* (pp. 237-267). Springer US.

Needleman, A., & Tvergaard, V. (1984). An analysis of ductile rupture in notched bars. *Journal of the Mechanics and Physics of Solids, 32*(6), 461-490.

Needleman, A. (1986). Effect of yield surface curvature on necking and failure in porous plastic solids. *Journal of applied mechanics, 53*, 491.

Needleman, A. (1987). A continuum model for void nucleation by inclusion debonding. *Journal of applied mechanics*, 54(3), 525-531.

Needleman, A., & Tvergaard, V. (1992). Analyses of plastic flow localization in metals. *Applied Mechanics Reviews, 45*(3S), S3-S18.

Nguyen, G. D., Korsunsky, A. M., & Belnoue, J. P. H. (2015). A nonlocal coupled damage-plasticity model for the analysis of ductile failure. *International Journal of Plasticity, 64*, 56-75.

Nielsen, K. L., Dahl, J., & Tvergaard, V. (2012). Collapse and coalescence of spherical voids subject to intense shearing: studied in full 3D. *International Journal of*

Fracture, 1-12.

Nix, W. D., & Gao, H. (1998). Indentation size effects in crystalline materials: a law for strain gradient plasticity. *Journal of the Mechanics and Physics of Solids, 46*(3), 411-425.

Nübel, K., & Huang, W. (2004). A study of localized deformation pattern in granular media. *Computer Methods in Applied Mechanics and Engineering, 193*(27), 2719-2743.

Oh, S. I., Chen, C. C., & Kobayashi, S. (1979). Ductile fracture in axisymmetric extrusion and drawing. *J. Eng. Ind. Trans. ASME, 101*(1), 36-44.

Okazaki, T. (2004). *Seismic Performance of Link-to-Column Connections in Steel Eccentrically Braced Frames*. (Doctoral dissertation). The University of Texas at Austin, Austin, Texas.

Okazawa, S. (2010). Structural bifurcation for ductile necking localization. *International Journal of Non-Linear Mechanics, 45*(1), 35-41.

Orowan, E. (1949). Fracture and strength of solids. *Reports on progress in physics, 12*(1), 185.

Ortiz, M., Leroy, Y., & Needleman, A. (1987). A finite element method for localized failure analysis. *Computer methods in applied mechanics and engineering, 61*(2), 189-214.

Ortiz, M., & Quigley, J. J. (1991). Adaptive mesh refinement in strain localization problems. *Computer Methods in Applied Mechanics and Engineering, 90*(1-3), 781-804.

Ottosen, N. S., & Runesson, K. (1991). Properties of discontinuous bifurcation solutions in elasto-plasticity. *International Journal of Solids and Structures, 27*(4), 401-421.

Oyane, M. (1972). Criteria of ductile fracture strain. *Bulletin of JSME*, 15(90), 1507-1513.

Panontin, T. L., & Sheppard, S. D. (1995). The relationship between constraint and ductile fracture initiation as defined by micromechanical analyses. In *Fracture Mechanics: 26th Volume*. ASTM International.

Pardoen, T., & Delannay, F. (1998). Assessment of void growth models from porosity measurements in cold-drawn copper bars. *Metallurgical and Materials Transactions A, 29*(7), 1895-1909.

Pardoen, T., & Hutchinson, J. W. (2000). An extended model for void growth and coalescence. *Journal of the Mechanics and Physics of Solids, 48*(12), 2467-2512.

Pardoen, T., & Brechet, Y. (2004). Influence of microstructure-driven strain localization on the ductile fracture of metallic alloys. *Philosophical Magazine, 84*(3-5), 269-297.

Park, I. G., & Thompson, A. W. (1988). Ductile fracture in spheroidized 1520 steel. *Acta Metallurgica, 36*(7), 1653-1664.

Peerlings, R. H. J., de Borst, R., Brekelmans, W. A. M., & de Vree, J. H. P. (1996). Gradient enhanced damage for quasi-brittle materials. *International Journal for numerical methods in engineering, 39*, 3391-3403.

Peerlings, R. H. J., Poh, L. H., & Geers, M. G. D. (2012). An implicit gradient plasticity–damage theory for predicting size effects in hardening and softening. *Engineering Fracture Mechanics, 95*, 2-12.

Petch, N. J. (1953). The cleavage strength of polycrystals. *J. Iron Steel Inst., 174*, 25-28.

Pijaudier-Cabot, G., & Bažant, Z. P. (1987). Nonlocal damage theory. *Journal of engineering mechanics, 113*(10), 1512-1533.

Pijaudier-Cabot, G., Bodé, L., & Huerta, A. (1995). Arbitrary Lagrangian–Eulerian finite element analysis of strain localization in transient problems. *International Journal for Numerical Methods in Engineering, 38*(24), 4171-4191.

Pineau, A., Benzerga, A. A., & Pardoen, T. (2016). Failure of metals I: Brittle and ductile fracture. *Acta Materialia, 107*, 424-483.

Poh, L. H., & Swaddiwudhipong, S. (2009). Gradient-enhanced softening material models. *International Journal of Plasticity, 25*(11), 2094-2121.

Poirier, J. P. (1980). Shear localization and shear instability in materials in the ductile field. *Journal of Structural Geology, 2*(1-2), 135-142.

Puttick, K. E. (1959). Ductile fracture in metals. *Philosophical magazine, 4*(44), 964-969.

Rabotnov, Y. N. (1969). Creep rupture. In *Applied mechanics* (pp. 342-349). Springer Berlin Heidelberg.

Rahman, R., & Haque, A. (2012). A peridynamics formulation based hierarchical multiscale modeling approach between continuum scale and atomistic scale. *International Journal of Computational Materials Science and Engineering, 1*(03), 1250029.

Rahman, R., & Foster, J. T. (2014). Bridging the length scales through nonlocal hierarchical multiscale modeling scheme. *Computational Materials Science, 92*, 401-415.

Renard, K., Idrissi, H., Schryvers, D., & Jacques, P. J. (2012). On the stress state dependence of the twinning rate and work hardening in twinning-induced plasticity steels. *Scripta Materialia, 66*(12), 966-971.

Rice, J.R. (1968). A Path Independent Integral and the Approximate Analysis of Strain Concentration by Notches and Cracks. *Journal of Applied Mechanics, 35*, 379-386.

Rice, J. R., & Tracey, D. M. (1969). On the ductile enlargement of voids in triaxial stress

fields*. *Journal of the Mechanics and Physics of Solids, 17*(3), 201-217.

Rice, J. R. (1976). *The localization of plastic deformation* (pp. 207-220). Division of Engineering, Brown University.

Rice, J. R. (1977). The localization of plastic deformation. In *Theoretical and Applied Mechanics*, edited by W. T. Koiter, pp. 207-10. North-Holland, Amsterdam.

Rice, J. R., & Rudnicki, J. W. (1980). A note on some features of the theory of localization of deformation. *International Journal of solids and structures, 16*(7), 597-605.

Ristinmaa, M. (1997). Void growth in cyclic loaded porous plastic solid. *Mechanics of Materials, 26*(4), 227-245.

Ritchie, R. O., Server, W. L., & Wullaert, R. A. (1979). Critical fracture stress and fracture strain models for the prediction of lower and upper shelf toughness in nuclear pressure vessel steels. *Metallurgical and Materials Transactions A, 10*(10), 1557-1570.

Rolshoven, S. (2003). *Nonlocal plasticity models for localized failure* (Doctoral dissertation, Institut de structures SECTION DE GÉNIE CIVIL POUR L'OBTENTION DU GRADE DE DOCTEUR ÈS SCIENCES PAR Dipl.-Ing. Physikalische Ingenieurwissenschaft, TU Berlin).

Rousselier, G. (1987). Ductile fracture models and their potential in local approach of fracture. *Nuclear engineering and design, 105*(1), 97-111.

Rousselier, G. (2001). Dissipation in porous metal plasticity and ductile fracture. *Journal of the Mechanics and Physics of Solids, 49*(8), 1727-1746.

Saanouni, K., Forster, C., & Hatira, F. B. (1994). On the anelastic flow with damage. *International Journal of Damage Mechanics, 3*(2), 140-169.

Samal, M. K., Seidenfuss, M., Roos, E., Dutta, B. K., & Kushwaha, H. S. (2009). A mesh-independent Gurson-Tvergaard-Needleman damage model and its application in simulating ductile fracture behaviour. *Proceedings of the Institution of Mechanical Engineers, Part C: Journal of Mechanical Engineering Science, 223*(2), 283-292.

Scheyvaerts, F., Onck, P. R., Tekoglu, C., & Pardoen, T. (2011). The growth and coalescence of ellipsoidal voids in plane strain under combined shear and tension. *Journal of the Mechanics and Physics of Solids, 59*(2), 373-397.

Shabrov, M. N., & Needleman, A. (2002). An analysis of inclusion morphology effects on void nucleation. *Modelling and Simulation in Materials Science and Engineering, 10*, 163-183.

Shi, M. X., Huang, Y., & Hwang, K. C. (2000). Plastic flow localization in mechanism-based strain gradient plasticity. *International Journal of Mechanical Sciences, 42*(11), 2115-2131.

Silling, S. A. (2000). Reformulation of elasticity theory for discontinuities and long-range forces. *Journal of the Mechanics and Physics of Solids, 48*(1), 175-209.

Silling, S. A., & Lehoucq, R. B. (2010). Peridynamic theory of solid mechanics. *Advances in applied mechanics, 44*, 73-168.

Silling, S., & Askari, A. (2014). *Peridynamic model for fatigue cracks*. (Report No. SAND2014-18590). Albuquerque, NM: Sandia National Laboratories.

Simo, J. C., Oliver, J., & Armero, F. (1993). An analysis of strong discontinuities induced by strain-softening in rate-independent inelastic solids. *Computational mechanics, 12*(5), 277-296.

Siruguet, K., & Leblond, J. B. (2004). Effect of void locking by inclusions upon the plastic behavior of porous ductile solids-I: theoretical modeling and numerical study of void growth. *International Journal of Plasticity, 20*, 225-254.

Smith, C. M., Deierlein, G. G., & Kanvinde, A. M. (2014). *A stress-weighted damage model for ductile fracture initiation in structural steel under cyclic loading and generalized stress states.* (Report No. 187). Stanford, CA.

Smith, C., Kanvinde, A., & Deierlein, G. (2017). A local criterion for ductile fracture under low-triaxiality axisymmetric stress states. *Engineering Fracture Mechanics, 169*, 321-335.

Stone, R. V., Cox, T. B., Low, J. R., & Psioda, J. A. (1985). Microstructural aspects of fracture by dimpled rupture. *International Metals Reviews, 30*(1), 157-180.

Swanson, J. and Leon, R. (2000). Bolted Steel Connections: Tests on T-Stub Components. *Journal of Structural Engineering, 126*(1), 50-56.

Taylor, G. I. (1938). Plastic strain in metals. *Journal of the Institute of Metals, 62*, 307-324.

Tekoglu, C., Leblond, J. B., & Pardoen, T. (2012). A criterion for the onset of void coalescence under combined tension and shear. *Journal of the Mechanics and Physics of Solids, 60*(7), 1363-1381.

Tekoglu, C. (2014). Representative volume element calculations under constant stress triaxiality, Lode parameter, and shear ratio. *International Journal of Solids and Structures, 51*(25), 4544-4553.

Thomason, P. F. (1968). A theory for ductile fracture by internal necking of cavities. *J Inst Metals, 96*(12), 360-365.

Thomason, P. F. (1985). Three-dimensional models for the plastic limit-loads at incipient failure of the intervoid matrix in ductile porous solids. *Acta Metallurgica, 33*, 1079-1085.

Toribio, J. (1997). A fracture criterion for high-strength steel notched bars. *Engineering*

fracture mechanics, 57(4), 391-404.

Torki, M. E., Benzerga, A. A., & Leblond, J. B. (2015). On void coalescence under combined tension and shear. *Journal of Applied Mechanics, 82*(7), 071005.

Tvergaard, V. (1981). Influence of voids on shear band instabilities under plane strain conditions. *International Journal of fracture, 17*(4), 389-407.

Tvergaard, V. (1982). On localization in ductile materials containing spherical voids. *International Journal of Fracture, 18*(4), 237-252.

Tvergaard, V., & Needleman, A. (1984). Analysis of the cup-cone fracture in a round tensile bar. *Acta metallurgica, 32*(1), 157-169.

Tvergaard, V. (1987). Effect of yield surface curvature and void nucleation on plastic flow localization. *Journal of the Mechanics and Physics of Solids, 35*(1), 43-60.

Tvergaard, V. (1989). Material failure by void growth to coalescence. *Advances in applied Mechanics, 27*, 83-151.

Tvergaard, V. (1990). Analysis of tensile properties for a whisker-reinforced metal-matrix composite. *Acta metallurgica et materialia, 38*(2), 185-194.

Tvergaard, V. (1993). Necking in tensile bars with rectangular cross-section. *Computer Methods in Applied Mechanics and Engineering, 103*(1-2), 273-290.

Tvergaard, V., & Needleman, A. (1995). Effects of nonlocal damage in porous plastic solids. *International Journal of Solids and Structures, 32*(8-9), 1063-1077.

Tvergaard, V., & Niordson, C. (2004). Nonlocal plasticity effects on interaction of different size voids. *International Journal of Plasticity, 20*(1), 107-120.

Tvergaard, V. (2008). Shear deformation of voids with contact modelled by internal pressure. *International Journal of Mechanical Sciences, 50*(10), 1459-1465.

Tvergaard, V. (2009). Behaviour of voids in a shear field. *International Journal of Fracture, 158*(1), 41-49.

Tvergaard, V. (2012). Effect of stress-state and spacing on voids in a shear-field. *International Journal of Solids and Structures, 49*(22), 3047-3054.

Tvergaard, V. (2015). Behaviour of porous ductile solids at low stress triaxiality in different modes of deformation. *International Journal of Solids and Structures, 60*, 28-34.

Vermeer, P. A., & Brinkgreve, R. B. J. (1994). A new effective nonlocal strain measure for softening plasticity. *Localization and bifurcation theory for soils and rocks*, R. Chambon, J. Desrues, & I. Vardoulakis, eds., Balkema, Rotterdam, The Netherlands, 89-100.

Voyiadjis, G. Z., & Kattan, P. I. (1990). A coupled theory of damage mechanics and finite

strain elasto-plasticity-II. Damage and finite strain plasticity. *International Journal of Engineering Science, 28*(6), 505-524.

Voyiadjis, G. Z., & Abu Al-Rub, R. K. (2006). A finite strain plastic-damage model for high velocity impacts using combined viscosity and gradient localization limiters: Part II-numerical aspects and simulations. *International Journal of Damage Mechanics, 15*(4), 335-373.

Wcisło, B., & Pamin, J. (2017). Local and non-local thermomechanical modeling of elastic-plastic materials undergoing large strains. *International Journal for Numerical Methods in Engineering, 109*(1), 102-124.

Weck, A. G. (2007). *The role of coalescence on ductile fracture.* (Doctoral dissertation). McMaster University, Hamilton, Ontario.

Weck, A., & Wilkinson, D. S. (2008). Experimental investigation of void coalescence in metallic sheets containing laser drilled holes. *Acta Materialia, 56*(8), 1774-1784.

Weck, A., Wilkinson, D. S., Maire, E., & Toda, H. (2008). Visualization by X-ray tomography of void growth and coalescence leading to fracture in model materials. *Acta Materialia, 56*(12), 2919-2928.

Wells, A. (1961, September). Unstable crack propagation in metals: cleavage and fast fracture. In *Proceedings of the crack propagation symposium* (Vol. 1, No. 84).

Wen, H., & Mahmoud, H. (2015). New Model for Ductile Fracture of Metal Alloys. I: Monotonic Loading. *Journal of Engineering Mechanics, 142*(2), 04015088.

Wierzbicki, T., Bao, Y., Lee, Y. W., & Bai, Y. (2005). Calibration and evaluation of seven fracture models. *International Journal of Mechanical Sciences, 47*(4), 719-743.

Wierzbicki, T., & Xue, L. (2005). *On the effect of the third invariant of the stress deviator on ductile fracture.* (Report No. 136). Cambridge, MA: Massachusetts Institute of Technology, Impact and Crashworthiness Laboratory.

Wilner, B. (1988). Stress analysis of particles in metals. *Journal of the Mechanics and Physics of Solids, 36*(2), 141-165.

Wilkins, M. L., Streit, R. D., & Reaugh, J. E. (1980). *Cumulative-strain-damage model of ductile fracture: simulation and prediction of engineering fracture tests.* (Report: UCRL-53058). San Leandro, CA: Lawrence Livermore National Laboratory, Science Applications, Inc.

Wong, W. H., & Guo, T. F. (2015). On the energetics of tensile and shear void coalescences. *Journal of the Mechanics and Physics of Solids, 82*, 259-286.

Wu, J. Y., Li, J., & Faria, R. (2006). An energy release rate-based plastic-damage model for concrete. *International Journal of Solids and Structures, 43*(3), 583-612.

Wu, S., & Wang, X. (2010). Mesh dependence and nonlocal regularization of one-

dimensional strain softening plasticity. *Journal of engineering mechanics, 136*(11), 1354-1365.

Xue, L. (2007a). *Ductile fracture modeling-theory, experimental investigation and numerical verification*. (Doctoral dissertation). Massachusetts Institute of Technology, Cambridge, MA.

Xue, L. (2007b). Damage accumulation and fracture initiation in uncracked ductile solids subject to triaxial loading. *International Journal of Solids and Structures, 44*(16), 5163-5181.

Xue, L. (2008). Constitutive modeling of void shearing effect in ductile fracture of porous materials. *Engineering Fracture Mechanics, 75*(11), 3343-3366.

Xue, L., & Wierzbicki, T. (2008). Ductile fracture initiation and propagation modeling using damage plasticity theory. *Engineering Fracture Mechanics, 75*(11), 3276-3293.

Xue, L. (2010). Localization conditions and diffused necking for damage plastic solids. *Engineering Fracture Mechanics, 77*(8), 1275-1297.

Zhang, G., Le, Q., Loghin, A., Subramaniyan, A., & Bobaru, F. (2016). Validation of a peridynamic model for fatigue cracking. *Engineering Fracture Mechanics, 162*, 76-94.

Zhang, K. S., Bai, J. B., & Francois, D. (2001). Numerical analysis of the influence of the Lode parameter on void growth. *International Journal of Solids and Structures, 38*(32), 5847-5856.

Zhang, Y. Q., Liu, G. R., & Han, X. (2004). Analysis of strain localization for ductile materials with effect of void growth. *International journal of mechanical sciences, 46*(7), 1021-1034.

Zhang, Z. L., Thaulow, C., & Ødegård, J. (2000). A complete Gurson model approach for ductile fracture. *Engineering Fracture Mechanics, 67*(2), 155-168.

Zienkiewicz, O. C., & Huang, G. C. (1990). A note on localization phenomena and adaptive finite-element analysis in forming processes. *Communications in applied numerical methods, 6*(2), 71-76.

Zybell, L., Hütter, G., Linse, T., Mühlich, U., & Kuna, M. (2014). Size effects in ductile failure of porous materials containing two populations of voids. *European Journal of Mechanics-A/Solids, 45*, 8-19.

Vita

Yazhi Zhu was born in December 1987 in Yixing, Jiangsu, China, the son of Huajuan Ma and Huyuan Zhu. After graduating from Jiangsu Yixing high school in 2006, he was enrolled at Southeast University in Nanjing, China. He received his Bachelor of Engineering in Civil Engineering from Southeast University in June 2010. In the fall of 2010, he re-entered the Southeast University, for pursuing a Master of Science in Structural Engineering, which he received in June 2013. In August 2013, he entered the doctoral program at The University of Texas at Austin in the Department of Civil, Architectural, and Environmental Engineering and was specialized in structural engineering.

Permanent e-mail address: yzzhu@utexas.edu

This dissertation was typed by the author.